Amplifier control using machine learning and coloured optical packet switching node design in optical networks

Maria José Freire Hermelo

INSTITUT POLYTECHNIQUE DE PARIS

NNT : 2020IPPAS024

Thèse de doctorat

Amplifier control using machine learning and coloured optical packet switching node design in optical networks

Thèse de doctorat de l'Institut Polytechnique de Paris
préparée à Télécom SudParis

École doctorale n°626 École doctorale de l'Institut Polytechnique de Paris (EDIPP)
Spécialité de doctorat : Réseaux, informations et communications

Thèse présentée et soutenue à Évry, le 16/12/2020, par

MARIA FREIRE-HERMELO

Composition du Jury :

Yves Jaouen Professeur, Télécom Paris	Président
Nicola Calabretta Professeur associé, Eindhoven University of Technology	Rapporteur
Bruno Fracasso Professeur, IMT Atlantique	Rapporteur
Ramon Casellas Chercheur Senior, CTTC	Examinateur
Christine Tremblay Professeur, École de Technologie Supérieure Montréal	Examinateur
Catherine Lepers Professeur, Télécom SudParis	Directeur de thèse
Antoine Lavignotte Maître de Conférence, Télécom SudParis	Co-directeur de thèse
Dominique Chiaroni Ingénieur de Recherche, Nokia Bell Labs	Invité

ECOLE DOCTORALE

Titre : Contrôle des amplificateurs par apprentissage machine et conception de nœuds de commutation de paquets optiques colorés dans les réseaux optiques

Mots clés : Amplificateurs à fibre dopée à l'erbium, apprentissage machine, réseaux optiques, commutation de paquets optiques colorés, excursion de puissance optique, qualité de transmission

Résumé : Le débit de données et la consommation d'énergie sont les principaux défis auquels doivent faire face les réseaux optiques. Afin de réduire la consommation d'énergie, les réseaux opérateurs de transport optiques basés sur le concept de commutation de circuits optiques (OCS), deviennent optiquement transparents, réduisant les conversions optique/électrique (O/E) et électrique/optique (E/O). Pour faire face à l'augmentation du débit de données, on utilise des formats de modulations complexes et la technique de multiplexage en polarisation et on économise le spectre des fibres optiques en considérant une grille en longueurs d'onde plus flexible que la grille fixe ITU-T WDM. On développe des transpondeurs flexibles capables de sélectionner différents formats de modulation et longueurs d'onde; on développe également des multiplexeurs optiques d'insertion/extraction reconfigurables (ROADMs) basés sur des commutateurs sélectifs en longueur d'onde (WSSs).
Ces réseaux flexibles prennent également en compte un trafic plus dynamique. Dynamisme et flexibilité impactent fortement les équipements des réseaux optiques, y compris les nœuds optiques d'un point de vue couche physique et couche de contrôle. Lorsque des canaux ou demandes sont ajoutés et/ou extraits, l'excursion de puissance optique des amplificateurs à fibre dopée à l'erbium (EDFAs) varie temporellement ce qui implique qu'elle doit être contrôlée dynamiquement. Dans ce contexte, le concept de réseau défini par le soft (SDN: Software Defined Network) prend tout son sens et l'introduction des techniques d'apprentissage machine (ML) permet d'entrevoir une aide au concept de SDN pour la gestion et le contrôle dynamique des réseaux optiques.
Dans la première partie de ce travail de thèse, nous étudions l'excursion de puissance optique dans les réseaux de transport optiques dynamiques. Afin d'en atténuer les effets indésirables, nous introduisons et mettons en œuvre un module de prédiction et de précompensation de l'excursion de puissance en utilisant les méthodes ML. Comme les altérations de la couche physique (PLIs : Physical Layer Impairments) s'accumulent le long du chemin optique entre les noeuds source et destination de réseau, nous associons à l'excursion de puissance optique le rapport signal/bruit optique (OSNR: Optical Signal to Noise Ratio) et le taux d'erreur binaire (BER: Bit Error Rate), afin d'estimer la qualité de transmission (QoT: Quality of Transmission) de nouvelles configurations de canaux. Ensuite, en utilisant l'approche d'apprentissage par renforcement (RL), nous attribuons un format de modulation et une longueur d'onde aux différents canaux de façon automatique afin de réduire la probabilité de blocage des demandes entrantes dans les nœuds optiques.
Dans la deuxième partie de ce travail de thèse, nous présentons notre contribution en tant que partenaire du projet ANR N-GREEN. Le principal objectif de N-GREEN est de proposer une nouvelle génération de routeurs peu consommateurs en énergie en considérant une architecture de réseau. Dans ce projet, nous abordons une architecture de réseau basée sur la commutation optique de paquets colorés (OPS: Optical Packet Switching) en rupture avec celle considérée dans la première partie de cette thèse. Dans le cadre de ce projet, nous avons caractérisé expérimentalement un commutateur optique 2×2 basé sur des amplificateurs optiques à semi-conducteurs (SOAs). Cette caractérisation nous a permis de valider un réseau en anneau constitué de 10 noeuds en cascade. En envisageant une configuration de commutateur 16×16, la caractérisation expérimentale, dans des configurations à canal unique et WDM, laisse entrevoir des possibilités intéressantes pour la transmission de données à très haut débit.

Title : Amplifier control using machine learning and coloured optical packet switching node design in optical networks

Keywords : Erbium doped fiber amplifiers, machine learning, optical networks, coloured optical packet switching, optical power excursion, quality of transmission

Abstract : Data rate and energy consumption are the major concerns in optical networks. In order to reduce energy consumption, transport operator networks based on optical circuit switching (OCS) concept, are becoming optically transparent, reducing optical to electrical (O/E) and electrical to optical (E/O) conversions. To face data rate increase, complex modulation formats and dual-polarization systems are considered and fiber spectrum is saved using network resources in a more efficient way, giving rise to a flexible frequency grid. Flexible transponders are developed to tune modulation formats and wavelengths and reconfigurable optical add/drop multiplexers (ROADMs) based on wavelength selective switches (WSSs) are studied.

Flexible networks consider also a more dynamic traffic. Dynamism and flexibility lead to a deep transformation of the optical networks, including optical nodes, from both physical and control layer point of view. When channels are added and/or dropped, optical power excursion from erbium doped fiber amplifiers (EDFAs) has to be controlled dynamically. In that context, software defined networking (SDN) assisted by machine learning (ML) techniques is envisaged as promising candidate for the management and the dynamic control of optical networks.

In this context, in the first part of our PhD work, we deal with optical power excursion in dynamic optical transport networks. In order to mitigate undesirable effects, we introduce and implement power excursion prediction and pre-compensation module using ML methods. As physical layer impairments (PLIs) accumulate along the path, we consider optical power excursion together with optical signal to noise ratio (OSNR) and bit error rate (BER), to estimate quality of transmission (QoT) of unseen channel configurations. Afterwards, using a reinforcement learning (RL) approach, we establish an autonomous impairment aware modulation format and wavelength assignment procedure, and we show that this permits to reduce the blocking probability of the incoming demands in optical nodes.

In the second part of our PhD work, in the context of the N-GREEN project from the French national agency of research, we address a disruptive network architecture based on coloured optical packet switching (OPS). The main objective of N-GREEN is to propose a new generation of energy efficient routers. In the N-GREEN project, we perform the experimental characterization of an optical 2×2 switch based on semiconductor optical amplifiers (SOAs). This characterization leads to the proof of concept of a ring network with 10 nodes in cascade. Envisaging a 16×16 switch configuration, the experimental characterization, in single channel and WDM configurations, unveil interesting possibilities for the transmission of ultra-high data rates.

Institut Polytechnique de Paris
91120 Palaiseau, France

Acknowledgements

I would like to thank the following people without whom my PhD work would not have been completed.

My supervisor, Catherine Lepers, for her continuous guidance and support during the whole PhD process, research and writing. Her invaluable insights have been decisive in the development of the work presented here. Without her motivation and enthusiasm, this PhD would not be possible.

My co-supervisor, Antoine Lavignotte, always supportive and willing to assist in each stage of the work. His thoughtful comments and recommendations have been of great importance to complete this work.

The reviewers, Nicola Calabretta and Bruno Fracasso, for reviewing my manuscript and helping to greatly improve it.

All the jury members, Yves Jaouen, Christine Tremblay, Ramon Casellas and Dominique Chiaroni for accepting to evaluate my work, providing fruitful comments and suggestions.

Djamel Amar, Franck Gillet and Sébastien Mansfeld, for advising and collaborating in the first steps of this research project.

Christine Tremblay and Dipankar Sengupta, for their patience, always willing to help in any possible way: experimental measurements, meetings, reviews... Their knowledge and experience have been of incredible valuable.

All the people involved in the ANR N-GREEN project, especially Atchutananda Surampudi, Alexandre Shen, Mengdi Song, Cédric Ware, Yves Jaouen, Eloise de Carvalho Rodrigues, Dominique Chiaroni, not only for their help in the experimental work but also for sharing their knowledge.

All the people that indirectly contributed to this work: Nicolas Montes and Loic Duboquet for their help in software subjects and Ydalia Garcia, Patricia Fixot, Sandra Gchweinder, Zahia Zendagui and Veronique Guy for facilitating all required administrative procedures.

The people from the RST and EPH departments, especially my colleagues for their support, always creating a great atmosphere: Nesrine, Franklin, Nazhatul, Marwan, Souha, Mariana, Mohammed, Ana, Fabien, Jose.

My family and friends for their understanding and encouragement. And specially, my fiance for his unconditional support.

Contents

Acronyms

A2C Advantage Actor Critic.

A3C Asynchronous Advantage Actor Critic.

AGC Automatic Gain Control.

ASE Amplified Spontaneous Emission.

AWG Arrayed Waveguide Grating.

B2B Back-to-Back.

BER Bit Error Rate.

BMRx Burst-Mode-Receiver.

CBR Case Based Reasoning.

CC Current control.

CD Chromatic Dispersion.

CNN Convolutional Neural Network.

CSI Channel State Information.

DCM Dispersion Compensating Module.

DDPG Deep Deterministic Policy Gradient.

DP Dual Polarization.

DP-MZM Dual Polarization-Mach Zehnder Modulator.

DSO Digital Sampling Oscilloscope.

DSP Digital Signal Processing.

E/O Electrical to Optical.

EDF Erbium Doped Fiber.

EDFA Erbium Doped Fiber Amplifier.

EVM Error Vector Magnitude.

FDL Fiber Delay Line.

FEC Forward Error Correction.

FF First Fit.

FF-Center First-Fit closest to the CENTER of the band.

FF-L2H First-Fit from Lowest to Highest frequencies.

FFT Fast Fourier Transform.

FWM Four-Wave Mixing.

GFF Gain Flattening Filter.

GMPLS Generalized Multi-Protocol Label Switching.

GN Gaussian Noise.

HT Holding Time.

IA-RWA Impairment-Aware Routing and Wavelength Assignment.

IAT Inter-Arrival Time.

IGN Incoherent Gaussian Noise.

ILM Integrated Laser Modulator.

ILP Integer Linear Programming.

IPDR Input Power Dynamic Range.

ISI Intersymbol Interference.

k-NN k-Nearest Neighbors.

LC Liquid Crystal.

LCoS Liquid Crystal on Silicon.

LiNbO3 Lithium Niobate.

LP Linear Programming.

MEMS MicroElectroMechanical Systems.

ML Machine Learning.

MPLS Multiprotocol Label Switching.

NF Noise Figure.

NLI NonLinear Interference.

NN Neural Network.

O/E Optical to Electrical.

OADM Optical Add/Drop Multiplexer.

OCS Optical Burst Switching.

OPS Optical Packet Switching.

OSA Optical Spectrum Analyzer.

OSC Optical Supervisor Channel.

OSNR Optical Signal to Noise Ratio.

PC Polarization Controller.

PCA Principal Component Analysis.

PDME Polarization Division Multiplexer Emulator.

PLC Planar Lightwave Circuit.

PLI Physical Layer Impairments.

PLZT Lead Lanthanum Zirconate Titanate.

PMD Polarization Mode Dispersion.

POADM Packet Optical Add/Drop Multiplexer.

PPO Proximal Policy Optimization.

QAM Quadrature Amplitude Modulation.

QoS Quality of Service.

QoT Quality of Transmission.

QPSK Quadrature Phase-Shift Keying.

RAM Random Access Memory.

ReLU Rectified Linear Unit.

RF Random Forest.

RL Reinforcement Learning.

ROADM Reconfigurable Optical Add/Drop Multiplexer.

RWA Routing and Wavelength Assignment.

SCH Separate Confinement Heterostructure.

SD-FEC Soft Decision Forward Error Correction.

SDM Spatial Division Multiplexing.

SDN Software Defined Networking.

SMF Single-Mode Fiber.

SNR Signal to Noise Ratio.

SOA Semiconductor Optical Amplifier.

SPM Self-Phase Modulation.

SRS Stimulated Raman Scattering.

SVM Support Vector Machine.

TRPO Trust Region Policy Optimization.

VOA Variable Optical Attenuator.

WDM Wavelength Division Multiplexing.

WSADM WDM-Slotted Add/Drop Multiplexer.

WSS Wavelength Selective Switch.

XPM Cross-Phase Modulation.

List of Figures

List of Tables

Main introduction

Year by year the number of internet users, devices and connections increase continuously [1]. Video streaming, web services, gaming, social applications and file sharing are some of the most hungry applications representing a large part of the global traffic [2]. Apart from high capacity, 5G wireless networks request low latency and precise synchronization [3]. All these factors shape the evolution of optical networks.

First generation of opaque optical networks was based on point-to-point links, where at each node, all the traffic had to undergo optical to electrical (O/E) and electrical to optical (E/O) conversions. All the intelligence of the network, routing and switching capabilities, resided in the electrical domain.

Second generation initiated the road towards transparency, reducing the network cost and improving its energy-efficiency [4], [5]. First, erbium doped fiber amplifiers (EDFAs) allowed to compensate fiber propagation losses in wavelength division multiplexing (WDM) systems avoiding O/E-E/O conversions. After, the introduction of optical add-drop multiplexers (OADMs) introduced the optical bypass concept, i.e. traffic for which the current node is not its final destination can pass-through the node, escaping again from unnecessary O/E-E/O conversions. This second generation has acquired intelligence, including an optical control plane, which permits to perform switching functionalities, usually based on an electrical control. Although current second generation, includes already reconfigurability capabilities, e.g. using reconfigurable optical add-drop multiplexers (ROADMs), it relies mainly on static traffic.

Third generation of optical networks is still under active development phase. Photonics community considers the circuit switching-based operation as fundamental in the optical systems currently in use. An interesting alternative discussed in the literature, although still immature due to optical buffering and optical signal processing issues, could be potentially based on optical packet switching (OPS) operation [6]. Presumably preserving optical circuit switching, third generation will be likely to be based on transparency, exploiting all-optical switching.

In order to answer to the high-capacity requirements imposed by the traffic, third generation is expected to grow on dynamism and flexibility. Under dynamic traffic conditions, where

channels are often added and dropped, dynamic reconfiguration capabilities allow for a more efficient use of the available spectrum [7]. Flexible optical networks, where instead of a fixed frequency grid of 50 GHz frequency spacing, a flexible frequency grid with 12.5 GHz frequency slots is considered, permit to assign a channel to any multiple of the fundamental slot, contributing to optimize the spectrum usage [8]. Furthermore, due to the independence of modulation formats and data rates given by the use of transparent nodes, flexible frequency grid can be combined with mixed line rates and different modulation formats, upgrading the network performance.

To exploit these capabilities, flexibility and dynamism, optical control plane is gaining more importance, with software defined networking (SDN) becoming more popular [9]. Control and management of the network is therefore carried out by soft-controllers. However, with optical networks becoming more and more complex, controllers need to be provided with intelligence. Machine learning (ML) techniques have demonstrated to be able to provide this intelligence at network and physical layer level, supporting different tasks as routing and wavelength assignment (RWA), optical amplifier control or quality of transmission (QoT).

In this context, the first part of the PhD thesis has addressed the control plane. With physical layer impairments (PLIs) accumulating along the path in transparent networks, a customised control of the physical layer must be executed. Our work contributes to build autonomous optical networks, able to deal with different impairments as optical power excursion (permanent power transients) coming from optical amplifiers. Algorithms used with the aim of achieving this purpose can be already introduced in the short-term in dynamic and flexible optical networks. Making decisions in an autonomous way, these envisaged approaches built on ML techniques allow to rapidly take actions based on the current network state with the objective of improving the system performance. The actions considered here include optical input launch channel power adjustment and modulation format and wavelength assignment. Each action is optimized pursuing a particular objective. Optical input launch channel power is adjusted with the aim of reducing mean optical power excursion at the output of a link. Modulation format and wavelength assignment is performed in order to reduce blocking probability while taking into consideration optical signal to noise ratio (OSNR), bit error rate (BER) and optical power excursion. In the second part, work has been particularly focused on the physical layer, analyzing the performance of optical nodes exploiting optical switching capabilities under packet mode operation.

Contributions

In this manuscript, contributions are organized in two main parts:

- ML techniques for physical layer control: In order to improve the performance of dynamic and flexible transparent optical networks, we have devoted effort to develop techniques providing intelligence to the network:

  - Initially oriented to optical amplifier control and focusing on a particular impairment, optical power excursion due to optical amplifiers, two different solutions are proposed based on ML techniques:
    * Optical power excursion prediction using neural networks (NNs) [10]. These estimations can be used during RWA process in order to reduce optical power excursions.
    * Power precompensation based on reinforcement learning (RL) with the aim of mitigating optical power excursion [11].
  - Beyond optical amplifier control, but still dealing with the optical power excursion problematic, we have addressed the wavelength assignment problem:
    * Impairment aware modulation format and wavelength assignment based on RL has been proposed. Considering jointly optical power excursion with OSNR and BER, this solution allows to autonomously allocate traffic requests reducing blocking probability compared to other heuristic approaches. Implemented for two different scenarios, fixed and flexible frequency grid, the algorithm demonstrates not only to reduce blocking probability but also to contribute to spectrum defragmentation by reducing mean optical power excursion [12].

- Coloured optical packet switching in the N-GREEN project: This contribution examines OPS in the framework of the N-GREEN project, developing a new generation of routers for energy efficient networks. Our contribution to the N-GREEN project was:

  - Experimental characterization of the N-GREEN switch: In this context, we have performed the experimental characterization of a 2×2 optical switch based on semiconductor optical amplifiers (SOAs), which has revealed impressive capabilities handling high data rates [13]. Up to a switch capacity of 1 Pb/s is estimated, when the 2×2 optical switch is integrated as part of a high port count switch. A possible application for this type of switch may be the backplane, interconnecting the switch fabrics with processing boards, substituting current electronic interconnections [14].

Thesis organization

This PhD thesis is organized as follows:

Chapter 1 introduces our research context. Through the evolution of optical networks towards transparent networks, some key concepts about optical networks and their constituent elements are presented, highlighting the role of SDN aided by ML techniques. In addition, OPS, key idea on the disruptive solution proposed in the N-GREEN project, is briefly discussed.

Envisaging dynamic and flexible optical networks, Chapter 2, after introducing ML techniques, presents the optical power excursion problematic and the work performed in the last years in

order to mitigate its effect on the system performance. Then, our contributions are introduced. First, using ML, optical power excursion prediction is demonstrated. Second, optical power excursion mitigation by means of power predistortion based on RL is proven.

In the same scenario, but including OSNR and BER in our study in order to solve to wavelength assignment problem, an impairment aware modulation format and wavelength assignment algorithm based on RL is presented in Chapter 3. After a state of the art of RWA proposed solutions, our RL-based approach is presented. Including different parameters, as optical power excursion, OSNR and BER, the RL algorithm succeeds in intelligently allocating traffic requests in two different scenarios, fixed and flexible frequency grid.

Focusing on a possible future transition to packet switching operation, as part of ANR (French National Research Agency) N-GREEN project, Chapter 4 describes the experimental characterization, in single channel and WDM configuration, of a 2×2 optical switch based on SOAs working as optical gates.

Finally, conclusions are drawn, summarising results and providing open future research lines.

1 Research context

The already dramatic exponential traffic growth experienced in optical communication systems has been pushed even further by 5G applications, including new requirements as low latency and accurate synchronization [3]. Although traffic predictions are not obvious, several works have been forecast future traffic trends [15], [16]. Interface rates and system capacities evolution over the last ~ 30 years, and extrapolation for the next ~ 20 years is shown in Fig. 1.1. While CMOS-based packet processing technologies are increasing by ~ 40 % each year, system capacity is only increasing by ~ 20 %. This alarming ~ 40 %/~ 20 % ratio is expected to lead to an optical capacity crunch [17]–[19]. Another disturbing subject is the energy consumption. Information and communication technology systems account already for 5 % of the total electricity consumption [19]. System capacity increase is accompanied by an increment in the energy consumption. Evolution towards transparent optical networks together with a responsible and adequate energy planning scheme are decisive for the development of future optical networks.

Bearing this in mind, five physical dimensions have been explored in order to increase the capacity (Fig. 1.2) [17], [21]:

- Time: Symbol rate, pulse shape.
- Quadrature: Real and imaginary part.
- Polarization: Orthogonal polarizations.
- Frequency: WDM.
- Space: Different spatial paths (cores, modes).

In fact, the ~ 20 % increase in system capacity has mainly been driven by two physical dimensions: (1) quadrature, using high-order modulation formats, (2) polarization, including

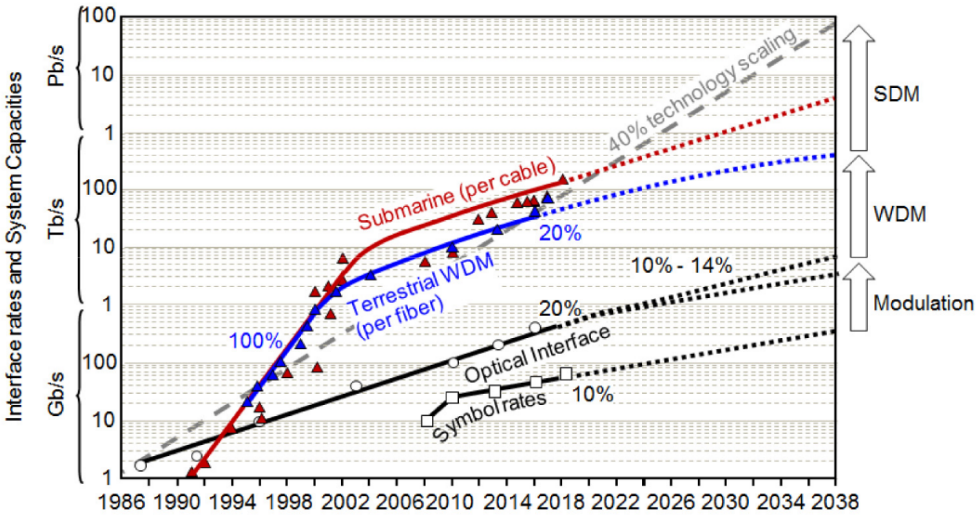

Figure 1.1 – Evolution of commercial optical transmission systems [20].

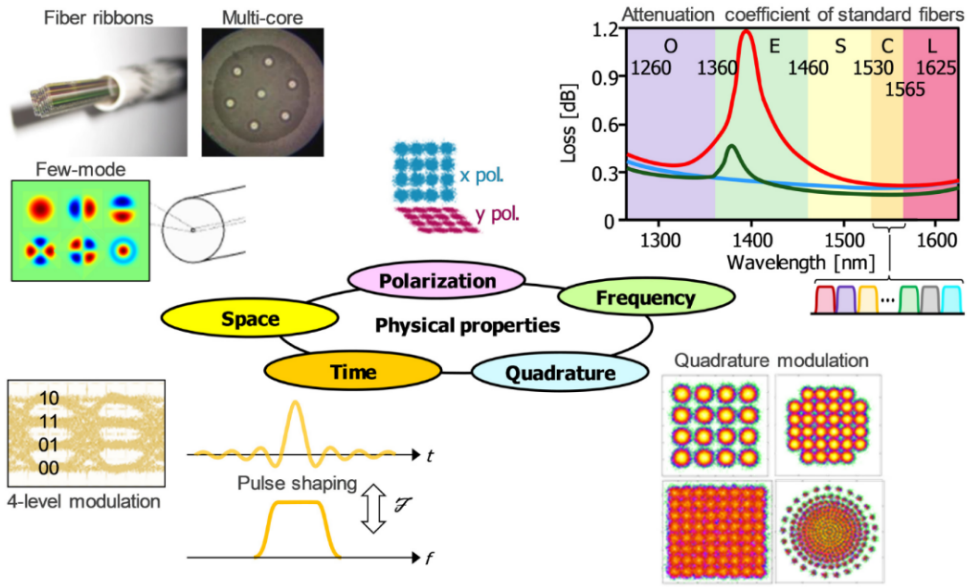

Figure 1.2 – Five physical dimensions to increase capacity [20].

polarization division multiplexing [22]. However, this increase will not be sustainable over the next years, intensifying the research in spatial division multiplexing (SDM) techniques.

Another strategy to squeeze the fiber capacity intends to use resources in a more efficient way. On the one hand, preserving optical circuit switching (OCS) in transparent optical networks, but allowing dynamic demands instead of the current static traffic, allows for a more efficient spectrum usage. On the other hand, flexible line cards supporting the adjustment of physical parameters permit to accommodate diverse traffic demands, increasing again the efficiency. Some of these tuneable parameters are data rate, modulation format and

frequency, considering a flexible frequency grid enabling optical super-channels [8]. Apart from dynamism and flexibility, which must be supported not only by line cards but also by the optical nodes, the third fundamental piece in order to really exploit these compelling capabilities is intelligence. ML techniques integrated in SDN-based architectures provide intelligent management and network control, leading to network automation [20], [23]. Typical functionalities to be included are RWA tasks, which become more complicated in dynamic and flexible networks. Many other capabilities may be also integrated: power control techniques, critical in dynamic optical networks or PLI prediction and mitigation, crucial in transparent optical networks with PLIs accumulating along the lightpaths.

In this context, during the first part of the PhD thesis, we have addressed physical layer control tasks by means of ML techniques providing network automation capabilities. Chapter 2 deals with the power control task in transport optical networks with a fixed grid. In particular, we have addressed optical power excursions[1] due to wavelength-dependent gain in optical amplifiers, worrisome matter under dynamic traffic conditions. Chapter 3 couples optical power excursion together with QoT, to perform impairment aware modulation format and wavelength assignment, complex problem in dynamic and flexible optical networks.

In the second part, a disruptive solution with respect to the first one is proposed. Instead of OCS, OPS is considered. Although immature in terms of optical buffering and optical signal processing, OPS has been envisaged in the literature as a long-term solution, offering higher bandwidth efficiency [24]. Chapter 4 considers an optical node for OPS networks, developed in the framework of the N-GREEN (New Generation of Routers for Energy Efficient Networks) project. By exploiting transparency and the use of integrated transceivers, this innovative optical node reduces energy consumption, main concern in optical networks. As part of the N-GREEN project, Chapter 4 presents the work performed on the experimental characterization of an optical switch, constituent element of the complete envisioned N-GREEN node.

This chapter gives a brief overview of the network evolution in Section 1.1, with a focus on optical node in Section 1.2. Considering an SDN-based architecture, Section 1.3 examines the impressive role ML techniques are starting to play in optical networks, providing intelligence to the network. Finally, Section 1.4 describes the distinctive characteristics of the optical network operation studied in Chapter 4.

1.1 Network Evolution

In optical network architectures, three main different segments can be distinguished (Fig. 1.3): long-haul (core), metropolitan (metro) and access. Long-haul networks are the core of the optical network, interconnecting continents. On the other side, access networks are the closest to the end users. In between long-haul and access networks, metro networks connect the

[1] Optical power excursions are permanent power transients, extensively addressed in Chapters 2 and 3.

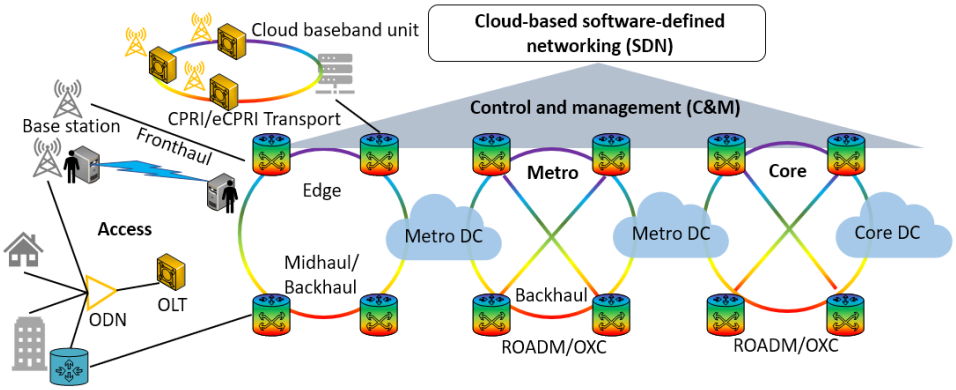

Figure 1.3 – Optical network architecture, based on [17].

long-haul and access networks, covering cities or regions.

Since a couple of years, optical transport networks have been evolved from opaque to transparent networks.

Opaque networks include regenerators in each intermediate node, involving O/E-E/O conversions. Contrary to opaque networks, transparent optical networks, also called all-optical networks, establish end-to-end connections in which signals are always kept in the optical domain, bypassing intermediate nodes without undergoing O/E-E/O conversions. These networks facilitate the transition to flexible optical networks, where bit rates, modulation and signal formats can be tuned matching the traffic demands. However, as a consequence of the lack of regeneration, PLIs accumulate along the path, limiting the reach. One of these PLIs, optical power excursion is dealt with in Chapters 2 and 3.

Translucent networks combine both types of nodes: nodes including bypassing capabilities (transparent) and nodes performing O/E-E/O conversions (opaque).

1.2 Optical node evolution

In the first generation of optical networks, based on opaque point-to-point links, only transport functionality was performed in the optical domain [25]. Routing and switching of demands were implemented in the electrical domain. For transmission, traffic was multiplexed on different wavelengths onto a fiber. For reception, traffic was demultiplexed in the original wavelengths to be delivered to the client or to be transmitted again, after regeneration, E/O conversion and multiplexing.

Second generation of optical networks included the notion of optical bypass: traffic which destination is not the current node can pass-through the node without undergoing E/O-O/E conversions. Considering approximately 50 % of the traffic in a node corresponds to pass-through traffic, optical bypass represented a significant reduction in cost and energy

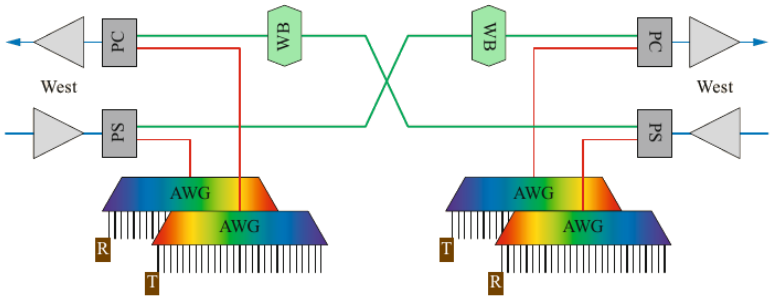

Figure 1.4 – Wavelength blocker ROADM architecture [28]. In the figure: array waveguide grating (AWG), power combiner (PC), power splitter (PS), receiver (R), transmitter (T), wavelength blocker (WB).

consumption, by avoiding transponders [25]. Key enabling technologies are the OADM and ROADMs, the latter including reconfiguration capabilities, allowing to add/drop wavelengths on the fly.

OADMs and ROADMs are used in the intermediate nodes, where three functionalities are available: channel adding, channel dropping and channel optical bypass. It is possible to visualize an ROADM as two (de)multiplexers connected back-to-back: (1) the first one demultiplexes the different wavelengths, dropping some of them, (2) the second one multiplexes the wavelengths passing through, together with added wavelengths [26]. Two sections can be distinguished in an ROADM: mux/demux and a switch core, in order to include the add/drop/bypass capabilities [27]. Besides, a control layer, which will be described in the next section, manages the ROADM operation.

First commercialized ROADMs integrated wavelength blockers. Able to deal with up to 100 channels in a fixed frequency grid, there were the selected option for the long-haul applications (backbone) [27]. Usually based on a broadcast and select architecture (Fig. 1.4), using an optical splitter, traffic is transferred to a demultiplexer and a wavelength blocker, with the blocker deciding which wavelengths to terminate and which wavelengths to pass-through. After the wavelength blocker, an optical coupler allows to add wavelengths.

Whereas ROADMs integrating wavelength blockers were used in the backbone, planar lightwave circuits (PLCs) based ROADMs were popular in the metro ring networks, as the one illustrated in Fig. 1.5 [27], [29]. A power splitter allows dropping channels through a first demultiplexer. For adding channels, wavelengths are also first demultiplexed. Then, for each wavelength, a 2×2 switch decides whether a wavelength is added or the existing wavelength passes through (optical bypass). Finally, wavelengths are again multiplexed into the fiber. The disadvantage of this architecture is that all the channels, included the ones bypassing the ROADM, have to be demultiplexed and multiplexed introducing filtering losses [26].

None of them, wavelength blocker or PLC based ROADMs are suitable for multi-degree architecture. In this sense, wavelength selective switches (WSSs) have become very popular in

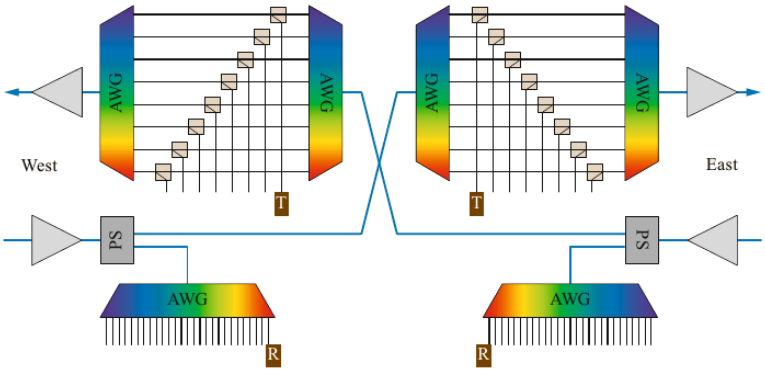

Figure 1.5 – PLC-ROADM architecture [28]. In the figure: array waveguide grating (AWG), power splitter (PS), receiver (R), transmitter (T).

ROADM architectures, allowing for more scalability [30]. Based on different technologies as microelectromechanical systems (MEMS) or liquid crystals (LCs), WSS functionality is similar to a demultiplexer. However, while a demultiplexer is based on fixed frequencies, a WSS allows to direct any wavelength, waveband or group of wavelengths to any output fiber. Configuration can be modified easily using an electrical interface. ROADM degree 2 architecture based on WSSs is shown in Fig. 1.6a. A first WSS is located at the input of the ROADM. One of its outputs is used for the pass-through signals and another is used for the dropping channels. A second WSS is used for adding channels. Based on the same principle, a multi-degree architecture is shown in Fig. 1.6b. Note that by slicing the spectrum in small slices of 6.25 GHz bandwidth, WSS architectures are also able to work on flexible frequency grid [27].

ROADMs have continued to evolve, mainly at the mux/demux section, in order to include new functionalities: colorless, directionless and contentionless [31]:

- Colorless: Any wavelength can be transmitted/received at any port. If a transceiver changes its wavelength, it does not need to be moved to another port. Architectures as the one shown in Fig. 1.6b, based on array waveguide gratings (AWGs) are colored. Some approaches which can be used at the mux/demux section of the ROADM architecture in order to become colorless are: (1) optical power splitter connected to a WSS, (2) AWG followed by an optical cross-connect, (3) power splitter followed by tuneable filters [27].

- Directionless: A transponder can access any fiber. This can be achieved by using colorless mux/demux together with power splitters and WSS [27].

- Contentionless: Wavelength blocking is avoided. This property can be accomplished by: (1) using multicast switches (Fig. 1.7a), (2) using WSSs (Fig. 1.7b) [27].

In the long-term ROADMs will keep progressing in order to adapt to future use-case scenarios. To increase capacity, dynamic traffic conditions are envisaged. In this scenario, time

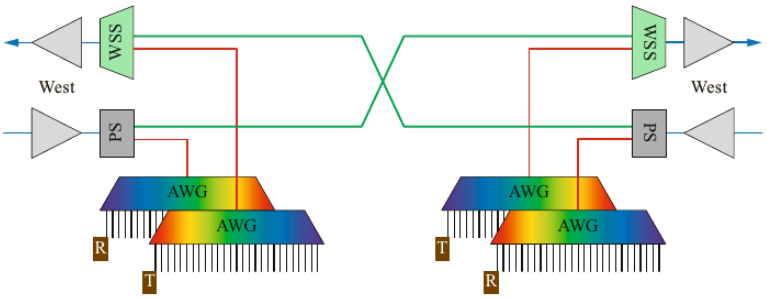

(a) Degree 2. In the figure: array waveguide grating (AWG), power splitter (PS), receiver (R), transmitter (T).

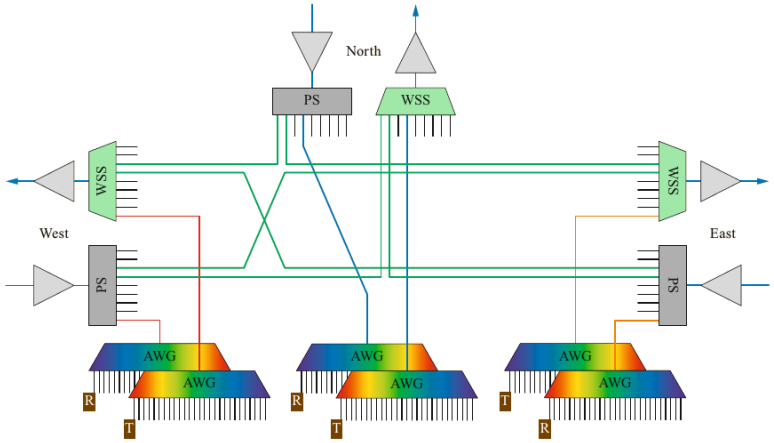

(b) Degree 3. In the figure: array waveguide grating (AWG), power splitter (PS), receiver (R), transmitter (T).

Figure 1.6 – WSS based ROADM architectures [28].

constraints are limiting. Main time-consuming tasks are the software functions in charge of provisioning functionalities residing at the control layer, which must be accelerated. Nevertheless, other aspects have to be considered too, as the laser tuning speed and the switching time. MEMS-based switches meet the requirements for OCS, but their switching response is not fast enough in case of OPS operation [14].

An important challenge, addressed in this PhD thesis, is the impact of dynamically adding/-dropping channels in the system performance, considering optical power excursion produced in optical amplifiers along the link.

1.3 SDN decision aided with machine learning methods

The SDN paradigm is a strong disruptive approach which has an important impact on the control layer of optical backbone networks. During decades, Generalized Multi-Protocol Label Switching (GMPLS) [32], [33] was a promising candidate to extend label switching Multi-Protocol Label Switching (MPLS) to the first three layers of the network. SDN changed that

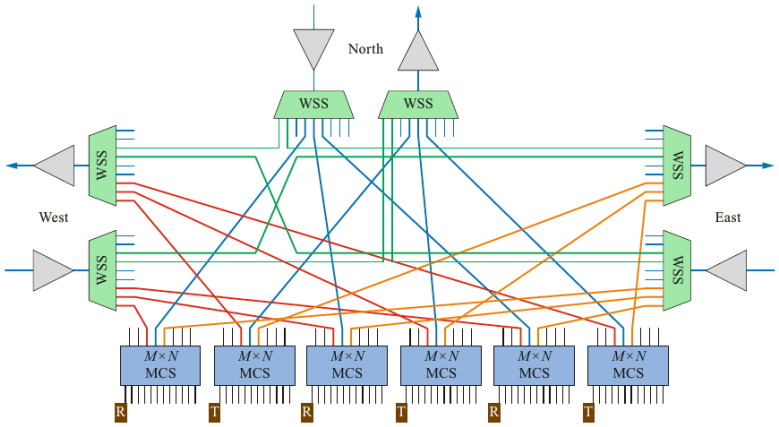

(a) Using multicast switches. In the figure, multicast switch (MCS).

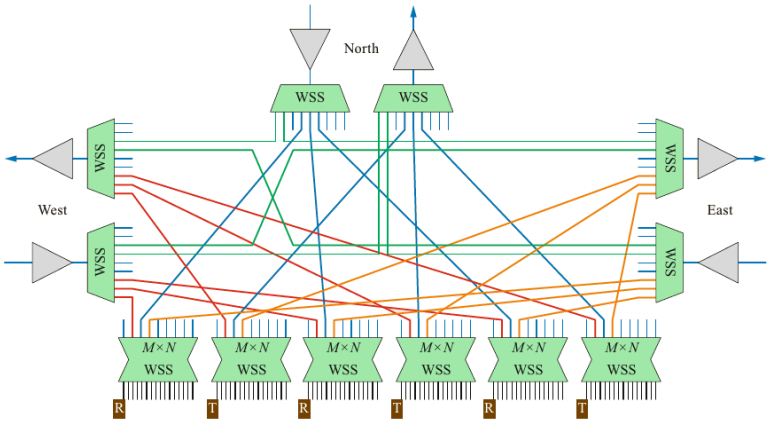

(b) Using WSSs.

Figure 1.7 – ROADM colorless, directionless, contentionless architectures [27].

due to the separation of control and data plane [34]:

"In the SDN architecture, the control plane and data plane are decoupled, network intelligence and state are logically centralized, and the underlying network infrastructure is abstracted from the applications[35], [36]."

According to this definition, SDN includes three layers (Fig. 1.8):

- Infrastructure or data layer: Lowest layer, it includes physical and virtual resources. Physical and virtual switches are hardware-based and software-based switches, respectively. Whereas virtual switches support commonly SDN, physical switches do not always do, depending on the vendor. Open ROADM is an initiative dedicated to provide open software control for different proprietary systems [38]. The data layer acts based on instructions coming from the control layer. Apart from switches, transceivers are also physical elements which can be controlled through an SDN interface, in order to exploit

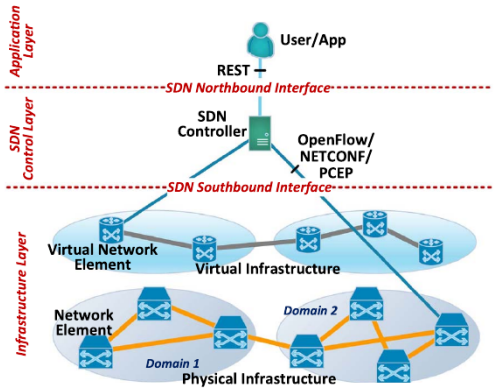

Figure 1.8 – SDN-based optical network architecture [37].

its flexibility in data rate, modulation formats, forward error correction (FEC) properties or frequency grid.

- Control layer: Between the data and the application level, control plane is the key layer in SDN-based architectures, managing the network. Using several interfaces, it converts the requirements coming from the application plane to policies, controlling the physical layer. Several interfaces can be distinguished:
  - Southbound interfaces between control and data plane, with OpenFlow being the most commonly used [39].
  - Northbound interfaces between control and application plane.
  - Eastbound/westbound interfaces between different SDN controllers.
- Application layer: This highest layer performs network applications by using the control layer, including network monitoring or traffic provisioning.

Although this is the general implementation, two main trends are considered in the implementation of SDN systems: white box and bright box. In the white box approach, all control capabilities of the network nodes are given to the SDN controller, which has a full view of the network. There is no communication between network nodes. The bright box approach, more scalable, allows communication between SDN controllers [37].

Different functionalities can be implemented through SDN. Most popular ones aimed RWA, including also impairment aware RWA (IA-RWA), key issue in transparent networks, guaranteeing sufficient QoT when PLIs are considered. Another interesting capability that can be enabled by SDN is the optical power control, fundamental in dynamic optical networks. When channels are added or dropped, power instabilities in optical amplifiers must be limited, in order not to deteriorate the system performance. These functionalities are addressed in this PhD thesis where optical power excursion in optical amplifier is predicted, compensated and coupled with impairment aware modulation format and wavelength assignment algorithm using ML techniques.

ML methods, which once trained, provide a very fast response, have gained popularity in the last years. Integrated in the SDN controllers, they can fulfill the time constraints required in dynamic optical networks, still providing close to optimal solutions [23]. ML techniques have been applied at physical and network layer, implementing different functionalities [40].

Several topics have been addressed at the physical layer by ML algorithms:

- QoT estimation: In order to perform IA-RWA, the knowledge about QoT for any lightpath has to be available, allowing to make decisions, assigning traffic demands to lightpaths providing an adequate QoT. Required knowledge can be obtained from analytical formulas, implying high complexity, or approximated ones, lacking accuracy. ML algorithms have been proposed to solve this problem [41]–[43]. This subject is developed in Chapter 3, where we propose QoT estimation based on ML techniques using optical power excursion as input feature.
- Optical amplifier control: As mentioned before, optical power excursions due to optical amplifiers under dynamic traffic operation conditions produces undesired effects in the system performance. Difficult to approximate, as they depend on optical amplifiers' physical characteristics, ML algorithms have demonstrated to provide a high accuracy in its prediction [44], [45], as we will show in Chapter 2.
- Modulation format recognition: Flexible optical networks include flexible transceivers where modulation format is a tuneable parameter to be adjusted. Modulation format recognition is a desirable capability at the receiver, in order to adjust the demodulation process, even before information from the transmitter is received. Several works have dealt with this matter by means of ML techniques [46]–[48].
- Nonlinearity mitigation: Complex analytical models are required in order to estimate nonlinearities, which greatly affect QoT. Due to this complexity, ML methods are a promising candidate to estimate or compensate nonlinearities [49], [50].
- Optical performance monitoring: To ensure QoT and help in the fault management process, optical performance monitoring becomes necessary. To reduce the number of monitors deployed in the network, ML techniques may be useful by estimating performance parameters based on known gathered data [51].

At the network layer, ML techniques have been applied to accomplish several purposes:

- Traffic prediction and virtual topology design: At the design phase, traffic prediction helps to reduce overprovisioning. During the network operation, it allows to use resources in a more efficient way. Analogous reasoning can be applied to the virtual topologies (connecting nodes without a direct physical link). Based on gathered data, ML techniques are able to extract traffic characteristics or even to make predictions on the traffic [52], [53].

- Failure management: Fault detection, localization and identification are intricate tasks which can be solved by ML methods, helping to restore the traffic [54], [55].

- Traffic flow classification: Traffic differentiation can contribute to optimize resource allocation problems. By working on historical data, ML methods are able to perform traffic classification, e.g. differentiating elephants from mice flows [56].

- Path computation: Routing is a fundamental functionality at the network layer. Complex process, it becomes even more complex when impairments are considered. Different approaches based on ML techniques have been proposed, e.g. optimizing physical layer parameters, as modulation format, for a given lightpath [57].

1.4 Optical packet switching vision in the N-GREEN project

OCS is the fundamental operation mode in transport optical networks, providing high Quality of Service (QoS) [58]. Dedicated end-to-end circuits are established between source and destination nodes before starting data transmission. During the transmission, the network resources allocated to this particular transmission cannot be accessed by other transmissions. When the transmission ends, the path is removed and the corresponding allocated resources released [59]. Although wavelength converters are occasionally available, OCS may be sometimes subject to wavelength continuity constraints, i.e. same wavelength has to be kept from source to destination, reducing its flexibility. Transparent optical networks working in OCS reduce energy-consumption compared to the ones using electrical switches. However, using pre-established connections, OCS could limit the efficiently use of network resources [60].

Subject of debate [60], [61], OPS has been deeply studied in the literature as successor of OCS in order to decrease energy consumption and increase network resource use. OPS is a technique whose origin is in data signal transmission, bursty in nature [59]. Different to OCS, the data is in this case split into small units or packets. Each packet is composed of a header (or label) and a payload, with the header including control and addressing information. Edge routers are in charge of attaching and detaching labels to the packets. Once the packet reaches a node, based on the routing information obtained after extracting and processing the label, routing and contention resolution tasks are performed. Also, label is accordingly modified and reattached to the payload which remains the same [58]. Note that buffers are required in OPS in order to solve contention, increasing complexity. On the opposite, high efficient bandwidth utilization can be achieved with OPS.

In order to allow OPS mode, important progress is being done in optical switching and burst mode receivers (BMRx) already reaching 10 Gb/s for operation in passive optical networks [62]. Despite these advances, for OPS to become a reality, several challenges have to be faced, as synchronization, buffering, wavelength conversion, optical header processing and regeneration [59].

- Synchronization: In slotted networks, fixed-length packets are transmitted in fixed-duration timeslots. After suffering delays, packets arrive at nodes at any moment during a timeslot. Thus, synchronization is mandatory in order to realign the packets with respect to timeslots at the output ports. The most common approach makes use of optical switches interconnected by fiber delay lines (FDLs) of different lengths, providing a controllable variable delay [63].

- Buffering: One of the most important open issues in OPS is the fact that there is no component equivalent to an electronic random access memory (RAM). Similar to the approach used for synchronization, one of the most common solutions is the implementation of programmable delay units based on a cascade of optical switches and FDLs of different lengths [64]. Simple solution, it is in turn bulky. In order to reduce the contention and the memory needs, combination of FDLs with wavelength converters has also been investigated [65]. Another proposed solution has utilized recirculating loops, where switch output ports were connected to the input ports through FDLs. In such manner, packets are recirculating until the port is available at the expense of noise accumulation resulting in a need for amplification [64]. A most recent approach has used nonlinear effects, e.g. four-wave mixing (FWM) in SOAs or stimulated Raman and Brillouin scattering in fibers, reducing the group velocity, thus reducing the speed of light in the medium, e.g. SOAs and fiber [66]–[68]. Its main constraint is the bandwidth, limiting the bit rate.

- Wavelength conversion: Important functionality allowing not only contention resolution but also wavelength routing [65], [69]. Considered to be essential for future transparent optical networks, its adoption in each node of the network seems unlikely due to its cost and the maturity of the technology [70].

- Optical header processing: Some demonstrations can be found in the literature, as an all-optical header processing module using two main blocks: an optical correlator to recognize the header and an all-optical flip-flop memory to store the header [65].

- Regeneration: Re-amplification and re-shaping (2R), or re-amplification, re-shaping and re-timing (3R) are regeneration tasks complicated to solve exclusively in the optical domain. However, some demonstrations of all-optical regenerators have been implemented based on: nonlinear fiber Sagnac interferometer switch [71], symmetric-Mach-Zehnder-type interferometric semiconductor switch [72], electroabsorption modulators [73]. Going further, all-optical single channel regeneration techniques have been extended to multi-channel [74].

All these complex issues have led to the opening of an intermediate option, becoming very popular for data-center networks [14]: hybrid opto-electronic packet switching. In this case, in order to solve contention, packets are allowed to undergo O/E-E/O conversions [75]. Several approaches have been demonstrated in this scenario, combining electronics and photonics [76], [77].

1.5 Summary

In this chapter, the research context of the PhD thesis is presented. To answer data bit rate and power consumption challenges, optical networks are shown to evolve to transparent flexible optical networks. A focus on optical node evolution shows that new node architectures have to respond to the same challenges. Progress at the control layer, adopting SDN-based architectures, is analyzed to fill with the new dynamism and flexibility features in optical networks. Nevertheless, this new concept of networks implies an increasing complexity at physical and network layers, which can be addressed by ML techniques assisting the SDN controllers. In this scenario, we have proposed optical power excursion prediction and precompensation (Chapter 2). Using synthetic data, high accuracy was obtained for optical power excursion prediction. After precompensation reductions of 86 %, 74 %, 62 %, for 12-channel, 24-channel and 40-channel configurations were achieved. In Chapter 3, using optical power excursion together with OSNR and BER, we have developed an impairment aware modulation format and wavelength assignment algorithm reducing blocking probability (ratio of blocked traffic demands with respect to arrived demands).

A disruptive solution to optical flexible network is considered in Part 2, based on multi-coloured OPS, developing a new generation of routers for energy efficient networks. The work presented in Chapter 4, in the framework of the N-GREEN project, is focused on the experimental characterization of a 2×2 switch integrated in the N-GREEN node. The obtained results, in single channel and WDM configurations, confirm the feasibility of working at higher data rates, envisaging a 16×16 switch configuration.

Part I
Machine learning techniques for physical layer control

2 Optical power excursion prediction and precompensation

Artificial intelligence, driven by several elements as computational power growth, development of ML libraries and "big data", is becoming essential, providing impressive performance in different fields as computer vision, speech recognition, robotics and more recently optical networks. As a proof of this, European photonics community has identified artificial intelligence enabled optical networks as one of the main research topics for the next years [78].

Optical amplifier control is one of the fields where ML can make the difference. In dynamic optical networks, wavelength dependent gain in optical amplifiers, producing power excursions is still an issue to be solved. Here, two approaches based on ML techniques are proposed in order to mitigate power excursion undesired effects (OSNR degradation and nonlinearities). First approach relies on power excursion prediction which can afterwards be used for wavelength assignment. Second approach presents a power precompensation solution reducing power excursions at the output of a link.

First, Section 2.1 gives an introduction to ML techniques, as some of them will be used in the proposed approaches. Section 2.2 introduces the power excursion problematic together with the state of the art of the solutions found in the literature. Section 2.3 describes the experimental validation of a double-stage amplifier, used in the following, to bring the work performed in simulations closer to the real world. Section 2.4 and Section 2.5 present the two proposed approaches: power excursion prediction and power precompensation. Experimental work presented in this chapter was performed by Network Technology Lab, École de technologie supérieure (Canada), without my participation.

2.1 Machine learning techniques overview

ML techniques are incredibly evolving over the last years. At the end of 2018, DeepMind [79] has shown how close a computer program, AlphaZero, is to master any kind of game without human guidance, exclusively by self-playing. One year after, MuZero [80], also developed by DeepMind, matched AlphaZero's superhuman performance without knowing the game

rules. Present already in real-world applications as image and speech recognition, product recommendation or medical diagnosis, ML techniques have started to gain popularity also in optical network applications. From physical layer to network layer, ML techniques are demonstrating to be able to improve optical network performance being of aid in different tasks: optical amplifier control, QoT estimation, optical monitoring, RWA, failure detection, etc. [40]. During the PhD thesis, ML techniques have been extensively used, having an important role in Chapter 2 and Chapter 3. This section provides ML fundamentals and a short review on most popular ML techniques.

2.1.1 Fundamentals

The first question to solve is: What is ML? A very popular definition is given in [81], where ML is defined as:

"A computer program is said to learn from experience E with respect to some class of tasks T and performance measure P, if its performance at tasks in T, as measured by P, improves with experience E. (Mitchell, 1997, p.2)"

To better understand the precedent definition and the ideas behind ML, some examples are given:

- ML algorithm learning to classify images of dogs and cats (Fig. 2.1a):
  - Task T: classification of images in two categories: (1) dog, when there is a dog in the picture and (2) cat, when there is a cat in the picture.
  - Performance P: Percentage of images successfully classified.
  - Experience E: Dataset of images containing photos of cats and dogs.
- ML algorithm learning to predict prices of houses based on specific features e.g. size, number of rooms... (Fig. 2.1b):
  - Task T: Prediction of house prices.
  - Performance P: Accuracy of the prediction.
  - Experience E: Dataset of features (size, number of rooms...) and corresponding prices.

In these previous two examples, the two most common types of tasks are established: (1) classification, where the algorithm assigns an input to a category, e.g. image classification, (2) regression, with the algorithm estimating a numerical value, e.g. predicting the prices of houses based on specific features. Depending on the task, also different performance measures can be utilized, as accuracy or error rate. Note that the performance measurement should be done in a separated dataset, not used during training, called test set.

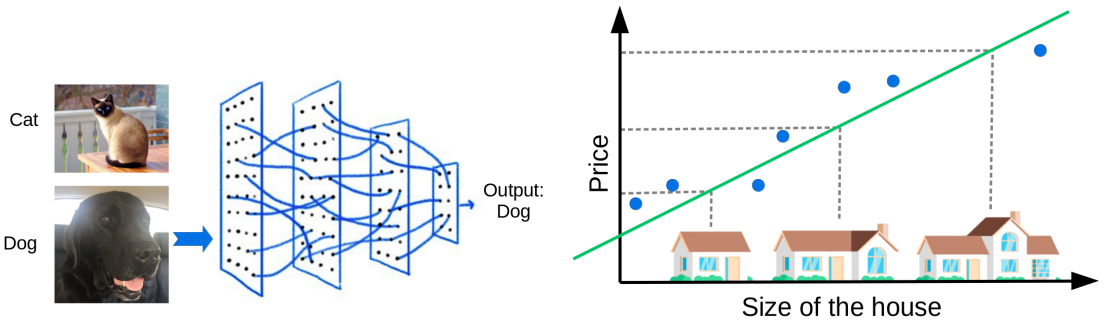

(a) Image classification.

(b) House prices prediction.

Figure 2.1 – ML examples.

Continuing with the second ML application proposed before, linear regression can serve as ML algorithm to predict house prices. Using linear regression, the predicted price y is calculated as [82]:

$$y = \boldsymbol{w}^T \boldsymbol{x}, \tag{2.1}$$

where $\boldsymbol{x}$ is a vector containing the input features and $\boldsymbol{w}$ is a weight vector estimated during training in order to get the best approximation. In order to find these $\boldsymbol{w}$ parameters, an objective function $J(\boldsymbol{w})$ is minimized, by using gradient descent. Note that an objective function which is minimized can be also called cost function, loss function or error function [82]. In this case, the objective function corresponds to the error between the estimations and the target values t. The error to minimize during the training $\text{MSE}_{\text{train}}$ can be written as [82]:

$$J(\boldsymbol{w}) = \text{MSE}_{\text{train}} = \frac{1}{m} \sum_i \left(\boldsymbol{y}^{(\boldsymbol{training})} - \boldsymbol{t}^{(\boldsymbol{training})} \right)_i^2, \tag{2.2}$$

where m is the total number of samples in the training set. The test error MSE_{test} is defined in the same way, but is measured over the n samples constituting the test set [82]:

$$\text{MSE}_{\text{test}} = \frac{1}{n} \sum_i \left(\boldsymbol{y}^{(\boldsymbol{test})} - \boldsymbol{t}^{(\boldsymbol{test})} \right)_i^2. \tag{2.3}$$

Note for classification problems, instead of mean squared error, accuracy is used:

$$\frac{\text{Number of correct predictions}}{\text{Number of total predictions}}. \tag{2.4}$$

The ability of the ML algorithm to be effective when tested on new data is called generalization.

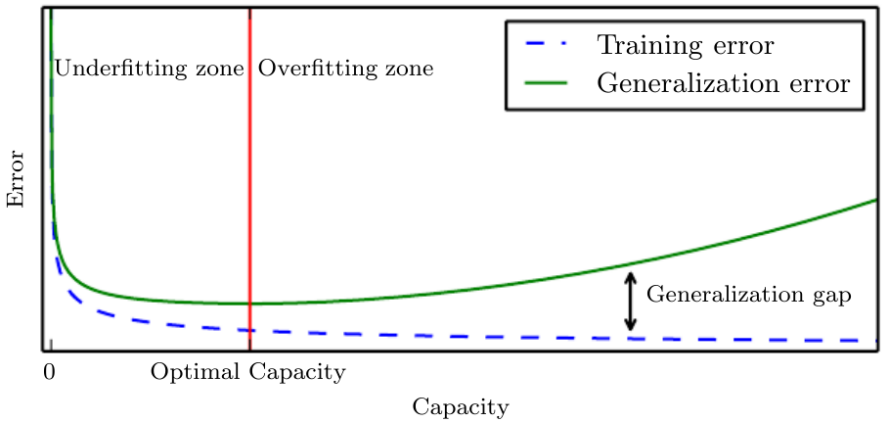

Figure 2.2 – Relationship between capacity and error [82].

During the learning phase, a primary goal is to reduce the training error, computed on the training set. After the training, the ML algorithm is executed on new data, with the performance measured by the test error (generalization error) calculated on the test data. The test error will be larger than the training error, but the gap between them should be small. When the training error is too large, the ML algorithm presents an underfitting problem. On the opposite, when the training error is low but the test error is high, the ML algorithm exhibits an overfitting problem. Different approaches have been used in order to reduce the overfitting problem:

- Capacity reduction: Algorithms with high capacity tend to overfit when the task to solve does not require such capacity. As an example, consider an ML model based on polynomial. For a particular degree N the output is given by:

$$y = \sum_{i=1}^{N} w_i x_i + w_0. \tag{2.5}$$

  As represented in Fig.2.2, using this model with different N degrees in order to solve a simple task will usually derive in underfitting if the degree is very low and overfitting if it is very high. Reducing the degree polynomial (capacity), without falling in underfitting, allows to fix overfitting.

- Regularization: By adding a tuning parameter, the flexibility of the ML algorithm is penalized, therefore preventing overfitting. An example of regularization operates on penalizing larger weights over small weights, by minimizing the function $J(\boldsymbol{w})$:

$$J(\boldsymbol{w}) = \mathrm{MSE}_{\mathrm{train}} + \lambda \boldsymbol{w}^T \boldsymbol{w}, \tag{2.6}$$

  where λ is a parameter chosen beforehand.

Differently to $\boldsymbol{w}$ values, other parameters cannot be estimated during the training. They affect the performance of the ML model but there is no formula to calculate their values. These external parameters are called hyperparameters, as the degree of the polynomial in regression. In order to tune hyperparameters, the training set is subdivided in two subsets: a training set (~ 80% of the original training set) where the training is performed, and a validation set (~ 20% of the original training set) where the performance of the hyperparameters used in the training is measured. By training the ML model for different hyperparameters and comparing the performance on the validation set, hyperparameters are optimized.

2.1.2 Algorithms: Supervised, unsupervised and reinforcement learning

According to the type of experience used during the learning phase, ML algorithms can be classified under three main categories: supervised learning, unsupervised learning and RL (Fig. 2.3). Supervised learning refers to all the techniques making use of a labelled training dataset, where each input $\boldsymbol{x}$ has an associated output y. Based on these labelled samples, the algorithm is instructed, in a way that after the training it is able to predict an output y from a new input $\boldsymbol{x}$ not present in the dataset. On the contrary, in unsupervised learning, training data is not labelled, the algorithm has to figure out by itself hidden patterns in order to be able to learn some probability distribution $p(\boldsymbol{x})$ or even to extract properties. The third group of ML techniques, RL, learn by interaction with an environment rather than from a dataset. In general, unsupervised learning algorithms are able to extract patterns from data, supervised learning algorithms are used for prediction and classification tasks and RL allows autonomous system control. Following this general rule, in this thesis, supervised learning is used for optical power excursion prediction and RL algorithms are used (in the present chapter and in Chapter 3) to learn to optimize launch input powers and the wavelength assignment process. For supervised learning, we have focused our work on NNs, which have become very popular in the last years, outperforming other supervised algorithms [83].

Supervised learning

Some of the most common supervised learning methods are described in the following, always based on a labelled training dataset.

Linear regression Introduced before, coming from classic statistics, linear regression is a simple technique which assumes a linear relationship between the inputs $\boldsymbol{x}$ and the output y.

Probabilistic supervised learning The main goal of this family of algorithms is to estimate a probability distribution $p(y|\boldsymbol{x})$ [82]. This is the case of logistic regression, Naives Bayes and Bayesian networks.

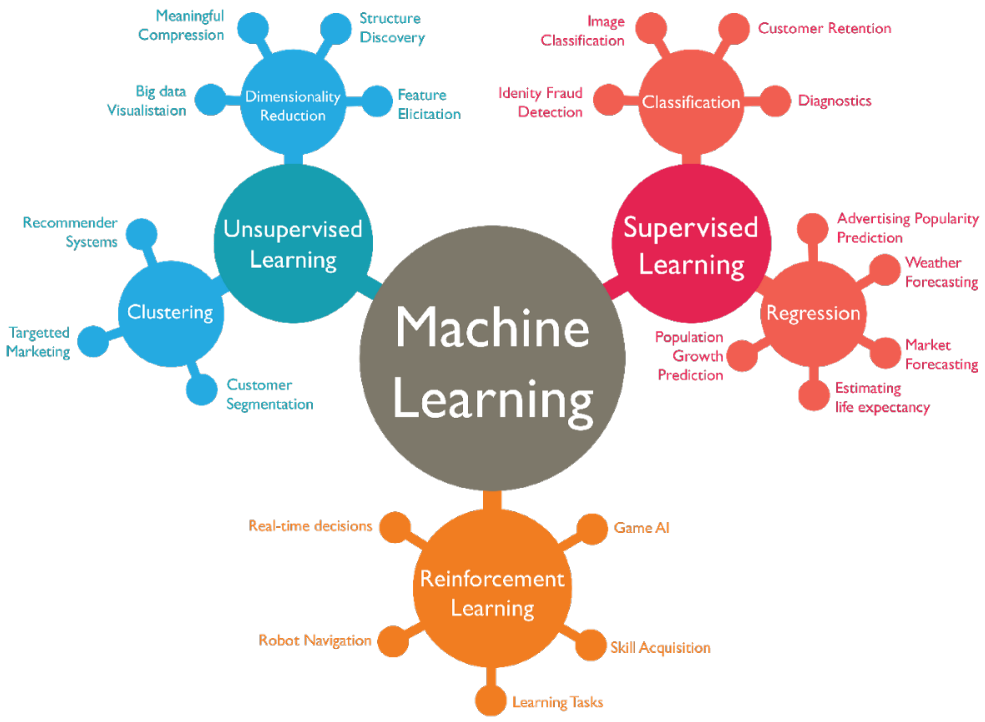

Figure 2.3 – ML techniques and their applications [84].

Support Vector Machines Different from probabilistic supervised learning, support vector machines (SVMs) do not output a probability but a class identity. In order to do this, SVMs estimate a hyperplane that optimally separates the different classes [82].

k-nearest neighbors (k-NN) They do not require a training stage. For a chosen number of neighbors N, the algorithm calculates the distance of the test sample to each of the samples in the dataset. Based on the labels of the k nearest samples, it returns the average of the k samples. Simple; however, this algorithm becomes slower as the number of samples in the dataset increases.

Decision trees With a flowchart like architecture, decision trees make predictions based on simple decisions, where each decision maps to a region breaking in sub-regions (child nodes) depending on the outcome of the decision. Random forests (RF), also based on decision trees, combine the output of multiple random decision trees.

Neural networks NNs are a nonlinear data modelling tool based on a high-interconnected node structure which will be used in Chapter 2 and Chapter 3. In general, NNs map an input $\boldsymbol{x}$ to an output y by estimating a function approximation $y = f(\boldsymbol{x}, \boldsymbol{w})$. The function $f(\boldsymbol{x}, \boldsymbol{w})$ depends not only on the input $\boldsymbol{x}$ but also in a set of parameters $\boldsymbol{w}$, learnt throughout the

training phase [82]. Data used for training is labelled, i.e. each input $\boldsymbol{x}$ is associated to its corresponding output t. Organized in layers, the general structure can be seen in Fig. 2.4, where between the input layer, i.e. first layer, and the output layer, i.e. last layer, there are a variable number of hidden layers. Each layer is composed by nodes working in parallel. Each unit, reminding to a neuron, gathers input data coming from other nodes and calculates an output activation value. A nonlinear function (activation function) is then applied on the received activations. Thus, for the first hidden layer, a linear combination is performed first, calculating the activations $\boldsymbol{a}$:

$$\boldsymbol{a} = \left(\boldsymbol{W^{(1)}}^T \boldsymbol{x}\right), \tag{2.7}$$

where $\boldsymbol{W^{(1)}}$ is the matrix representation of the mapping parameters between the first and second layer. Then, the activation function $h(\cdot)$ is applied on eq. 2.7:

$$\boldsymbol{z} = h(\boldsymbol{a}). \tag{2.8}$$

The same procedure is followed for the next layers. If there is only one hidden layer, with second layer being already the output layer and having only one output unit, the activations are calculated as:

$$a = \left(\boldsymbol{w^{(2)}}^T \boldsymbol{z}\right), \tag{2.9}$$

where $\boldsymbol{w^{(2)}}$ is the vector representation of the mapping parameters between the hidden layer and the output layer. Then, activation function $g(\cdot)$ is applied in order to obtain the output:

$$\mathrm{y} = g(a). \tag{2.10}$$

There are no feedback connections, information propagates always forward. If feedback connections are included, they are referred as recurrent NNs. More details about NNs are provided in Appendix A.

During the training, the NN adjusts the parameters $\boldsymbol{w}$ in order to get, for each $\boldsymbol{x}$, an estimated value y close to the true value t. In order to do this, gradient descent on a cost function is used [82]. Different cost functions can be utilized, similarly as for the linear regression shown in Section 2.1.1. Some of the most common are:

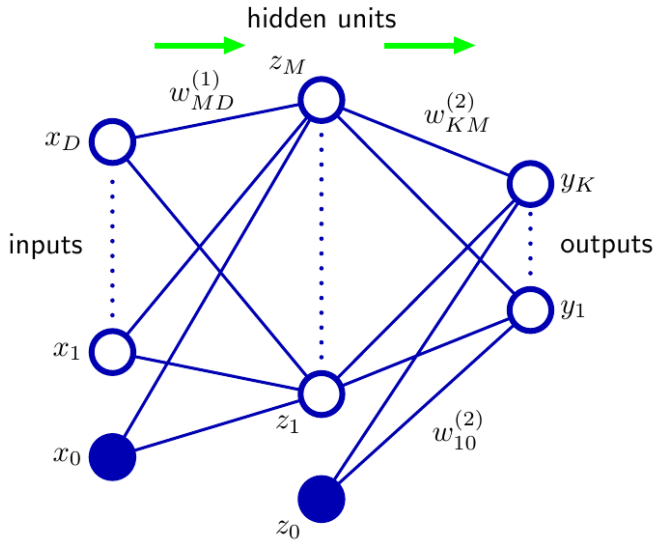

Figure 2.4 – General NN diagram [85].

- Mean squared error: Commonly used as loss function for regression tasks:

$$\frac{1}{m}\sum_{i=1}^{m}\left(y_i - t_i\right)^2, \tag{2.11}$$

  measuring the difference between the true values $\boldsymbol{t}$ and the estimated values $\boldsymbol{y}$ in the m samples existing in the training dataset.

- Cross-entropy: Demonstrated to be faster for classification tasks, it is the most common loss function [85]. When only two classes are considered, the binary cross-entropy loss is given by:

$$-\frac{1}{m}\sum_{i=1}^{m}\left(t_i \log\left(y_i\right) + (1-t_i)\log\left(1-y_i\right) t_i\right), \tag{2.12}$$

  where again, as before, $\boldsymbol{t}$ and $\boldsymbol{y}$ are the true and estimated values in the m samples of the dataset. Intuitively, the loss is larger when the estimated value is far from the true value.

The cost function is associated to the activation function used in the output unit. At the output layer, the hidden features undergo the last transformation, producing the final output. Here, some of the most popular output units are introduced:

- Linear: The output is a linear combination of the hidden features y = $\boldsymbol{w}^T\boldsymbol{z}$. It is typical for regression tasks with mean squared error cost function.

- Sigmoid: The output can be seen as a probability $P(y=1|\boldsymbol{x})$, limited between 0 and 1:

$$y = \sigma\left(\boldsymbol{w}^T \boldsymbol{z}\right), \tag{2.13}$$

  with $\sigma(\cdot)$ the logistic sigmoid function:

$$\sigma(x) = \frac{1}{1+e^{-x}}. \tag{2.14}$$

  Note that the sigmoid unit provides a value between 0 and 1, as a probability. For binary classification, a 0.5 threshold is used to distinguished the two classes. However, this threshold can be modified.

- Softmax: Also calculating a probability, but considering multiple classes.

Although previous activation functions (linear, sigmoid, softmax) can also be used in the hidden layers, other are more popular, as sigmoid and hyperbolic tangent (tanh), currently substituted by rectified linear unit (ReLU):

$$h(\boldsymbol{z}) = \max(0, \boldsymbol{z}), \tag{2.15}$$

which is widely used nowadays, as it presents a faster training than other activation functions, as tanh [86].

Unsupervised learning

Unsupervised learning works on unlabelled data, determining new data representations. Most popular types of unsupervised learning can be classified in: (1) based on data compression, searching for low dimensional representations as principal component analysis (PCA), (2) based on clustering, sparse representation, aggregating data in different groups, as k-means clustering.

Principal component analysis By using compression, PCA learns a new representation of the data with a lower dimension, still preserving as much information as possible from the original data [82].

k-means Simple unsupervised learning algorithm consisting on grouping data in a set of k clusters [82]. Each cluster has a centroid μ, the center of the cluster. Starting from randomly selected k centroids, in a first step, distances of each of the samples in the dataset to each the centroids are calculated. Then, samples are assigned to the nearest centroid. Finally, each

centroid is updated to the average value of the samples assigned to this corresponding cluster. The process is repeated until the centroids are stable.

Reinforcement learning

Learning by interaction with an environment is the fundamental basis of RL algorithms, used in Chapter 2 and Chapter 3. In psychology, this idea is already present since the early twentieth century. Law of effect, developed by Edward Lee Thorndike [87], establishes that actions leading to pleasant outcomes are expected to reoccur whereas actions coupled with unpleasant outcomes are less likely to be repeated:

> Of several responses made to the same situation, those which are accompanied or closely followed by satisfaction to the animal will, other things being equal, be more firmly connected with the situation, so that when it recurs, they will be more likely to recur; those which are accompanied or closely followed by discomfort to the animal will, other things being equal, have their connections with that situation weakened, so that, when it recurs, there will less likely to occur. The greater the satisfaction or discomfort, the greater the strengthening or weakening the bond. (Thorndike, 1911, p.244)

Similarly, RL algorithms learn by interacting with an environment. Suppose an RL algorithm learning to play chess. At the beginning, it does not have any knowledge about chess, not knowing which the objective is. Thus, it moves the pieces randomly. Some of these random actions will result in favorable outcomes like capturing pieces or promoting a pawn; nevertheless, other actions will be followed by unfortunate events, as giving away pieces. All the experience collected by trial and error is valuable and based on it, the RL algorithm learns to intelligently determine which is the most profitable move to make in its turn, in order to get it closer to win. Putting too much trust in the gathered experience, can lead to sub-optimal performance, where the RL algorithm keeps playing long but it never wins because it never discovered the right moves. Balance between exploration of new actions and exploitation of previous knowledge must be achieved.

In general, two entities are distinguished in an RL method, as shown in Fig. 2.5: agent and environment. The agent, is a learner, perceiving the environment, taking actions and analyzing the outcomes. Everything surrounding the agent, constituting a separated entity, is called environment. Interactions between agent and environment take place at discrete timesteps $t = 0, 1, 2....$ At each timestep:

- The agent collects an observation s_t, called state, containing relevant information about the environment at the timestep t. Although carrying pertinent information, not all the information has to be included in a state; it is possible some pieces of information are

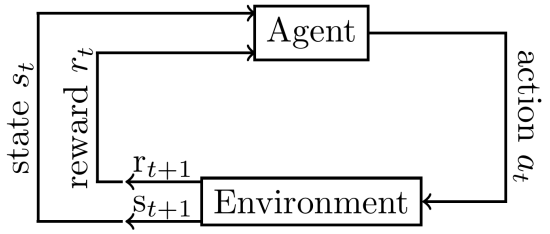

Figure 2.5 – RL agent-environment interaction [88].

hidden. Despite of this, in general, states have the Markov property, i.e. next state s_{t+1} can be determined based on the current state s_t and action a_t at timestep t.

- At the same timestep t, the agent chooses an action a_t, following a policy π_t which takes into account the current state s_t. The policy is described as a function $\pi_t(s,a)$ mapping each state s and action a to a probability of selecting action a in the current state s. Policy function should be optimized, in order to assign maximum probabilities to the actions providing better results.

- In the next time step $t+1$, the environment delivers a reward to the agent r_{t+1} and moves to the next state s_{t+1}. Reward values depend on action outcomes: high rewards and low rewards are associated to satisfying and unsatisfying results, respectively.

Previous interactions continue until a terminal state is reached, e.g. in the previous example, until the agent wins or loses the game. Each of these sequences of agent-environment interactions are called episodes. The end of an episode, is followed by a reset which drives the environment to the initial state, starting a new episode. Although here the analysis is restricted to episodic tasks, not always tasks are required to be episodic, e.g. many control tasks are continuous tasks lacking terminal states.

Maximizing the long-term reward is the main goal of RL algorithms. This long-term reward can be defined as a cumulative reward R_t, sum of the rewards between the current timestep t and the timestep at which a terminal state is reached T:

$$R_t = r_{t+1} + r_{t+2} + r_{t+3} + ... + r_T. \tag{2.16}$$

This definition becomes questionable for continuous tasks, where the terminal state occurs at $T = \infty$. Consequently, the cumulative reward could also turn up being an infinite value. To solve this issue, a discount rate γ is introduced in eq. 2.16:

$$R_t = r_{t+1} + \gamma r_{t+2} + \gamma^2 r_{t+3} + ... = \sum_{k=0}^{\infty} \gamma^k r_{t+k+1}, \tag{2.17}$$

with $0 \leq \gamma \leq 1$. For $\gamma = 0$, the discounted reward is equal to the immediate reward r_{t+1}. In general, maximizing the immediate reward and ignoring future rewards is not a good option, as it can block the progress to a path accounting with most advantageous future rewards. As γ increases, future rewards become more significant. The farther into the future, the less importance the reward has, e.g. at timestep k the reward is scaled by γ^k, but at timestep $k+1$ the reward is scaled by γ^{k+1}, its value is γ times less. Typical values for γ are close, but not equal, to 1.

Nevertheless, estimating discounted rewards is unpractical, as each sequence of state-actions generates a different discounted reward. Thus, most RL methods determine value functions, estimating an expected return when the agent is at a particular state and follows a particular policy. Different value functions can be defined, as the state-value function or the action-value function. The state-value function $V_\pi(s)$, represents the expected return when a policy π is followed:

$$V_\pi(s) = \mathbb{E}_\pi \left[R_t | S_t = s \right] = \mathbb{E}_\pi \left[\sum_{k=0}^{\infty} \gamma^k r_{t+k+1} \middle| S_t = s \right], \tag{2.18}$$

where $\mathbb{E}_\pi\{\cdot\}$ represents the expected return after following policy π. Action-value function $Q_\pi(s,a)$ is defined in an identical way, determining expected return received when starting in s and selecting action a, afterwards following policy π:

$$Q_\pi(s,a) = \mathbb{E}_\pi \left[R_t | S_t = s, A_t = a \right] = \mathbb{E}_\pi \left[\sum_{k=0}^{\infty} \gamma^k r_{t+k+1} \middle| S_t = s, A_t = a \right]. \tag{2.19}$$

Different features can be considered in order to classify RL algorithms [89]:

- Model-based / model-free: Model-based methods try to learn a representation of the environment, being able to anticipate states and/or rewards. On the opposite, model-free algorithms operate on state-action pairs without creating an environment model.

- Policy-based / value-based: Policy-based methods directly approximate the policy, probability of selecting an action from the action space, allowing to know which action to take at each step. Value-based methods approximate all the values for each action, selecting the action maximizing the reward.

- On-policy / off-policy: On-policy methods work on optimizing the same policy used for taking decisions whereas off-policy methods use different policies for optimizing and taking decisions.

Policy gradient algorithms

Value-based methods, estimating all the values for each action result impracticable for continuous action spaces or large action spaces. In this case, which is also the case of the tasks presented here, policy-based methods are more convenient.

Essentially, policy-based algorithms approximate policies. Although they may need a value-function to learn the policy parameters $\boldsymbol{\theta}$, they do not need it in order to select an action at each state. Note that the value function used for learning the policy can also be learnt, having therefore associated value parameters $\boldsymbol{w}$. The policy π, probability of selecting an action a when being at a state s and using policy parameters $\boldsymbol{\theta}$ is expressed as:

$$\pi(a|s,\boldsymbol{\theta}) = p\left(A_t = a|S_t = s, \boldsymbol{\theta}_t = \boldsymbol{\theta}\right). \tag{2.20}$$

Gradient is the most popular method in order to estimate policy parameters. The main idea behind it is to maximize an objective function $J(\boldsymbol{\theta})$, measuring performance, which is equivalent to maximize the gradient of the objective function $J(\boldsymbol{\theta})$ with respect to the policy parameters $\boldsymbol{\theta}$. This is done in an iterative manner. At each step the policy parameters are updated using a stochastic estimate of the gradient $\widehat{\nabla_\theta J(\boldsymbol{\theta}_t)}$ with respect to $\boldsymbol{\theta}_t$ according to:

$$\boldsymbol{\theta}_{t+1} = \boldsymbol{\theta}_t + \alpha\widehat{\nabla_\theta J(\boldsymbol{\theta}_t)}. \tag{2.21}$$

The objective function $J(\boldsymbol{\theta})$ can be directly defined from the value function V_{π_θ} following policy π_θ from an initial state s_0:

$$J(\boldsymbol{\theta}) = V_{\pi_\theta}(s_0). \tag{2.22}$$

From eq. 2.22, it seems difficult to compute $\nabla_\theta J(\boldsymbol{\theta}_t)$ with respect to policy parameters, as policy changes affect state distribution. However, policy gradient theorem, which is demonstrated in [88], helps to solve this problem, establishing an analytical formula which does not require the state distribution derivative:

$$\nabla_\theta J(\boldsymbol{\theta}) \propto \sum_s \mu(s) \sum_a Q_\pi(s,a)\nabla_\theta \pi(a|s,\theta), \tag{2.23}$$

where $\mu(s)$ is on-policy distribution under π. Developing more eq. 2.23, as explained in Appendix B, a general formulation stated in [90] is achieved. Policy gradient methods maximize the expected total reward by continuously estimating the gradient $g := \nabla_\theta \mathbb{E}[\sum_{t=0}^{\infty} r_t]$, following

the formula:

$$g = \mathbb{E}\left[\sum_{t=0}^{\infty} \Psi_t \nabla_\theta \log \pi_\theta(A_t|S_t)\right], \tag{2.24}$$

where Ψ_t can adopt different forms:

- $\sum_{t=0}^{\infty} r_t$: total reward
- $\sum_{t'=t}^{\infty} r_{t'}$: reward following action
- $\sum_{t'=t}^{\infty} r_{t'} - b(S_t)$: baselined version
- $Q_\pi(S_t, A_t)$: state-action value function
- $A_\pi(S_t, A_t)$: advantage function
- $r_t + V_\pi(S_{t+1}) - V_\pi(S_t)$ temporal difference residual

where:

$$V_\pi(S_t) := \mathbb{E}_{\substack{S_{t+1:\infty} \\ A_{t:\infty}}}\left[\sum_{l=0}^{\infty} r_{t+l}\right], \tag{2.25}$$

$$Q_\pi(S_t, A_t) := \mathbb{E}_{\substack{S_{t+1:\infty} \\ A_{t+1:\infty}}}\left[\sum_{l=0}^{\infty} r_{t+l}\right], \tag{2.26}$$

$$A_\pi(S_t, A_t) = Q_\pi(S_t, A_t) - V_\pi(S_t). \tag{2.27}$$

Actor-critic methods

Policy gradient methods learning to estimate not only the policy function but also a value function are called actor-critic methods. Two entities are distinguished: an actor learning the policy and a critic learning a value function. Four of the most popular actor-critic methods are described here: advantage actor critic (A2C) [91], deep deterministic policy gradient (DDPG) [92], trust region policy optimization (TRPO) [93] and proximal policy optimization (PPO) [94].

- A2C is a synchronous, deterministic version of asynchronous advantage actor critic (A3C), developed by Google's DeepMind [91] based on parallel agents. It is an on-policy algorithm where the policy gradient is based on an advantage function eq. 2.27. Whereas

in A3C agents can be working on different version policies, leading to discrepancies, in A2C this issue is solved by waiting until all the agents finish before executing updates. This ensures in each iteration all the agents start from the same policy.

- DDPG is an off-policy actor-critic algorithm. In order to encourage exploration, the exploration policy μ' is built by adding noise sampled from a noise process N:

$$\mu'(S_t) = \mu(S_t|\boldsymbol{\theta}_t^{\mu}) + N. \tag{2.28}$$

  Target values are varied slowly by means of 'soft' updates: $\tau << 1 : \boldsymbol{\theta}' \leftarrow \boldsymbol{\theta} + (1-\tau)\boldsymbol{\theta}'$.

- TRPO is an off-policy algorithm considering the policy π to optimize and the policy β collecting trajectories. The objective function uses the discounted visitation frequencies of an state $\rho_{\pi_{old}}(s)$ as:

$$\begin{aligned} J(\boldsymbol{\theta}) &= \sum_{s\in\mathscr{S}} \rho^{\pi_{\theta_{\text{old}}}} \sum_{a\in\mathscr{A}} \left(\pi_\theta(a|s)\hat{A}_{\theta_{\text{old}}}(s,a)\right) \\ &= \sum_{s\in\mathscr{S}} \rho^{\pi_{\theta_{\text{old}}}} \sum_{a\in\mathscr{A}} \left(\beta(a|s)\frac{\pi_\theta(a|s)}{\beta(a|s)}\hat{A}_{\theta_{\text{old}}}(s,a)\right), \end{aligned} \tag{2.29}$$

  where $\boldsymbol{\theta}_{\text{old}}$ are the old parameters previous to update. Using importance sampling:

$$J(\boldsymbol{\theta}) = \mathbb{E}_{s\sim\rho^{\pi_{\theta_{\text{old}}}},a\sim\beta}\Big[\frac{\pi_\theta(a|s)}{\beta(a|s)}\hat{A}_{\theta_{\text{old}}}(s,a)\Big]. \tag{2.30}$$

  TRPO defines an additional constraint on the policy update, expressed as a maximum Kullback-Leibler divergence between the old and the new policies $D_{KL}^{\rho_{\theta_{old}}}(\theta_{old},\theta) < \delta$:

$$\mathbb{E}_{s\sim\rho^{\pi_{\theta_{\text{old}}}}}[D_{\text{KL}}(\pi_{\theta_{\text{old}}}(.|s)\|\pi_\theta(.|s)] \leq \delta, \tag{2.31}$$

  preventing the old and new policies from differing too much.

- PPO, simpler than TRPO, uses as objective function the ratio between the new and the old policy scaled by the advantage:

$$J(\boldsymbol{\theta}) = \mathbb{E}_t\left[\frac{\pi_\theta(a|s)}{\pi_{\theta_{old}}(a|s)}\hat{A}_{\theta_{old}(s,a)}\right] = \mathbb{E}_t\left[r(\boldsymbol{\theta})\hat{A}_{\theta_{old}}(s,a)\right], \tag{2.32}$$

  where $r(\boldsymbol{\theta}) = \frac{\pi_\theta(a|s)}{\pi_{\theta_{old}}(a|s)}$. In order to avoid instabilities by restricting the update, the objective function is clipped, being:

$$J_\theta^{clip} = \mathbb{E}_t\left[\min(r(\boldsymbol{\theta})\hat{A}_{\theta_{old}}(s,a),\ \text{clip}(r(\boldsymbol{\theta}),1-\epsilon,1+\epsilon)\hat{A}_{\theta_{old}}(s,a))\right]. \tag{2.33}$$

  The function clip$(\cdot)$ limits the change ratio in the interval $[1-\epsilon,1+\epsilon]$ with ϵ being a hyperparameter.

2.2 Optical power excursion challenge

Channel load modifications cause power dynamics (Appendix C). A change in the channel load implies a change in the amplifier input power. As a result, at the output of an EDFA operated at fixed pump, first, fast power changes characterized by undershooting or undershooting (power transients) are observed. After these power transients, once the power becomes stable, persistent power deviations remain (power excursions), deviating the output power from the desired power which would be obtained for an ideal amplifier with flat gain.

2.2.1 Optical amplifier modules

Two main different types of control are usually available in EDFAs: automatic gain control (AGC) which keeps a constant mean EDFA gain level for any input power and automatic power control which provides constant mean output power for any gain. AGC mode is preferred in terrestrial optical networks to reduce the undesired effects of power dynamics on WDM signals. In general, implementing AGC requires: (1) detection of signal power variations, (2) generation of an error signal (3) amplifier adjustment in order to reduce the error signal [95]. Different approaches have been proposed to introduce gain control capabilities in EDFAs: pump power adjustment, gain clamping and continuous wave extra channel insertion.

Pump power adjustment consists on modifying the pump power until the desired mean gain is achieved, usually involving feedforward or feedback loops. Feedforward loops, modifying the pump power depending on the input power values, have been demonstrated [96]. A similar method, including a supervisory channel, has also been developed [97]. Feedback loops acting on pump power as a response to the output power in order to keep a constant mean gain have also been validated [95]. Even more, combination of feedforward and feedback loops have also been investigated in order to reduce the time response [98], [99].

Another method allowing to keep a constant mean gain is gain clamping, which consists on adding an additional input optical control channel keeping the gain constant. In [100], two Bragg reflectors are connected to the input and the output of an erbium doped fiber (EDF), permitting the signals to pass transparently but reflecting the control channel. Thus, the amplifier oscillates at the control wavelength while the gain is kept constant. A ring laser can also be used to adjust the gain. In this case, the control channel circulates in a feedback loop including an attenuator in order to readjust the gain [101].

As in gain clamping, other alternatives also include an extra-channel. However, the additional channel in this case is transmitted along with the other channels, without being restricted to a feedback loop. The mean gain is kept constant by modifying the power of the extra-channel [102].

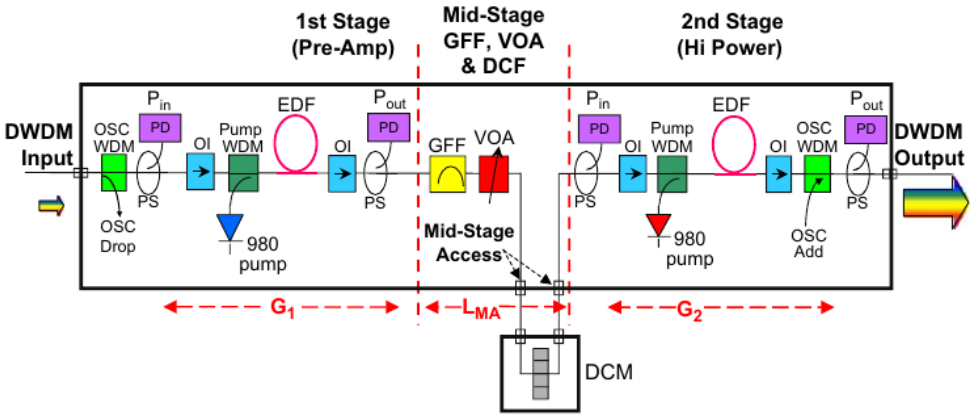

Figure 2.6 – EDFA module architecture [103]. In the figure: dispersion compensating module (DCM), gain flattening filter (GFF), optical isolator (OI), optical supervisor channel (OSC), photodiode (PD), power splitter (PS), variable optical attenuator (VOA).

Currently, AGC mode based on electronic control loop is the most popular approach from the previous solutions. Shown in Fig. 2.6, typical commercial amplifier modules including AGC capabilities are based on complex architectures making use of multistage amplifiers (cascade of amplifiers) with additional elements:

- Optical supervisor channel (OSC) module for monitoring the amplifier.
- Gain flattening filter (GFF) eliminating amplifier gain ripples due to wavelength dependent gain.
- Variable optical attenuator (VOA) in between two stages in order to modify the tilt. When attenuation is increased, the pump power has also to be increased in order to keep the same power at the output of the second stage. As a consequence, the tilt changes but the output power does not, also keeping the same gain.
- Dispersion compensating module (DCM) cancelling the dispersion introduced by the fiber.

These amplifier architectures incorporate various control capabilities:

- Gain control based on electronic loops. As discussed before, feedfordward, feedback or both can be used in order to keep a desired constant mean gain. Time response is limited by the electronics.
- Tilt control based on VOA. Main sources of tilt changes are the frequency dependent attenuation in fibers and the stimulated Raman scattering (SRS), with the latter being the dominant. When a signal and a pump photon (at higher frequency) travel in a nonlinear

medium, as a fiber, the signal photon can stimulate the emission of a second photon by Stokes-shifting the frequency of the pump photon until matching the signal photon. The excess of energy of the pump photon can be released in vibrational modes [104]. For WDM signals, SRS produces a transfer of energy from the channels at higher powers to the channels at lower frequencies [105].

- Amplified spontaneous emission (ASE, Appendix C) correction: For a noiseless amplifier, the gain G is given by:

$$G = \frac{P_{meas}^{out}}{P_{meas}^{in}} = \frac{P_{sig}^{out}}{P_{sig}^{in}}, \tag{2.34}$$

where P_{meas}^{in} and P_{sig}^{in} are the measured input power and the signal input power, and P_{meas}^{out} and P_{sig}^{out} are the measured and signal output power. However, once the noise is included in the calculations, the gain is rewritten as:

$$G = \frac{P_{meas}^{out}}{P_{meas}^{in}} = \frac{P_{sig'}^{out} + P_{ASE}}{P_{meas}^{in}}, \tag{2.35}$$

with $P_{sig'}^{out}$ the signal output power when the noise is included. The output power can be therefore expressed as:

$$P_{sig'}^{out} = GP_{meas}^{in} - P_{ASE}, \tag{2.36}$$

meaning that some of the output power is corresponds to ASE noise. In order to keep the same signal output power as if there would be no noise, the gain has to be corrected:

$$G_{corr} = \frac{P_{sig}^{out} + P_{ASE}}{P_{meas}^{in}} = \frac{P_{sig}^{out}}{P_{meas}^{in}} + \frac{P_{ASE}}{P_{meas}^{in}} = G + \frac{P_{ASE}}{P_{meas}^{in}} = G + ASE_{corr}. \tag{2.37}$$

This correction factor ASE_{corr} is precalculated and stored in a table, so it can be used during amplifier operation [106], [107]. When the input power is low (e.g. low number of channels) or the gain is small this factor becomes important.

2.2.2 Optical power excursion problem in WDM systems

Although complex amplifier structures including several control options reduce optical power excursions, they do not cancel them, leaving residual power excursion. Main reason behind residual power excursions is the wavelength dependent gain, which is determined by the specific physical EDFA characteristics as erbium concentration [95] (Appendix C). Analytical investigation on power excursion on a single stage amplifier operating in AGC mode is given in [108]. Some definitions are required previous to this analysis. As signal, a WDM signal is considered with P_{tot}^{in} total input power and P_{tot}^{out} total output power. For each channel in the

WDM signal, P_j^{in} and P_j^{out} are the input and output powers at the channel j. Regarding to the amplifier, G_M is defined as mean gain and G_{TC} the target gain selected by AGC. Mainly due to the wavelength dependent gain, the gain at a channel j is determined by $G_M g_j t_j$, being g_j and t_j the gain ripple and tilt in channel j. Gain ripple corresponds to the gain non-flatness of the amplifier whereas gain tilt refers to the gain slope with reference to another channel. When the amplifier operating point changes, the gain ripple is also modified and tilted. Tilt can also be affected by SRS and wavelength dependent attenuation in fibers. Based on the previous definitions, total input power P_{tot}^{in} is expressed as:

$$P_{tot}^{in} = \sum P_j^{in} + N_I, \tag{2.38}$$

where N_I is the optical noise power at the input of the amplifier. The output power seen by the AGC controller can be expressed in terms of the target gain including a noise correction factor N_C, from eq. 2.37 [107]:

$$P_{tot}^{out} = G_{TC}\left(P_{tot}^{in} + N_C\right). \tag{2.39}$$

When channels are added or dropped, pump powers are adjusted in order to keep the same gain. Note the controller works on adjusting the mean output gain but not the individual gain at each channel, implying that the output power at each channel of the WDM signal is adjusted by a factor f:

$$P_j^{out} = f G_M g_j t_j P_j^{in}. \tag{2.40}$$

Therefore, the total output power P_{tot}^{out} including the noise introduced by the amplifier N_R is given by:

$$P_{tot}^{out} = f G_M \sum_j P_j g_j t_j + f G_M N_R g_R + f G_M N_I g_I, \tag{2.41}$$

where g_I and g_R represent the average gain ripple experienced by the input and generated noises. From eq 2.38-2.41, defining $R = G_{TC}/G_M$, the factor adjustment is expressed as:

$$f = R\left(\frac{\sum_j P_j^{in} + N_I + N_C}{\sum_j P_j^{in} g_j t_j + g_R N_R + g_I N_I}\right), \tag{2.42}$$

which depends on channel input powers and amplifiers gains. Finally, the output power at

channel at an specific channel, e.g. channel 1 is given by:

$$P_1^{out} = RG_M P_1 + G_M \sum_{j \neq 1} \left(R - f g_j t_j\right) + G_M \left(R - f g_I\right) N_I - f G_M g_R N_R + R G_M N_C, \tag{2.43}$$

which shows the dependence of the power excursions on the factor $(R - f g_j t_j)$ averaged over all the channels. This analysis demonstrates how residual power excursions do exist even under AGC and how they fluctuate depending on the input power channels and gains. Producing undesired optical mean power excursions, its effect in WDM systems can be significant. As a result, nonlinearities and OSNR degradation are observed [95].

2.2.3 State of the art of the technical solutions

Solving optical power excursions is an open topic investigated for years. Different approaches have been proposed in order to flatten amplifier gain. Based on gain clamping characteristics in inhomogeneous lasers, gain flattening has been accomplished by placing an amplifier working under saturation conditions in a ring laser configuration [109]. By cooling the fiber, inhomogenous characteristics are boosted producing a flattened gain. Other different techniques made use of a two-stage amplifier with complementary gain [110] or spatial hole burning in an erbium doped twincore fiber [111]. Active optical filtering has also been studied in order to flatten the gain, using acousto-optic tunable filters [112] or Mach-Zehnder filters [113]. Passive optical filters utilizing an optical notch filter [114], a filter based on D-fiber with grating [115] and fiber photosensitive blazed grating [116] have also been shown.

Passive optical filtering have become the preferred approach, with thin-film filters being the solution widely adopted [117]. Presenting an adequate performance in static conditions, residual power excursion remain under dynamic operation including channel load changes, as seen in Section 2.2.2. Thus, considering the amplifier response looks almost unpredictable, the first challenge to solve is how to predict the amplifier behaviour at different operating points. Once this first challenge is overcome, another still remains: how to use this new prediction ability in order to mitigate power excursions.

Different alternatives have been considered in order to face the first challenge, building an amplifier representation providing the amplifier response under different operating conditions. Most of the proposals are based on: amplifier modelling, amplifier characterization and use of historical data.

Amplifier modelling has been studied to estimate the amplifier response. Different analytical and semi-analytical models have been developed over the years [118]:

- Standard confined doping model: Version of the main EDFA model using the assumption of confined doping [119].

- Transcendental power equation model [120].
- Linear Power Equation model: Approximation of transcendental power equation model [121].
- Exact power equation model: Extension of the transcendental power equation model using explicit expression for the EDFA gain [118].

In order to use these models amplifier physical parameters are required to be known. For example, standard confined doping model requires to know the absorption coefficient, the stimulated emission coefficient, the background loss coefficient and the saturating parameter [119]. Furthermore, these models are usually computationally expensive. Assumptions to simplify the model usually are accompanied with lower performance. A simple gain model has been used in [122], [123]. Using that estimation, the approximated gain $\hat{g}(\lambda_i)$ for a channel at λ_i considering N channels at locations $\lambda_1, \lambda_2, ..., \lambda_N$, is given by:

$$\hat{g}(\lambda_i) = g(\lambda_i) + \frac{\sum_{j=1}^{N} \left(g_s(\lambda_j) - g(\lambda_j)\right)}{N}, \tag{2.44}$$

where $g_s(\lambda_i)$ represents the gain at λ_i when a single channel at λ_i is transmitted, and $g(\lambda_i)$ represents the gain at λ_i when the whole band of WDM channels are transmitted. Allocating channels in the wavelengths with reduced gain deviations according to the model has been demonstrated to cut down gain deviations, but only by 5-15 %.

Another possible option is amplifier characterization, involving measuring the true gain amplifier response at the different WDM load configurations, requiring therefore a high number of sources. Fortunately, number of sources can be substantially reduced by using broadband edge-emitting LEDs probes [124] or a non-uniform WDM source spacing [125]. Still, characterization is a time-consuming task, involving offline experimental measurements. More recently, an online alternative, based on using weak probes has been presented. Using 10 % of the total WDM channels as weak probes, gain spectrum and power excursion estimation have been demonstrated [126]. Although weak-probe sampling can be done during network operation without disrupting the service, it demands sources and continuous measurements.

A third possibility, typically based on ML techniques, attracting a lot of attention in the last years, is based on predicting the amplifier behaviour using the information extracted from historical data. Required data can be obtained offline, gathered previous to network operation, or online collected during network operation. As an example of offline operation, for a particular amplifier, an ML model based on NNs has been trained in order to estimate its gain [127]. The dataset used for training and test contained experimental measurements, input powers to the amplifier and corresponding output powers, performed under different conditions: variable channel loads and input powers. When applied online, during network operation, instead of modelling an isolated amplifier, a complete link is considered. ML-based power

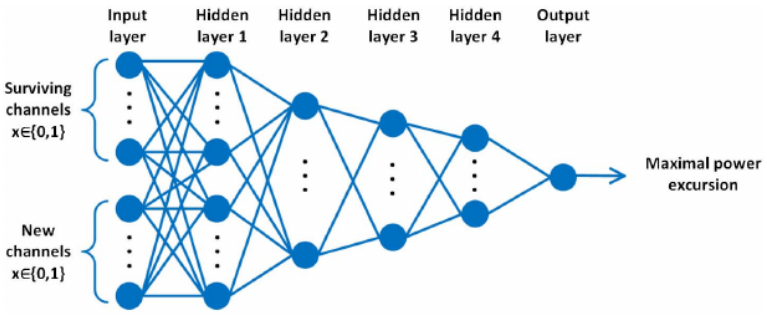

Figure 2.7 – NN architecture used to predict maximal power excursion [44].

standard deviation estimation after transmission in a cascade of two and three amplifiers has been demonstrated [128]. The selected ML algorithm was kernel bayesian regression trained on a experimental dataset. The collected dataset contained input active channels and power deviations at the output of the link, for different channel loads. No input power channel values were required as the input powers were fixed. Later, a similar work from the same group used deep NNs (Fig. 2.7) in a more complex link scenario, which included ROADMs, predicting maximum optical power excursion for a given channel load configuration [44], [129]. ML-techniques can be combined with other methods as characterization, in order to enhance the performance. Trained on data experimentally measured (including as measured inputs: input power, frequency and locked gain; as measured outputs: gain and noise figure (NF, Appendix C)), an NN is able to extrapolate gain and NF under new configurations, not measured before, with different input power, channel frequency and set gain [130]. Another proposed approach has been a hybrid ML EDFA model using an analytical model together with experimental measurements [131].

Still open to improvement, estimating the amplifier behaviour at different operating conditions can be performed, as demonstrated in the previous paragraphs. At this point, another question arises, how the available knowledge can be used in order to mitigate power excursions.

Wavelength assignment can be seen as a direct application. Previous approaches provide a 'module' able to approximate power excursion at the output of an amplifier or cascade of amplifiers. When a request for adding a channel is received, this module is executed several times, each time assuming the channel to be added is allocated in a different frequency out of the available ones. Every time, the module returns an estimation of gain or power excursion corresponding to the tested configuration. Of all these trials, some will present a lower power excursion than others, even below a particular established threshold, becoming candidates for allocating the channel to be added. Reported results have been presented in [44], [122], [123], [126], [128], [129].

Amplifier operating control techniques represent another opportunity to reduce power excursion. It can be used as complement of power excursion aware wavelength assignment

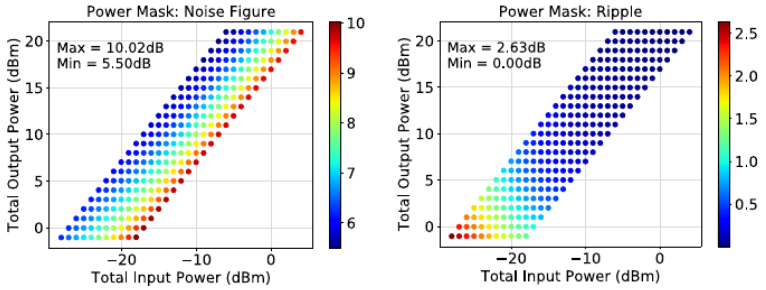

Figure 2.8 – Amplifier power masks for gain and NF [134].

methods introduced in the last paragraph. Once a new channel is added, the total launched power at the input of the amplifier or cascade changes, changing therefore the operating point and gain flatness with it. Controlling the operating point can enable power excursion reductions. Most of these works rely on power masks as the one shown in Fig. 2.8. For a particular input power and locked gain, gain and NF are measured. The process is repeated for numerous input powers and gains in order to have a complete characterization of the power mask. Still, the obtained power mask built on discrete measurements provides discrete outputs, not being able to give information about each input power and gain combination. Trying to solve this issue, by providing an interpolated response, NNs [132] and case based reasoning (CBR) [133] have been proposed, learning from the original discrete power mask. Typically, based on this information, the problem to solve is formulated as the optimization of a parameter measuring performance, as gain flatness or OSNR, by adjusting the amplifier gain. When OSNR is optimized, some works neglected nonlinearities, other used incoherent Gaussian-noise (IGN) model [134] and other imposed a threshold for the launch power [135]. Up to here, the gain adjustment of a single amplifier has been considered. Nevertheless, most of these works targeted cascades of amplifiers, being a crucial issue how to choose the right procedure in order to optimize the performance of the whole link. Some schemes trust on global methods, carrying out an exhaustive search of the optimum operating point among all the possible points [136]. Contrarily, other approaches use local methods, where each amplifier has only access to its state information along with input and output power, with optimization being accomplished through a single step or iterative process gradually adjusting the gains at each amplifier [137].

Previous approaches aim to reduce power excursion but they are unable to cancel them. Distributing signal power in two different wavelengths which produce opposite power excursions, has been used in order to cancel power discrepancies [138]. This cancellation can be done using wavelengths causing equal and opposite power excursion or by using wavelengths causing opposite power excursions with a variable dwell time. Including guardbands, fast laser switching has been experimentally demonstrated to cancel power excursions without impacting the BER. However, using dual wavelengths can result in inefficient use of the spectrum for a high channel load. To address this issue, guidelines to work combining single and dual-wavelength sources, limiting the number of each source type, have been developed [139] .

Other methods rely on cancelling the output power excursions by applying power precompensation at the input of the amplifier or link. Simple iterative method has been demonstrated in [140] using as precompensation powers in each channel P^i_{new}:

$$P^i_{new} = P_{TOT} \frac{1/G_i}{\sum_1^N 1/G_i}, \tag{2.45}$$

where P_{TOT} is the total input power, G_i the gain at channel i and N the total number of channels. Interesting approach, presented differences with regard to the scenarios presented in the last paragraphs. Firstly, instead of amplifiers working on AGC, fixed pump was assumed and secondly, input power was fixed. These assumptions greatly simplify the problem. Furthermore, continuous monitoring is required. Gain equalization by means of power pre-emphasis combined with unequal amplifier parameters has also been presented [141]. Amplifier response was based on analytical model using the transcendental equation including the dynamics of the reservoir, i.e., the total number of excited ions, thus requiring physical amplifier parameters and being quite complex. Several works have worked on the OSNR (or other similar performance measurement) optimization by means of launched power per channel adjustment, in scenarios going from optical point to point link to mesh networks. In order to solve this complex problem different methods have been proposed: game theory [142], an iterative algorithm [143], [144], particle swarm optimization [145], convex solution methods applied to convex objectives [146]. With most of these works considering flat gain amplifiers, these solutions turned out to be computationally complex and time consuming. An ML approach to preadjust the power has been presented, reducing the power discrepancy in defragmentation process [45]. First, two ML-models were trained and validated. One, using ridge regression for approximating the magnitude of the impact, i.e. influence of each channel in the output power excursion. Another, using logistic regression for estimating the correlation, whether an increase in a channel input power produces a increase (decrease) in the optical power excursion. Then, the model was used to adjust in a single step, the input powers of the defragmented super-channel reducing the power excursion in comparison to the case where no power pre-adjustment was applied.

2.3 Experimental validation of an amplifier model

As it will be shown in the next sections, the work presented here is mostly based on simulations. In order to make this synthetic data as close as possible to reality, amplifier characteristic curves experimentally measured, by Network Technology Lab, École de technologie supérieure (Canada), have been used in the simulations. The objective of this section is to describe how these experimental characteristic curves were measured and how they have been utilized by an amplifier model in order to estimate the gain and noise for a given operating point. Results obtained using the model are compared with results obtained experimentally. The following section structure is followed. First, in Section 2.3.1, the measurements done at

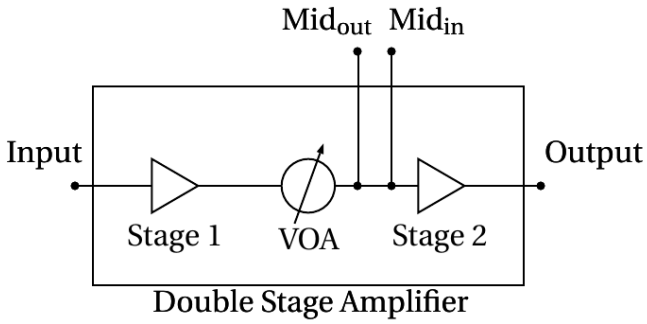

Figure 2.9 – Simplified scheme of a double-stage amplifier.

Network Technology Lab, École de technologie supérieure (Canada) are explained in detail. Second, the description of the model used to estimate the amplifier response is introduced in Section 2.3.2 together with the procedure followed to validate the model in simulations. Finally, Section 2.3.3 compares gain characteristics obtained experimentally with the ones obtained in simulations.

As mentioned in the previous section, complex amplifier architectures including several stages of EDFAs together with additional components have become popular, providing a control layer to the amplifier. The amplifier here characterized is a double-stage amplifier including: gain flattened amplifier stages in order to use the whole C-band [118], a VOA for tilt control in between the two amplifier stages (Fig. 2.9) and noise correction techniques [106], [107].

2.3.1 Amplifier experimental characterization

As it will be explained in Section 2.3.2, the characteristic curves required to model the amplifier behaviour are: dynamic gain and noise characteristics. The setup, at Network Technology Lab, École de technologie supérieure (Canada), used in order to perform the aforementioned characterization is depicted in Fig. 2.10. Two lasers are combined at the input of the double-stage amplifier:

- One laser acting as gain saturating laser at a fixed wavelength λ_m = 1550.918 nm (LD1, on the top left of Fig. 2.10).
- One tuneable laser acting as probe laser. For this purpose, a comb source followed by a wavelength blocker (selecting the desired wavelength) were used, as can be seen in the bottom left of Fig. 2.10.

To monitor the output of the amplifier, an optical spectrum analyzer (OSA) is connected at the output of the amplifier.

The characterization procedure included three different measurements, defined as follows:

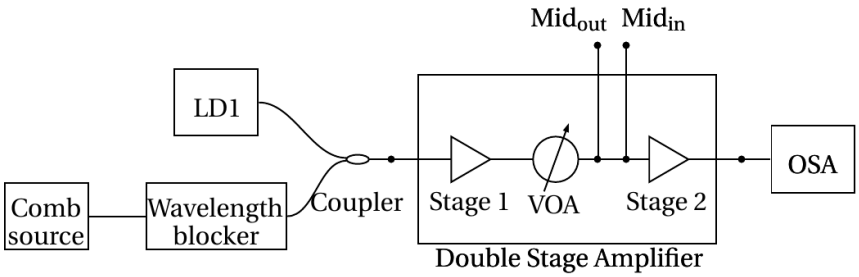

Figure 2.10 – Amplifier characterization: Experimental setup (Network Technology Lab, École de technologie supérieure).

- Measurement 1 - Dynamic Gain 1, $G_1(\lambda)$: To fix the inversion level of the EDFA, LD1 is set to a relatively large power of −15.7 dBm and injected into the amplifier at the measurement wavelength λ_m = 1550.918 nm. LD2, the probe laser, at a considerable lower power of −30 dBm, is swept in a bandwidth 1530.72–1562.23 nm.
- Measurement 2 - Dynamic Gain 2, $G_2(\lambda)$: Measurement 1 is repeated with a higher power in LD1 of −5.5 dBm.
- Measurement 3 - Noise: With the same setup as measurement 1, LD2 is turned off.

All three measurements were done in current control (CC) mode [95], i.e. for a fixed pump power value, for different values of the VOA 0 dB, 5 dB, 10 dB and 20 dB in between the two stages of the double-stage amplifier (see Fig. 2.9). From these measurements, Fig. 2.11a, Fig. 2.11c, Fig. 2.11e and Fig. 2.11g show the dynamic gains [147] calculated from Measurement 1 and Measurement 2, for VOA values of 0 dB, 5 dB, 10 dB and 20 dB, respectively. As expected, the gain tilt increases as the attenuation introduced by the VOA in the mid-stage increases. Spectral noise power determined from Measurement 3 is represented in Fig. 2.11b, Fig. 2.11d, Fig. 2.11f and Fig. 2.11h, corresponding to the same VOA values 0 dB, 5 dB, 10 dB and 20 dB. From the results, noise spectral power decreases as the introduced attenuation increases. This is due to the fact that the VOA attenuates the power at the output of the first stage, producing an increase in the pump power in order to keep the output power, therefore decreasing the noise.

2.3.2 Amplifier model based on experimental characterization

The amplifier model, based on the so-called 'black-box' model [147], used the characteristic curves calculated during the characterization described in Section 2.3.1. Note that, from the characterization, the following set of characteristic curves were obtained:

- Dynamic gains (Measurement 1 and Measurement 2): Two curves describing the dynamic wavelength dependent gains of the amplifier at two different input powers.

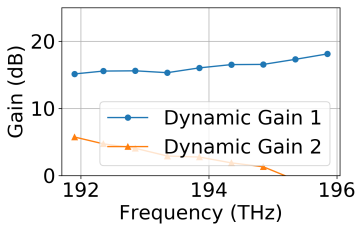

(a) Dynamic gain - VOA 0 dB.

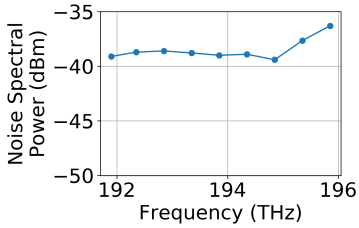

(b) Noise spectral power - VOA 0 dB.

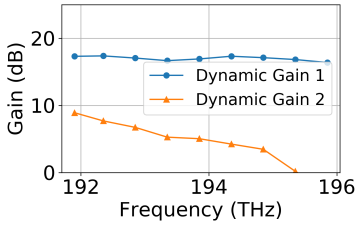

(c) Dynamic gain - VOA 5 dB.

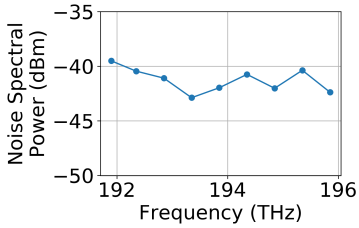

(d) Noise spectral power - VOA 5 dB.

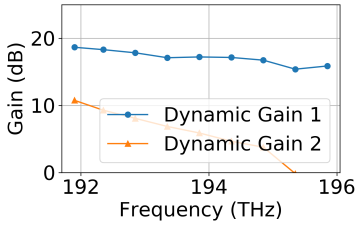

(e) Dynamic gain - VOA 10 dB.

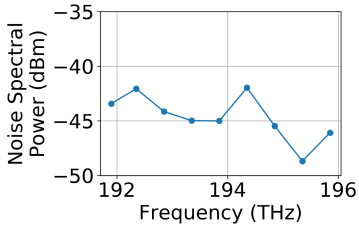

(f) Noise spectral power - VOA 10 dB.

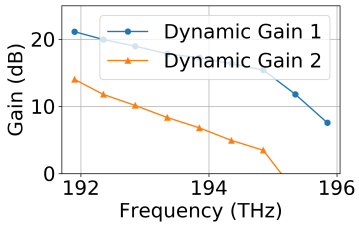

(g) Dynamic gain - VOA 20 dB.

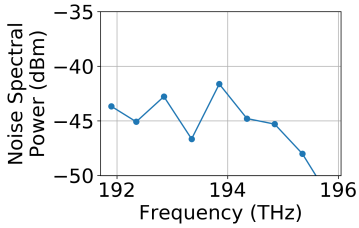

(h) Noise spectral power - VOA 20 dB.

Figure 2.11 – Dynamic gain curves (left) and noise spectral power (right) in CC mode for VOA 0 dB, 5 dB, 10 dB and 20 dB.

- Noise characteristics (Measurement 3): Noise power reflecting the wavelength dependency, under the assumption that noise is independent on the saturating conditions.

For each operating point, the gain G at each wavelength λ is calculated based on the two

dynamic gain curves previously measured $G_1(\lambda)$ and $G_2(\lambda)$:

$$\log \mathrm{G}(\lambda, \Delta \mathrm{G}) = \log \mathrm{G}_2(\lambda) + \mathrm{T}(\lambda) \log \Delta \mathrm{G}, \tag{2.46}$$

where $\log \Delta \mathrm{G}$ represents the gain difference $\log \mathrm{G}(\lambda_{\mathrm{ref}}) - \log \mathrm{G}_2(\lambda_{\mathrm{ref}})$ at a reference wavelength λ_{ref} and $\mathrm{T}(\lambda)$ is the tilt:

$$\mathrm{T}(\lambda) = \frac{\log \mathrm{G}_1(\lambda) - \log \mathrm{G}_2(\lambda)}{\log \mathrm{G}_1(\lambda_{\mathrm{ref}}) - \log \mathrm{G}_2(\lambda_{\mathrm{ref}})}. \tag{2.47}$$

In AGC mode, a specific locked gain $\mathrm{G}_{\mathrm{lock}}$ can be expressed as:

$$\mathrm{G}_{\mathrm{lock}} = \frac{\mathrm{P}_{\mathrm{out}}}{\mathrm{P}_{\mathrm{in}}} = \frac{\sum_\lambda \mathrm{P}_{\mathrm{in}}(\lambda)\mathrm{G}(\lambda) + \int_{-\infty}^{\infty} \mathrm{S}(f, \mathrm{G}(\lambda))\, df}{\sum_\lambda \mathrm{P}_{\mathrm{in}}(\lambda)}, \tag{2.48}$$

where $\mathrm{P}_{\mathrm{in}}(\lambda)$ and $\mathrm{G}(\lambda)$ are the input power and the experienced gain at each wavelength and $\mathrm{S}(f, \mathrm{G}(\lambda))$ is the noise power spectral density, which assuming constant NF approximation is only dependent on the gain:

$$\mathrm{S}(\lambda, \log \Delta \mathrm{G}) = \left(10^{NF(\lambda)/10} G(\lambda, \log \Delta \mathrm{G}) - 1\right) h\nu. \tag{2.49}$$

with h and ν, Plank constant and frequency, respectively. Therefore, in AGC mode, gain and noise responses can be approximated for locked gain $\mathrm{G}_{\mathrm{lock}}$ using eqs. 2.46, 2.47 and 2.48. However, the experimentally characterized amplifier is compensating for the ASE noise (noise correction). Therefore, an adjustment of the locked gain in the simulations is required in order to have the same gain as in the experimental measurements. As seen in Section 2.2.1, this adjustment consists in increasing the gain by the factor related with the ASE noise, calculating the gain for simulations as $\mathrm{G}_{\mathrm{lock,adj}}$:

$$\mathrm{G}_{\mathrm{lock,adj}} = \mathrm{G}_{\mathrm{lock}} + \frac{\int_{-\infty}^{\infty} \mathrm{S}(f, \mathrm{G}(\lambda))\, df}{\sum_\lambda \mathrm{P}_{\mathrm{in}}(\lambda)}. \tag{2.50}$$

As the NF is considered to be constant, in order to calculate the spectral noise density from eq 2.49, the gain $\mathrm{G}(\lambda)$ is required, which was approximated by the average gain obtained from measurements. This makes the model more accurate at high loads, where the correction factor can be neglected, and at low channel loads, if the noise power spectral density is known. Improvements in the model are required in order to be applied during dynamic wavelength operation including low channel load. This limit can be neglected for amplifiers not including noise correction, as they calculate the locked gain in same conditions as the original model.

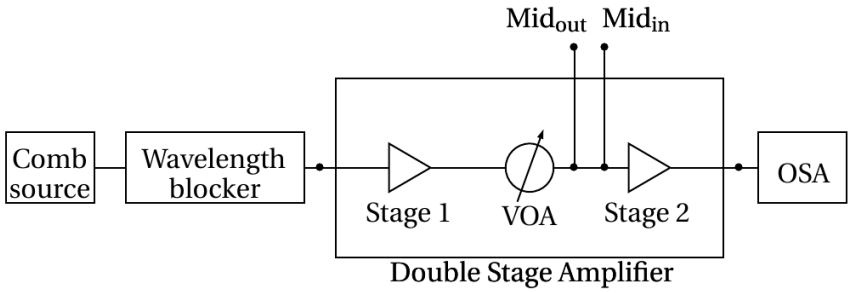

Figure 2.12 – Amplifier model validation: Experimental setup (Network Technology Lab, École de technologie supérieure).

2.3.3 Model validation

In order to validate the model, experimental measurements and simulations were carried out under different conditions, always working in AGC mode with a locked gain of 15 dB and VOA at 5 dB. First, experimental and simulation setups are described, with the experimental setup at Network Technology Lab, École de technologie supérieure (Canada). Afterwards, the comparison of obtained results under different operating conditions are shown.

Experimental setup

Experimental setup is shown in Fig. 2.12. At the input of the double-stage amplifier a comb source together with a wavelength blocker are configured in order to generate a particular channel configuration using a 50 GHz frequency spacing. For each measurement, following parameters must be precised: number of active channels, channel frequencies and input channel powers. After passing through the double-stage amplifier working in AGC mode at 15 dB and with VOA at 5 dB, the output spectrum is recorded.

Simulation setup

A similar simulation setup was developed in VPItransmissionMaker^{TM} (hereafter called VPI, Appendix D), as seen in Fig. 2.13, using parameterized signals based on a power signal representation [148]. For the same input configurations as in the experimental measurements, the channels were multiplexed at the input of the amplifier to be demultiplexed again at its output in order to measure the output powers per channel at the receivers (RXs). The amplifier model was also configured with the same parameters as in the experimental setup, locked gain 15 dB and VOA at 5 dB (using the characteristic curves corresponding to VOA at 5 dB),

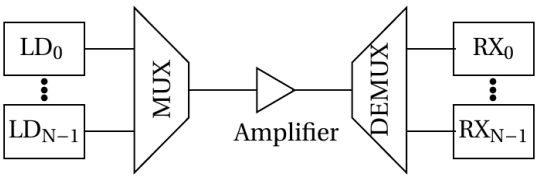

Figure 2.13 – Amplifier model validation: Simulation setup.

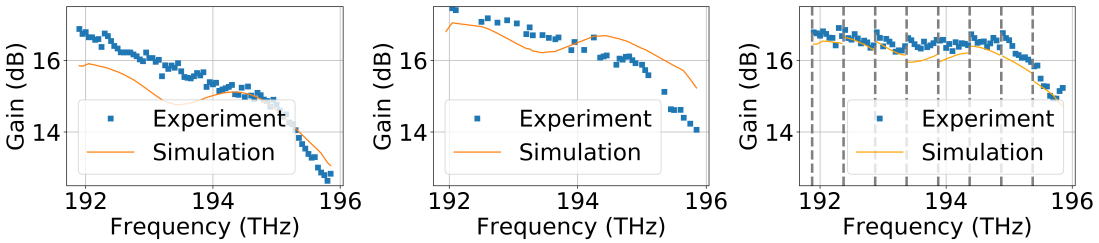

(a) 80 ch.-Gain (b) 40 ch.-Gain (c) 10 ch.-Gain

Figure 2.14 – Gain for 80 channels, 40 random channels and 10 channels swept in the band representing 8 different measurements, separated by vertical dashed lines.

Obtained results under different operating conditions

Considering a maximum of 80 channels in a 50 GHz frequency grid, in the range [191.9 – 195.85] THz, first, for a fixed input channel power, three different input channel loads were examined:

1. 80 channels: all the channels were active.
2. 40 channels: 40 random channels.
3. 10 channels: 10 active channels sweeping in the band i.e. first measurement with the first 10 channel frequencies in the range [191.9 – 192.35] THz, second measurement with the next 10 channel frequencies in the range [192.4 – 192.85] THz, etc. (8 different measurements).

Figure 2.14 illustrates the results obtained in experimental measurements and simulations for the three different cases considered: 80 channels, 40 random channels and 10 channels (each vertical dashed line separates each 10-channel measurement). For all of them, there is a good agreement between the experimental measurements and simulations.

Secondly, for a particular channel configuration, 12 channels in a 100 GHz frequency spacing in the frequency range [191.9 – 193.0] THz, different input channel powers were tested. As it can be seen in Fig. 2.15, showing the difference between experimental measured gain and the

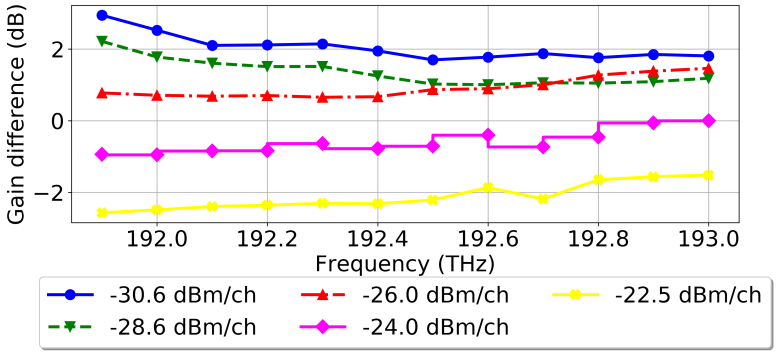

Figure 2.15 – Gain difference between experimental measurement and simulation for different input peak powers.

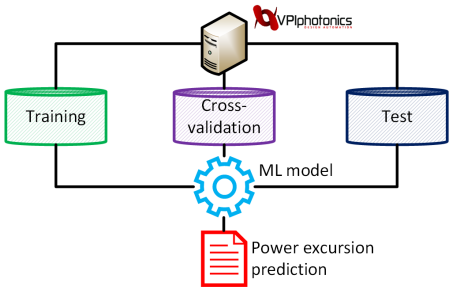

Figure 2.16 – Optical power excursion prediction: Development diagram.

simulated gain for the different input peak powers per channel (ch) considered, the model shows a good performance for medium powers. For high input powers, the experimental gain is lower than expected, probably due to homogeneous and mutual inhomogeneous gain saturation effect [95]. The model is not working so well in the saturation regime, where the gain should decrease (Appendix C). For low input power, the difference is likely to be due to the noise correction factor.

2.4 Optical power excursion prediction based on neural networks

Pointed out in Section 2.2.3, several recent works have demonstrated the utility of ML in predicting optical power excursions. In the case presented here, optical power excursion prediction based on NNs is demonstrated using a synthetic dataset. The procedure followed for the development and test of the ML module is shown in Fig. 2.16. First step is the generation of the dataset, in this case a synthetic dataset created using VPI. An NN model is then trained and validated. Finally, the performance of the NN predicting optical power excursion is evaluated. Next sections are organized as follows. First, the dataset generation is described. Afterwards, the NN module, training, validation and test are detailed.

A simplified diagram of the simulated setup is illustrated in Fig. 2.17, where 80 transmitters

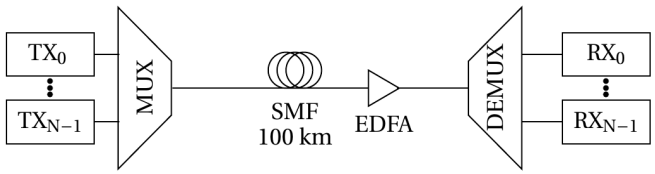

Figure 2.17 – Optical power excursion prediction: Simulation setup.

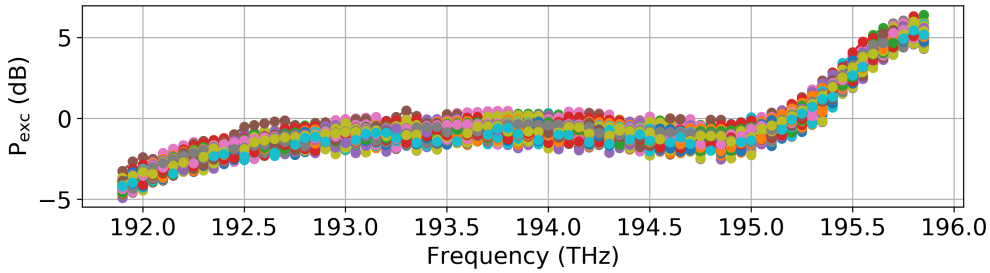

Figure 2.18 – Optical power excursion prediction: Dataset.

using a 50 GHz frequency grid are considered [149]. Every channel carries modulated data at 100 Gb/s using 16 quadrature amplitude modulation (QAM) modulation. Power per channel is fixed to be the same and equal to 0 dBm. Number of active channels and frequency allocation are parameters to configure in each simulation. Generated signals are multiplexed and transmitted over a 100 km single-mode fiber (SMF). After propagating through the fiber, a single stage EDFA operating in AGC mode at 20 dB gain compensates the losses introduced by the fiber. Finally, received channels are demultiplexed and sent to the corresponding receivers where optical power excursions are measured.

In each simulation a random channel load in the range 40 % to 87.5 % is selected. Wavelength assignment is also performed randomly. Following this procedure, a total of 300 simulations were executed, saving for each simulation the active channels and the corresponding output power excursions. Output power excursions of the complete dataset are shown in Fig. 2.18.

This dataset is used to train an NN. The input feature vector to the NN is a vector of 80 values, with each value indicating whether the channel is active or not. The input layer is connected to a hidden layer with 160 neurons using ReLU as activation function (Section 2.1.2). The choice of this activation function is justified on the basis of its performance and fast training in comparison with another activation functions as $tanh$ [86]. After the hidden layer, the output layer with 80 outputs returns the power excursion in every channel. As the output power excursion is a real number, linear activation is used.

The NN model has been developed in Keras, high level NN application programming interface running on TensorFlow Python library [150]. Training and validation were performed using 80 % and 15 % of the dataset respectively. During training, stochastic gradient descent with a batch size equal to the 10 % of the training dataset has been used for optimization.

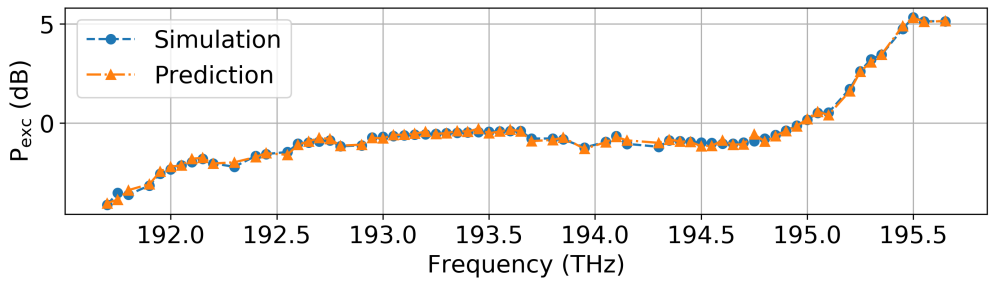

Figure 2.19 – Estimated power excursion calculated by simulation and the predicted values using the presented approach, for one of the samples of the test dataset.

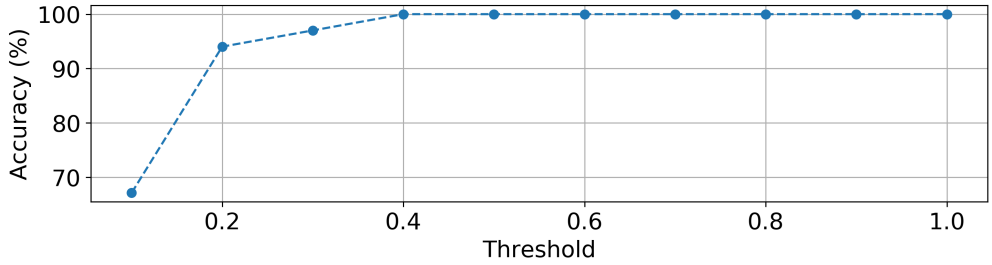

Figure 2.20 – Accuracy on a test sample from the test set.

Remaining 5 % of the dataset has been utilized for test purposes. For one of the samples of the test dataset, Fig. 2.19 shows the estimated power excursion calculated by simulation and the predicted values using the NN, which are very close.

On the same sample, Fig. 2.20 illustrates the algorithm accuracy as a function of the minimum acceptable difference between the real values and the predicted values. Considering a 1 dB threshold, small in comparison to the 3 dB critical value, the NN provides 100 % accuracy. Lowering the threshold to 0.2 dB, the NN still achieves above 90 % of accuracy.

2.5 Optical power excursion precompensation based on reinforcement learning

As in current optical networks wavelength conversion is not always an option, additional wavelength continuity constraints must be considered. In these conditions, reducing optical power excursion by selecting wavelengths which undergo lower power excursions is not a possibility. Adjusting the operating point of each optical amplifier could be a solution, although at the expense of requiring a continuous control of each amplifier in the link. In this sense, precompensation techniques, as the one discussed here represent an effective end-to-end approach, transparent to the network, without the necessity of any intermediate component control.

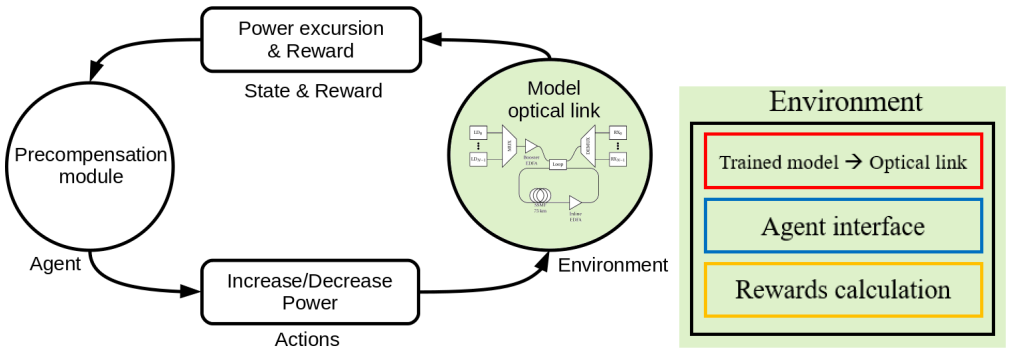

(a) RL general model.

(b) Environment details.

Figure 2.21 – RL approach for optical power excursion precompensation.

The objective is to minimize the power excursion at the output of a point-to-point link by adjusting the channel input powers at the transmitter side. The reported method, based on RL techniques, allows to solve this complex optimization difficulty by directly learning on the gathered data from the point-to-point link. The fine tuning of the input powers, in small steps of 0.1 dB, allows smooth power transitions, reducing undesired impact on the established lightpaths.

As introduced in Section 2.1.2, RL methods learn by interaction between a learner (agent) with the outside world (environment) (Fig. 2.21a). In the power precompensation scenario presented here, the power precompensation module (agent) interacts with optical amplified link (environment). For each power excursion at the output of the link, the power precompensation module (agent) takes an action changing the input channel powers in small steps of 0.1 dB. As a consequence of this action, depending whether the power excursion increases or decreases, the power precompensation module receives a reward. Through this process, the agent learns which actions maximize the expected reward and therefore it learns to minimize the power excursion.

This learning task can be broken in episodes. Each episode starts with the environment in the initial state, which is considered to be the one with the input power distributed equally among the channels. During the episode, the output power excursion evolves depending on the actions taken by the precompensation module. Finally, the episode ends when the maximum optical power excursion is below a threshold and the agent wins, or when optical power excursion increases or the maximum number of steps to achieve this threshold is over and the agent loses. In any case, after the end of an episode, a new episode begins.

In the following, environment and agent, together with its joint learning, are described in more detail under different circumstances. In Section 2.5.1, DDPG algorithm is adopted whereas in Section 2.5.2 a comparison among different policy-gradient methods is provided including also a study for different channel loads. Section 2.5.3 validates the RL-based precompensation approach, trained based on synthetic data, in an experimental testbed.

2.5.1 Development of a reinforcement learning algorithm for precompensation

In this first approach of power precompensation using RL techniques, DDPG has been selected as RL algorithm to implement the agent. Before going into detail about the agent implementation, the environment is introduced. Once environment and agent are described, the obtained results are analyzed.

Environment: Model based on simulations

The existence of a good match between experimental and simulation results, as revealed in Section 2.3, authorizes the direct usage of simulations as an environment to train the RL algorithm. Although this was the strategy adopted at the beginning, unfortunately turned out to be slow, as many interactions with the environment are required to take place in order to motivate the agent to learn. This is the main reason to develop a model able to replace the simulations. The selected model is based on NNs, as shown in Section 2.4 and successfully used in the literature to predict optical power excursion [10], [44], [127]–[129].

According to this, environment's generation is executed in three steps (Fig. 2.21b): (1) synthetic dataset generation based on VPI simulations, (2) NN model training (3) complete environment creation by integrating in a Python module the NN model together with a reward, being able to interact with the agent at each timestep.

Synthetic dataset generation Figure 2.22 illustrates the setup developed in VPI, used to create a synthetic dataset. First, a bank of transmitters allows to generate a maximum of 80 channels using a 50 GHz frequency grid in the frequency range [191.9, 195.85] THz. After multiplexing, the channels are first amplified in a booster amplifier and then transmitted in a loop for 10 times. Each pass in the loop is equivalent to traverse one span with 75 km fiber and an inline amplifier working in AGC mode at 15 dB gain in order to compensate the losses in the fiber. All the amplifiers included in the setup operate in AGC mode at 15 dB gain modelled using the experimental curves obtained in Section 2.3 for VOA at 5 dB without including noise correction (Section 2.3.2, Fig. 2.22b).

Input channel powers, frequency positions and number of active channels are parameters to be configured in each simulation. For the input powers, different distributions have been considered:

- Constant power for all the channels.
- Random input powers per channel.
- Predistorted input powers as explained in [140] in order to be able to predict equalized output powers.

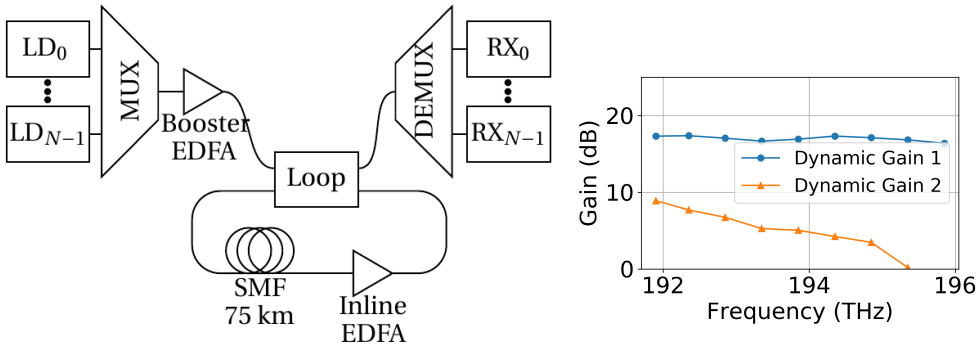

(a) Simulation setup.

(b) Amplifier gain dynamic curve.

Figure 2.22 – Power precompensation: (a) Simulation setup and (b) amplifier gain dynamic curve.

- Modified input powers determined in the previous cases by adding or subtracting 0.1 dB to all or some active channels.

Channel load was modified between 3.75 % and 100 % corresponding to 3 and 80 channels, respectively, with randomly frequency assignment. Approximately ~ 2000 simulations have been run in this way, storing for each simulation the input and output channel powers. The generated dataset has been used to train and test an NN model of the optical link environment.

NN model Using the previous dataset, an NN model, with 1 NN per channel, has been trained in Keras and TensorFlow Python libraries. The selected NN structure contains:

- Input layer: representing the input power in each channel, the number of neurons is equal to the number of channels.
- Hidden layer: 160 neurons using ReLU as activation function.
- Output layer: 1 neuron with linear activation in order to calculate the power deviation between the calculated output power and the desired power per channel which was considered to be −21.5 dBm.

The previous dataset was split in three fractions: 85% for training, 5% for validation and 10% for test purposes. After training using Adam [151] as method for stochastic optimization, an average mean squared error of 9.5×10^{-3} was obtained.

Environment entity The complete environment was developed as a Python module. Internally storing the current environment status, i.e. current channel input powers and corresponding output power excursions, at each interaction with the agent:

- The environment sends to the agent the current power deviation vector (state).
- The environment receives an action vector indicating for each channel whether the channel power is increased or decreased by 0.1 dB.
- After updating the input channel power using the received action, the environment calculates, using the NN model, the new power excursion (updated state).
- Depending on whether the power excursion has increased or decreased, a reward is returned to the agent together with the updated state.

Special attention requires the reward. The reward indicates to the agent whether the action has been 'good' or 'bad' bringing him closer or farther to minimize the power excursion. After testing different rewards, including continuous and discontinuous, the best results were obtained with an exponential of the distance [152] to the desired zero power excursion. Therefore, the reward varies between values close to 0 for large power excursions to values close to 1 for small power excursions. Apart from the continuous exponential two dedicated rewards were defined:

- Reward -1.0: For an episode ending after running off timesteps, doing a no-action, increasing the total input power above a threshold, increasing the power excursion.
- Reward 100.0: For an episode ending winning: the maximum power excursion is below a threshold, which in this case was considered to be 0.5 dB.

Agent: precompensation module

Considering that in the case studied here, a continuous state space (optical power excursion is a real value) and a high-dimension action space (increase or decrease the input power in each channel) make unpractical to use RL algorithms based on estimating value function, policy-gradient algorithms using actor-critic methods look like a suitable option. As presented in Section 2.1.2, in these algorithms, the agent is composed by two different entities: the actor and the critic. The actor decides which action to take depending on the current state, estimating the policy, whereas the critic evaluates the actions taken by the actor, learning a value function. In this specific case, the state corresponds to the current power excursion or deviation whereas the action is the fine tuning change in input power done by the precompensation module.

In this first approach, DDPG, a popular action-critic method introduced in Section 2.1.2 has been implemented in Tensorflow. Actor and critic were both defined as two separated NNs. The critic has as an input the state and action and returns as an output the expected reward based on the current reward given by the environment and the estimated discounted future reward. The actor takes as an input the current state and as an output the selected action. For training the actor, its NN weights are optimized based on the critic, by using the gradient, in order to get the maximum reward.

Similar as the environment, the actor-critic method has been developed in TensorFlow. For the actor, the NN has as input the power deviation. Thus, the required number of input neurons is equal to the number of channels. After one hidden layer, the output layer returns the power change or action. As the action can only take two values +0.1 or −0.1, the selected activation function for the output layer is the hyperbolic tangent ($tanh$). The number of output neurons is again equal to the number of channels. For the critic, the NN has as input the state and the action, which are followed by one hidden layer. After this first hidden layer, both are merged in a second one, which is finally connected to the output layer. As the critic returns an expected reward, the output layer has only one neuron and uses linear activation. Both of them using ReLU activation in the hidden layers and Adam method for optimization. Note that DDPG is an off-policy algorithm, copies of actor and critic are used as targets, doing soft-updates: $\tau << 1 : \theta' \leftarrow \theta + (1-\tau)\theta'$.

After explaining the working principle and implementation of actor and critic, it is worth to clarify how actions are chosen from the start. Part of the actions are chosen by exploiting the knowledge gathered in the interaction with the environment, but another part is chosen by exploration, randomly selecting actions from the action space. At the beginning, the actor has no knowledge about which is the best action, so most of the actions are random; with the time, as the actor starts to be able to distinguish between correct and incorrect actions, the exploration rate decreases exponentially until it reaches a minimum (ϵ-greedy exploration technique) [88]. This is kept until the end in order to leave always a possibility to learn from new action/states.

Results

The RL method has been trained for 12 channels in a 50 GHz frequency spacing, which approximately took 2 hours in a processor Intel core i7-8654U at 1.90 GHz. After training, Fig. 2.23 shows the evolution of the input channel power and output power excursion. Starting from a flat input channel power, the precompensation module modifies the input channel powers in steps of 0.1 dB until achieving a maximum absolute power excursion below 0.5 dB. As an example (Fig. 2.23), in the first channel, power excursion is reduced from 2.03 dB before starting the adjustment to approximately −0.34 dB after applying power precompensation.

2.5.2 Evaluation of different reinforcement learning methods

After this first approach to a power precompensation module adopting DDPG as selected RL method, different algorithms have been compared. The selected RL methods to be compared are the ones presented in Section 2.1.2: A2C, DDPG, TRPO and PPO. Instead of developing a customized implementation of these algorithms, available code part of Stable Baselines [153], implementations of RL algorithms based on OpenAI Baselines [154] has been utilized. Furthermore, the performance under different channel loads (12-channel, 24-channel, 40-channel, random-channel scenarios) in terms of optical power excursion reduction and training time

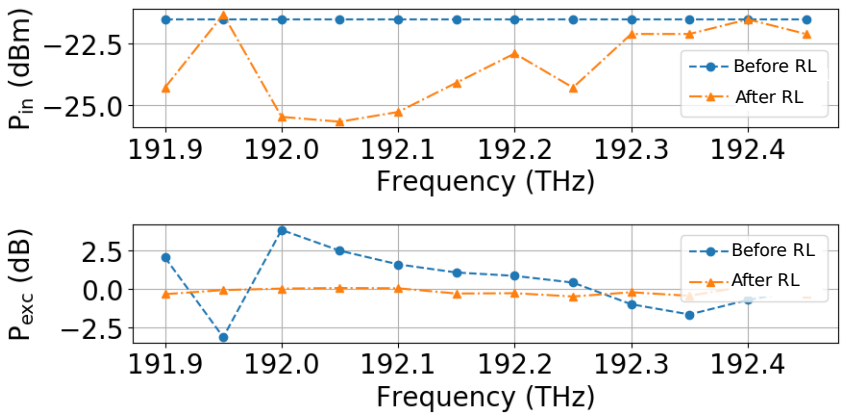

Figure 2.23 – Evolution of the input channel powers and power excursion for 12 channels after RL training.

has been compared. The present section follows the same structure as Section 2.5.1. First, environment and agents implementation and characteristics are discussed. Afterwards, obtained results are analyzed.

Environment: Model based on simulations

The developed environment is very similar to the one presented in Section 2.5.1. In the following, the procedure adopted in order to create the environment module is described, starting by the synthetic dataset generation, continuing with the NN model and finalizing with the complete integrated environment entity. Note that 4 enviroments are created corresponding to the 4 considered scenarios: 12-channel, 24-channel, 40-channel, random-channel scenarios.

Synthetic dataset generation Using almost the same setup as in Fig. 2.22 but considering only 5 spans in order to reduce the accumulated optical power excursion and assuming similar operating conditions for the amplifier model (AGC mode at 15 dB gain, VOA at 0 dB, no noise correction (Section 2.3.2)), simulations have been run in the same manner adjusting input channel powers, frequency positions and number of active channels at each simulation (Fig. 2.24). The considered channel load was slightly different, varying between 15 % and 100 % corresponding to 12 and 80 channels, respectively, with random frequency assignment. Storing in a dataset input channel powers used in each simulation and the corresponding output powers, the complete generated dataset comprises ~ 8000 simulations. From this complete dataset 4 separated datasets were created, corresponding to the 4 different channel load scenarios tested in this section. Therefore, the original dataset was used to construct 4 datasets:

- Dataset 12-channel model: ~ 1800 simulations subset containing simulations corre-

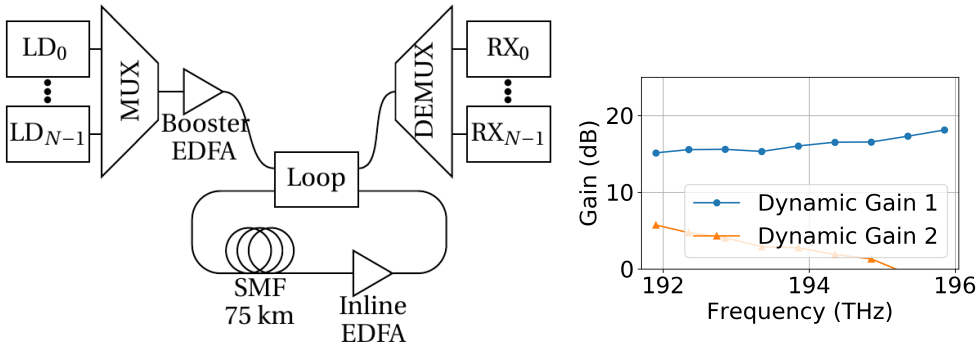

(a) Simulation setup.

(b) Amplifier gain dynamic curve.

Figure 2.24 – Power precompensation: (a) Simulation setup for algorithm comparison and (b) amplifier gain dynamic curve.

sponding to 12 channels in the 191.9 THz to 192.45 THz frequency range in a 50 GHz frequency spacing.

- Dataset 24-channel model: ~ 1800 simulations subset containing simulations corresponding to 24 channels in the 191.9 THz to 193.05 THz frequency range in a 50 GHz frequency spacing.
- Dataset 40-channel model: ~ 1800 simulations subset containing simulations corresponding to 40 channels in the 191.9 THz to 193.85 THz frequency range in a 50 GHz frequency spacing.
- Dataset random-channel model: complete original dataset of ~ 8000 simulations, containing simulations corresponding to random channels together with all the 3 previous cases.

NN model For each of the 4 datasets, an NN model with almost the same parameters as in Section 2.5.1 has been trained. The only difference is that the desired power per channel is considered to be −17.5 dBm, in order to optimize launch power but avoid nonlinearities [43], [155]. After training, 4 NN models are obtained for each of the 4 scenarios to test: 12 channel, 24 channel, 40 channel and random channel. Average mean squared error of 7.69×10^{-5}, 7.19×10^{-5}, 1.76×10^{-4} and 4.79×10^{-4} were obtained for the 4 NN models respectively.

Environment entity Accordingly, each of the 4 NN models has been integrated in a Python module able to interact with the agent. At each timestep, the environment sends the current state to the agent, receiving from the agent the action to take (increasing or decreasing input channel powers). Consequently, in the next timestep, the environment updates the state due to the executed action and delivers the corresponding reward to the agent. With regard to the environment created in Section 2.5.1 one main difference has to be mention, related with the reward. The limit in the number of timesteps to achieve an average power excursion below a

specific threshold has been removed, as now scenarios are more complex. The threshold used to determined whether an episode is successful has been kept to 0.5 dB of mean optical power excursion.

Agent: precompensation module

As agent, four different actor-critic algorithms presented in Section 2.1.2 have been used: A2C, DDPG, TRPO and PPO. Instead of developing custom implementations, existing implementations, part of Stable Baselines [153], based on OpenAI Baselines [154], have been utilized.

Based on TensorFlow, actor and critic are implemented as NNs. A2C, TRPO and PPO use the same actor-critic network architecture, with actor and critic sharing layers in the same NN model with 2 hidden layers of 128 neurons using $tanh$ activation. Both layers are shared for policy and value function estimation, receiving observations as an input and returning a latent representation for the policy and value function. The DDPG actor-critic network is different, as it is based on action-value function estimation. The actor chooses the action based on the input state, whereas the critic requires observation and action in order to estimate the value function. Actor and critic are therefore separated networks, both of them having also 2 hidden layers of 128 neurons. Some differences exist regarding activation. The critic uses only ReLU activation for all the layers. However, the actor uses ReLU activation for the hidden layers and $tanh$ for the output layer. Although this is the specific configuration for the 12-channel and 24-channel scenarios, only slight changes were done for the other scenarios and only regarding the number of neurons: 2 layers of 256 neurons for the 40-channel case and 2 layers of 512 neurons for the random-channel case.

RL exploitation-exploration dilemma is addressed differently depending on the RL method. Instead of using the ϵ-greedy exploration technique [88] as in the previous custom implementation of the DDPG method shown in Section 2.5.1, here, in order to improve exploration, during the training, DDPG adds noise to the actions following an Ornstein-Uhlenbeck process. A2C modifies the gradient formula using an entropy component [91]. TRPO and PPO rely on sampling actions according to the latest version of its stochastic policy [154].

For the 4 environments considered, agent and environment have been finally associated together in a Python software environment. Before training, models of each RL algorithm are defined with their specific hyperparameters. During training, interactions between agent and environment are succeeding, monitoring its evolution. After completion, performance of each of the trained agents is evaluated. Results obtained during training and evaluation are analyzed in the next section.

Results

RL-algorithms' training has been carried out on the 4 generated environments corresponding to 12-channel, 24-channel, 40-channel (with 50 GHz frequency spacing) and random number of channels (on a 50-GHz frequency grid). Before presenting the results, it is essential to mention that the training and test for all the 4 scenarios was identical except for:

- Each scenario requires its own developed environment.
- For the agent, specifically for the NN architectures used to approximate policy and value functions, differences in the number of neurons were required for each scenario (as indicated before: 2 layers of 128 neurons for the 12-channel case, 2 layers of 128 neurons for the 24-channel case, 2 layers of 256 neurons for the 40-channel and 2 layers of 512 neurons for the random-channel case).

During training, interactions between environment and agent have been monitored, with each interaction being called timestep. Learning curves, calculated as average rewards over a 100 episode window with respect to timesteps, are illustrated in Fig. 2.25, with each figure in Fig. 2.25, reproducing the results of each of the 4 scenarios.

Starting for the simplest scenario, the 12-channel case shown in Fig. 2.25a, all the algorithms manage to learn a suitable policy. TRPO presents the worst performance of all of them, achieving quite low rewards. A2C is able to get high rewards, although with an unstable behaviour, converging to lower rewards, at the end of the training. DDPG produces the best results, but PPO learns faster, achieving high scores within less than 50.000 timesteps.

The 24-channel scenario, more complex, shows a similar performance. Shown in Fig. 2.25b, PPO and DDPG demonstrate a better performance, with DDPG achieving the highest rewards in a shorter time. TRPO ends the training with very low rewards, not being enough to learn a policy which reduces the average power excursion below the threshold. A2C shows again an unstable behaviour, with rewards falling at the end of the training.

Same tendency continues in the 40-channel scenario shown in Fig. 2.25c. PPO learns smoothly, but DDPG keeps outperforming it (with higher rewards), now learning a policy in a similar number of timesteps. A2C keeps showing instabilities and TRPO fails to learn.

RL algorithm learning curve on the most complex environment considered here, the random-channel environment, is shown in Fig. 2.25d, only for the DDPG algorithm, as the other algorithms were not able to learn. Note that although the environment's channel load working range, previously indicated, is between 15 % and 100 %, during the RL-model training the range was reduced to between 15 % and 80 %. Thus, the RL-model is trained on random channel loads, where the number of active channels is randomly selected between 12 and 64 channels. For a particular number of channels, frequencies are randomly assigned out of the 80 possible frequencies. Comparing Fig. 2.25d with the previous learning curves obtained with the other

environments, scores are much lower. Previous scenarios achieved average reward of 100, meaning that the agent is always able to win an episode, i.e. reducing the average power excursion under the specific threshold. Now, an average reward of 5 is accomplished at the end of the training, implying that the agent is not winning. Nevertheless, the agent does learn, if the input power were randomly modified as at the beginning of the training, the average reward would become close to 0. This is visible in Fig. 2.25d inset using a different scale for the y-axis. There is therefore a slow increase in the number of rewards over the timesteps. The performance could be improved by upgrading the environment's model, increasing the size of the dataset size used for training.

After seeing the learning curves for the different scenarios, some remarks can be derived. First, A2C and TRPO do not seem to be suitable for this use case scenario. Best performance is obtained with DDPG and PPO, with DDPG being slightly better. However, it is also important to notice that PPO learns very smoothly, due to the restrictions in the policy updates, whereas DDPG presents a more abrupt learning curve, which could lead to instabilities. Better results could be achieved in PPO and TRPO by modifying the used hyperparameters.

Time required by each algorithm to learn a policy for each of the 4 scenarios in a processor Intel core i7-8654U at 1.90 GHz is illustrated in Fig. 2.26. In general, as the considered channel load increases, from 12 to 40 channels, the required time is kept quite constant. Focusing the attention in the two best performing algorithms, DDPG and PPO require almost the same amount of time in order to learn a suitable policy. For the random-channel scenario, convergence is not clear, all the training time, 300 k timesteps, is accounted, causing a considerable increase of the required training time.

As DDPG has been the algorithm showing better performance during training, it was selected to be tested after the training. In order to evaluate the performance of the learnt policy, DDPG was tested working on a deterministic mode, which disables random action selection used for exploration. Evolution of the input powers and corresponding power excursions for each of the 4 scenarios are shown in Fig. 2.27. Note the learnt policy, and therefore, the power evolution shown here, can vary from training to training. RL algorithms learn by trial and error, depending on the selected random actions and on the actor and critic NNs weight initialization, which can be different at each time the algorithm is trained, leading to different policies. Thus, solutions shown here are not unique, making RL methods very powerful on finding solutions which could be hidden. Taking as example the 12-channel case in Fig. 2.27a, before applying any precompensation, input channel powers (P_{in}) are equal and the corresponding maximum power excursion exceeds −5 dB. Step by step of 0.1 dB, input channel powers are modified reducing optical power excursion, until reaching the final input predistorted channel powers which produce an average power excursion below 0.5 dB. Same analysis can be applied to the 24-channel and 40-channel cases. During the RL algorithm training, we have not included upper or lower limits in the input channel powers. As in this case the accumulated optical power excursion at the end of the link (when the whole band is considered, as in Fig. 2.27d) varies from −5 dB to 5 dB, the input channel powers can be

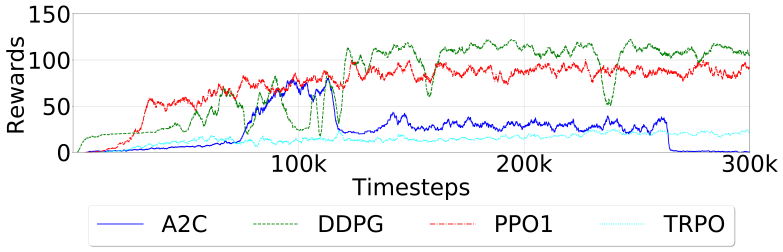

(a) Learning curves for 12 channels.

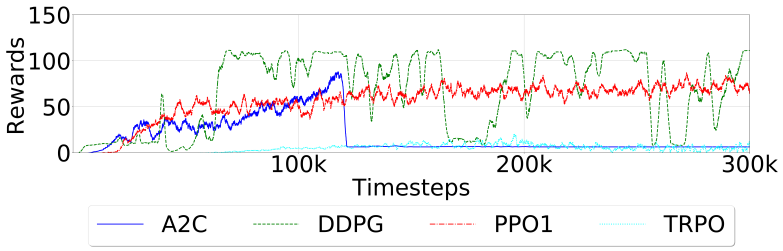

(b) Learning curves for 24 channels.

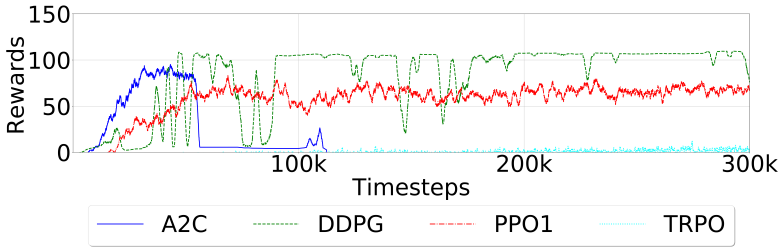

(c) Learning curves for 40 channels.

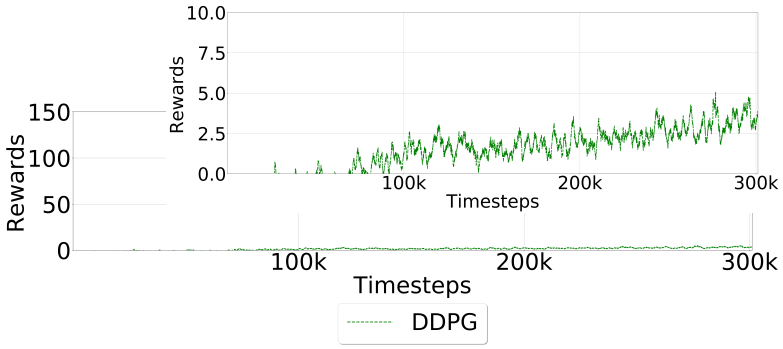

(d) Learning curves for random number of channels. Same graph with different axes in the inset.

Figure 2.25 – Power precompensation: Learning curves during training for 12 channels, 24 channels, 40 channels, and random number of channels.

importantly modified. In order to avoid problems related to OSNR and nonlinearities upper and lower limits in the input channel powers could be employed during training. The random-channel scenario in Fig. 2.27d shows a lower performance, but still presenting a considerable power excursion reduction. In order to get better results, a more accurate model based on a

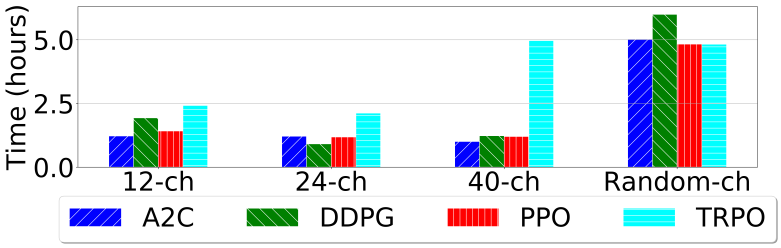

Figure 2.26 – Power precompensation: Time required by each algorithm to learn a policy.

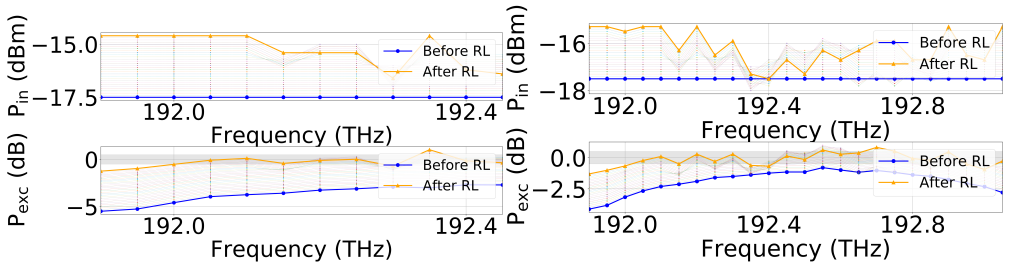

(a) Evolution - 12 channels.

(b) Evolution - 24 channels.

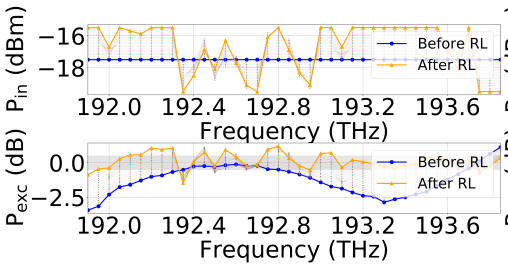

(c) Evolution - 40 channels.

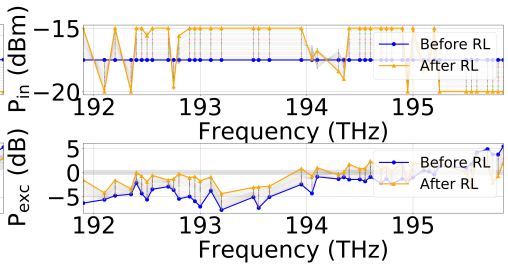

(d) Evolution - random number of channels.

Figure 2.27 – Power precompensation: Evolution of input powers and optical power excursion for an episode after training.

higher number of simulations is required.

Furthermore, histograms corresponding to Fig. 2.27 for the initial and final power excursions (before and after applying RL) are illustrated in Fig. 2.28. The bars represent the number of channels (NoCh) with a power excursion in the range indicated by the x-axis. For all the cases, power excursion values before applying precompensation are spread in a larger range, reaching larger maximum power excursions. After power precompensation using RL, power excursion variance is reduced with an average getting closer to 0 dB.

Another performance indicator, the average optical power excursion evolution during the deterministic evaluation done after training is shown in Fig. 2.29 for 12-channel, 24-channel and 40-channel scenarios. At the beginning of the episode, timestep= 0, the average power excursion is at the maximum. After each timestep, corresponding to each action the agent takes (modifying the input channel powers), the optical power excursion decreases smoothly,

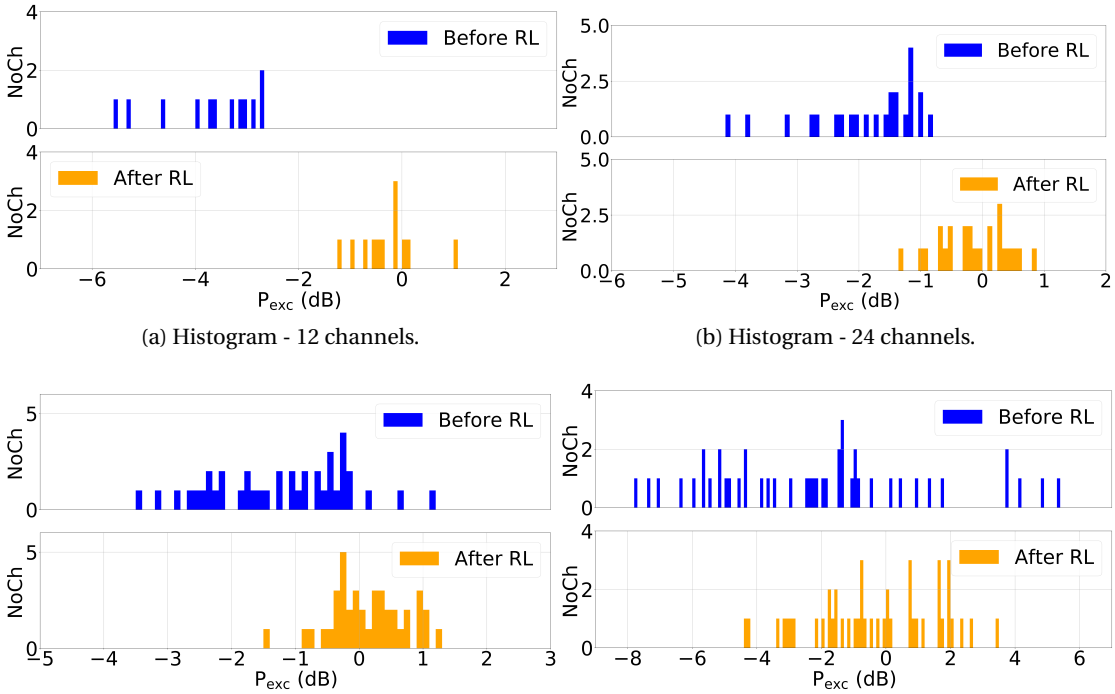

(a) Histogram - 12 channels.

(b) Histogram - 24 channels.

(c) Histogram - 40 channels.

(d) Histogram - random number of channels.

Figure 2.28 – Power precompensation: Histograms of the optical power excursion per channel after training.

demonstrating how this technique reduces impact on existing channels, avoiding power channel fluctuations. Finally, episodes end successfully when an average power excursion below the aforementioned threshold is reached. This means a power excursion reduction of 86 %, 74 %, 62 %, for 12-channel, 24-channel and 40-channel configurations, respectively. For the random-channel case, and averaging on 100 different episodes after training, a 28 % average reduction is obtained.

Finally, in order to better understand the impact of the optical power precompensation in the QoT, VPI simulations have been performed using modulated data at 32 Gb/s with dual polarization (DP) quadrature phase-shift keying (QPSK) modulation. For the 12-channel

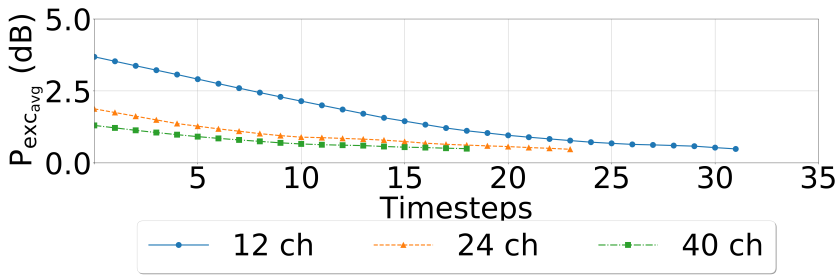

Figure 2.29 – Power precompensation: Mean optical power excursion evolution.

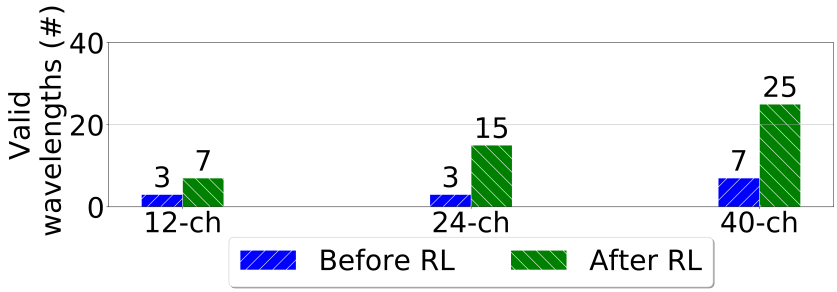

Figure 2.30 – Power precompensation: Valid wavelengths.

scenario, 2 simulations were carried out: one with equal channel power and the other with the predistorted powers shown in Fig. 2.27. Same procedure was followed for the 24 and 40-channel scenario. In all the cases, error free transmission was achieved, without requiring FEC techniques.

The same process was repeated for 128 Gb/s with DP-QPSK modulation. In this case, a pre-FEC BER threshold of 0.04 [156], was considered. The number of channels below the pre-FEC BER threshold for the 3 scenarios, before and after using RL are shown in Fig. 2.30. In all cases, after applying the power precompensation values calculated by the RL algorithm, the number of channels below the pre-FEC BER threshold increases, boosting the number of valid candidate wavelengths.

2.5.3 Experimental proof-of-concept of the reinforcement learning algorithm

After the remarkable performance obtained in previous sections, the RL-based power precompensation algorithm has been validated in a testbed. In order to do this, the same procedure, as in Section 2.5.1 and Section 2.5.2 has been followed with the difference that the environment presented here corresponds to a testbed. After power precompensation values to reduce the power excursion under a 0.2 dB threshold are obtained by means of RL, these same values are used in the testbed under the same setup configuration in order to validate the results. Note that results presented in the following are the outcome of a direct test of the RL algorithm in a testbed, without applying transfer learning or domain adaption, typical used in ML in order to facilitate the jump from a simulated world to a real world. This represents a real challenge for the RL model, making only possible to validate a proof-of-concept but without a high accuracy.

Environment: Model based on simulations

The environment considered this time is different from the previous cases, as it has to reproduce the one available at Network Technology Lab, École de technologie supérieure (Canada), shown in Fig. 2.31. After being amplified in a booster amplifier, transmitted signal traverses a cascade of 2 spans. Each span consists on a ~ 75 km fiber and an amplifier. All amplifiers in

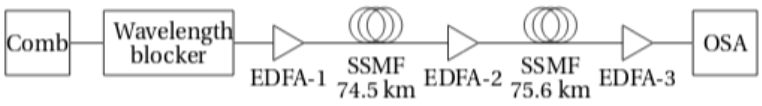

Figure 2.31 – Power precompensation proof of concept: Experimental setup (Network Technology Lab, École de technologie supérieure).

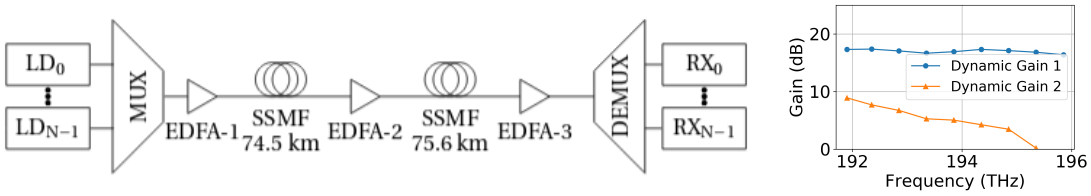

(a) Simulation setup.

(b) Amplifier gain dynamic curve.

Figure 2.32 – Power precompensation proof of concept: (a) Simulation setup and (b) amplifier gain dynamic curve.

the setup are double-stage amplifiers working in AGC mode at 15 dB gain with the VOA set to 5 dB including noise correction capabilities (Section 2.3.2).

Synthetic dataset generation Presented in Fig. 2.32, this setup is similar to the testbed shown in Fig. 2.31. All amplifiers operating in AGC mode at 15 dB gain have been modelled using the experimental curves obtained in 2.3 for VOA at 5 dB and including noise correction (Fig. 2.32b).

For a fixed number of 12 channels at fixed frequencies in the range [191.9, 193.0] using a 100 GHz frequency spacing, simulations were executed for different input channel powers according to:

- Constant power for all the channels.
- Random input powers per channel.
- Predistorted input powers as explained in [140].
- Modified input powers determined in the previous cases by adding or subtracting 0.1 dB to all or some active channels.

A dataset containing ~ 14.000 simulations has been generated, containing as in previous cases the input channel powers and the corresponding output powers.

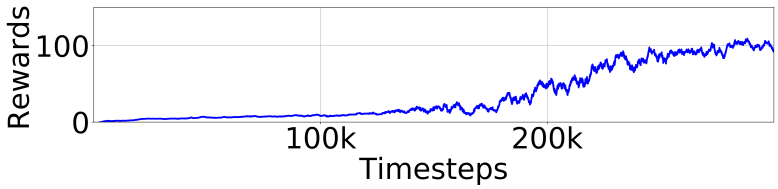

Figure 2.33 – Power precompensation proof of concept: Learning curve.

NN model Using the generated dataset, the trained NN model followed the same architecture and procedure than the ones described in Section 2.5.1 and Section 2.5.2. The only difference is the desired peak channel power was set to −25.5 dBm, offering a better agreement between simulations and experiments (Fig. 2.15). Mean squared error of 2.16×10^{-4} was obtained after training.

Environment entity The complete environment has been integrated in a Python module following the exact same method as in Section 2.5.2.

Agent: precompensation module

As after comparing different algorithms in Section 2.5.2, DDPG achieved the best overall performance, this has also been the algorithm used here as agent.

Results

Figure 2.33 illustrates the learning curve obtained during the training. After ~ 250 k timesteps, taking 3 hours and 25 min in a processor Intel core i7-8654U at 1.90 GHz, the RL algorithm learns a suitable policy.

After training the RL-based power precompensation module, the module was executed in deterministic mode. Figure 2.34 shows the evolution input power channels and corresponding power excursions. At the start, before applying the RL algorithm, all the input channel powers are set to the same power producing a maximum absolute power excursion of ~ 2.5 dB. At each timestep, input powers are modified, slowly decreasing the average power excursion. At the end of the episode, the average power excursion is decreased below the 0.2 dB threshold.

After this deterministic mode execution, the following information has been saved:

- Input channel powers before and after applying the RL-based precompensation module.
- Power deviation (difference between the output channel powers and the average output power) before and after applying the RL-based precompensation module.

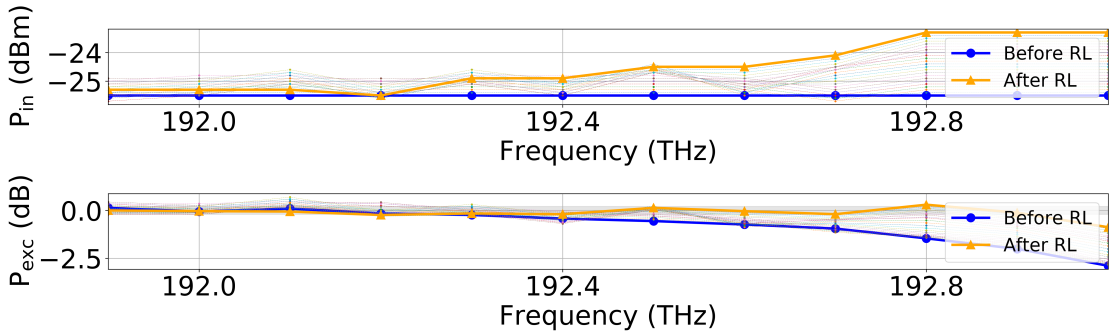

Figure 2.34 – Power precompensation proof of concept: Evolution of input channel powers and corresponding power excursions after training.

The input channel powers before and after precompensation are used in VPI simulations, using the setup shown in Fig. 2.32. Also, the same input channel powers are used to experimentally measure the output power using the setup shown in Fig. 2.31.

Due to the differences between the gain experimentally measured and the approximated gain calculated in the simulations (Fig. 2.15), likely related to the noise correction factor, experimental measurements and simulations are here compared in terms of the difference between the output channel powers and the average output power. Figure 2.35a shows this difference for both, experiments and simulations, before applying precompensation. Although the simulated and experimental gains are not exactly the same, the power deviations are quite similar. Similar curves are shown in Fig. 2.35b after applying the precompensation. Although the offset gain still exists, the output power deviation has been greatly reduced by a 63 %. Better results could be obtained by using transfer learning.

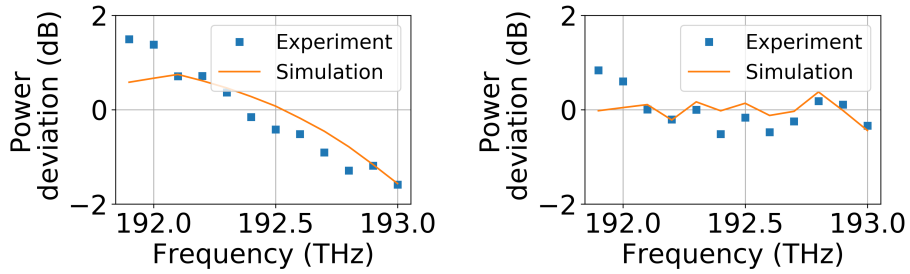

(a) Power deviation for equal channel power.

(b) Power deviation for predistorted channel power.

Figure 2.35 – Power precompensation proof of concept: Power deviation.

2.6 Conclusions

Optical power excursion problems have been investigated in this chapter. Current optical amplifier modules are able to reduce optical power excursions by introducing additional ele-

ments: (1) feedforward/feedback loops enabling AGC mode, (2) VOAs allowing to control the tilt, (3) gain flattening filters compensating amplifier gain non-flatness. Despite this built-in amplifier control, power excursions persist under dynamic wavelength configuration. As a first step towards solving this problem, different approaches have been utilized in order to estimate the amplifier response under different operating conditions. Most of these approaches correspond to one of the following categories, being based on: analytical or semi-analytical models, experimental characterization and historical data, with the latter usually related to ML techniques. Being able to estimate the amplifier response allows to mitigate power excursions by, e.g. assigning new channels to wavelengths producing smaller channel excursion, controlling the amplifier operating point or applying power precompensation at the transmitter.

Two solutions have been proposed here, which can be integrated in an SDN-based optical network architecture (Fig. 2.36). The first one, power excursion prediction based on NNs using a synthetic dataset which can be used for wavelength assignment and consequently optical power excursion reduction. The second solution, RL-based power precompensation, where input powers at the transmitter are adjusted in order to minimize power excursions at the output of an optical link. After testing several algorithms and scenarios, considerable power excursion reductions of 86 %, 74 %, 62 %, for 12-channel, 24-channel and 40-channel configurations, have been achieved, respectively. For the random-channel case, and averaging on 100 different episodes after training, a 28 % average reduction is obtained. For implementation in a real network, this approach can be applied online, during network operation, making use of monitored available information, therefore directly learning the environment model. Also, it could be deployed, as demonstrated here, generating first an environment model based on synthetic data. The power deviation has been reduced by 63 %, just by directly using the results obtained in simulations in a experimental testbed. In order to improve the performance, transfer learning could be possibly applied. Future work should include upper and lower limits in the input power channels.

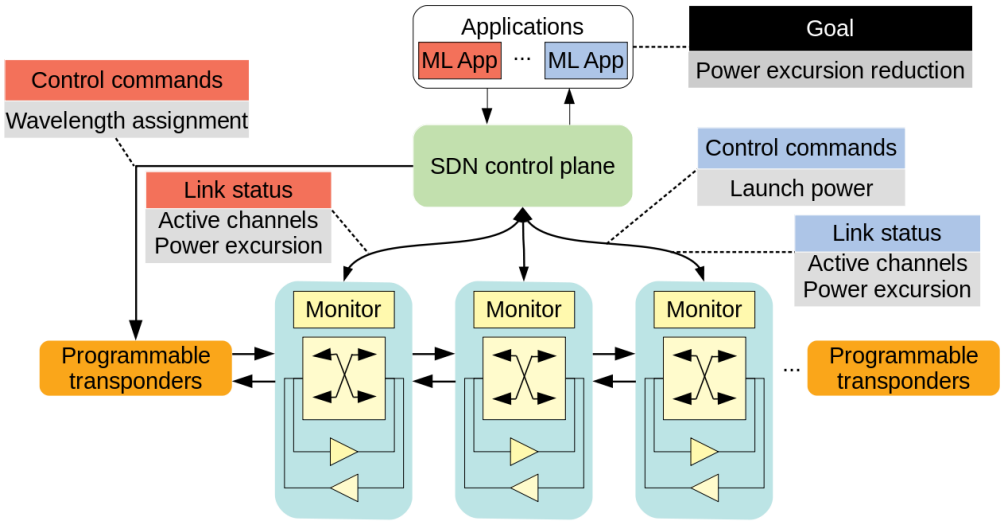

Figure 2.36 – Amplifier control in SDN-based optical network architecture (based on [17]).

3 Impairment aware modulation format and wavelength assignment

PLIs, accumulating along the lightpath, are critical in transparent or translucent optical networks. As a consequence, physical layer constraints must be included in the RWA process, which turns into an even more complex problem. Thus, before accepting any traffic request, candidate lightpaths need to be assessed in terms of QoT. In this chapter, QoT estimation based on NNs, considering optical power excursion as input feature is proposed. The implemented QoT model is used as environment for an RL algorithm, enabling impairment aware modulation format and wavelength assignment.

Section 3.1 and Section 3.2 review the state of the art of RWA and QoT estimation techniques, respectively. Section 3.3 describes the implementation of the QoT model and the impairment aware modulation format and wavelength assignment algorithm. Finally, Section 3.4 and Section 3.5 present the results obtained under fixed and flexible frequency grid configurations.

3.1 State of the art of routing and wavelength assignment

Different approaches have been scrutinized in order to perform IA-RWA. By including PLI constraints in a linear programming (LP) relaxation formulation, IA-RWA has demonstrated to outperform pure RWA (which does not consider impairments) [157]. In the following, Section 3.1.1 provides an overview of the traditional RWA methods, allowing to better understand IA-RWA techniques introduced in Section 3.1.2.

3.1.1 Traditional RWA formulation overview

A wide range of algorithms have been inspected in order to solve the NP-complete RWA problem [158]. At a first glance, two categories can be distinguished:

- Offline RWA algorithms address static lightpath assignment, corresponding to static

traffic. Connections are known in advance. RWA is executed during network planning.

- Online RWA algorithms target dynamic lightpath establishment, corresponding to dynamic traffic. RWA is performed during network operation.

Besides this categorization, RWA methods can be also classified as: one-step or multi-step algorithms [25]. One-step methods deal with RWA as a single problem. Most of them, targeting a static traffic situation where the traffic is known in advance, are based on integer linear programming (ILP) formulations optimizing an objective function (e.g. blocking ratio[1], number of utilized wavelengths or number of wavelengths per fiber) to serve a maximum number of requests [159]. Together with the objective function, wavelength, clash and network constraints must be defined: (1) wavelength constraints ensure a wavelength per connection, (2) clash constraints establish that two lightpaths on the same fiber cannot use the same wavelength, (3) network constraints guarantee the existence of a path between source and destination. For the network constraints, various mathematical formulations have been pondered, e.g. path, edge or arc-based formulations. Using weaker constraints, LP relaxation approaches yield bounds and solutions close to the optimal [160].

Multi-step RWA algorithms break the RWA problem in sub-problems: (1) routing, finding a path from source to destination; (2) wavelength assignment, allocating a wavelength for the selected path. Although leading to non-optimal solutions, dividing the RWA problem in sub-problems makes it more tractable. Numerous algorithm combinations can be identified in the literature, as routing by multicommodity flow formulation integrated with randomized rounding and wavelength assignment based on graph-coloring techniques [161].

Providing solutions close to optimal, heuristics have also been studied. From simple heuristics, allocating wavelengths to the longest lightpaths first [162], to more complex heuristic techniques, finding shortest paths based on wavelength-graph to maximize network throughput [163], diverse heuristic algorithms have been demonstrated. Multiple objectives have been addressed: minimizing the maximum load per link [164], minimizing the number of wavelengths required to establish the lightpaths [165], or minimizing the number of used wavelengths by rerouting lightpaths depending on their load [166].

In general, many heuristic approaches belong to the multi-step RWA algorithms group, decoupling the RWA problem in sub-problems. For the routing problem, three main categories are distinguished [158]: (1) single-path, the most simple, each source-destination pair is associated to a specific path, available beforehand, e.g. shortest path; (2) alternate paths, several paths are considered for each connection e.g. k-shortest paths; (3) adaptive routing, routes are selected in a more dynamic way e.g. least congested path. Also, to separately solve the wavelength assignment problem, different heuristic techniques have been studied [158]:

- Random wavelength assignment approach: From the set of available wavelengths a

[1] Ratio of blocked requests with respect to total requests.

random wavelength is selected.

- First-fit (FF) method: All the wavelengths are ordered using a specific criteria. The first available wavelength with the lowest index in the ordered list is selected.
- Least-used algorithm: The least used wavelength in the network is assigned, distributing the demands over the wavelengths. Apart from penalizing long wavelength paths, it introduces overhead to know which are the least used wavelengths.
- Most-used method: Opposite to least-used, new channels are assigned to the most used wavelengths in the network. It requires overhead, but it shows a better performance than least-used.
- Min-product algorithm: For multi-fiber cases, this algorithm assigns wavelengths into fibers, with the objective of minimizing the number of fibers.
- Least-loaded technique: Also for multi-fiber scenarios, in the link with the highest load, the wavelength with largest residual capacity is selected.
- Max-sum algorithm [167]: Knowing beforehand a matrix with all the possible paths (and corresponding assigned wavelengths), max-sum algorithm selects the wavelength minimizing the capacity loss considering all the paths after lightpath establishment. It can be used in single and multi-fiber networks.
- Relative capacity loss method [168]: Based on max-sum, the relative capacity loss instead of the capacity loss is minimized.

To avoid blocking long paths i.e. paths with multiple hops, additional algorithms have been included, as wavelength reservation and protecting threshold methods [169]. As they do not perform wavelength assignment, but only protection of long paths, they operate together with wavelength assignment algorithms. Wavelength reservation technique reserves some wavelengths for long paths, whereas in protecting threshold method, a wavelength is only assigned if the number of unused wavelengths is above a threshold.

3.1.2 Impairment Aware RWA problem formulation

Classical methods to solve RWA problems neglect PLIs. Although this is still correct when O/E, E/O conversions are available at each node, it becomes unreliable when transparent or translucent networks are traversed. In this case, PLIs must be taken into account. This can be done by evaluating the candidate lightpath before being assigned. Then, if the route satisfies the quality demands, the path is chosen. Otherwise, another path must be searched or the request is blocked. More complex solutions involve adding constraints to the classical RWA problem, leading to find new routes meeting these additional requirements. In the following, some approaches are presented, adopting almost the same classification as for the classical RWA problem.

Heuristic algorithms

Although they do not provide an optimal solution, they do get close to it much faster. As for the traditional RWA case, some of these algorithms tackle the problem as an unique problem, whereas other methods divide it in two separate sub-problems: (1) routing and (2) wavelength assignment.

Routing Frequently used, single-path routing selects a unique path, most commonly the shortest path using Dijkstra algorithm [170]–[177]. Instead of hops, to account for PLIs, other criteria have been examined in order to establish the shortest path, defining link cost in terms of minimum physical distance [178], highest Q-factor [178] or minimum FWM crosstalk [179].

Different from the previous approaches, multi-path routing takes into consideration several routes, commonly the k-shortest paths before selecting one [180], [181]. Analogously to the single-path approaches, the k paths can be selected on a different basis: minimum distance having less common links [182], least congested routes [174], highest Q-factor [183], [184], highest Q-factor combined with least congested constraints [185] or least number of O/E, E/O modules and global used wavelengths [186].

Wavelength assignment techniques Various heuristic algorithms have also been formulated for wavelength assignment. Traditional wavelength assignment techniques have been used. FF is utilized very often [170], [172], [178], [180], [187], [188]. FF using an ordered list with the least congested wavelength at the top has been demonstrated [174]. Another approach, FF with wavelength ordering assigns wavelengths following an ordered list maximizing spectral separation among channels, mitigating channel crosstalk [177]. A threshold may be also introduced [176]. In this way, the ordered list is only used when the crosstalk is small; for larger crosstalk, the wavelength minimizing the crosstalk is selected. Best fit has been explored [182] too, through several possibilities: selecting the least loaded wavelength, the wavelength providing maximum OSNR [174] and the wavelength producing the lowest FWM level [179]. For comparison, random assignment has been implemented, choosing a random wavelength from the available wavelength set, showing higher blocking ratio [171], [178].

RWA Several IA-RWA methods have been studied, solving the complete unified problem. An RWA algorithm based on Dijkstra's algorithm using Q-factor as performance measurement has been evaluated [189]. Furthermore, an algorithm targeting minimum crosstalk has been proven [190]. For each wavelength, a candidate path was calculated based on shortest path algorithm. Then, the one with minimum crosstalk was selected. A different technique, best-OSNR, has been implemented, selecting the route and corresponding wavelength maximizing OSNR [174]. Inter-domain problem has also been addressed by means of heuristics [191].

Metaheuristic algorithms

They reach optimal solutions without complex mathematical formulations. Ant colony optimization, selecting not a complete route but single hops (hop-by-hop until destination) based on the physical layer information available at each node and collected by monitoring, has been assessed [180]. Also, a genetic algorithm has been utilized, considering polarization mode dispersion and ASE [192]. Additionally, tabu-search metaheuristics have been inspected, outperforming local optimization heuristics [186]. As well, a predictive algorithm based on two-bit counters per lightpath indicating availability/unavailability has been introduced [182].

Optimization methods

IA-RWA has been solved by linear optimization as the traditional RWA problem [193]. ILP and binary ILP have been utilized, addressing offline impairment aware planning in transparent optical networks [194], [195]. Using a Q-factor analytical model, accounting only for linear impairments, RWA problem has also been solved by means of linear optimization [184]. One step further, RWA together with the placement regenerator problem have been addressed [196], [197]. Similarly, wavelength converter placement problem has been investigated [198]. Furthermore, IA-RWA using ILP in optical virtual private networks over WDM has been demonstrated [199] and mixed ILP formulation for virtual topology design has been introduced [200].

3.2 Quality of transmission estimation models

In order to operate, IA-RWA algorithms require QoT information, which can be obtained through analytical formulations. Although accurate, analytical models as the split-step Fourier method are complex and time consuming [201]. Different fiber propagation approximation models have been proposed over the years: based on Volterra series on the frequency domain [202] or in FWM by slicing the spectrum in spectral components [203]. Not working sufficiently well for dispersion compensated systems, these methods did not become very popular. With the increase of uncompensated links, a Gaussian noise (GN) model describing nonlinear propagation has been formulated [204], based on the following assumptions: (1) nonlinearities are relatively small, (2) after propagating through uncompensated link, signal acts as stationary Gaussian noise (3) nonlinear interference (NLI) behaves as additive Gaussian noise. This model produces approximate but accurate results, becoming useful as a tool for optical link design, but only for uncompensated optical links. Closed analytical formulas have been derived for ideal Nyquist-WDM[2] and non-Nyquist-WDM over one single span, multiple spans and Nyquist-WDM with distributed amplification [206]. For systems with large number of channels, it is possible to simplify the GN-model neglecting coherent interference among NLI generated in different spans, leading to a simpler IGN model. Although this model

[2] Channel bandwidth ideally equal to baud rate[205].

does not address network scenarios, with signals coming from different locations, its usage for dynamic reconfiguration optimization has been shown. Considering the IGN-model for the particular case of a point-to-point link where launch input powers can be adjusted and optimized in each span, maximizing OSNR at the end of a link is performed by maximizing the OSNR in each span. This strategy is useful to calculate OSNR for unestablished lightpaths under full spectrum load [207]. Although underestimating OSNR due to the full spectrum load assumption, this method ensures a continuous service.

Another strategy to determine QoT for intensity modulated signals is through Q-value estimation [208]. Assuming single channel propagation, a detailed numerical split-step Fourier method is used to estimate the static impairments (self-phase modulation (SPM), chromatic dispersion (CD), and filter concatenation). Other parameters, as ASE, cross-phase modulation (XPM), FWM and polarization mode dispersion (PMD) are introduced in the model by means of particular analytical models. Based on the obtained Q-value estimation, IA-RWA is performed. Experimental centralized and distributed approaches have been shown, with the centralized approach reducing the blocking ratio whereas the distributed approach reduced the lightpath setup time, still requiring a setup time in the order of seconds. An advanced hardware acceleration architecture has been tested requiring less than 1 second by using FPGAs [209].

In general, when an approximate model is used for QoT estimation, inaccuracies have to be accounted in margins [210]. Apart from inaccuracies in the model, these margins also include inaccuracies in the parameters required by the model or uncertainties introduced by the network operating condition e.g. channel load conditions. Although mandatory in optical networks, margin values must be optimized: too large margins lead to overprovisioning whereas too small margins lead to compromising QoT, requiring multiple attempts before establishing a lightpath. Transforming fixed value margins in adaptive margins, could help to set right values. This approach has been developed, considering system uncertainties coming from several parameters: channel power at detection, crosstalk and nonlinear phase after fiber propagation [211] or residual dispersion [212]. At network planning stage, these strategies have been able to reduce the number of regenerators.

Monitoring information appears to be promising in order to cut down margins by reducing uncertainties. Optical network monitoring availability has been examined [213]. Associating inaccuracies of the QoT estimators with monitor availability, i.e. routes equipped with monitors show reduced uncertainties in the QoT estimations, allows to reduce margins, therefore being able to accommodate more lightpaths. With monitors becoming more and more common, ML approaches, learning from the monitored data, are emerging as the logical way forward, in order to estimate QoT. Multiple examples of QoT estimation based on ML techniques are found in the literature. In an attempt to classify these works, different criteria may be considered: used method, estimated parameter, input features used, etc. Here, some of these works are mentioned, classified in terms of used algorithm and estimated parameter. A short summary is shown in Table 3.1.

Starting from a simple implementation based on regression, continuously monitored BER data has been used to estimate BER for unestablished lightpaths [214]. This estimation is performed using regression on the existing OSNR estimations calculated from measured data over different wavelengths, which is available in a database. Experimentally demonstrated, once a lightpath is established, corresponding new measurements are stored in the database, improving the estimation accuracy for future requests.

Also based on regression, a reduction of inaccuracies on estimated signal to noise ratio (SNR) from a QoT tool has been achieved by using gradient descent on a cost function based on the difference between estimated and measured SNR. Attributing SNR uncertainties to total output powers and amplifier NF values, the gradient descent algorithm reduces the difference between estimated and measured SNR by modifying these parameters in an iterative manner. Reduction on uncertainties has led to a reduction on the margins for future demands using the new learnt parameters stored in a centralized database, bringing a cost reduction by cutting overprovisioning [215]. Polynomial regression has also been used to reduce design margins, providing a better estimation of amplifier gain ripples connected to OSNR penalties [216]. As pointed in this work, the influence of power excursion in QoT has not been yet sufficiently investigated.

Using a method close to extended Kalman filtering, lightpath parameters have been adjusted in order to improve the Q-value estimations based on a physical layer model. Margin reductions in the order of 1 to 3 dB have been achieved [217].

Instead of relying on a single monitored parameter at the end of the link to estimate QoT, as in the previous case, multiple parameters can be also monitored: ASE, PMD, CD, and SPM [218]. Based on this information, BER is estimated by a QoT tool. All the parameters are stored in a database. When a request arrives and a lightpath candidate is selected, two cases can be distinguished: (1) parameters are present in the database, and therefore QoT can be directly estimated or (2) parameters are not present in the database and therefore unknown parameters have to be estimated by using network kriging [3] [219] or norm $l2$-normalization [220] (typically used in network tomography [221]). These methods make estimations based on the previous measured parameters and the spatial correlation among them, as some part of the links can be common to several lightpaths. As a result, QoT estimation reduces the number of attempts before establishing a successful connection for a particular blocking ratio. Monitor placement and how it affects the estimation accuracy have been discussed in [222]. Interference effects have also been included in the calculations showing better accuracy compared with the worst case scenario where all the channels are in use [223], [224]. Furthermore, network kriging and norm $l2$-normalization have been applied to estimate Q-value parameters for intensity modulation signals [225]. By measuring means of the distributions of the “0” and “1” symbols (μ_0, μ_1) and their respective noises considered as standard deviations (σ_0, σ_1), Q-factor and BER have been estimated based on the proposed algorithms.

[3] Network path characteristics prediction based on a small set of samples [219]

A more advanced ML technique, CBR, has been used for lightpath classification [42]. During offline operation, a database of lightpaths is generated containing different parameters: route, selected wavelength, total length, sum of co-propagating lightpaths per link and standard deviation of the number of total co-propagating lightpaths. Together with this information, the associated Q-factor is also stored in the database. When a traffic request arrives, similarity for each path is calculated, with the similarity considering a weighted Euclidean distance. The most similar case is selected, assuming the stored Q-value will be the same of the retrieved case. As a larger database increases the retrieval time, an algorithm variant which adjusts the database size by forgetting some information has also been developed. Comparison with other techniques has been shown [41], with CBR outperforming the percentage of successful classifications of lightpaths compared to naive Bayes, decision tree, RF and J4.8 tree [4]. Experimental demonstration of CBR for lightpath classification, but considering different attributes (channel wavelength, launch power, link length, active lightpaths in the link, total input power to the link and total power carried by the neighbour channels) and estimating error vector magnitude (EVM) instead of Q-value has also been presented [226].

Additionally, RF and k-NN have been studied for QoT classification. Both methods are compared in order to classify lightpaths according to BER [227]. Considering as input features number of links of the lightpath, lightpath total length, length of its longest link, traffic volume it serves and modulation format, results have shown RF gives better results in terms of performance and computation time. In an extended work [43], nonlinear effects have been included in the BER estimation model. Again, RF provided a better trade-off between computation time and accuracy.

Going one step further, an SVM has been trained on a synthetic dataset for QoT classification [228]. The dataset considered the following features: source and destination nodes, set of traversed links, corresponding wavelength, total length, sum of co-propagating lightpaths per link and standard deviation of that number. After training, the algorithm has been able to classify lightpaths according to low or high Q-values. Results showed SVM outperforming CBR in accuracy and computing time. Also using SVM, QoT of lightpaths based on BER estimation from OSNR calculation including nonlinearities as a function of link and signal parameters (total link length, span length, channel launch power, modulation format and data rate) has been validated [229], [230]. After comparing RF, k-NN and SVM, best results have been obtained with SVM. Furthermore, using a network emulator including optical power excursion [231], an SVM performing multi-class optical parameter-based prediction of QoT has been developed [232]. Each of the four classes corresponds to an OSNR threshold for a particular modulation format. C-band is divided in bins, representing a section of the EDFA gain. This information is used during training in order to account for optical power excursions.

NNs are one of the most popular ML techniques for QoT classification. Having as input features path length, number of EDFAs, link length and degree of destination node, a trained NN has been able to predict whether a lightpath Q-value is above or below a threshold [233].

[4] Algorithm used to generate a decision tree.

The work has been extended taking into account different wavelengths, including wavelength as a new input feature. In the proposed algorithm, every time a request is processed, a candidate lightpath is selected. After checking availability of transmitters and receivers and lightpath existence between source and destination, the Q-factor classification (above or below threshold) is performed using NN. If the Q-factor is below the considered threshold, a new wavelength candidate is chosen and the algorithm restarted [234]. This process is repeated until a wavelength is found and the request is processed or no wavelength fulfilling the requirements is found and the request is blocked.

OSNR prediction based on NN has been experimentally shown [235]. Transmitter (launch powers), optical path (EDFA input power, output power, gain, NFs, etc.) and receiver information together with OSNRs obtained through monitoring are stored in a database. Database information has been used to train an NN able to predict OSNR. This approach has been validated in a field-trial testbed.

Detailed comparison among k-NN, logistic regression, SVM and NN for QoT estimation has been shown [83]. Considering three different network scenarios, NN resulted to be the algorithm achieving the best generalization. Impact on accuracy due to training data size and due to the set of used features (number of hops, number of spans, total length, average and maximum link length, average span attenuation, average dispersion) has been analyzed.

Instead of lightpath parameters as features, eye diagram as an image has been used in order to train a convolutional neural network (CNN) able to estimate OSNR [236]. At the same time, the ML module has been trained for modulation format recognition. Compared with decision tress, k-NN, NN, and SVMs, CNN obtained the best results. Using directly raw data coming from a coherent receiver, an NN [237] first, and a CNN [238] afterwards, have been trained to estimate OSNR, without requiring specific lightpath features. Both works have been experimentally proven.

A particular case of multi-domain scenario has been addressed [239]. QoT using a deep NN has been experimentally implemented for a multi-domain scenario including different features as source and destination nodes, data rate path length, etc. The model has achieved high accuracy on classifying requests according to the BER (higher or lower with respect to the pre-FEC BER threshold).

Data collection reduction, a key aspect in ML applications, has been tackled by transfer learning, being able to learn fast from pre-trained models [240].

3.3 Impairment aware modulation format and wavelength assignment algorithm proposal

In this section, the proposed impairment aware modulation format and wavelength assignment algorithm is presented. First, Section 3.3.1 describes the use case scenario in detail. After,

ML method	Input data	Output data	Dataset	Ref
Regression	BER	OSNR	E	[214]
	SNR	SNR	S	[215]
Kalman fitering	BER	Q-value	E	[217]
Network kriging	Lightpath parameters	BER	S	[218], [222]–[224]
	σ_0, σ_1, μ_0, μ_0	Q-factor	S	[225]
CBR	Lightpath parameters	Q-factor	S	[42], [41]
	Lightpath parameters	EVM	E	[226]
RF	Lightpath parameters	BER	S	[227], [43]
SVM	Lightpath parameters	Q-factor	S	[228]
	Lightpath parameters	BER	S	[229], [230]
	OSNR, wavelength band	OSNR	S	[231]
NN	Lightpath parameters	Q-factor	S	[233], [234]
	Lightpath parameters	Q-factor	E	[240]
	Lightpath parameters	OSNR	E	[235]
	Lightpath parameters	OSNR	S	[83]
	Samples output receiver	OSNR	E	[237]
	Lightpath parameters	BER	E	[239]
CNN	Eye diagram	OSNR	S	[236]
	Samples output receiver	OSNR	E	[238]

Table 3.1 – Summary of QoT estimation approaches based on ML techniques. In the column corresponding to dataset, E and S refer to experimental and synthetic.

QoT estimation based on NN models is demonstrated in Section 3.3.2. Then, in Section 3.3.3, the QoT models are integrated in a environment used by an RL algorithm, learning to assign modulation format and wavelength to incoming traffic requests. Section 3.4 and Section 3.5 show the results obtained for a fixed and a flexible frequency grid configuration, respectively.

3.3.1 Numerical setup

The numerical setup, shown in Fig. 3.1, was developed in VPI. It consists on a variable number of transmitters, which outputs are multiplexed and amplified by a booster amplifier before being transmitted through a span, composed by 75 km of fiber followed by an inline amplifier. Then, the signal traverses an ROADM, which losses are adjusted by using a VOA to 15 dB. At the ROADM output, an amplifier compensates for the losses. After being transmitted through a second span, the signals are demultiplexed and sent to the corresponding receivers.

A more detailed description of the setup is given in the following. First, the input parameters to be configured are defined. Second, specific aspects of the general parameters and particular blocks included in the simulations are described. Third, results obtained for simulations in back-to-back (B2B) configuration and for different launch input powers are analyzed.

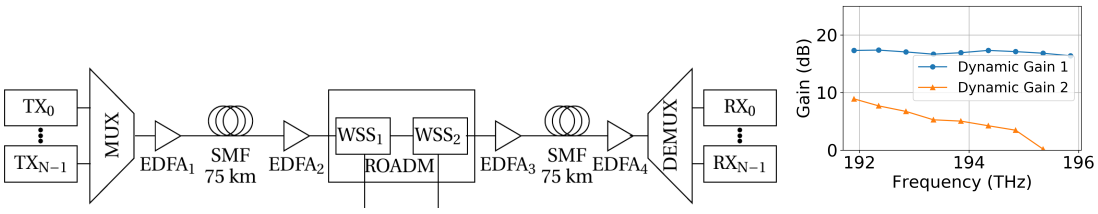

(a) Simulation setup.

(b) Amplifier gain dynamic curve.

Figure 3.1 – Setup for impairment aware modulation format and wavelength assignment and amplifier gain dynamic curve.

Input tuneable parameters

Three main input parameters must be configured in each simulation: data rate, modulation format and wavelength allocation.

Data rate and modulation format Two different data rates (128 Gb/s, 256 Gb/s) and two different modulation formats (DP-QPSK, DP-16-QAM) are considered, but only three possible combinations are allowed between them: 128 Gb/s DP-QPSK, 128 Gb/s DP-16-QAM and 256 Gb/s DP-16-QAM. Considering soft decision FEC (SD-FEC) with overhead of 21.875 %, the maximum allowed pre-FEC BER value[5] was fixed to 0.04, which is pessimistic according with the limits shown in [156]. Net data rates corresponding to 128 Gb/s and 256 Gb/s are 100 Gb/s and 200 Gb/s, respectively. Therefore, the three possible configurations are referred in the following as 100G-DP-QPSK, 100G-DP-16QAM and 200G-DP-16QAM (Table 3.2).

Data Rate (Gb/s)	Modulation	Label
128	DP-16QAM	100G-DP-16QAM
128	DP-QPSK	100G-DP-QPSK
256	DP-16QAM	200G-DP-16QAM

Table 3.2 – Considered data rate and modulation formats.

Frequency channel allocation Channels have been allocated in the C-band (1530- 1565 nm) using the ITU frequency grid [149]. For the fixed frequency grid, with a 50 GHz channel spacing, the possible center frequencies in THz are defined as:

$$193.1 + n \times 0.05. \tag{3.1}$$

[5] Predefined threshold for error-free post-FEC transmission.

The flexible frequency grid considers a slot center frequency granularity of 6.25 GHz, although the width slot granularity is 12.5 GHz. Analogously to eq. 3.1, flexible grid center frequencies in THz are determined by:

$$193.1 + n \times 0.00625. \tag{3.2}$$

In both cases, eq. 3.1 and eq. 3.2, n is a positive or negative integer including 0.

In the scenario presented here, 80 channels have been considered for the fixed grid case, where the first channel has been defined at:

$$193.1 - 24 \times 0.05 = 191.9 \text{ THz}. \tag{3.3}$$

Therefore, being the first channel centered at 191.9 THz and the 80th channel at 195.85 THz.

For the flexible grid case, the same total bandwidth of 4 THz was considered, with the first possible slot center frequency defined at:

$$193.1 - 195 \times 0.00625 = 191.88125 \text{ THz}, \tag{3.4}$$

and the last possible slot center frequency at 195.86875 THz. In both cases, the defined bandwidth goes from 191.875 THz to 195.875 THz, which corresponds to approx. 1531.5 nm to 1563.5 nm.

Main specific features

After defining the main configurable parameters and before defining the main output values obtained in each simulation, some information about the general parameters and main used building blocks is provided. First, the major global parameters set in the simulations are:

- `TimeWindow`: It is defined as the simulated period of time, impacting the resolution of spectral displays and the accuracy of BER estimations. The bigger is the simulated data, the more resolution of spectral displays and the more accuracy of BER estimations. At the same time, more time and more memory will be required to run each simulation. Furthermore, as Fast Fourier Transform (FFT) is intensively used in the simulations, a good practice is to keep this value as a power of two, in order to accelerate FFT computations.
- `SampleRateDefault`: By default, unless another specific sample rate is defined, this value is used as the sample rate value for all the blocks. As a reference, the sampling rate should be at least 2-3 times the total simulated bandwidth.

- `GreatestPrimeFactorLimit` (GPFL): It indicates the maximum prime factor of the number of samples in the simulated signal. In order to speed up simulations, by accelerating the FFT, this parameter should be kept as low as possible, ideally GPFL equals 2.

The number of simulated symbols and the number of samples per symbol must be integers. To guarantee this condition, for simulations with simultaneous propagation of signals with multiple symbol rates, as the case considered here, the simulated time window (`TimeWindow`) should be a multiple of some fundamental symbol rate $S_{Fundamental}$ of the simulated signals. As two different symbol rates are considered in the presented scenario, 16 Gbaud/s and 32 Gbaud/s, both symbol rates can be expressed in terms of fundamental symbol rate of $S_{Fundamental}$ = 16 Gbaud/s:

$$S_{100G-DPQPSK} = 32 \text{ Gbaud/s} = 2 \times S_{Fundamental}, \tag{3.5}$$

$$S_{100G-DP16-QAM} = 16 \text{ Gbaud/s} = 1 \times S_{Fundamental}, \tag{3.6}$$

$$S_{200G-DP16-QAM} = 32 \text{ Gbaud/s} = 2 \times S_{Fundamental}. \tag{3.7}$$

The simulated period is required to contain an integer number of simulated symbols. After the definition of the fundamental rate, the minimum possible `TimeWindow` is given by:

$$\text{TimeWindow}_{min} = \frac{1}{S_{Fundamental}} = 6.25 \times 10^{-11} \text{ s}, \tag{3.8}$$

containing one symbol of the 100G-DP-16QAM signal and two symbols of the 100G-DP-QPSK and the 200G-DP-16QAM signals. This means that for the minimum simulated window, at least two samples would be required, defining 2 as the minimum `GreatestPrimeFactorLimit`. Sampling rate should be at least 3 times the total simulated bandwidth. In this case, with 80 wavelengths spaced 50 GHz for the fixed grid scenario and 320 frequency slots of 12.5 GHz bandwidth for the flexible grid scenario, i.e. a total bandwidth of 4 THz, the sampling rate has been set to:

$$1024 \times S_{Fundamental} = 16.384 \text{ THz}, \tag{3.9}$$

larger than 3 times the total bandwidth, choosing 1024 as a multiplication factor in order to keep a number of samples power of two. Limited by the 16 GB RAM of the computer used for simulations during approximately the first half of PhD work (~ 18 months), the time window was tuned to the maximum possible:

$$\text{TimeWindow} = 8 \times \frac{1024}{S_{Fundamental}} = 2.56 \times 10^{-7} \text{ s}, \tag{3.10}$$

again, choosing 8 × 1024 to keep a power of 2, resulting in a total number of samples of:

$$\text{SampleRateDefault} \times \text{TimeWindow} = 8388608 = 2^{23}, \tag{3.11}$$

corresponding to a different number of simulated symbols and samples per symbol for each of the modulations and data rates considered here, as can be seen in Table 3.3. These values have been kept after changing PC in order not to increase simulation time. Depending on the channel load, time required to perform one simulation can be more than 1 hour.

Symbol Rate (Gbaud)	Modulation	Simulated symbols	Samples per symbol
16	DP-16-QAM	16384	512
32	DP-QPSK	8192	1024
32	DP-16-QAM	16384	512

Table 3.3 – Simulated symbols and samples/symbol for each modulation and data rate.

As before the multiplexer and after the demultiplexer a total maximum of 80 signals for the fixed grid and 106 signals for the flexible grid case can be transmitted, the sample rate at the transmitter and receiver has been kept lower, $16 \times S_{\text{Fundamental}}$, in order to have enough physical memory.

Figure 3.1 illustrates the used setup. To enable different channel spacings, the multiplexer is modelled using an ideal multiplexer. Every channel is filtered before the multiplexer in order to introduce its filtering effect. The signal coming out from the multiplexer is first amplified by a booster amplifier. The amplified signal is transmitted in a first span, composed by 75 km SMF and the EDFA acting as inline amplifier compensating the losses of the fiber. After the span, the signal traverses an ROADM, modelled by 2 WSSs [241], one for adding channels and other for dropping channels. In order to model the WSS, a bank of super Gaussian filters order $n = 6$ are used, approximating a MEMS-mirror based WSS with steep edges [242]. Higher orders can be achieved with liquid crystal on silicon (LCoS) [243]. Losses in the ROADM are adjusted with an optical attenuator to 15 dB. At the output of the ROADM, the signal is again amplified before being transmitted over a second span with the same characteristics. At its output, the signal is demultiplexed, filtered and processed by a coherent receiver. Finally, after digital signal processing (DSP), the BER of the received signal is calculated. All the amplifiers included in the setup are identical, corresponding to the double stage amplifier characterized in Section 2.3, operating in AGC mode at 15 dB with with VOA at 5 dB (dynamic curve in Fig. 3.1b). Some more details about the transmitter, the dual polarization coherent receiver and the DSP algorithms are given in the following.

Transmitter Dual polarization M-QAM/M-PSK transmitters have been used for signal generation. First, a series of randomly generated bits are mapped to symbols. As shown in Table 3.4,

for every modulation and data rate, parameters corresponding to bits per symbol and symbol rate needed to be adjusted accordingly. Then, a raised cosine filter with a roll-off factor of 0.1 has been used as a shaping filter to generate the driving signal to the IQ modulator.

In the optical part, the transmitter's laser source has been programmed with the corresponding channel frequency. The laser linewidth has been set to 100 kHz. A polarized beam splitter divides, then, the light in two polarizations, with each one of them being modulated by one IQ modulator, based on two single drive Mach Zehnder modulators. One of them modulates directly the incoming optical carrier and the other modulates the 90° phase-shifted optical carrier. Then, both polarizations are combined together, to finally set the average power with a noiseless amplifier to a selected specific value, equal for all the channels and optimized as it will be shown later.

	Bits per symbol per polarization	**Symbol rate (Gbaud)**
100G-DP-QPSK	2	32
100G-DP-16QAM	4	16
200G-DP-16QAM	4	32

Table 3.4 – Transmitter configuration.

Dual polarization coherent receiver At the dual polarization coherent receiver, both, input signal and local oscillator laser, are splitted in both polarizations. Each one of them is down-converted by a coherent receiver, filtered and sampled by an analog to digital converter. The coherent receiver, comprises 4 photodiodes. Every photodiode has been modelled ideally, with a responsitivity equal to 1.0. The chosen electrical filter has been a Bessel filter with a bandwidth of 0.6 times the symbol rate. For the analog to digital converter, a sampling rate of 2 samples/symbol has been selected, which translates in 64 Gsamples/s, 32 Gsamples/s and 64 Gsamples/s, for the 100G-DP-QPSK, 100G-DP-16QAM and 200G-DP-16QAM, respectively. Furthermore, the resolution has been set to 8 bits. The local oscillator has been parameterized as the local oscillator at the transmitter: emission frequency at the specific channel and 100 kHz linewidth.

DSP Several DSP techniques are applied to the received signal: CD compensation, equalization, frequency offset and phase offset compensation, synchronization and BER calculation. All these techniques are explained in more detail in the next paragraphs.

- CD compensation: Digital CD compensation in the frequency domain, compensating accumulated CD over the transmission line [244].
- Equalizer: Time domain equalizer based on constant modulus algorithm [245] for QPSK and multiple modulus algorithm [246] for 16-QAM.

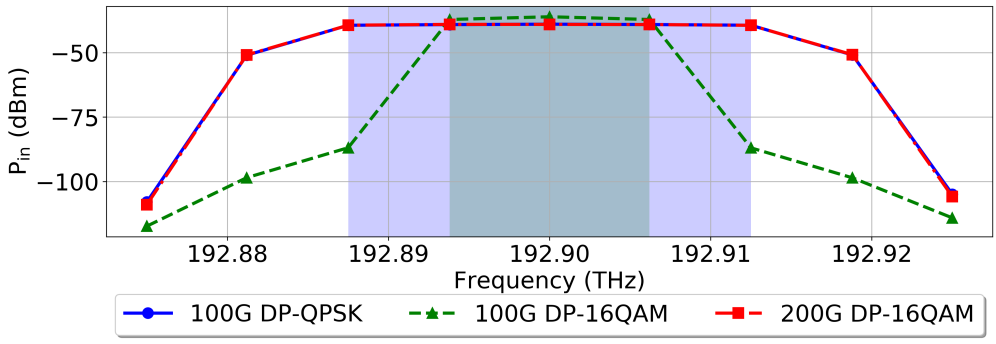

Figure 3.2 – Input channel power measured in slices of 6.25 GHz bandwidth.

- Carrier frequency recovery: Based on [247].
- Phase offset estimation: Sliding window implementation of Viterbi phase estimator [245] and [246], for dual-polarization mPSK signals and 16-QAM signals, respectively, are used.
- Synchronization: By using correlations between the received signal and the original signal for different delays, this module calculates the time offset. Based on this, the received signal is adjusted, aligned with the transmitted one.
- BER: First, symbol decisions are taken based on the closest constellation point to the received symbol (maximum likelihood detection). After demapping, the transmitted bits are compared to received bits. EVM values, symbol error rate and BER are calculated.

Measured performance parameters

Three main parameters, measuring the performance of the received optical signal have been monitored: optical power excursion, OSNR and BER. More details are given in the following.

Optical power excursion Using the same input channel configuration, but each time for a different data rate and modulation case (100G-DP-QPSK, 100G-DP-16QAM and 200G-DP-16QAM), measured power excursion was compared. For the same channel centered at frequency 192.9 THz the input power at the booster amplifier, measured in slices of 6.25 GHz bandwidth, is plotted in Fig. 3.2 for the three different modulation and date rate pairs considered here. Correspondingly, Fig. 3.3 illustrates the power at the output of the considered optical link. In the case of 100G-DP-QPSK and 200G-DP-16QAM, the power is mainly concentrated in 5 bandwidth slices, i.e. $5 \times 6.25\text{GHz} = 31.25$ GHz. Differently, the 100G-DP-16QAM occupies less spectrum, the power is accumulated over 3 bandwidth slices, i.e. $3 \times 6.25\text{GHz} = 16.25$ GHz. Using this data, optical power excursion in each slice i of 6.25 GHz bandwidth is calculated as:

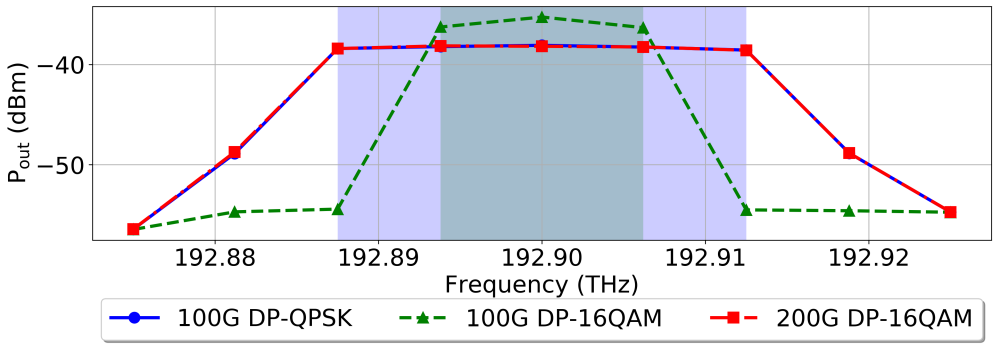

Figure 3.3 – Output channel power measured in slices of 6.25 GHz bandwidth.

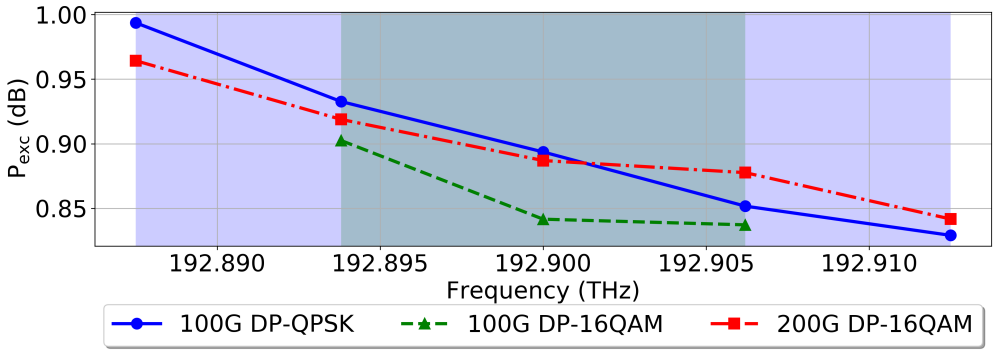

Figure 3.4 – Output power excursion measured in slices of 6.25 GHz bandwidth.

$$P_{exc_i} = \frac{P_{out_i}}{P_{in_i} G}, \tag{3.12}$$

where G is the desired average amplifier gain of 15 dB and P_{in_i}, P_{out_i} and P_{exc_i} are the input power, output power and power excursion at the slice i. Figure 3.4 represents the calculated power excursion per slice as expressed in eq. 3.12. Note that, as explained before, 100G-DP-QPSK and 200G-DP-16QAM considered 5 slices whereas 100G-DP-16QAM required only 3 slices. As expected, a larger signal bandwidth is influenced by a larger amplifier bandwidth being more sensitive to experience a larger power excursion. Finally, the power excursion for the complete channel is calculated as the average of the individual power excursions:

$$P_{exc} = \frac{\sum_i P_{exc_i}}{M}, \tag{3.13}$$

with M the total number of slices, $M = 3$ for 100G-DP-16QAM and $M = 5$ for 100G-DP-QPSK and 200G-DP-16QAM. In this example, the final power excursion per channel was 0.90 dB for 100G-DP-QPSK, 0.86 dB for 100G-DP-16QAM and 0.89 dB for 200G-DP-16QAM, with 100G-DP-16QAM suffering the smallest optical power excursion.

OSNR The OSNR obtained as one of the simulation outputs has been calculated from out-band measurements in every channel. The used reference bandwidth B_n has been fixed to 12.5 GHz. In order to do this measurement, signal power and noise power are required.

Firstly, the power at the center frequency in every channel (P_{TOT}) is measured over the reference bandwidth. This power measurement contains signal and noise. Secondly, two noise measurements are done at both edges of the reserved channel bandwidth (right and left), e.g. $+/-25$ GHz for fixed grid. This measurement is done in a smaller bandwidth B_{meas} in order to measure only noise, without including signal. Assuming a flat noise spectra, the noise approximation at each extreme of the channel in the reference bandwidth is directly calculated by using a multiplication factor (B_n/B_{meas}) on the two noise power measurements performed in the smaller bandwidth B_{meas} ($P_{outband-noise-right,B_{meas}}$, $P_{outband-noise-left,B_{meas}}$):

$$P_{outband-noise-right,B_n} = P_{outband-noise-right,B_{meas}} \frac{B_n}{B_{meas}}. \tag{3.14}$$

$$P_{outband-noise-left,B_n} = P_{outband-noise-left,B_{meas}} \frac{B_n}{B_{meas}}. \tag{3.15}$$

Then, the noise in the center frequency is estimated as the average of the two side values:

$$\hat{P}_{inband-noise,B_n} = \frac{P_{outband-noise-right,B_n} + P_{outband-noise-left,B_n}}{2}. \tag{3.16}$$

Finally, the OSNR is calculated as:

$$OSNR_{outband,B_n} = \frac{P_{tot,B_n} - \hat{P}_{inband-noise,B_n}}{\hat{P}_{inband-noise,B_n}}. \tag{3.17}$$

BER BER estimation for each channel has been obtained directly by a built-in VPI block, included in the setup.

Crosstalk and ISI penalties

Simulations have been performed in a B2B scheme, with the transmitter directly connected to the receiver, avoiding the optical link. The selected scenario considered a WDM configuration with 40 channels spaced 50 GHz. Although in each simulation all the channels have been configured using the same traffic demand type (modulation and data rate), simulations have been repeated for the three different traffic demands under study (Table 3.2). By adding noise in the system (noise loading), OSNRs have been adjusted in a range from 10 to 30 dB. OSNR due to noise loading is denoted in the following as $OSNR_{ASE}$, to keep the same nomenclature

as in the following section. Together with $OSNR_{ASE}$, in every simulation, BER measurements at the receiver have been stored. From the BER calculated in the simulations and using the formulas associating SNR and BER for Gray coding, for DP-QPSK and for DP-16-QAM given by eq. 3.18 and 3.19, respectively:

$$BER = \frac{1}{2}\text{erfc}\left(\sqrt{SNR/2}\right), \tag{3.18}$$

$$BER = \frac{3}{8}\text{erfc}\left(\sqrt{\frac{1}{10}SNR}\right), \tag{3.19}$$

it is possible to estimate the SNR. The corresponding OSNR, denoted $OSNR_{LIN}$, has been approximated using the relationship between OSNR and SNR for dual polarization given by:

$$OSNR = \frac{R_s}{B_n}SNR, \tag{3.20}$$

where B_n denotes the OSNR bandwidth, defined as 12.5 GHz (~ 0.1 nm) and R_s refers to the symbol rate, which takes the values defined in Table 3.4.

Figure 3.5 shows the BER with respect to OSNRs for the three different traffic demands. For low OSNR, the BER estimation calculated with VPI is not very accurate, represented by an abrupt BER cliff in Fig. 3.5. As ASE is not the only disturbance, but also crosstalk and intersymbol interference (ISI), both OSNRs, OSNR due to noise ($OSNR_{ASE}$) and the total linear OSNR ($OSNR_{LIN}$) are not equal, being $OSNR_{ASE} > OSNR_{LIN}$. As can be seen, DP-16-QAM is more sensitive to crosstalk and ISI. In the following, OSNR thresholds used for the three cases are set to: 16 dB, 20 dB and 20 dB for 100G DP-QPSK, 100G DP-16QAM and 200G DP-16QAM, corresponding to BER of approximately 10^{-3} [248], [249]. Based on Fig. 3.5, these thresholds are restrictive, taking into account that a pre-FEC BER[6] value limit of 0.04 is assumed for SD-FEC with overhead of 21.875 % [156] (Table 3.2). However, as the OSNR we measured in the simulations, is an estimation obtained from out-band measurements (eq. 3.17), we add a margin in order to prevent inaccuracies. All these thresholds are summarised in Table 3.5.

	OSNR threshold (dB)	**pre-FEC BER threshold**
100G-DP-QPSK	16	0.04
100G-DP-16QAM	20	0.04
200G-DP-16QAM	20	0.04

Table 3.5 – OSNR and pre-FEC BER thresholds for the considered traffic demands.

Using these results, it is possible to define a parameter χ^2_{XI}, associating both OSNRs ($OSNR_{ASE}$

[6] Predefined threshold for error-free post-FEC transmission.

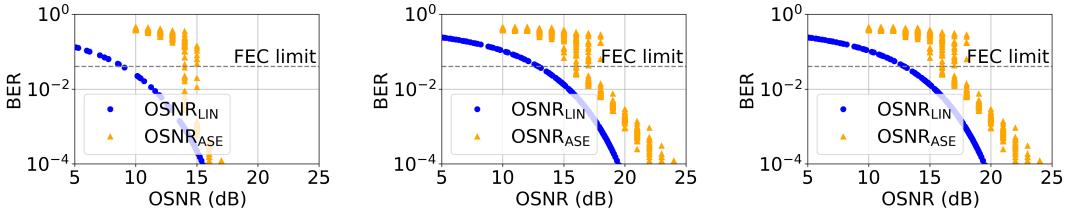

(a) 100G-DP-QPSK. (b) 100G-DP-16-QAM. (c) 200G-DP-16-QAM.

Figure 3.5 – Back-to-back simulation results.

and $\mathrm{OSNR_{LIN}}$) [250]:

$$\chi^2_{XI} = \frac{1}{\mathrm{OSNR_{LIN}}} - \frac{1}{\mathrm{OSNR_{ASE}}}. \tag{3.21}$$

This new defined parameter χ^2_{XI}, valuable to afterwards calculate the nonlinear OSNR, is directly the inverse of the OSNR due to crosstalk and ISI ($\mathrm{OSNR_{XI}}$) [250]:

$$\mathrm{OSNR_{XI}} = \frac{\mathrm{P_s}}{\sigma^2_{XI}} = \frac{1}{\chi^2_{XI}}, \tag{3.22}$$

where σ^2_{XI}, the noise variance due to crosstalk and ISI, depends on χ^2_{XI} as [250]:

$$\sigma^2_{XI} = \mathrm{P_s}\chi^2_{XI}. \tag{3.23}$$

Finally, the linear OSNR, $\mathrm{OSNR_{LIN}}$ is defined as follows [250]:

$$\mathrm{OSNR_{LIN}} = \frac{\mathrm{P_s}}{\sigma^2_{\mathrm{ASE}} + \sigma^2_{\mathrm{XI}}}, \tag{3.24}$$

where σ^2_{ASE} and σ^2_{XI} are the noise variances from ASE and crosstalk-ISI, respectively.

Launch input power adjustment

Selecting a suitable input launch power is of great importance, having a significant impact in the system performance: for low input launch powers, the system is limited by the noise whereas for high large launch powers, the system is limited by nonlinearities. In order to estimate the optimum launched power in the fiber, simulations have been performed in this case with varying input powers for 40 WDM channels spaced 50 GHz using 100G-DP-16QAM.

The OSNR, analogously to the previous section, has been estimated using the BER, from the equations 3.18 and 3.19. This OSNR, comprising linear and nonlinear effects, is referred as $\mathrm{OSNR_{TOT}}$:

$$\mathrm{OSNR_{TOT}} = \frac{\mathrm{P_s}}{\sigma^2_{\mathrm{LIN}} + \sigma^2_{\mathrm{NLI}}}, \tag{3.25}$$

where $\mathrm{P_s}$ is the signal power and both contributions: noise linear contribution σ^2_{LIN} and noise nonlinear contribution σ^2_{NLI} are considered. Consequently, it is possible to approximate the OSNR at low input launch powers by $\mathrm{OSNR_{LIN}} = \frac{\mathrm{P_s}}{\sigma^2_{\mathrm{LIN}}}$ and at high input launch powers by $\mathrm{OSNR_{NLI}} = \frac{\mathrm{P_s}}{\sigma^2_{\mathrm{NLI}}}$. In the following, the calculation of both OSNRs is explained in more detail.

Linear OSNR Seen in the previous section, $\mathrm{OSNR_{LIN}}$ can be expressed in terms of the OSNR due to ASE noise ($\mathrm{OSNR_{ASE}}$) and the OSNR due to crosstalk and ISI ($\mathrm{OSNR_{XI}}$). Taking into account that $\mathrm{OSNR_{XI}}$ can be calculated from σ^2_{XI} obtained in B2B simulations, only the $\mathrm{OSNR_{ASE}}$ needs to be calculated here. For doing this, the ASE noise spectral density $\mathrm{S_{ASE}}$, is defined as:

$$\mathrm{S_{ASE}} = h\nu\mathrm{NF}(\mathrm{G}-1), \tag{3.26}$$

where h is the Planck's constant, ν is the frequency, NF is the amplifier noise figure and G is the amplifier gain. For a bandwidth $\mathrm{B_0}$ the noise power becomes:

$$\mathrm{P_{ASE}} = h\nu\mathrm{NF}(\mathrm{G}-1)\mathrm{B_0}. \tag{3.27}$$

In a cascade of $\mathrm{N_A}$ amplifiers, where the first amplifier acts as a booster amplifier and the following $\mathrm{N_A}-1$ are inline amplifiers compensating the losses in the fiber spans, the total noise power at the output of the $\mathrm{N_A}$th amplifier is given by [251]:

$$\mathrm{P_{ASE}} = N_A\left(h\nu\mathrm{NF}(\mathrm{G}-1)\mathrm{B_0}\right). \tag{3.28}$$

Using equation 3.28 and considering the signal power at the output of the amplifier cascade $\mathrm{P_{sig,out/ch}}$ as the transmitted power per channel at the output of the transmitter ($\mathrm{P_{tx/ch}}$) after being amplified by the booster ($\mathrm{P_{sig,out/ch}} = \mathrm{P_{tx/ch}G}$), the linear OSNR at the output of the cascade is calculated as:

$$\mathrm{OSNR_{LIN}} = \frac{\mathrm{P_{sig,out/ch}}}{\sigma^2_{ASE} + \sigma^2_{XI}} = \frac{\mathrm{P_{tx/ch}G}}{N_A\left(h\nu\mathrm{NF}(\mathrm{G}-1)\mathrm{B_0}\right) + \sigma^2_{XI}}. \tag{3.29}$$

Note that, as an approximation, the ROADM together with the amplifier at its output, is approximated as one span.

Nonlinear OSNR From eq. 3.25 and after calculating the $OSNR_{LIN}$, there is enough information to estimate the OSNR due to nonlinearities $OSNR_{NLI}$ as:

$$OSNR_{NLI}^{-1} = OSNR_{TOT}^{-1} - OSNR_{LIN}^{-1}. \tag{3.30}$$

Furthermore, nonlinear OSNR ($OSNR_{NLI}$) is usually expressed in terms of a nonlinear factor α_{NLI}, independent of the power:

$$OSNR_{NLI} = \frac{1}{\alpha_{NLI} P_{sig,out/ch}^2}. \tag{3.31}$$

Combining eq. 3.30 and eq. 3.31, the nonlinear factor is given by:

$$\alpha_{NLI} = \frac{OSNR_{TOT}^{-1} - OSNR_{ASE}^{-1}}{P_{sig,out/ch}^2}. \tag{3.32}$$

Using eq. 3.32, the nonlinear factor has been estimated, allowing to calculate the nonlinear OSNR.

Finally, using the previous analytical formulations on the results (BER) obtained on simulations using different launch input powers, the following parameters have been estimated:

- $OSNR_{TOT}$: OSNR estimated from the BER, therefore including linear and nonlinear effects (eq. 3.19 and eq. 3.20).
- $OSNR_{LIN}$: OSNR including linear noise ASE, crosstalk and ISI (eq. 3.29).
- $OSNR_{NLI}$: OSNR including only nonlinear noise (eq. 3.31).

Figure 3.6 illustrates the obtained results. As can be seen, for low input powers, where nonlinearities can be neglected, the linear OSNR approximation considering ASE noise, crosstalk and ISI is very close to the total OSNR. Not shown in the Figure, but tested, if the crosstalk and ISI are neglected, the approximation suffers a small deviation ($\sim$ 1 dB). For high input powers, the OSNR including only nonlinear effects is close to the total OSNR.

The break point power and the power which maximizes OSNR are plotted in Fig. 3.6. Theoretically, the break point power (P_B), where the $OSNR_{LIN}$ and $OSNR_{NLI}$ asymptotes cross each

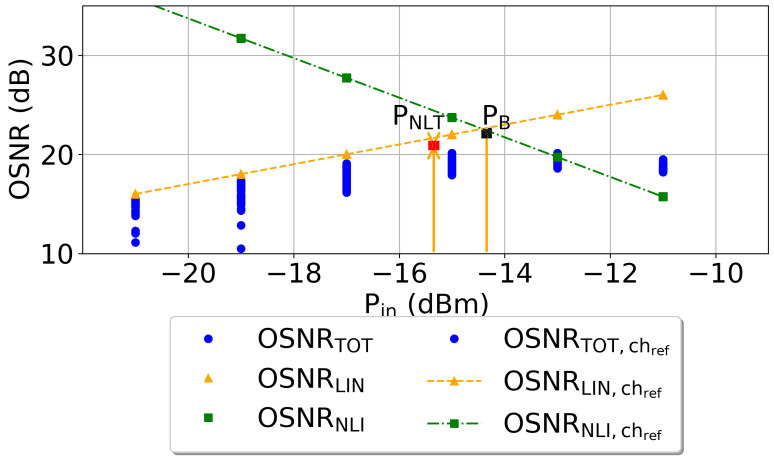

Figure 3.6 – OSNR for different input launch powers.

other, is calculated as:

$$\mathrm{P_B} = \left(\frac{\sigma^2_{ASE} + \sigma^2_{XI}}{\alpha_{NLI}} \right)^{\frac{1}{3}}. \tag{3.33}$$

The power which maximizes the OSNR ($\mathrm{P_{NLT}}$) is calculated using the derivative condition:

$$\frac{d\mathrm{OSNR_{TOT}}}{d\mathrm{P}} = 0. \tag{3.34}$$

Solving eq. 3.34, $\mathrm{P_{NLT}}$ is expressed as:

$$\mathrm{P_{NLT}} = \left(\frac{\sigma^2_{ASE} + \sigma^2_{XI}}{2\alpha_{NLI}} \right)^{\frac{1}{3}}. \tag{3.35}$$

As seen in the Fig. 3.6, the optimum launch power P_{NLT} is −15.77 dBm. In the following work, the same input channel power has been used independently of the modulation. To determine the input power channel, a more conservative approach has been adopted. According to [43], [155], optimum launch power, depends on the span attenuation. Input power per channel has been therefore determined as:

$$P_{TX} = \frac{G - 22}{3}, \tag{3.36}$$

being −17.5 dBm in this case, lower than the optimum values calculated before, in order to avoid nonlinearities.

3.3.2 Quality of Transmission estimation

For the setup detailed in the previous section (Section 3.3.1), an ML model able to anticipate the QoT for each channel in a particular channel configuration has been developed based on NNs. Three different NNs have been trained in order to forecast optical power excursion and predict whether the channel OSNR and BER are above or below a threshold (see Table 3.5). First, a dataset to train the NNs has been generated. Then, NNs have been trained and validated. This process has been performed for two scenarios: fixed and flexible frequency grid.

Dataset generation

Considering first a fixed frequency grid, simulations have been performed under the next input parameter conditions:

- Data rate and modulation format: Assuming moderate data rate traffic, most of the traffic demands correspond to 100G traffic requests. In particular, 20 % of the total traffic requests have been assigned to 200G-DP-16QAM channels and the remaining 80 % has been uniformly distributed between the 100G-DP-QPSK and 100G-DP-16QAM channels [252].
- Channel load: Four different average channel loads have been considered, 20 %, 40 %, 60 % and 80 %, with a deviation of $+/-5$ %.
- Frequency allocation: Random assignment.

A total number of ~ 2.400 simulations have been executed, distributed approximately equally among the 4 considered average channel loads of 20 %, 40 %, 60 % and 80 % (~ 2400/4 =~ 600 simulations per scenario).

The same procedure has been followed for a flexible grid scenario. In this case, the total number of simulations is ~ 3.000. As fixed grid channel configurations are compatible with flexible grid[7], simulations performed for a fixed grid scenario are included as part of the flexible grid dataset.

Time required to execute each simulation (more than 1 hour depending on the channel load, more channels require more time) was the main constraint at this point, limiting the dataset sizes to ~ 2.400 and ~ 3.000 simulations. Larger datasets would allow to achieve more accurate models. However, our work does not aim to achieve the best accuracy, but to demonstrate: (1) the importance of optical power excursion as input feature in an NN model predicting QoT, which can be shown even with lower accuracy models and (2) the usage of an RL algorithm to autonomously perform modulation format and wavelength assignment; comparison between

[7] Fixed grid frequency spacing is 50 GHz, multiple of the 12.5 GHz flexible grid frequency slot.

the RL algorithm and other algorithms is performed on the same environment, i.e. equal conditions, thus, having a lower accuracy affects all the algorithms equally, allowing still a fair comparison.

Machine learning models

Three different NNs have been developed dedicated to the three different parameters to predict: optical power excursion, OSNR and BER. Corresponding code has been developed in Python making use of Keras and Tensorflow libraries. All the NN architectures have adopted Adam as optimizer. As loss function, mean squared error function has been used for the optical power excursion regression (eq. 2.11) and binary cross-entropy for the OSNR and BER classification (eq. 2.12)[8]. For the training, the dataset has been divided using 85 % for training, 5 % for validation and 10 % for test purposes.

For the fixed grid scenario, five different NN model possibilities have been trained for each parameter (optical power excursion, OSNR and BER) targeting different channel loads:

- 20 %: Model trained on a dataset containing only simulations with a 20 % average channel load (~ 600 simulations). This model is only valid for 20 % average channel load.
- 40 %: Model trained on a dataset containing only simulations with a 40 % average channel load (~ 600 simulations). This model is only valid for 40 % average channel load.
- 60 %: Model trained on a dataset containing only simulations with a 60 % average channel load (~ 600 simulations). This model is only valid for 60 % average channel load.
- 80 %: Model trained on a dataset containing only simulations with a 80 % average channel load (~ 600 simulations). This model is only valid for 80 % average channel load.
- Variable: Model trained on a dataset containing simulations at 20 %, 40 %, 60 % and 80 % average channel load (total ~ 2.400 simulations). This model is valid 20 %, 40 %, 60 % and 80 % average channel loads.

As better performance was achieved by training on the complete dataset with variable channel load, the flexible grid models have been trained only in the complete dataset of ~ 3.000 simulations, for variable channel load (20 %, 40 %, 60 % and 80 %).

[8] As explained in Section 2.1.2, mean squared error is a common loss function for regression tasks, whereas cross-entropy is common for classification tasks.

The main difference among the fixed grid and the flexible grid NN models is regarding vector sizes. Fixed grid models use 80 value vectors for the input and output layers, one value per 50 GHz channel. However, flexible grid models use 640 value vectors for the input and output values, each value representing 6.25 GHz sub-slot. Note that in flexible grid, 12.5 GHz is the slot width granularity and 6.25 GHz the central frequency granularity. Therefore, the 80 values from fixed grid become $80 \times (50/6.25) = 640$ values in the flexible grid.

Hyperparameters, as number of layers and number of units per layer, were adjusted empirically. Different combinations were tried, choosing the ones providing better performance in terms of mean squared error and accuracy (Section 2.1.1). Similar results could be obtained with different architectures.

Optical power excursion For the fixed grid case, the NN trained to predict optical power excursion has adopted the following architecture:

- Input layer: 80 neurons corresponding to 80 channels. Four possible values are allowed, representing: unused channel, 100G-DP-QPSK channel, 100G-DP-16QAM channel and 200G-DP-16QAM channel. In the following, this vector is called channel state information (CSI) vector.
- Hidden layer: 160 neurons with ReLU activation (Section 2.1.2).
- Output layer: 80 neurons representing the optical power excursion in each channel. Linear activation is used, as optical power excursion is a real value.

The same NN architecture was trained with the 5 datasets (20 %, 40 %, 60 %, 80 % and variable channel load), as seen in Fig. 3.7. After training, best results (Table 3.6) with the lowest minimum squared error have been obtained for the complete dataset, trained with a variable channel load (20 %, 40 %, 60 %, 80 %).

	20 %	**40 %**	**60 %**	**80 %**	**Variable**
Mean squared error	0.27	0.39	0.31	0.16	0.10

Table 3.6 – Fixed grid: Mean squared error optical power excursion regression.

Flexible grid model is identical to the fixed grid model, but considering 640 neurons instead of 80, due to the frequency grid. Thus, the length of the CSI vector is also 640 instead of 80. Furthermore, two more hidden layers have been included, with 320 and 160 neurons, respectively. Obtained mean squared error after training was 0.10, as for the fixed grid model. Although more simulations would allow to reduce the mean squared error, it is sufficient for our purpose.

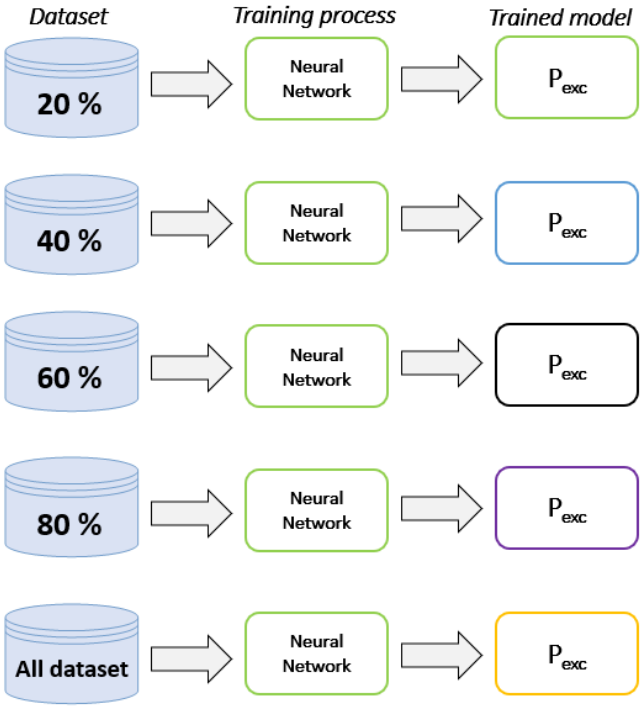

Figure 3.7 – NN models for optical power excursion prediction.

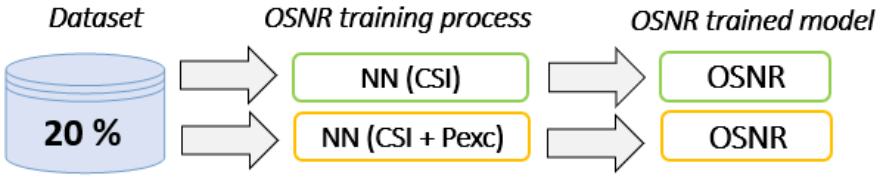

Figure 3.8 – NN models for OSNR classification.

OSNR Two different architectures have been considered for the OSNR prediction. The first one, using only the CSI vector (state information about active channels and their modulation formats) and the second one including optical power excursion as input feature. Details about the developed models for the fixed grid scenario are given in the following. Note that for the fixed grid, each NN architecture was trained on the different datasets of 20 %, 40 %, 60 %, 80 % and variable channel load (process for the 20 % channel load is shown in Fig. 3.8).

The NN architecture based only on CSI has followed the structure:

- Input layer: 80 neurons corresponding to CSI vector.
- 3 hidden layers: 160 neurons, 320 neurons and 160 neurons.
- Output layer: 80 neurons representing for each channel, whether the OSNR is above or below the minimum required OSNR value: 16 dB, 20 dB, 20 dB for 100G-DP-QPSK, 100G-DP-16QAM and 200G-DP-16QAM, respectively (Section 3.3.1, Table 3.5).

Including optical power excursion as input feature, the NN architecture has been defined as:

- Input layer: 160 neurons, the first 80 neurons corresponding to CSI vector, the second 80 neurons corresponding to the optical power excursion.
- Hidden layers: First hidden layer with 160 neurons connected to the CSI vector and 160 neurons connected to the optical power excursion. Both hidden layers are merged in a second hidden layer with 320 neurons, followed by a third hidden layer with 160 neurons.
- Output layer: 80 neurons representing for each channel, whether the OSNR is above or below the minimum required OSNR value: 16 dB, 20 dB, 20 dB for 100G-DP-QPSK, 100G-DP-16QAM and 200G-DP-16QAM, respectively (Section 3.3.1, Table 3.5).

Regarding activation, hidden layers have used ReLU activation whereas output layers have used sigmoid activation, compatible with binary cross-entropy loss function (Section 2.1.2). Accuracy obtained on the test set after the training is shown in Table 3.7. As for the power excursion model, the accuracy is improved when the complete dataset, for variable channel load, is used for training. Furthermore, when power excursion is included as input feature, the accuracy improves by 7.44 % when trained in the complete dataset (92.01% – 84.57% = 7.44%). In this particular case, with a cascade of optical amplifiers introducing a large power excursion, power excursion conveys important information for the OSNR estimation. It is important to note that, for an optical link different from the one considered here (Figure 3.1) producing a smaller optical power excursion (< 5 dB), the importance of the power excursion as input feature for predicting OSNR could have less impact.

Input features	20 **%**	40 **%**	60 **%**	80 **%**	**Variable**
CSI	91.05 %	80.85 %	73.79 %	71.6 %	84.57 %
CSI + power excursion	93.98 %	88.70 %	84.07 %	81.9 %	92.01 %

Table 3.7 – Fixed grid: Accuracy OSNR classification.

For flexible grid scenario, the difference again is only the number of components for the input and output vectors (80 for fixed and 640 for flexible grid). Obtained results for the complete dataset are shown in Table 3.8. Similarly to the fixed grid case, including optical power excursion improves accuracy. Furthermore, compared to fixed grid results, accuracy is higher. In the flexible grid model, many of the output values correspond to unused sub-slots, easy to predict by the NN model, therefore increasing the accuracy.

BER Analogously to the OSNR, different input features have been considered in order to predict BER. Four architectures have been developed using as input features: (1) only CSI vector, (2) CSI vector and optical power excursion, (3) CSI and OSNR information, (4) CSI,

Input features	Variable
CSI	97.59 %
CSI + power excursion	98.05 %

Table 3.8 – Flexible grid: Accuracy OSNR classification.

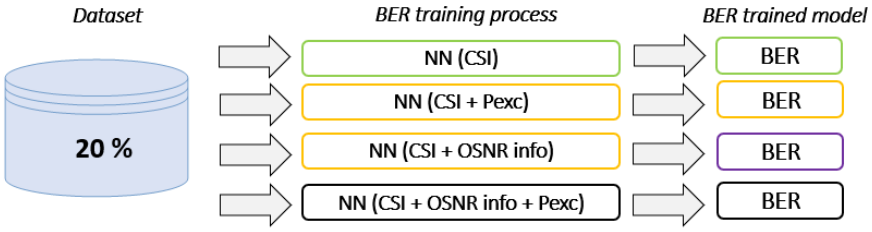

Figure 3.9 – NN models for BER classification.

optical power excursion and OSNR information. When OSNR information is included as input feature, not the particular real-value OSNR but the OSNR classification information (being above or below the OSNR limits defined in Table 3.5) is used. Developed models for the fixed grid scenario are described in the following. As for the OSNR models, note that for the fixed grid, each NN architecture was trained on the different datasets of 20 %, 40 %, 60 %, 80 % and variable channel load (process for the 20 % channel load is shown in Fig. 3.9).

When only CSI vector is considered as input vector, the architecture has been defined as follows:

- Input layer: 80 neurons corresponding to CSI vector.
- 3 hidden layers: 160 neurons, 320 neurons and 160 neurons.
- Output layer: 80 neurons representing whether the BER in each channel, is above or below the pre-FEC BER threshold considered to be 0.04 (Section 3.3.1, Table 3.5).

NN architecture has been modified to include optical power excursion as input feature, following:

- Input layer: 160 neurons, the first 80 neurons corresponding to CSI vector, the second 80 neurons corresponding to the optical power excursion.
- Hidden layers: First hidden layer with 160 neurons connected to the CSI vector and 160 neurons connected to the optical power excursion. Both hidden layers are merged in a second hidden layer with 320 neurons, followed by a third hidden layer with 160 neurons.

- Output layer: 80 neurons representing whether the BER in each channel, is above or below the pre-FEC BER threshold of 0.04.

The architecture used when CSI vector and OSNR information are used as input features is identical to the previous one, only substituting optical power excursion by OSNR information.

The fourth architecture, using CSI vector, optical power excursion and OSNR information as input features, has been defined as follows:

- Input layer: 320 neurons, the first 80 neurons corresponding to CSI vector, the second 80 neurons corresponding to the optical power excursion and the third 80 neurons corresponding to OSNR information.
- Hidden layers: First hidden layer with 160 neurons connected to the CSI vector, second 160 neurons connected to the optical power excursion and third 160 neurons connected to the OSNR information. The three hidden layers are merged in a second hidden layer with 320 neurons, followed by a third hidden layer with 160 neurons.
- Output layer: 80 neurons representing whether the BER in each channel, is above or below the pre-FEC BER threshold of 0.04.

As for the OSNR case, hidden layers have used ReLU activation whereas output layers have used sigmoid activation compatible with binary cross-entropy (Section 2.1.2). Accuracy calculated on the test set after training is shown in Table 3.9. Again, training on the complete dataset, for variable channel load, offers better performance. Regarding the input features, using CSI vector together with power excursion and OSNR information outperforms all the other models. However, the difference in performance with respect to using only CSI and power excursion is neglectable, likely due to the fact that the considered OSNR thresholds are very restrictive, corresponding to BER of $\sim 10^{-3}$. It is important to highlight that including optical power excursion, as for the OSNR model, significantly improves the model.

Input features	20 **%**	40 **%**	60 **%**	80 **%**	**Variable**
CSI	87.22 %	76.76 %	71.33 %	70.05 %	83.14 %
CSI + power excursion	91.86 %	87.21 %	84.31 %	82.30 %	93.21 %
CSI + OSNR info	90.87 %	82.03 %	77.43 %	75.90 %	88.63 %
CSI + power excursion + OSNR info	93.22 %	88.83 %	86.07 %	83.40 %	93.43 %

Table 3.9 – Fixed grid: Accuracy BER classification.

For flexible grid, same architectures with larger input and output vectors have been used (80 for fixed and 640 for flexible grid). Results are shown in Table 3.10. As in the OSNR classification model, accuracy looks higher due to the number of components. Many of output values correspond to inactive sub-slots, being not difficult for the NN model to predict, producing

an increase in accuracy. Nevertheless, the important aspect here is again that using power excursion as input feature improves accuracy.

Input features	Variable
CSI	97.49 %
CSI + power excursion	98.16 %
CSI + OSNR info	97.91 %
CSI + power excursion + OSNR info	97.49 %

Table 3.10 – Flexible grid: Accuracy BER classification.

After training and testing NN models predicting optical power excursion and classifying OSNR and BER, for fixed and flexible grid, we conclude that using complete dataset, for variable channel loads, produces better results than training for particular channel loads. Furthermore and more important, we have demonstrated the importance of optical power excursion as input feature in QoT models based on NNs. These NN models are used in the next section as part of the environment in an RL algorithm.

3.3.3 Reinforcement learning approach

RL algorithms have been presented in Section 2.1.2. In Chapter 2, an RL method has been investigated for optical power excursion precompensation in an optical link. In this chapter, we propose an RL algorithm performing modulation format and wavelength assignment. As always in RL algorithms, an agent must interact with an environment in order to learn, by trial and error (Fig. 3.10). In this case, the environment corresponds to the optical link and the agent to the entity deciding modulation format and wavelength assignment for each received traffic demand. At each timestep, the agent receives a request from the environment for adding (input demand) or dropping (output demand) a channel. Based on the current state (channel configuration: channel frequencies and their modulation formats), the agent selects an action:

- For an add request, the action indicates to the environment, which wavelength and modulation format is selected for the new channel.
- For a drop request, the action indicates the wavelength of an active channel which will replace the dropped channel by using wavelength conversion. The action can also indicate that no channel is wavelength converted.

After adding or dropping the channel according to the agent instructions, the environment estimates the QoT of the new channel configuration, by using the NN models developed in Section 3.3.2. Then, the environment sends to the agent the updated state and next demand together with a reward:

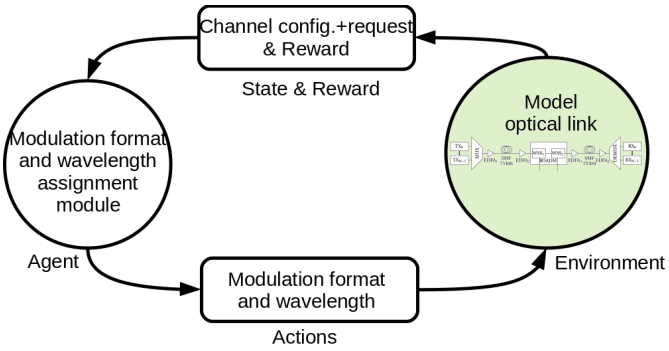

(a) RL general model.

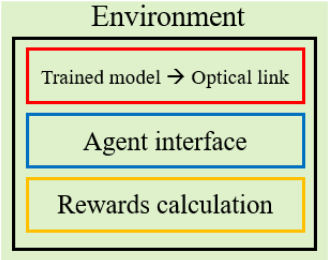

(b) Environment details.

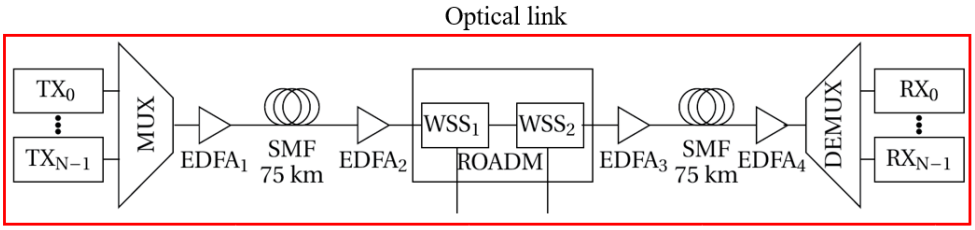

(c) Modelled optical link.

Figure 3.10 – RL approach for impairment aware modulation format and wavelength assignment.

- Negative reward if the QoT is not fulfilled for all the active channels. The episode[9] is terminated.
- Positive reward if the QoT is fulfilled for all the active channels. The episode continues.

Through these interactions the agent learns to optimize the modulation format and wavelength assignment.

This solution based on an RL algorithm allows to find an almost optimal solution for this complex problem. Once trained, RL time response is immediate, compared to other solutions as ILP. RL is faster, even when compared to ML supervised algorithms estimating QoT. Common strategy, when ML supervised algorithms are used, is to first look for candidate wavelengths with a specific QoT (based in ML techniques). Another algorithm is in control of deciding which of the candidate wavelengths is assigned. Depending on the used algorithm, this strategy may end up being time consuming. Another important aspect of our implementation is that power excursion is considered together with BER and OSNR. Power excursion turns to have a significant impact on the QoT also helping spectrum defragmentation[10] [12]. Compared to other parameters, optical power excursion is an impairment simple to monitor, even in transparent optical networks, as there is no need of O/E-E/O conversions. Also, it is

[9] Sequence of agent-environment interactions, from an initial to a terminal state (Section 2.1.2).

[10] Similar to resource fragmentation in computers, spectrum fragmentation produces problems in flexible optical networks, generating isolated or non-contiguous frequency slots that cannot allocate a channel [253], [254].

important to highlight that, not only the changes in QoT when channels are added, but also when channels are dropped are considered. When a channel is dropped, the RL-based algorithm, knowing QoT in other established channels will be impacted, can decide to replace the dropped channel by one of the active channels (by using wavelength conversion), mitigating the QoT and power excursion fluctuation.

Environment and agent are explained in detail in the following paragraphs. In order to assess the performance of the trained RL algorithms four different strategies for wavelength assignment are used, which will be explained at the end of the present section. These algorithms will be compared by interacting on the same environment, as the RL agent. Different from the RL approach, these algorithms do not learn from the interaction with the environment.

Environment

The environment presented here, represents the optical link previously defined (Fig. 3.1, Fig. 3.10c) which we have modelled with NNs in Section 3.3.2. These NN models allow to estimate optical power excursion and classify channels according to OSNR and BER, being a main element in the complete environment. However, for building a complete environment, rewards and traffic demands must be included (Fig. 3.10b).

For the traffic demands, we consider that only one channel can be added or dropped at a time. Arrivals follow a Poisson process with an exponential holding time (HT) of average 600 s [208], with the load being adjusted by tuning the inter-arrival time (IAT) as load = HT/IAT. For a given channel configuration, the environment experiences a particular power excursion, OSNR and BER at each channel (which are estimated with the developed NN models). The state vector exchanged with the agent contains the CSI vector together with the type of request (add/drop) and the data rate, only for the adding case (100G/200G). The reason to also consider drop as requests is that dropping channels impacts the QoT of the other established channels. In order to mitigate these fluctuations, the developed environment allows to apply wavelength conversion on an active channel in order to occupy the frequency of the channel about to be dropped, also contributing to defragmentation [255]. The actions selected by the agent, are composed by 4 components. The interpretation of the action information depends on the request:

- For an add request, the first component indicates the index of the channel (frequency slot for flexible grid) where the channel has to be added, the third component selects the modulation format of the new channel (DP-QPSK or DP-16-QAM) and the fourth component indicates the number of slots to be used (1 or 2), only valid for the 200G requests. For the particular case of 200G requests, it is possible to use 1 wavelength (50 GHz bandwidth) or 2 wavelengths (100 GHz bandwidth, carrying 100G per wavelength). Second component is not used for add requests.
- For a drop request, the first, third and fourth components are not used. The second

component indicates the index of a channel (frequency slot for flexible grid) where an active channel is allocated. This active channel is wavelength converted and it replaces the channel about to be dropped (e.g. channel 2 is going to be dropped and its position will be replaced by channel 4 by using wavelength conversion). In case no active channel is selected for wavelength conversion, the channel is dropped, leaving the wavelength free for future demands.

Once the environment receives the action, it extracts the information according to the different components. After that, it updates the channel state. Then, it calculates the new power excursion and classifies the channels according to being above or below the threshold for the OSNR and BER. All of this is done by using the NN models trained before. Depending on the outcome, a specific reward is delivered to the agent. If all active channels have sufficient QoT, the reward is calculated as an exponential of the mean optical power excursion, being close to 1 for low power excursion and close to 0 for large power excursions, penalizing large power excursions. In case the QoT is not good enough, the episode is terminated with a negative reward (Section 2.1.2).

After terminating an episode, the environment is reset, starting with a new channel configuration at a particular load. These initial channel configurations have been calculated beforehand, in order to speed up the process, by using the ML models previously developed. For doing this, channels have been assigned to random wavelength frequencies, and only the configurations keeping all channels above the OSNR and BER threshold have been kept in a list. At each environment reset, the initial channel configuration is randomly selected from this list.

At this point, a slight modification was performed in the NN models developed in Section 3.3.2. The chosen optical link configuration was selected in order to have a considerable power excursion at the output of the link. However, this made difficult to find channel configurations where all the channels achieve a sufficient QoT. This, together with the fact that sometimes the developed NN models predict that a channel has lower QoT than in reality has, limited even more the process of finding valid channel configurations. To solve this issue, finding a better balance between valid and invalid channel configurations, we modified the threshold of the sigmoid at the output of the NNs classifying OSNR and BER, reducing the number of channels wrongly classified as having a low QoT (Section 2.1.2). As a consequence, model accuracies for OSNR and BER were reduced to ~ 82 % for fixed grid and ~ 95 % for flexible grid. Nevertheless, as all the algorithms compared in Section 3.4 and Section 3.5 used the same environment, based on the same NN models, the comparison is still fair and valid, even if the environment is less accurate.

Agent

RL-based agent has been adopted from Stable Baselines [153]. The selected algorithm has been an implementation of the PPO, similar to the one used in the previous chapter, but using

multiple workers as A2C, resulting to be faster.

Wavelength assignment strategies for comparison with reinforcement learning approach

For comparison, three different wavelength assignment algorithms were considered. We chose that these algorithms only act on input demands (adding channels). For output demands (dropping channels), they do not perform any reconfiguration in the remaining active channels. When a channel is dropped, no channel can replace it occupying its frequency by using wavelength conversion capabilities. Only future input demands can occupy the bandwidth freed by the dropped channel. These three strategies are described in the following:

- FF from lowest to highest frequencies (FF-L2H): Frequencies are ordered from lower to higher frequencies. The first channel available in the list is assigned. For 100G requests, DP-QPSK is always the selected modulation.
- FF closest to the center of the band (FF-Center): The available wavelength (slot for flexible grid) closer to the center of the band is selected. For 100G requests, DP-QPSK is always the selected modulation.
- NN based: Using the NN models developed before (Section 3.3.2), a random channel satisfying the restrictions in terms of QoT is selected. For 100G requests, DP-QPSK is always the selected modulation.

Comparison in terms of blocking probability

The four strategies (RL, FF-L2H, FF-Center, NN) are compared in terms of blocking probability, defined as:

$$P_{\text{blocking}} = \frac{\text{Blocked requests}}{\text{Total number of requests}}, \tag{3.37}$$

where the total number of requests includes adding and dropping requests and the number of blocked requests corresponds to the number of requests which produced the end of an episode, with the QoT being lower than the specified thresholds.

In order to calculate the blocking probability, the trained RL algorithm interacted with the environment, for a total of 50.000 requests. Every time a demand is blocked, terminating an episode, the environment is reset, starting a new episode. Sequence of episodes is continued, accumulating the number of blocked requests and received requests, until total number of requests reaches 50,000 requests.

Blocking probability is estimated in the same way for the other three strategies (FF-L2H, FF-Center, NN), interacting with the same environment.

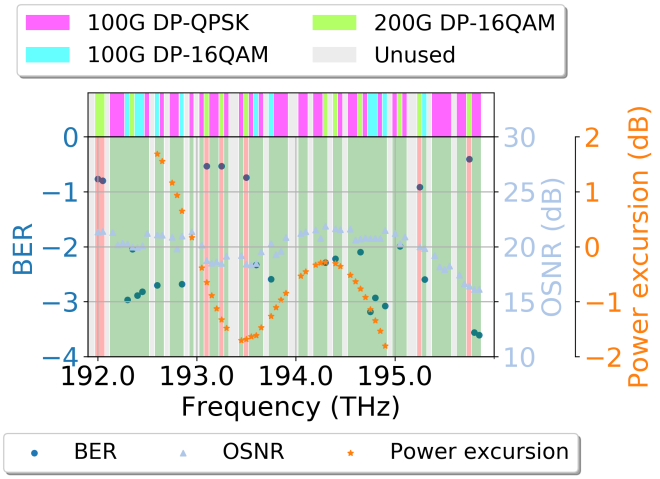

Figure 3.11 – Fixed grid: Example of obtained power excursion, OSNR and BER obtained for a particular channel configuration.

In the following sections we consider two scenarios, fixed and flexible grid. For both of them, we have first trained the RL algorithm. Afterwards, we have compared its performance with the other three strategies (FF-L2H, FF-Center, NN) in terms of blocking probability as presented here.

3.4 Fixed grid

Figure 3.11 shows results obtained for one of the ~ 2.400 simulations performed under a fixed frequency grid configuration used in Section 3.3.2 to train the NN models now integrated as part of the RL environment. On the top of the figure, distribution in the frequency band of the three different traffic demands is shown: 100G-DP-QPSK, 100G-DP-16QAM and 200G-DP-16QAM, with each traffic type represented by one colour. In the bottom of the figure, power excursion, OSNR and BER estimated in the simulation, for each of the active channels, are plotted. For channels having a BER below the pre-FEC BER threshold, a green vertical bar is used. A red vertical bar indicates a BER above the pre-FEC BER limit.

As introduced in Section 3.3.1, considering SD-FEC with overhead of 21.875 %, the pre-FEC BER limit is set to 0.04 [156]. Minimum required OSNRs are: 16 dB, 20 dB and 20 dB, for 100G-DP-QPSK, 100G-DP-16QAM and 200G-DP-16QAM, respectively. During the simulations, we have observed 200G-DP-16QAM channels were more sensitive to power fluctuations. Therefore, an upper power excursion limit of +1.0 dB is considered for 200G-DP-16QAM. All these values are summarised in Table 3.11 and used to train two different impairment aware modulation format and wavelength assignment algorithms: one considering BER and the other considering OSNR together with power excursion limits. Both of them, use power excursion information, with the reward used during training using this information to penalize large power excursion.

	100**G-DP-QPSK**	100**G-DP-16QAM**	200**G-DP-16QAM**
Power excursion threshold	-	-	+1.0 dB
OSNR threshold	16.0 dB	20.0 dB	20.0 dB
BER threshold	0.04	0.04	0.04

Table 3.11 – Power excursion, OSNR and BER thresholds.

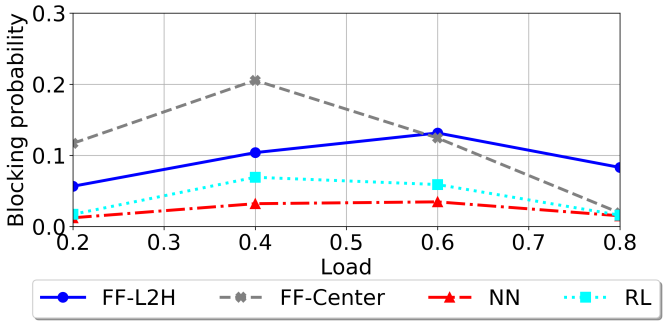

Figure 3.12 – Fixed grid: Blocking probability comparison for OSNR aware algorithm.

3.4.1 OSNR aware wavelength assignment

In a first approach, the environment has considered OSNR and optical power excursion limits. After adding or dropping a channel, the environment estimates the new power excursion and whether the OSNR in each channel is above or below the threshold. The episode is terminated if one or more channels are below the OSNR threshold or the power excursion is above the established limit only for the 200G-DP-16QAM channels. (Table 3.11).

After training, blocking probability for the RL algorithm is compared with the other three wavelength assignment strategies: (1) FF-L2H, (2) FF-Center, (3) NN based (assigning a channel to a frequency fulfilling the OSNR and power excursion requirements). Results are shown in Fig. 3.12. Blocking probability is lower for lower channel loads. Then, as the channel load increases, blocking probability also increases, reaching its maximum between 40 % and 60 %; however, it decreases towards the highest 80 % channel load. This unexpected behaviour is explained by two factors: (1) inaccuracies in the model, leading to incorrectly classify as suitable lightpaths the ones that are not, (2) higher channel occupation is more stable as e.g. power excursion presents less variability for higher channel loads. In addition, for the highest channel load, blocking probability is similar for almost all the methods, as there are few frequencies available. The lowest blocking probability is obtained by using directly the NN models, i.e. assigning directly a frequency fulfilling the OSNR and power excursion constraints. The RL approach is, however, close to have the lowest blocking probability. Apart from being autonomous, the RL algorithm generalizes better, performing very good in any scenario, as it will be seen in the remaining part of the chapter.

Figure 3.13a illustrates an example of the evolution of modulation format and wavelength

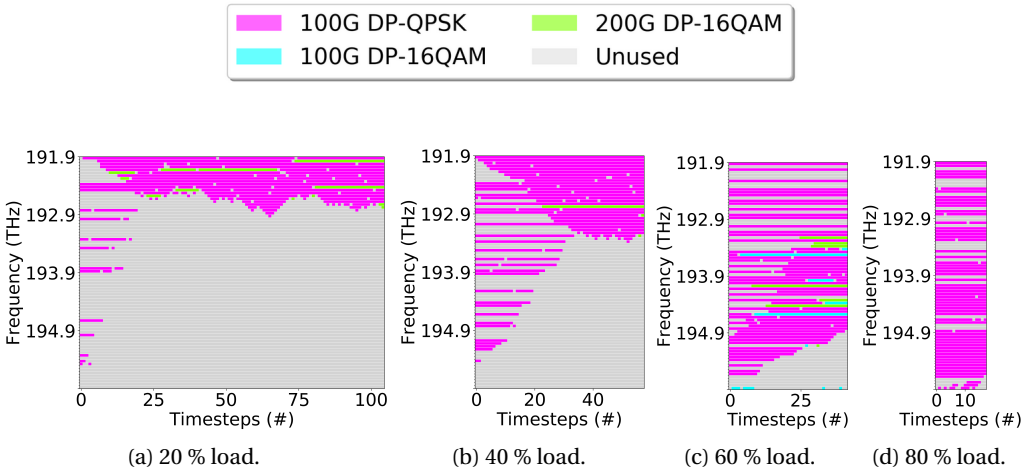

(a) 20 % load. (b) 40 % load. (c) 60 % load. (d) 80 % load.

Figure 3.13 – Fixed grid: Channel assignment evolution under RL-algorithm control for OSNR aware algorithm.

assignment when the RL algorithm is used for a 20 % channel load. At timestep 0, a random channel configuration is observed; with time passing, the RL algorithm assigns channels to the lower frequencies where the power excursion is lower due to the amplifier characteristics (dynamic curve in Fig. 3.1b), defragmenting the spectrum. Assignment to lower frequencies is not only done when a channel is added but also when it is dropped. When a channel from lower frequency is dropped, the RL algorithm replaces it with a channel from a higher frequency, also contributing to defragmentation. Regarding modulations, 100G requests are assigned to 100G-DP-QPSK and 200G requests are assigned to 200G-DP-16QAM. Similar behaviour can be seen for the 40 % load case (Fig. 3.13b). When the load increases up to 60 % (Fig. 3.13c), still higher frequencies are avoided, but it can be seen that some of the 100G requests are assigned to 100G-DP-16QAM, as power excursion is usually lower and by occupying less spectrum produces less nonlinearities. Finally, for the highest 80 % load, 100G-DP-QPSK is again mainly used as modulation format (Fig. 3.13d).

3.4.2 BER aware wavelength assignment

Compared to the previous strategy, here, only BER has been considered as a limit (power excursion is included in the reward). Therefore, an episode is terminated if one or more of the channels are above the pre-FEC BER threshold of 0.04. After training, blocking probabilities are shown again in comparison to the other techniques: (1) FF-L2H, (2) FF-Center, (3) NN based, assigning channels to frequencies fulfilling the BER requirements. As before for the OSNR-aware algorithm, due to inaccuracies in the model and the fact that higher channel loads offer more stability (power excursion varying less abruptly), blocking probability for higher channel loads drops slightly. As seen in Fig. 3.14, among all of them, RL-algorithm obtains the best results. Compared to Fig. 3.12, blocking probabilities are lower, as the limits used in the OSNR case have been more restrictive.

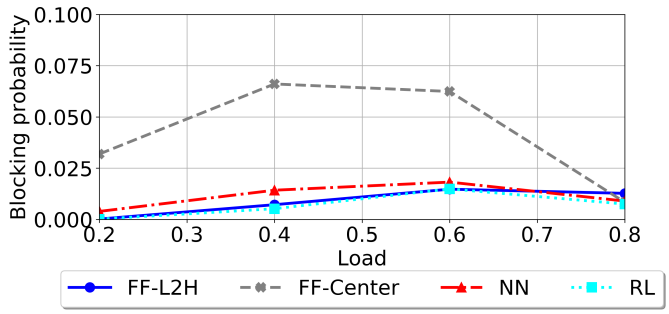

Figure 3.14 – Fixed grid: Blocking probability comparison for BER aware algorithm.

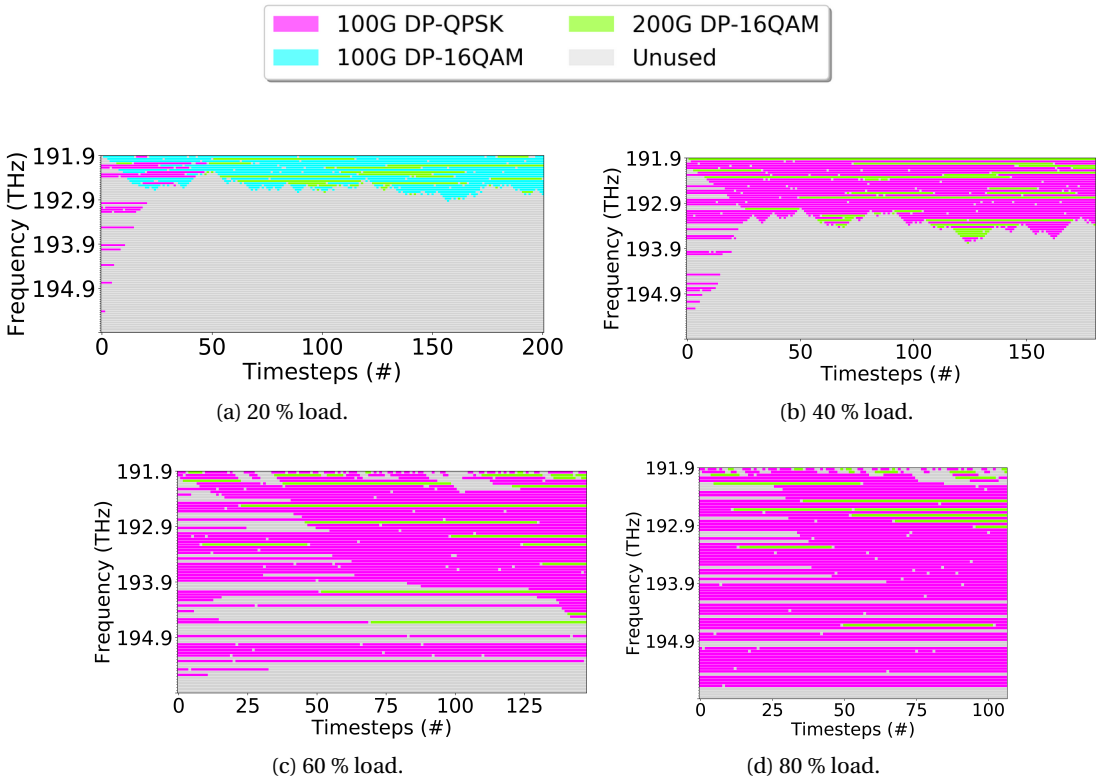

(a) 20 % load.

(b) 40 % load.

(c) 60 % load.

(d) 80 % load.

Figure 3.15 – Fixed grid: Channel assignment evolution under RL-algorithm control for BER aware algorithm.

Evolution of the channel assignment in one episode for 20 % channel load is shown in Fig. 3.15a. As for the OSNR case, due to the amplifier characteristics (dynamic curve in Fig. 3.1b), RL algorithm assigns channels to the lower frequencies, directly each time a channel is added or indirectly when a channel is dropped and an existing channel replaces it. The main difference is that, here, 100G requests are assigned to DP-16QAM. Similar behaviour is observed for 40 %, 60 % and 80 % in Fig. 3.15b, Fig. 3.15c and Fig. 3.15d. But, contrarily to the 20 % channel load, 100G requests are assigned to DP-QPSK.

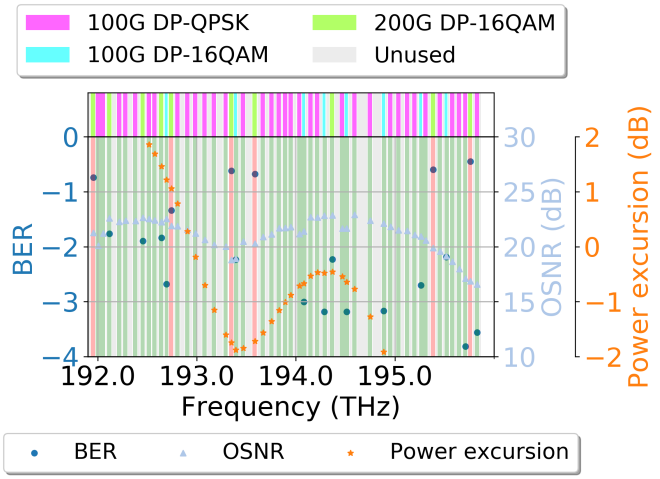

Figure 3.16 – Flexible grid: Example of obtained power excursion, OSNR and BER obtained for a particular channel configuration.

3.5 Flexible grid

Figure 3.16 illustrates the results obtained for a particular simulation using a flexible frequency grid. Results are very similar to the ones obtained for fixed grid and shown in Fig. 3.11. The main difference is the number of frequency slots used by each of the three pairs of data rate and modulation formats: 100G-DP-QPSK and 200G-DP-16QAM require 4 frequency slots (4×12.5 GHz) whereas 100G-DP-16QAM requires only 3 frequency slots (3×12.5 GHz). The same limits in BER, OSNR and power excursion have been applied here (Table 3.11) to train two different impairment aware modulation format and wavelength assignment algorithms: one algorithm considering BER and the other considering OSNR together with power excursion limits. Power excursion information is always included in the reward, penalizing large power excursions. Results are shown in the following paragraphs.

3.5.1 OSNR aware wavelength assignment

As for the fixed grid case, the RL algorithm has been trained considering OSNR and power excursion limits. Same value limits have been considered. Each time a channel is added (dropped), OSNR and power excursion per channel are calculated. If all the channels are above the OSNR threshold and below the power excursion threshold (for the 200G-DP-16QAM channels), the episode continues, sending the updated state information, the new request and the calculated reward (using the power excursion) based on the last update. On the opposite, if one or more of the channels are below the OSNR threshold or above the power excursion threshold (only for the 200G-DP-16QAM channels) the episode is terminated, sending a negative reward.

After training, blocking probability for different channel loads (20 %, 40 %, 60 %, 80 %) is

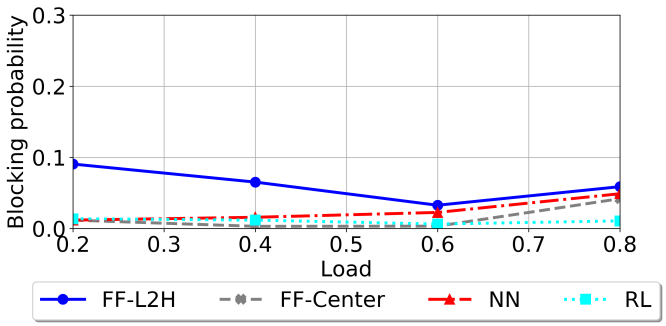

Figure 3.17 – Flexible grid: Blocking probability comparison for OSNR aware algorithm.

compared with the 3 same algorithms as before: (1) FF-L2H, (2) FF-Center, (3) NN. Results are shown in Fig. 3.17. Best results are obtained with the FF-Center and the RL algorithm, with the last one outperforming all of them for 20 % and 80 % channel load. Differently to the results obtained for the fixed grid, blocking probability monotonously increases with the channel load, as the 80 % channel load now suffers the consequences of spectrum fragmentation. Although these results cannot be directly compared to the ones obtained for the fixed grid scenario (two different environment models are used, one for the fixed and one for the flexible grid, therefore results should not be directly compared among them), in general it is possible to conclude that the use of flexible grid allows to reduce the blocking probability.

Figure 3.18 shows the channel allocation evolution when the RL algorithm is used, for the different channel loads (20 %, 40 %, 60 %, 80 %). In all of them, similar behaviour is observed. Channels are allocated in the lower frequencies, with lower power excursion due to amplifier characteristics (dynamic curve in Fig. 3.1b), leading to spectrum defragmentation. Regarding modulation, different from the fixed grid results selecting DP-QPSK for 100G requests, in the flexible grid scenario DP-16-QAM is predominantly preferred for both 100G and 200G requests. As 100G-DP-16QAM occupies less bandwidth in the flexible grid case, its usage allows to save spectrum. However, there are some exceptions. Due to the OSNR restriction, sometimes DP-QPSK is also assigned for the 100G and 200G requests. In fact, for the 20 % channel load, DP-QPSK is the predominant modulation format.

3.5.2 BER aware wavelength assignment

After OSNR together with optical power excursion, BER limits have been considered. Done as for the fixed grid scenario, an episode is terminated if at least one of the channels presents a BER above the pre-FEC BER threshold. Otherwise, the episode is continued, providing a reward dependent on the optical power excursion. As in the previous cases, blocking probability obtained after training the RL algorithm is compared to the other three methods previously defined: (1) FF-L2H, (2) FF-Center, (3) NN based. This time, illustrated in Fig. 3.19, RL algorithm is the best performing one, except for the 20 % channel load where FF-L2H is slightly better. When channel allocation using the RL algorithm is evaluated (Fig. 3.20), results

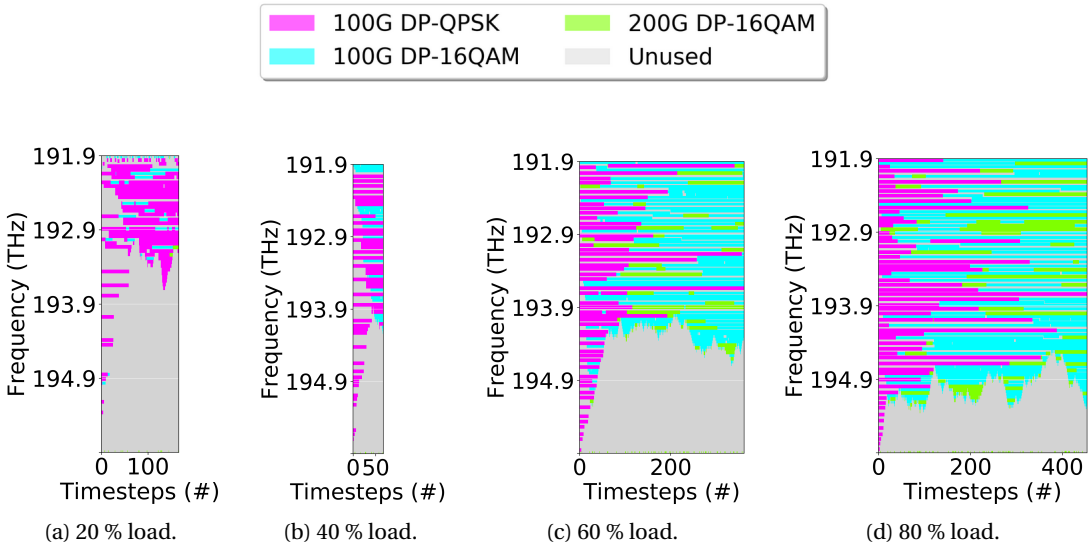

(a) 20 % load. (b) 40 % load. (c) 60 % load. (d) 80 % load.

Figure 3.18 – Flexible grid: Channel assignment evolution under RL-algorithm control for OSNR aware algorithm.

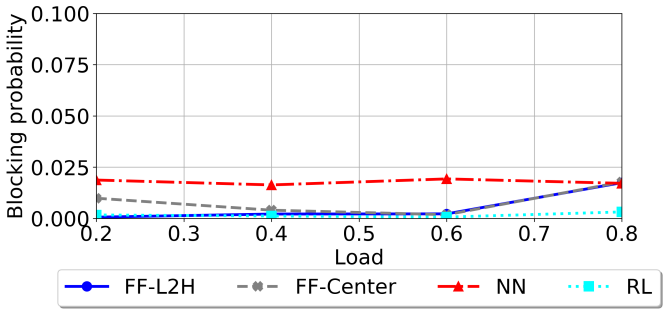

Figure 3.19 – Flexible grid: Blocking probability comparison for BER aware algorithm.

are very similar to the ones shown in Fig. 3.18 for the OSNR aware algorithm, with channels allocated in the lower part of the spectrum. However, in this case, DP-16-QAM is used almost exclusively as modulation format for both 100G and 200G requests, contributing to lower power excursion and spectrum saving.

3.6 Conclusions

In this chapter, impairment aware modulation format and wavelength assignment based on RL has been demonstrated. To this end, first RWA assignment problem has been presented. Required to work in transparent/translucent networks, IA-RWA algorithms have been introduced. In order to consider impairments, QoT estimation based on ML algorithms has become popular in the last years. As a first part of the work developed in this chapter, for a particular optical link developed in VPI, QoT models estimating power excursion and classifying wavelengths in terms of OSNR and BER have been implemented. Although better performance could

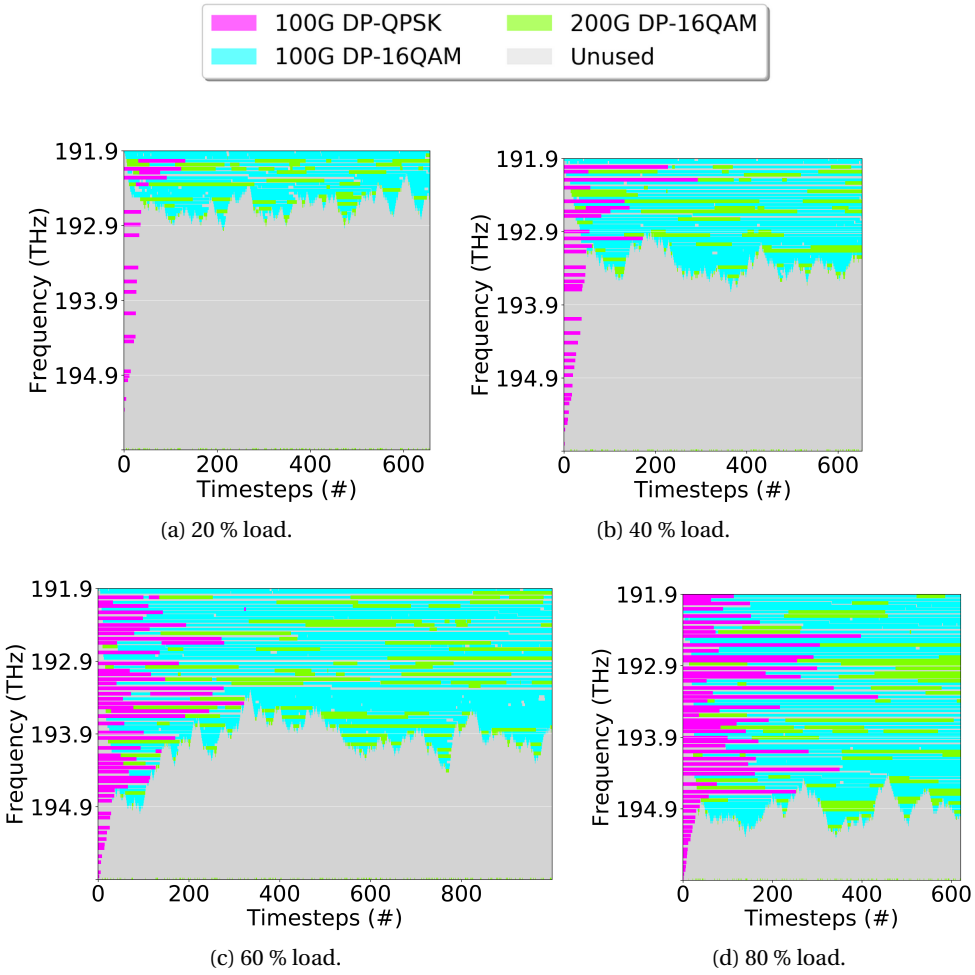

(a) 20 % load.

(b) 40 % load.

(c) 60 % load.

(d) 80 % load.

Figure 3.20 – Flexible grid: Channel occupation evolution under RL-algorithm control for BER aware algorithm.

have been obtained by increasing the training dataset size, the significance of optical power excursion as input feature to the OSNR and BER models has been demonstrated. In a second part, QoT models have been integrated in an environment receiving dynamic traffic requests used to train an RL algorithm. After training, the RL algorithm is able to assign modulation format and wavelength to channel requests, outperforming other heuristic methods in terms of blocking probability. As an example, for 80 % channel load, blocking probability reduction of 10 % and 81 % for fixed and flexible frequency grid have been achieved, respectively, with respect to the best-performing heuristic algorithm used for comparison. Besides performance, the presented algorithm also contributes to spectrum defragmentation, operating in an instantaneous manner after training. As in Chapter 2, this application can be integrated in an SDN-based optical network architecture (Fig. 3.21).

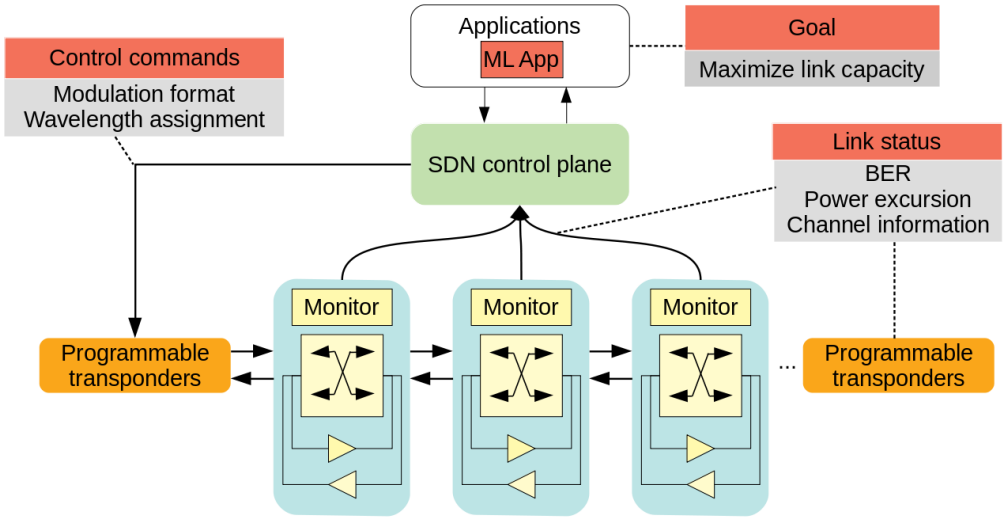

Figure 3.21 – Dynamic modulation format and wavelength assignment in SDN-based optical network architecture (based on [17]).

Part II

Coloured optical packet switching in the N-GREEN project

4 Experimental characterization of an SOA-based photonic integrated switch

With the aim of reducing cost and energy consumption, N-GREEN (New Generation of Routers for Energy Efficient Networks) project, funded by ANR (French National Research Agency), proposed a new node and network architecture based on WDM packet switching [256]. Two main innovations were introduced in the N-GREEN project: a WDM-slotted add/drop multiplexer (WSADM) and a ultra-high capacity backplane based on optical switches.

This chapter is focused on the WDM backplane. Operating on aggregated traffic at very high data rates, the proposed full-protected WDM backplane uses optical switching enabling internal channel capacities close to 1 Petabit/s, hardly feasible using only electronic technologies. Including load balancing capabilities, optical switch sizes of 4×4 and 16×16 have been considered, based on smaller 2×2 switching elements. Fundamental element in the WDM backplane architecture, a photonic-integrated 2×2 SOA switch has been designed and fabricated at III-V Lab (France) in the framework of the N-GREEN project. This chapter collects the work performed on the experimental characterization of the 2×2 switch, in order to determine its operating range in single channel and WDM configurations. All this experimental work was done outside Télécom SudParis, in Nokia Bell Labs (project leader), Télécom Paris and III-V Lab. Part of the experimental measurements were performed by myself whereas some others were performed in collaboration with the previous mentioned partners.

Section 4.1 provides an overview on optical switching technologies. Section 4.2 describes the N-GREEN project architecture along with its main innovations including the WDM backplane, made of 2×2 optical switches, object of this study. Once context has been provided, Section 4.3 reports on the experimental characterization of the 2×2 optical switch.

4.1 Optical switching overview

Many technologies and architectures have been investigated for optical switching. The simplest optical switching elements are the 1×2 (1 input, 2 outputs) or 2×2 (2 inputs, 2 outputs) modules. Larger switching matrices $M \times N$ are built by interconnection in cascade of the previous basic elements. These switching modules may be classified as digital or analog [156]. Digital switching elements have only two positions (on, off). Therefore, a $N \times N$ switching matrix made of 2×2 digital switching elements requires N^2 switching elements. Benes architecture is able to reduce the number of switching elements; however, this architecture may be blocking [257]. Analogue actuators allow to direct the light in different directions, reducing the number of switching elements in a $N \times N$ switching matrix to $2N$ at the expense of complexity. Besides optical matrices using digital switching elements or analogue actuators, Clos architecture, also based on smaller switching units, builds a $N \times N$ switch by using three stages, reducing the number of switching elements [258]. Regarding technologies, several criteria have been used to classify optical switching elements, being one of the most common, the physical effect exploited for switching operation [64], [259] which is used in the following:

- **Opto-mechanical switching:** Using the movement of a fiber or an optical component, the most common opto-mechanical switches are based on MEMS. Always relying on movement, some work on diffractive or interference effects [260], although most of them work directly on the reflective effect modifying light propagation direction. A typical structure consists of an array of micro-mirrors which movement is activated by an electrostatic or electromagnetic principle. Usually made of silicon substrate with a metal coating, micro-mirrors can be fabricated using micromachining technologies (bulk, surface or combination) [156], allowing to be batch-fabricated [14]. Typical architectures are: (1) 2D, with signals travelling in a 2D plane (Fig. 4.1a) and MEMS having only two positions (on, off) and (2) 3D, with signals travelling in a 3D space, with MEMS rotating in two axes. Although 2D architectures are easier to control, they require a larger number of micro-mirrors. For a $N \times N$ switch, N^2 micro-mirrors are arranged in a 2D structure whereas only N or $2N$ micro-mirrors are used in a 3D implementation. As a consequence, although 50×50 2D MEMS optical switches have been demonstrated [261] only 32×32 are commercially available [262], compared to the 320×320 3D MEMS optical switches already in the market [263].
- **Electro-optic switching**: Based on Pockels effect, which varies the refractive index when a voltage is applied, or carrier injection [156]. The most popular switches in this category are the guided wave electro-optic switches (Fig. 4.1b) based on Lithium Niobate (LiNbO3) substrates, also used for modulators, controlling the switching by deflection or diffraction. According to the switching curve, output optical power versus voltage, two types of LiNbO3 switches can be distinguished: (1) digital, switching state can be maintained in a voltage range, and (2) interferometric, several values for a switching voltage. Stability with regard to the drive voltage converts digital in the preferred ones [14]. Maximum commercial sizes are 8×8 and 1×16 on LiNbO3 [264], [265] and lead lanthanum

zirconate titanate (PLZT) [266], [267]. LCs based switches can also be included in this category [259]. Molecular alignment in LCs (state of matter with a rod-like molecular order intermediate between solids and liquids) can be modified by applying an electric field, altering optical properties, as polarization and birefringence. Polarization-based LC switches (Fig. 4.1c) require additional components, as polarization splitters and combiners, making polarization dependent loss a critical issue. Birefringence-based LC switches are usually referred as refractive-index-based LC switches, where switching is performed by transmission or total reflection driven by the refractive index changes in the LC cells. Compact architectures can be obtained with LCoS technology used for WSSs, commercially available [268].

- **Acousto-optic switching:** Waveguide switching category exploiting refractive index modulation by acoustic waves operating on beam deflection or collinear mode conversion [64]. As in electro-optic switches, LiNbO3 is most popular material used for this type of switches. Acousto-optic Q-switches for lasers are available in the market [269].

- **Thermo-optic switching:** This waveguide based category utilizes temperature dependence of the refractive index in materials as polymers [14]. Similar to electro-optic switches, thermo-optic switches can be built as digital switches, based on mode coupling or interferometric structures. Thermo-optic switches up to 16×16 ports are commercially available [270].

- **Magneto-optic switching**: Type under investigation, magneto-optic switches are based on Faraday effect. Advances in magneto-optic materials as bismuth-substituted iron garnets and orthoferrites have increased the interest in this type of technology [259]. Maximum commercial sizes up to 16×16 are available [271].

- **Switching based on nonlinear effects:** Due to Kerr effect, changes in the refractive index of a material occur in response to applied electric fields [259]. As the light propagates, it undergoes a phase shift due to the refractive index change produced in the interaction with the optical nonlinear medium (fibers and SOAs). Switching can be performed by using an optical gate at the output of the medium. Some types of nonlinear effects based switches include: nonlinear optical mirrors, Mach–Zehnder interferometers, ultrafast nonlinear interferometers and non-interferometric-based switches.

- **Amplifier based switching:** Although fiber based amplifiers can be used, SOAs are the preferred option. SOA structure (Appendix C), similar to a laser one, includes an active region in between n-type and p-type cladding layers. Amplification is produced by stimulated emission when the light passes through the active region. In order to use SOAs for switching purposes, working as gates, control can be performed electrically or optically. The electrical control is based on bias current, operating the SOA in the linear regime (Fig. 4.1d). On the contrary, using optical control the SOA is operated in the nonlinear regime by injecting auxiliary light beams. Two types of nonlinear effects can be considered: new frequency components generation (FWM) and alteration of a

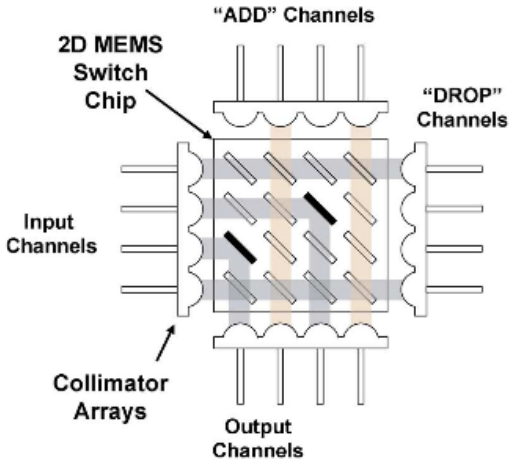

(a) Schematic of 2-D MEMS optical switch [273].

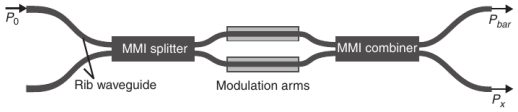

(b) Schematic of a 2 × 2 electro-optic switch [259].

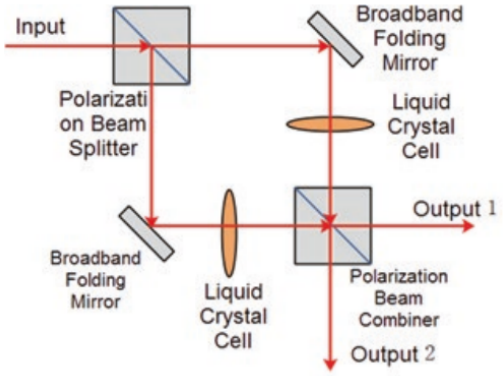

(c) Structure of 1 × 2 LC optical switch [14].

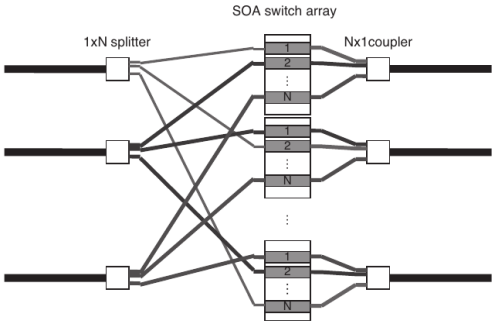

(d) SOA broadcast and select switch architecture [259].

Figure 4.1 – Optical switching technologies: (a) Schematic of 2-D MEMS optical switch [273], (b) Schematic of a 2 × 2 electro-optic switch [259] (c) Structure of 1 × 2 LC optical switch [14] and (d) SOA broadcast and select switch architecture [259].

property as (polarization, phase or amplitude). An element sensitive to the modified property produces the switching (polarization beam splitter, SOA interferometer, AWG). SOAs targeting switching applications, working as ON/OFF gates, are commercially available with very high switching speed < 1 ns [272].

Table 4.1 [14] shows a comparison of most popular commercial optical switch technologies based on several aspects: switching speed, insertion loss, power efficiency, scalability, reliability, implementation cost and application. MEMS based switches are characterized by a low switching speed; suitable for circuit switching, they are inadequate for packet switching. LC switches, also with low switching speed, offer high power efficiency but with a lower scalability, being appropriate ROADMs or WSSs. Thermo-optic switches present a higher power consumption but also a high reliability, making them adequate for protection switching. Finally,

	MEMs	LC (LCoS)	Electro-optic	SOA	Thermo-optic
Switching speed	10 – 20 ms	100 ms	~ ns	~ ns	5 – 10 ms
Insertion loss	Medium	High	High	Low	Low
Power efficiency	Medium	High	High	Low	Low
Scalability	Large 320 × 320	Medium 1 × 20	Medium 32 × 32	Medium 16 × 16	Small 8 × 8
Reliability	Low	High	High	Medium	High
Implementation cost	Medium	Low	High	High	Low
Application	OCS, WSS	ROADM, protection switching, WSS	OPS, optical modulators	OPS, WSS	Protection switching

Table 4.1 – Comparison of commercial optical switching technologies [14].

electro-optic and SOA based switches with high switching speed are the best candidates for packet switching although limited in scalability. SOA based switches have been the option selected in the N-GREEN project, introduced in Section 4.2.

4.1.1 Future optical interconnections

Typical interconnections at data centers are still based on cascade of electrical switches. This architecture produces difficulties [14]: (1) inefficiencies in terms of latency, throughput and power consumption, (2) limits in the transmitted data rate imposed by the ratio of the length of the electrical interconnection to the total cross-sectional dimension $\sqrt{(}A)$ of the interconnect wiring [274], meaning that the transmission distance limit for 25 Gb/s for a typical electrical interconnect is less than 1 cm [14], (3) inability to reconfigure in order to absorb traffic peaks.

On the one hand, SDN for reconfiguration is being considered as potential candidate to solve reconfigurability limitations. On the other hand, as investigated in several works [275]–[277], optical interconnections appear to be a suitable choice to lower energy consumption, outperforming electrical interconnects also in transmission length and offered bandwidth. However, the lack of optical RAM limits its application. Hybrid solutions making use of photonics and electronics appear to be the optimal successors of electrical interconnects [278], [279], with optical-electrical printed circuit boards [280] connected to optical-electrical-backplanes, and reconfigurable optical switches as a key technology [281].

4.2 N-GREEN project

Funded by ANR (French National Research Agency), N-GREEN project started in 2016 for a 3-year duration. Partners contributing to N-GREEN project were: Nokia Bell Labs (project

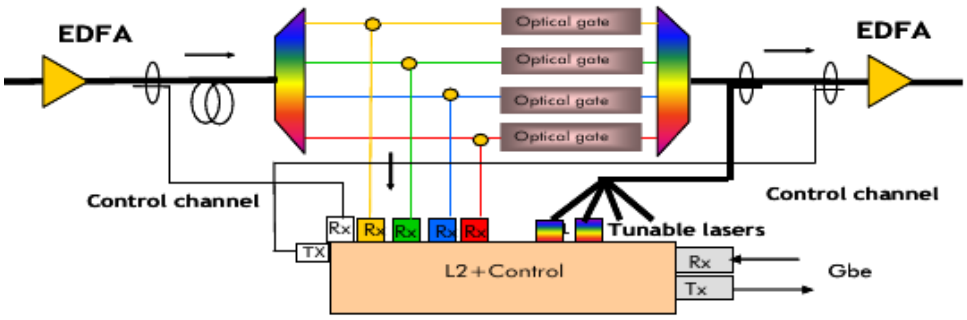

Figure 4.2 – Scheme of the POADM [284].

leader), Télécom SudParis, Télécom Paris, IMT Atlantique, Université de Versailles and III-V Lab, all of them in France.

Some of the N-GREEN predecessors were the European project DAVID and the ECOFRAME project. European project DAVID considered the usage of out-band headers (in a separeted channel) for the metro ring and in-band for the backbone [282], as synchronization between header and payload channels is simpler in ring networks. Used in N-GREEN project, out-band labels allow to separate control and switching planes.

Similar to DAVID project, out-band labels have also been utilized in the ECOFRAME project in a metro-ring architecture based on optical slot switching technology [283]–[285]. Considering a slotted ring with 10 μs timeslot, the packet optical add/drop multiplexer (POADM) (Fig. 4.2), precursor of the N-GREEN concept which will be shown afterwards, used optical gates based on SOAs in order to let pass or block optical packets at sub-wavelength granularity. Combiners and splitters were available to add and drop the packets, requiring a tuneable transceiver for adding or dropping a packet at any available wavelength.

To cut down the cost and the energy consumption, N-GREEN project came up with the idea of a new network architecture and node design, based on WDM packet switching [256]. A WDM packet, also called coloured optical packet, as introduced in [286], is formed by the aggregation of data units (e.g. Ethernet frames) in a container, which is afterwards distributed in several wavelengths. As exposed in [287], this strategy presents several benefits as reductions in cost and power consumption by exploiting optical integration using WDM transceivers. Two main innovations were introduced in the project:

- WSADM: Based on a POADM structure, as a novelty, it operates on WDM packets. Each WDM packet occupies one timeslot, composed by 10 times 1 μs timeslot over 10 wavelengths.

- Ultra-High Capacity WDM Backplane: Working on WDM packets and based on optical switching, the WDM backplane proposed in N-GREEN is able to offer internal channel

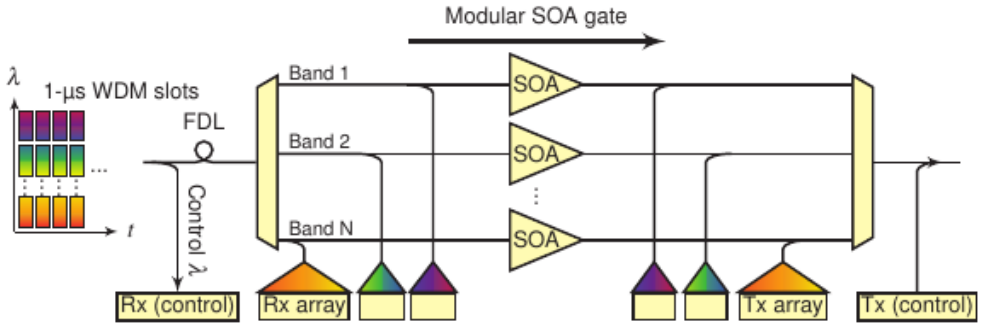

Figure 4.3 – Scheme of the WSADM [256].

capacities close to 1 Petabit/s.

4.2.1 WSADM

At each optical timeslot, the WSADM manages the WDM packet stream offering several possibilities: (1) drop and erase, (2) drop and continue and (3) drop and add. Figure 4.3 shows its general structure. N-GREEN project considers an out-band labeling approach, with a dedicated control channel in a separate wavelength. As a first step, an optical coupler at the WSADM input establishes a second path dedicated to the control channel recovery and header processing tasks. To do this, first, the control channel is selected in the optical domain rejecting any other wavelengths. After O/E conversion, synchronization and data recovery, the header is ready to be processed. Depending on the information extracted from the header, a control board (not included in the figure), configures the WSADM's elements in order to execute one of previous functionalities (drop and erase, drop and continue or drop and add).

Coming back to the main optical path in Fig. 4.3, header processing time is absorbed by an FDL connected to the optical coupler's output. In order to operate at waveband level, a waveband demultiplexer is used with each output connected to an SOA acting as optical gate. Depending on the previously extracted header information, the SOA is configured to block or let pass (optical bypass) the WDM packet. For the dropping functionality in each subband, before the optical gate, a splitter directs the WDM packets to the receivers. In a similar way, for the adding functionality, a combiner allows to inject WDM packets generated at the transmitters. Finally, subbands are multiplexed and the control channel is reinserted by means of an optical coupler.

Note that in order to build the WDM packets, a buffer has to previously store the packets coming from the line cards. A shift register is then used to convert the 10 μs series data into parallel data in 10 wavelengths by 1 μs.

By exploiting WDM, reducing the frequency in the electrical interfaces, a simpler and less power-consuming node is proposed in N-GREEN. Also, relying on a simpler node architecture (e.g. using one SOA per waveband instead of one SOA per wavelength) cost is cut down.

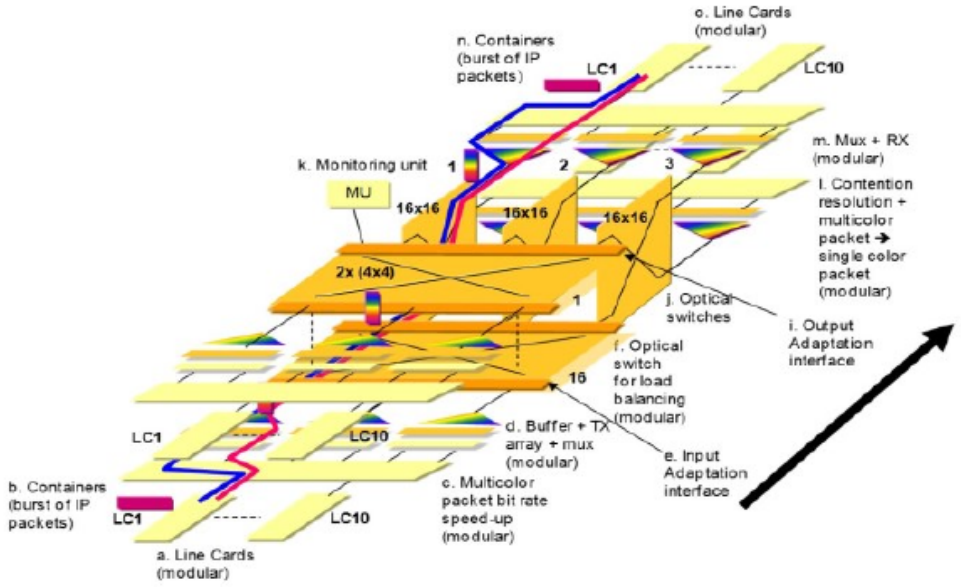

Figure 4.4 – Scheme of the WDM backplane [287].

4.2.2 Ultra-High Capacity WDM backplane

A hybrid switch fabric is proposed in the N-GREEN project in order to reduce the energy consumption compared to the traditional electrical backplane included in switch routers.

Similar to the WSADM, data aggregation in slots of 10 μs is the first step. However, the backplane manages higher data rates than the WSADM, slots of 10 μs at 1 Tb/s are considered. WDM packets are built using a shift register to redistribute the data over 10 buffers, corresponding to the 10 wavelengths. Contention resolution is addressed by the buffer usage.

As illustrated in Fig. 4.4, when the control board acting as scheduler, triggers a WDM packet dispatch, the WDM packet is sent to a first stage $1+1$ 4×4 WDM switch used for load balancing, including protection in case of failure. In the next step, the WDM packet is routed to one of the 3 16×16 optical switches available in parallel, keeping a load of 33.33 % in each of three switches. With this scheme, in case of failure of one of the switches, traffic is routed using the other 2, guaranteeing the protection. Finally, WDM packets are stored again in buffers in order to retrieve the 10 μs slot which is processed at the client.

4.2.3 Network scenarios

N-GREEN project considers two main network scenarios: metro and core network. At the metro network, a bidirectional ring topology, working in a timeslot basis is considered. As indicated before, each timeslot of 1 μs carries one WDM packet distributed over 10 wavelengths. Slot assignment is communicated in the dedicated control channel. Two types of nodes are available in the metro network:

SOA	Input	Output
SOA-1	2	1
SOA-2	1	1
SOA-3	1	2
SOA-4	2	2

Table 4.2 – Switch correspondence among SOA, input and output.

- The metro node belongs only to the ring. The main building block is the WSADM, duplicated in each direction of the double ring in order to protect the network in the event of a fiber cut. Apart from the WSADM, a control board and data board centralizing the add and drop traffic are part of the metro node.

- The edge node belongs to the metro and core networks. It terminates the traffic from the ring, avoiding resonances. Besides, it aggregates packets from the metro network at 10 Gb/s per wavelength to the core network at 100 Gb/s per wavelength.

At the core network, the network topology can be a ring, an interconnection of rings or a mesh topology. The N-GREEN core node is able to switch between different buses. At the node, a data board aggregates the traffic at 1 Tb/s, creating WDM packets at 10 Tb/s (1 Tb/s on 10 wavelengths). This traffic is switched at the hybrid backplane, with a total internal switching capacity of 16×10 Tb/s$\times 3 \times 2 = 960$ Tb/s, nearly 1 Petabit/s.

4.3 Experimental characterization of the 2 x 2 N-GREEN switch

The optical switch is the key element in the proposed WDM backplane. The 4×4 and 16×16 optical switches are composed by smaller 2×2 switching elements, as the photonic-integrated 2×2 SOA switch fabricated at III-V Lab (France) in the framework of the N-GREEN project (Fig. 4.5a). Reference element, the section is focused on its experimental characterization.

The scheme of the 2×2 SOA switch is shown in Fig. 4.5b. Each of the two inputs (*Input-1* and *Input-2* in Fig. 4.5b) is connected to a 3-dB coupler in order to create the two possible paths to the two possible outputs. The switching functionality, forwarding (optical bypass) or blocking packets, is performed by 4 SOAs acting as optical gates. Signal coming out from the 4 SOAs are combined in the two available outputs (*Output-1* and *Output-2* in Fig. 4.5b). Table 4.2 shows the correspondence among SOA, input and output according to the Fig. 4.5b.

Experimental characterization presented here considered different aspects: static and dynamic. Dynamic characterization includes two distinctive scenarios: (1) continuous mode at 128 Gb/s DP-QPSK, (2) packet mode at ~ 10 Gb/s OOK. Results are presented in the next paragraphs.

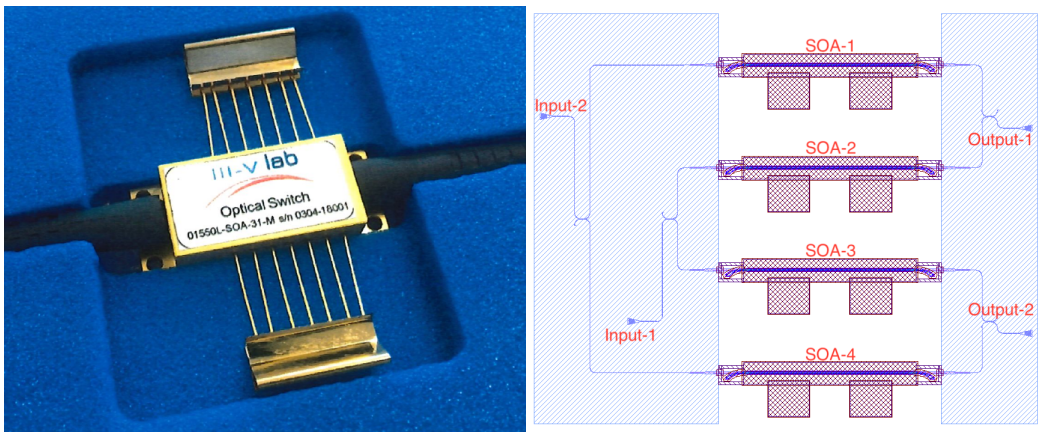

(a) Integrated 2 × 2 switch. (b) Scheme of the 2 × 2 switch.

Figure 4.5 – Image (a) and scheme (b) of the 2 × 2 switch.

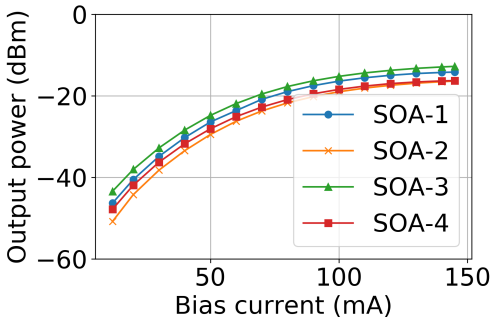

Figure 4.6 – Output power for different bias current.

4.3.1 Static characterization

Without injecting an input signal, only connecting the power meter to the output of the switch, the ASE noise power was measured for different bias currents. Results are shown in Fig. 4.6.

SOA comparison

A static characterization of the switch's fiber-to-fiber gain $G = P_{out}/P_{in}$ at different input optical power (P_{in}) values was performed for each SOA by injecting a continuous-wave laser at $\lambda_0 = 1542$ nm. A VOA and a polarization controller (PC) were used to respectively adjust the power and polarization of the input signal. The output power was measured using an OSA. Results are shown in Fig. 4.7a. As can be seen, in the small signal region, the switch presents a maximum fiber-to-fiber gain, including the internal switch coupling losses, between 0 and −2 dB depending on the given SOA. The gain saturation occurs for an input power between −3 dBm and 0 dBm for all the SOAs in the 2 × 2 switch. Above this level, in the saturation region, the gain decreases sharply.

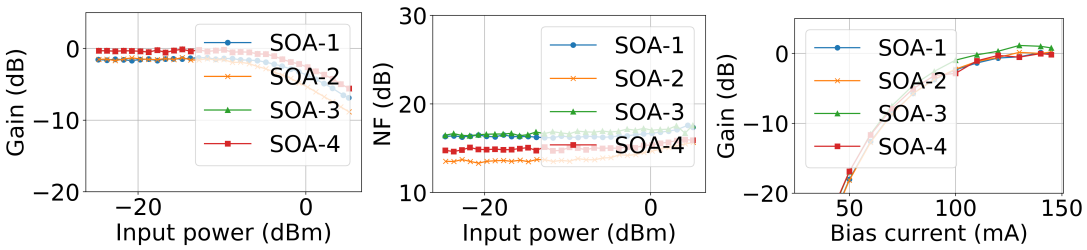

(a) Fiber-to-fiber gain with respect to input power.

(b) NF with respect to input power.

(c) Fiber-to-fiber gain with respect to bias current.

Figure 4.7 – Static Characterization - SOA comparison: (a) Fiber-to-fiber gain with respect to input power, (b) NF with respect to input power and (c) Fiber-to-fiber gain with respect to bias current.

The corresponding NF, illustrated in Fig. 4.7b, was calculated based on optical source-substraction method [288]. According to it, NF is calculated using:

$$NF = \frac{P_{ASE}}{GhvB_0} + \frac{1}{G} - \frac{P_{SSE}}{GhvB_0}, \tag{4.1}$$

where:

- v: Signal frequency.
- G: Gain at the signal frequency v, previously measured.
- P_{ASE}: Noise spectral density, out-band measure.
- P_{SSE}: Source spontaneous spectral density, measured during calibration, bypassing the switch.
- B_0: bandwidth resolution OSA.

Using the same setup, but fixing the input power to −25 dBm, Fig. 4.7c shows the fiber-to-fiber gain measured at different bias currents. For low bias current, the injected signal is absorbed and there is no amplification. However, above the transparency current, the injected signal produces stimulated emission being therefore amplified.

As the performance of the 4 SOAs is comparable, only one SOA is used in the subsequent experimental work.

Wavelength dependency

The same measurements described previously were repeated in order to compare fiber-to-fiber gain and NF for two different wavelengths $\lambda_0 = 1542$ nm and $\lambda_0 = 1550$ nm. From these

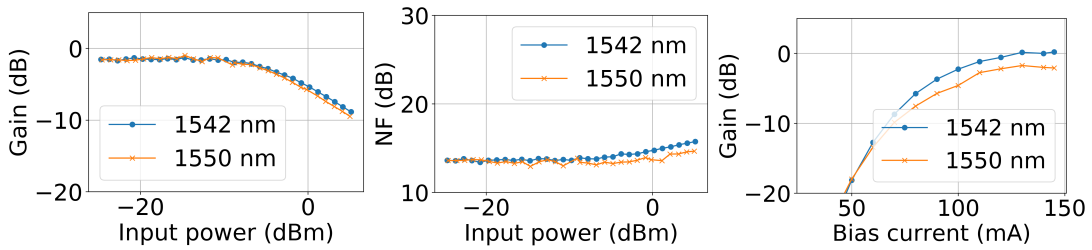

(a) Fiber-to-fiber gain with respect to input power.

(b) NF with respect to input power.

(c) Fiber-to-fiber gain with respect to bias current.

Figure 4.8 – Static Characterization - Wavelength comparison: (a) Fiber-to-fiber gain with respect to input power, (b) NF with respect to input power and (c) Fiber-to-fiber gain with respect to bias current.

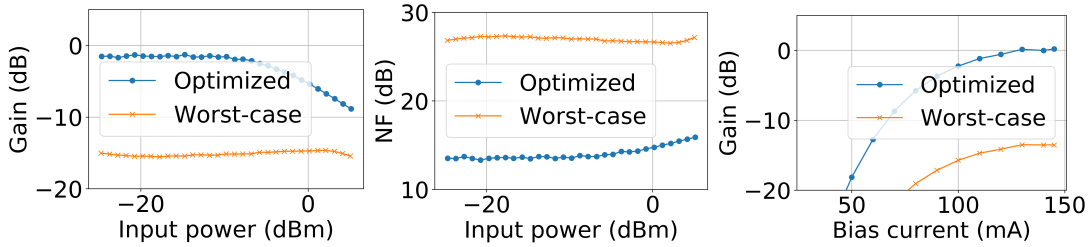

(a) Fiber-to-fiber gain with respect to input power.

(b) NF with respect to input power.

(c) Fiber-to-fiber gain with respect to bias current.

Figure 4.9 – Static Characterization - Polarization comparison: (a) Fiber-to-fiber gain with respect to input power, (b) NF with respect to input power and (c) Fiber-to-fiber gain with respect to bias current.

results shown in Fig. 4.8, one can see that the behavior for these two wavelengths is quite close.

Polarization dependency

Polarization dependency, critical parameter in SOAs, was assessed repeating the measurements for two different input signal polarizations: optimum polarization in order to achieve maximum output power, and worst-case polarization minimizing the output power. Results in Fig. 4.9 illustrates how critical it is the polarization, which is always optimized in the measurements performed for the dynamic characterization in the next section.

4.3.2 Dynamic characterization

Dynamic characterization was carried out in two different testbeds:

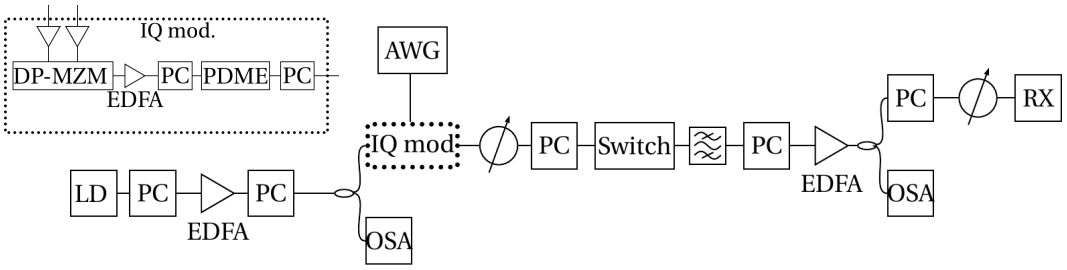

Figure 4.10 – Setup continuous mode single ch. at 128 Gb/s DP-QPSK (Télécom Paris). In the figure: arbitrary waveform generator (AWG), dual polarization-Mach Zehnder modulator (DP-MZM), IQ modulator (IQ mod.), laser diode (LD), optical spectrum analyzer (OSA), polarization division multiplexer emulator (PDME), polarization controller (PC), receiver (RX).

- Continuous mode at 128 Gb/s DP-QPSK (Télécom Paris).
- Packet mode at ~ 10 Gb/s OOK (Nokia Bell Labs).

Considering the switch use-case scenario is as part of the backplane, an optimal testbed would consider packet switching mode at high data rate. Two scenarios were examined: one oriented towards high data rate and the other towards packet mode. Detailed information is provided in the next paragraphs. During the measurements polarization adjustment was crucial. Note that crosstalk in SOAs is not critical [1].

Continuous mode at 128 Gb/s DP-QPSK

Figure 4.10 illustrates a scheme of the setup used for the switch dynamic characterization. The signal, 64 Gb/s QPSK, is generated in Matlab and downloaded to the arbitrary waveform generator (AWG in Fig. 4.10) with a sampling rate of 32 Gsamples/s. Inside the IQ-modulator (IQ mod.), this signal drives a dual polarization-Mach Zehnder modulator (DP-MZM), which output is amplified by an EDFA. Using a polarization division multiplexer emulator (PDME), a DP-QPSK signal of 128 Gb/s is generated with the polarization adjusted using a PC. After the IQ-modulator, an optical attenuator and a PC allowed to control the input power and polarization of the optical input signal to the switch. The switch output is filtered and amplified before reaching an optical coupler which sends 10% of the received signal to an OSA and the other 90% to a coherent receiver after adjusting the polarization and controlling the power using, respectively, a PC and a VOA. Finally, the signal is captured by a digital sampling oscilloscope (DSO) of 64 Gsamples/s. After the signal is captured by the DSO, offline digital signal processing (frequency offset estimation, channel equalizer, phase offset estimation) is carried out in Matlab. Note that to avoid frequency offset at the receiver, the same laser source, after controlling its polarization, being amplified and linearly polarized, is used as local oscillator at the receiver.

[1] With Mach–Zehnder interferometers, we are closer to 15 dB (in dynamic range) than 45 dB. With SOAs the crosstalk is not critical.

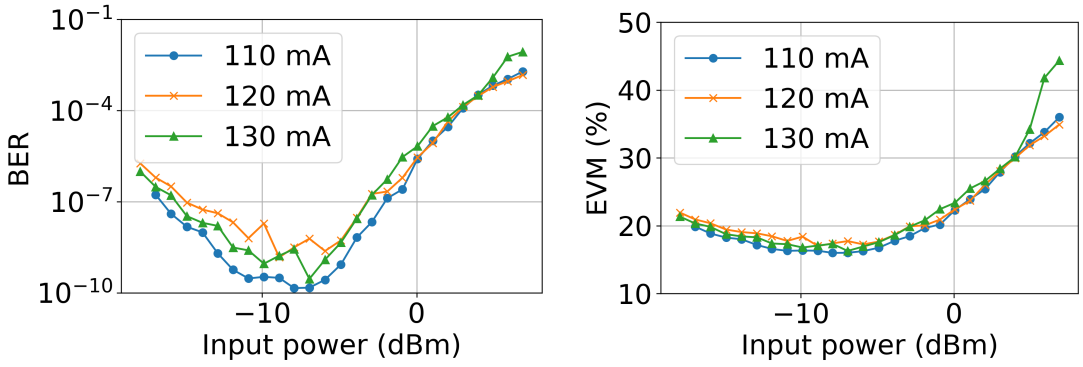

(a) BER for different input powers.

(b) EVM for different input powers.

Figure 4.11 – Dynamic Characterization continuous mode, single ch. 128 Gb/s DP-QPSK: (a) BER, (b) EVM with respect to input power.

Bias Current (mA)	**Optimum Channel Input Power (dBm)**	**EVM (%)**	**BER**
110	-7.93	15.99	1.4×10^{-10}
120	-8.89	17.01	1.48×10^{-9}
130	-6.94	16.28	2.89×10^{-10}

Table 4.3 – Dynamic Characterization continuous mode, single ch. 128 Gb/s DP-QPSK: Summary.

For different input powers, EVM was measured, and BER estimated from the EVM measurements [289]. Measurements were done for 3 different bias currents: 110, 120 and 130 mA. Figures 4.11a and 4.11b show the obtained results. For low input powers the performance is limited by the noise. As the power increases, the BER (EVM) decreases, until an optimum value is reached. For larger powers, performance starts deteriorating, due to gain saturation. Similar results were obtained for the three different bias currents considered. Table 4.3 summarises the optimum input powers for each of the three bias currents. Considering a BER threshold of 10^{-9}, error free transmission can be achieved.

Received constellations for three different input powers, measured during the characterization (Fig. 4.11), −17.88, −6.94, and 1.04 dBm, using the 110 mA bias current are plotted in Fig. 4.12. The first constellation (Fig. 4.12a) with the lowest of the input powers (−17.88 dBm) is noisy, showing a symmetrical broadening of the constellation symbols, suffering from a low OSNR. For a higher input power (Fig. 4.12b), the constellation is less noisy, having a higher quality. However, for even higher input power (Fig. 4.12c), entering the saturation regime, constellation points are rotated due to the refractive index change in the SOA producing a nonlinear phase change [290].

After the single channel measurements, the next step was WDM, closer to the use case for

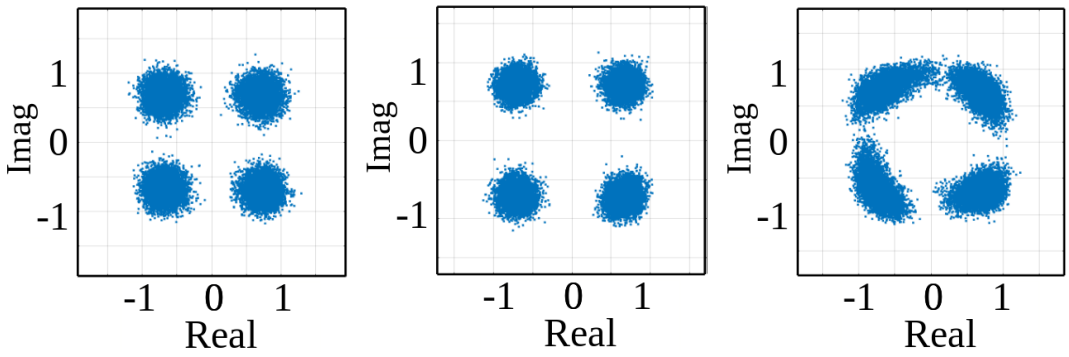

(a) Input power −17.88 dBm. (b) Input power −6.94 dBm. (c) Input power 1.04 dBm.

Figure 4.12 – Dynamic Characterization continuous mode, single ch. 128 Gb/s DP-QPSK: Constellations.

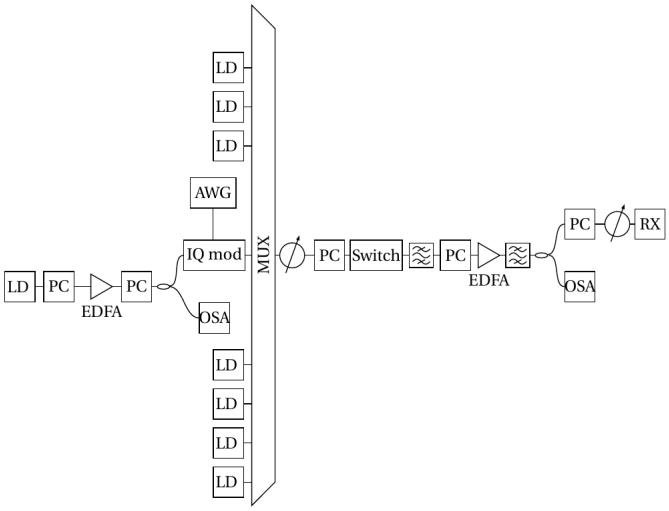

Figure 4.13 – Setup continuous mode WDM 128 Gbps DP-QPSK (Télécom Paris). In the figure: arbitrary waveform generator (AWG), IQ modulator (IQ mod.), laser diode (LD), multiplexer (MUX), optical spectrum analyzer (OSA), polarization controller (PC), receiver (RX).

which the switch was designed. The setup is shown in Fig. 4.13. Compared to the single channel setup in Fig. 4.10), few modifications were introduced:

- Seven laser signals are multiplexed with the optical modulated signal. The wavelength of the modulated signal was 1542 nm. Using a non-uniform frequency spacing, all 8 wavelengths are indicated in Table 4.4.
- An optical band pass filter is included before the receiver to select the modulated signal.

As for the single channel case presented before, BER and EVM were measured for different input power values, also considering the same three bias currents (110, 120, 130 mA). Results

λ_1 (nm)	λ_2 (nm)	λ_3 (nm)	λ_4 (nm)	λ_5 (nm)	λ_6 (nm)	λ_7 (nm)	λ_8 (nm)
1539.371	1540.953	1541.746	1542.0	1542.539	1543.333	1544.128	1544.924

Table 4.4 – Dynamic Characterization continuous mode, WDM 128 Gb/s DP-QPSK: Wavelengths.

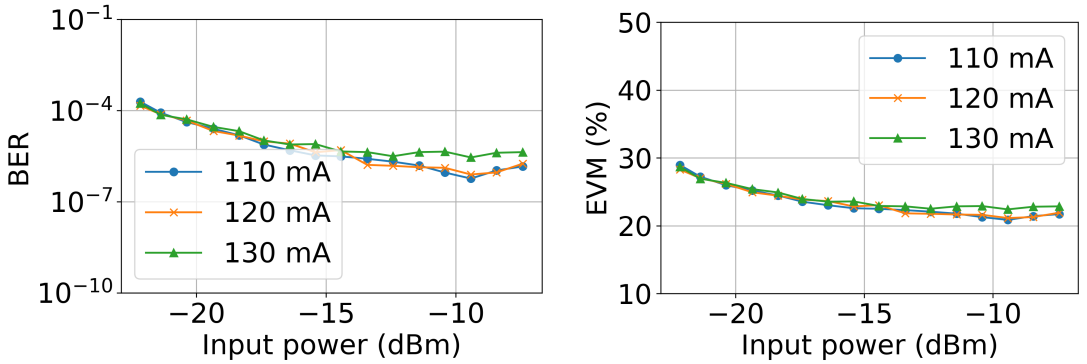

(a) BER for different input powers.

(b) EVM for different input powers.

Figure 4.14 – Dynamic Characterization continuous mode, WDM 128 Gb/s DP-QPSK: (a) BER, (b) EVM with respect to input power.

are shown in Fig. 4.14. Although the behaviour is the same, with performance limited at low powers by the noise and at high powers for gain saturation, in this case, the optimum powers are slightly lower (Table 4.5) due to nonlinearities. Contrarily to the single channel case, the BER threshold of 10^{-9} could not be achieved in the WDM scenario, suggesting that FEC techniques are needed.

Packet mode at 10 Gb/s DP-QPSK

In a different testbed at Nokia Bell Labs, a separate dynamic characterization of the switch was performed, this time in a packet transmission mode [13]. Again two different scenarios were considered: single channel and WDM.

Setup for single channel case is illustrated in Fig. 4.15. Data at 9.95328 Gb/s using NRZ-

Bias Current (mA)	**Optimum Input Power (dBm)**	**EVM (%)**	**BER**
110	-9.42	20.86	5.8×10^{-7}
120	-9.42	21.13	7.88×10^{-7}
130	-9.42	22.41	2.87×10^{-6}

Table 4.5 – Dynamic Characterization continuous mode, WDM 128 Gb/s DP-QPSK: Summary.

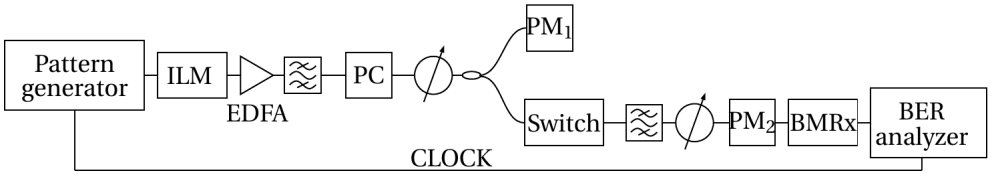

Figure 4.15 – Setup packet mode single ch. at 10 Gb/s (Nokia Bell Labs, France). In the figure: burst mode receiver (BMRx), integrated laser modulator (ILM), polarization controller (PC), power meter (PM).

Data rate	9.95328 Gb/s
Modulation	NRZ-OOK
Frame format	8 slots of 10240 bits
Preamble format	Two 12.8 ns clock patterns and one pattern of 1's between the two clocks
Guard band format	Series of 0's of 20 ns
ILM Maximum optical power	3 dBm
ILM extinction ratio	10.5 dB

Table 4.6 – Parameters for packetized data.

OOK (PRBS-2^7-1) modulates an integrated laser modulator (ILM) at $\lambda_0 = 1549.3$ nm. After amplification and filtering, the signal polarization is optimized (PC) to obtain maximum output optical power out of the switch. Then, a VOA allows to control the input power injected in the switch, passing through SOA-3 (Fig: 4.5b). The output of the switch is connected to a band-pass filter centered at λ_0 removing the ASE noise introduced by the amplifiers. Another VOA varies the received power P_{rx} (at PM_2) at the BMRx [291]. The BMRx has a clock recovery time of < 4 ns, fast-power-dynamic-range of 5 dB and sensitivity of −17 dBm at BER of 10^{-9}. Finally, the BER is measured with a BER analyzer on the payload of the optical slots. Some more detailed parameters can be found in Table 4.6.

In the WDM case, shown in Fig. 4.16, the channel at λ_0 is coupled with multiple channels ($\lambda_1 - \lambda_8$ in Table 4.7) which are separated by 0.8 nm and injected at 1.2 dBm optical power per channel. Similar as before, the switch launched optical power P_{in} is varied using the VOA. For each P_{in}, the PC is adjusted maximizing switch output optical power. The received power P_{rx} at the BMRx (at PM_2) is modified with the VOA. Again, the BER is measured with a BER analyzer on the payload of the optical slots.

For both scenarios (single channel and WDM), in a first set of measurements, a series of input

λ_1 (nm)	λ_2 (nm)	λ_3 (nm)	λ_4 (nm)	λ_5 (nm)	λ_6 (nm)	λ_7 (nm)	λ_8 (nm)
1546.12	1547.72	1548.51	1550.92	1551.72	1552.52	1554.13	1554.94

Table 4.7 – WDM wavelengths used for dynamic characterization.

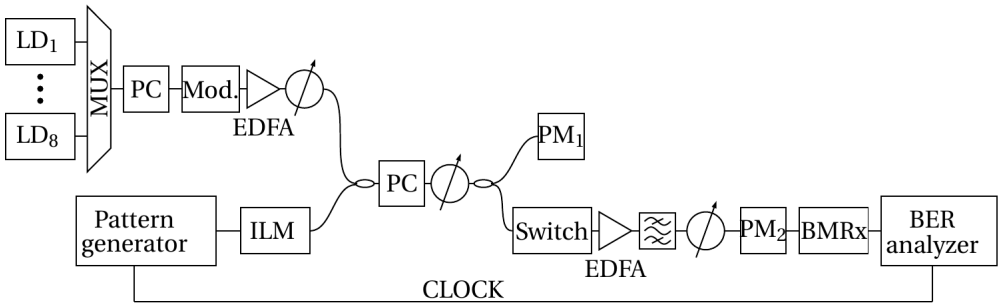

Figure 4.16 – Setup packet mode WDM at 10 Gb/s (Nokia Bell Labs, France). In the figure: burst mode receiver (BMRx), integrated laser modulator (ILM), laser diode (LD), modulator (mod.), multiplexer (MUX), polarization controller (PC), power meter (PM).

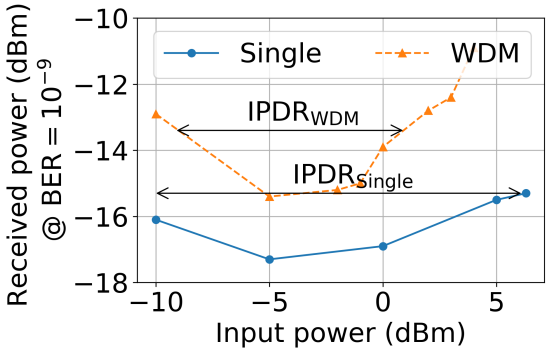

Figure 4.17 – Dynamic characterization: P_{rx} vs. P_{in} at a BER of 10^{-9} for single and WDM cases.

powers P_{in} was evaluated. For each input power, the received power P_{rx} was adjusted in order to keep the BER fixed at 10^{-9}. Results are illustrated in Fig. 4.17. The measured input power dynamic range (IPDR), defined as the range of P_{in} for which P_{rx} remains constant within a penalty of 2 dB, is 16 dB for the single channel case. In the WDM scenario, due to the presence of nonlinear effects [292], the IPDR is reduced to 10 dB, still allowing a sufficient operation range.

In a second set of measurements, while the input power P_{in} was kept constant, the P_{rx} was varied and the BER measured at the BER analyzer. Figure 4.18 shows the measured BER vs. P_{rx} obtained in this process, repeated for several input power values in the single channel and WDM scenarios. The B2B curve, measured bypassing the switch for λ_0, is also plotted for reference at $P_{in} = 0$ dBm. For the single channel scenario, BER of 10^{-9} could be achieved with a power penalty below 1.2 dB in comparison to the B2B reference measurement. For WDM, the power penalty increases, moderately, to 2.8 dB at $P_{in} = 0$ dBm, 3.7 dB at $P_{in} = 2$ dBm and 4.04 dB at $P_{in} = 4$ dBm. When compared to the single channel scenario, also larger differences between curves can be observed due to the nonlinear effects produced (on the main channel λ_0) from other channels.

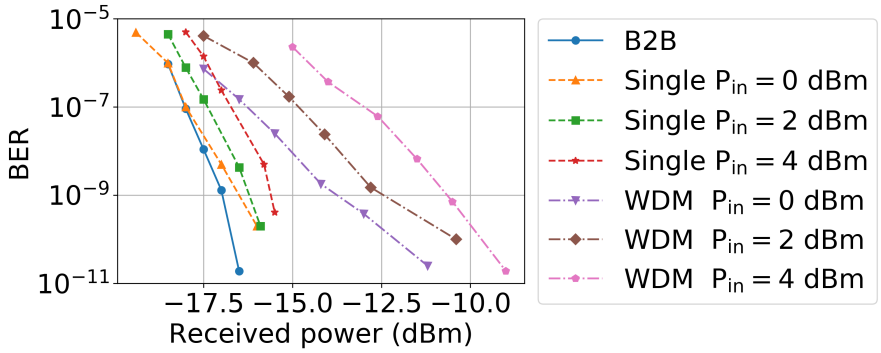

Figure 4.18 – Dynamic characterization: BER vs. P_{rx} at different P_{in} for B2B, single channel and WDM cases.

4.4 Conclusions

At the optical layer, evolution from circuit switching to packet switching offers the possibility to more efficiently use the spectrum resources. Since all-optical packet switching presents still some unsolved issues, as optical buffering, hybrid optical-electrical approaches appear to be the medium-term solutions exploiting the capabilities in both domains. In this context, N-GREEN project proposed a new network architecture based on WDM packets. The validation of the proposed energy-efficient node together with its adoption for a Nokia product are the major outcomes of the project.

More in detail, N-GREEN project included two main innovations: a WSADM and a WDM backplane based on optical switching, which has been the main subject in this chapter. This hybrid WDM backplane with a total switch capacity of 1 Pb/s, achieved thanks to the use of 4×4 and 16×16 optical switches is made of smaller 2×2 switching elements. To this end, developed and fabricated in the N-GREEN project, a 2×2 SOA-based photonic integrated switch was experimentally characterized. Through its experimental characterization, its capability to work on large IPDR has been demonstrated, for both single channel and WDM scenarios. Penalties introduced by nonlinearities when operating in WDM configuration are tolerable. These promising capabilities, large IPDR and possibility to work at high data rates by including FEC, allow to envisage a 16×16 switch configuration based on a cascade of 7 2×2 switches using a Benes architecture.

Conclusions and perspectives

Apart from exploiting physical dimensions, in order to cope with the traffic requirements, optical networks will improve in dynamism and flexibility. Under these conditions, network management will become more complex requiring to control several aspects at the physical layer. Including ML techniques in SDN controllers allows to improve network performance. In the first part of this PhD thesis, we have investigated different approaches contributing to engineer autonomous optical networks based on ML techniques. Furthermore, in order to reduce energy consumption, optical networks are evolving towards transparency, keeping OCS as fundamental mode. As an alternative, photonics community has investigated OPS to increase network utilization. In the second part of the PhD thesis, we have examined this possibility in the context of the N-GREEN project, through the experimental characterization of a 2×2 switch.

Three main contributions can be distinguished:

First contribution has addressed optical amplifier control in order to mitigate optical power excursion due to wavelength dependent gain in optical amplifiers. Although commercial amplifier modules consider complex architectures, with several amplifier stages and gain flattening filters, optical power excursion is still a matter of concern: working well under static traffic conditions, optical power excursion become again visible under dynamic operating conditions (adding/dropping channels), changing the amplifier operating point for which the gain flattening filter is not optimized. Difficult to predict, as it directly depends on the physical amplifier characteristics, ML techniques have been started to be also applied in this particular field. In this thesis, optical power excursion prediction using NNs for an EDFA under dynamic traffic operation has been demonstrated, which may be useful in an RWA process. Although convenient to alleviate the undesirable effects optical power excursion produces in WDM systems, prediction does not solve the optical power excursion problem. To this aim, power precompensation based on RL has also been investigated reducing the optical power excursion at the output of an optical link, comprising several spans. As advantages with respect to other techniques, the presented RL algorithm, once trained, is able to operate in an autonomous way providing a fast response.

Second contribution has been focused towards QoT estimation. With PLIs accumulating along the lightpath, IA-RWA must be used in order to guarantee QoT, especially when transparent or translucent optical networks are considered. In order to optimize the assignment process, IA-RWA methods require knowledge about PLIs or QoT estimation. Taking into account analytical models are usually time consuming, ML techniques appear to be promising in order to solve both problems: QoT estimation and wavelength assignment, by utilizing the available data coming from optical monitoring. In the work presented here, first, QoT estimation has been performed based on NNs. Obtained estimations have been afterwards used as environment for an RL algorithm with the aim of performing impairment aware modulation format and wavelength assignment reducing blocking probability, while working in an autonomous manner and offering fast execution.

Third contribution have studied the technology required to be available for a future generation of optical networks considering OPS. Part of N-GREEN project, which proposed a new node design and architecture, the work presented here targeted one of its two main innovations: an ultra-high capacity WDM backplane based on optical switching. Fundamental component in the WDM backplane are the 16×16 and 4×4 switches, composed by smaller 2×2 switches. In the N-GREEN framework, a 2×2 SOA switch has been developed and fabricated in III-V Lab (France). Together with other two partners in the N-GREEN project, Nokia Bell Labs (project leader) and Télécom Paris, the experimental characterization of a 2×2 optical switch has been performed. After analyzing the experimental results, its large IPDR and capacity to work with high data rate signals have been demonstrated, opening the door to more complex architectures required for the backplane, as the 16×16 and 4×4 switches.

In more detail, the contributions by chapter are described in the following:

- Chapter 1 serves as general introduction to optical network and node evolution. The role of ML techniques in SDN has been also discussed. In the framework of the N-GREEN project, possible adoption of OPS has been studied.
- Chapter 2 deals with optical power excursion introduced by optical amplifiers. First, a global overview on ML techniques is given, summarizing the most common ML methods, with NNs and RL being extensively used in this work. After introducing optical power excursion problematic, two main approaches have been proposed to handle this issue. The first one relies on predicting power excursion by using NNs. Knowing power excursion values in advance allows to allocate channels in an appropriate way, facilitating the wavelength assignment process. The second one uses RL techniques in order to pre-adjust input channel powers reducing the optical power excursion at the output of an optical link containing several spans. Three main aspects have been studied:
  - Algorithms: Several well-known RL algorithms (A2C, DDPG, TRPO and PPO) have been compared in terms of performance and training time on our developed environment.

  - Environment complexity: Different channel load configurations have been studied, with different number of active channels, allowing again to compare the achieved performance.
  - Adaptability of the develop approach to be used in a real setup: Although previous work has been based on synthetic data, amplifier models have made used of the experimental characterization of a real double-stage amplifier, work done in collaboration with Network Technology Lab, École de technologie supérieure (Canada). Proof of concept of the RL predistortion technique (based on synthetic data) on an experimental setup, also in collaboration with Network Technology Lab, École de technologie supérieure (Canada), using the experimentally characterized amplifier has been evaluated.

  As a result, DDPG and PPO have been found as the best performing algorithms in our particular case, both of them performing well for the different channel configurations reducing the mean optical power excursion to 0.5 dB. Although OSNR and BER have not been considered, an improvement of the QoT when RL predistortion is used has been demonstrated. Regarding the proof of concept on an experimental testbed, promising results have been found, with a reduction of the power deviation at the output of the link.

- Chapter 3 examines QoT estimation and RWA problems. First, a QoT estimation tool based on NNs including optical power excursion as input feature has been proposed, demonstrating to improve the achieved accuracy. Then, the QoT estimation models have been integrated into an environment used for training of an RL algorithm able to implement impairment aware wavelength and modulation assignment in a mixed line rate optical link (100G-DP-QPSK, 100G-DP-16QAM and 200G-DP-16QAM). Compared to different heuristic techniques, the proposed approach reduces blocking probability. It takes advantage of wavelength conversion capabilities, rearranging the spectrum every time a channel is dropped, indirectly performing spectrum defragmentation. Two scenarios have been studied:

  - Fixed grid: In this scenario, the RL algorithm decides to assign most of the 100G and 200G traffic demands to DP-QPSK and DP-16-QAM, respectively, making use of the lower frequencies in the band, due to the amplifier characteristics.
  - Flexible grid: the RL algorithm allocates again most of the traffic to the lower frequency slots in the band (due to the amplifier characteristics). However, it decides to assign both 100G and 200G traffic demands to DP-16-QAM, which occupies less frequency slots, saving spectrum resources.

- Chapter 4 tackles OPS, which could become a reality in the long-term. In this context, a 2×2 optical switch based on SOAs, developed by III-V Lab in the N-GREEN project framework, has been experimentally characterized in two different testbeds: continuous mode (Télécom Paris) and packet mode (Nokia Bell Labs). From the obtained results, in

single mode and WDM operation, the optical switch presents a large IPDR and capacity to work at high data rates, being a suitable option for the backplane once integrated in a larger switch (16×16, 4×4).

Multiple research lines are open from this point:

- For the RL power precompensation approach:
  - Direct training of the RL algorithm in an experimental testbed.
  - Generation of a new environment model trained on a large dataset from experimental measurements.
  - Implementation of more complex amplifier models.
  - Launch power optimization to improve QoT, e.g. by OSNR flattening together with the optical power excursion reduction.
- For the RL impairment aware wavelength and modulation format assignment approach:
  - Consideration of ROADM filtering penalties.
  - More complex scenarios, including routing capabilities and/or mixed grid networks (fixed and flexible node grid combination).

List of publications

International conferences

[1] M. Freire, E. De Carvalho Rodrigues, A. Surampudi, F. Gillet, C. Ware, A. Lavignotte, and C. Lepers, "Experimental characterization of an SOA-based photonic integrated switch", in *2018 Asia Communications and Photonics Conference (ACP)*, 2018, pp. 1–3.

[2] M. Freire, S. Mansfeld, D. Amar, F. Gillet, A. Lavignotte, and C. Lepers, "Predicting optical power excursions in erbium doped fiber amplifiers using neural networks", in *2018 Asia Communications and Photonics Conference (ACP)*, 2018, pp. 1–3.

[3] M. Freire, D. Sengupta, A. Lavignotte, C. Tremblay, and C. Lepers, "Dynamic power predistortion implementation with reinforcement learning for excursion-free amplified optical systems", in *24th International Conference on Optical Network Design and Modelling*, Barcelona, Spain, 2020.

[4] C. Lepers, M. Freire, A. Lavignotte, D. Sengupta, and C. Tremblay, "Optical amplifier control in optical networks using machine learning", in *Photonic Networks and Devices*, Optical Society of America, 2020, NeM3B–5.

National French conferences

[1] M. Freire, F. Gillet, A. Lavignotte, and C. Lepers, "Machine learning for optical amplifier control in optical networks", in *JNOG 2019: 39ème Journées Nationales d'Optique Guidée*, 2019.

Journals

[1] M. Freire, D. Sengupta, A. Lavignotte, C. Lepers, and C. Tremblay, "Proof of concept of a reinforcement learning based power preadjustment module in optical networks", *Journal of Lightwave Technology*, Manuscript to be submitted for publication.

[2] M. Freire, D. Sengupta, A. Lavignotte, C. Tremblay, and C. Lepers, “Reinforcement learning for excursion-free amplified optical systems”, *Journal of Lightwave Technology*, Manuscript to be submitted for publication.

Seminars

[1] M. Freire, F. Gillet, A. Lavignotte, and C. Lepers, “Machine learning for optical amplifier control in optical networks”, in *Journée GdR ISIS "Codage, modulation et traitement du signal pour les communications optiques"*, Télécom Paris, Paris, France, 2019.

[2] C. Lepers, M. Freire, A. Lavignotte, D. Sengupta, and C. Tremblay, “Optical amplifier control in optical networks using machine learning”, in *IP Paris Electrical Engineering Artificial Intelligence Day*, Télécom Paris, Paris, France, 2020.

Summer Schools

[1] M. Freire, S. Mansfeld, A. Lavignotte, F. Gillet, and C. Lepers, “Predicting optical power excursion in EDFAs with neural networks”, in *Data Science Summer School*, Campus Polytechnique, Palaiseau, France, 2018.

Appendix

A Neural networks

To complete the overview in Section 2.1, a more detailed description about feedforward network operation is presented [85], revealing how, after the NN has been trained, outputs are estimated by forward propagation of data from input to output. Considering the structure in Fig. 2.4, with D inputs $x_1, x_2, ...x_D$ and a first hidden layer with M neurons, the first step is to calculate M linear combinations corresponding to the M nodes using the coefficients ${w_j}^{(1)}$ (estimated during training) for the first hidden layer (superscript (1) specifying the hidden layer number 1):

$$a_j = \sum_{i=1}^{D} w_{ji}^{(1)} x_i + w_{j0}^{(1)}. \tag{A.1}$$

Using common nomenclature, $w_{ji}^{(1)}$ are referred as weights, $w_{j0}^{(1)}$ as biases and a_j as activations. At each neuron, an output z_j is calculated by applying a nonlinear activation function $h(\cdot)$ on the inputs:

$$z_j = h(a_j). \tag{A.2}$$

This process of linear combinations followed by nonlinear transformations is repeated for each layer, e.g. for a hidden layer 2:

$$a_k = \sum_{j=1}^{M} w_{kj}^{(2)} z_j + w_{k0}^{(2)}, \tag{A.3}$$

$$z_k = h(a_k), \tag{A.4}$$

until reaching the output layer. Coming back to the structure in Fig.2.4, a 1 hidden layer NN

and assuming sigmoid function activation $\sigma(\cdot)$ in the output layer, the output is given by:

$$y_k(\boldsymbol{x}, \boldsymbol{w}) = \sigma\left(\sum_{j=1}^{M} w_{kj}^{(2)} h\left(\sum_{i=1}^{D} w_{ji}^{(1)} x_i + w_{j0}^{(1)}\right) + w_{k0}^{(2)}\right). \tag{A.5}$$

Instead of defining weights and biases separately, another common used nomenclature, includes an additional input x_0 which value is always 1, hence eq. A.1 and eq. A.5 are rewritten as:

$$a_j = \sum_{i=0}^{D} w_{ji}^{(1)} x_i, \tag{A.6}$$

$$y_k(\boldsymbol{x}, \boldsymbol{w}) = \sigma\left(\sum_{j=0}^{M} w_{kj}^{(2)} h\left(\sum_{i=0}^{D} w_{ji}^{(1)} x_i\right)\right). \tag{A.7}$$

Once the operation is explained, the challenge is how to perform the training, in order to get to know the weights. The idea behind NN training is to minimize a cost function (error function) by using stochastic gradient descent. Defining $\boldsymbol{t} = t_1, t_2, ..., t_N$ as the N target vectors associated to the $\boldsymbol{X} = \boldsymbol{x}_1, \boldsymbol{x}_2, \ldots, \boldsymbol{x}_N$ independent inputs included in the training dataset and assuming they follow a Gaussian distribution with β being the precision of the Gaussian noise, the error function $E(\boldsymbol{w})$ to minimize is given by [85]:

$$E(\boldsymbol{w}) = \frac{1}{2} \sum_{n=1}^{N} \{y(\boldsymbol{x}_n, \boldsymbol{w}) - t_n\}^2. \tag{A.8}$$

Therefore, the optimum coefficients $\boldsymbol{w}_{ML}$ can be found by minimizing eq. A.8, making also possible to calculate the β values [85]:

$$\frac{1}{\beta_{ML}} = \frac{1}{N} \sum_{n=1}^{N} \{y(\boldsymbol{x}_n, \boldsymbol{w}_{ML}) - t_n\}^2. \tag{A.9}$$

Due to its simplicity, gradient descent optimization has been the technique selected in order to find the $\boldsymbol{w}$ coefficients minimizing the error function, i.e. discover the $\boldsymbol{w}$ weights bound to $\nabla E(\boldsymbol{w}) = 0$. Note that the algorithm does not guarantee that the identified minimum is a global minimum; it can also be a local minimum. In general, starting from some initial values $\boldsymbol{w}^{(0)}$, weights are optimized in each update τ following:

$$\boldsymbol{w}^{(\tau+1)} = \boldsymbol{w}^{(\tau)} - \eta \nabla E(\boldsymbol{w}^{(\tau)}), \tag{A.10}$$

where η is the learning rate parameter. The value selected for the learning rate parameter is critical: a small learning rate yields to slow convergence whereas a large learning rate can fail to converge. Weights updates can be performed after processing the whole dataset (batch methods) or after processing each sample in the training dataset (stochastic gradient descent):

$$\boldsymbol{w}^{(\tau+1)} = \boldsymbol{w}^{(\tau)} - \eta \nabla E_n(\boldsymbol{w}^{(\tau)}), \tag{A.11}$$

with E_n denoting the error function calculated for the n sample in the dataset. Intermediate solutions, very commonly used, update the weights on training dataset subsets (batches). One of the advantages of stochastic gradient descent, is that makes more difficult to fall on local minima, as an stationary point for one sample in the dataset does not have to be an stationary point for the whole dataset.

The last missing part, when looking at eq. A.11 is how to efficiently calculate the derivatives. Error backpropagation method is the answer, making possible to calculate the derivative by backpropagating information from the output towards the input layer. This can be intuitively explained by the fact that the cost function depends on the output. A complete proof based on applying the chain rule is provided in [85]. Before describing the main steps followed in the algorithm, some definitions are required. In the following, a regular NN will be considered. As explained before, at each neuron, first, an activation a_j is calculated as a linear combination of the inputs z_i and associated weights w_{ji}:

$$a_j = \sum_i w_{ji} z_i. \tag{A.12}$$

Secondly, a nonlinear transformation $h(\cdot)$ is applied on the activation:

$$z_j = h(a_j). \tag{A.13}$$

At the output layer, the output y_k is directly calculated as:

$$y_k = \sum_i w_{ki} z_i. \tag{A.14}$$

The error function is defined as before:

$$E_n = \frac{1}{2} \sum_k \left(y_{nk} - t_{nk}\right)^2. \tag{A.15}$$

Demonstrated by applying the chain rule, derivatives can be calculated as a multiplication,

Error propagation
1. Apply an input vector x_n to the network and forward propagate through the network using eq. A.12 and A.13 to find the activations of all the hidden and output units. 2. Evaluate δ_k for all the output units using eq. A.18 3. Backpropagate the δ's using eq.A.19 to obtain δ_j for each hidden unit in the network 4. Use eq. A.16 to evaluate the required derivatives.

Table A.1 – Error propagation [85].

expressed as [85]:

$$\frac{\partial E_n}{\partial w_{ji}} = \delta_j z_i, \tag{A.16}$$

where δ_j's, usually called errors, are given by:

$$\delta_j = \frac{\partial E_n}{\partial a_j}. \tag{A.17}$$

Different expressions are obtained for the δ's at the output and the hidden layer:

- At the output layer:

$$\delta_k = y_k - t_k. \tag{A.18}$$

- At the hidden layers:

$$\delta_j = h'(a_j) \sum_k w_{kj} \delta_k. \tag{A.19}$$

From eq. A.19, δ's are calculated from the output layer towards the input layer, propagating backwards. The procedure is summarized in Table A.1.

B RL Policy gradient algorithms

Policy gradient theorem [88] establishes the analytical formula:

$$\nabla_\theta J(\boldsymbol{\theta}) \propto \sum_s \mu(s) \sum_a Q_\pi(s,a) \nabla_\theta \pi(a|s,\theta), \tag{B.1}$$

where $\mu(s)$ is on-policy distribution under π. Eq. B.1 is proportional to a sum over states weighted by the frequency occurrence of the states, therefore being possible to write it as an expectation on sample states S_t [88]:

$$\nabla_\theta J(\boldsymbol{\theta}) = \mathbb{E}_\pi \left[\sum_a Q_\pi(S_t,a) \nabla_\theta \pi(a|S_t,\theta) \right]. \tag{B.2}$$

In order to introduce sample actions A_t using the same method as for introducing sample states S_t, it is required to multiply and divide by $\pi(a|S_t,\theta)$ [88]:

$$\nabla_\theta J(\boldsymbol{\theta}) = \mathbb{E}_\pi \left[\sum_a \pi(a|S_t,\theta) Q_\pi(S_t,a) \frac{\nabla_\theta \pi(a|S_t,\theta)}{\pi(a|S_t,\theta)} \right]. \tag{B.3}$$

In that way, the sum over actions is weighted by $\pi(a|S_t,\theta)$, which is needed to apply the expectation, replacing a by A_t [88]:

$$\nabla_\theta J(\boldsymbol{\theta}) = \mathbb{E}_\pi \left[Q_\pi(S_t,A_t) \frac{\nabla_\theta \pi(A_t|S_t,\theta)}{\pi(A_t|S_t,\theta)} \right]. \tag{B.4}$$

Finally, as $\ln(x)' = 1/x$, the following expression is obtained [88]:

$$\nabla_\theta J(\boldsymbol{\theta}) = \mathbb{E}_\pi \left[Q_\pi(S_t,A_t) \nabla_\theta \ln(\pi(A_t|S_t,\theta)) \right], \tag{B.5}$$

which is the foundation of many policy gradient algorithms.

C Optical amplification

Optical amplifiers allow to compensate the attenuation caused by optical fibers and other components. Independent of bit rate and modulation format, they play a key role in optical networks. However, they present several issues as gain non-flatness and noise generation. First, principles of light amplification, fundamental in optical amplifiers, are introduced. After, two of the most common optical amplifiers, EDFAs (used in Chapter 2 and Chapter 3) and SOAs (used in Chapter 4), are briefly reviewed. As seen in Fig. C.1, both of them present a large bandwidth appropriate for WDM applications. However, EDFAs posses a higher gain and lower insertion noise, becoming preferred option for system applications (booster amplifiers, inline amplifiers and preamplifiers). SOAs, showing higher nonlinear effects and photonic integration capabilities, are dominant in functional applications (e.g. optical switches, wavelength converters).

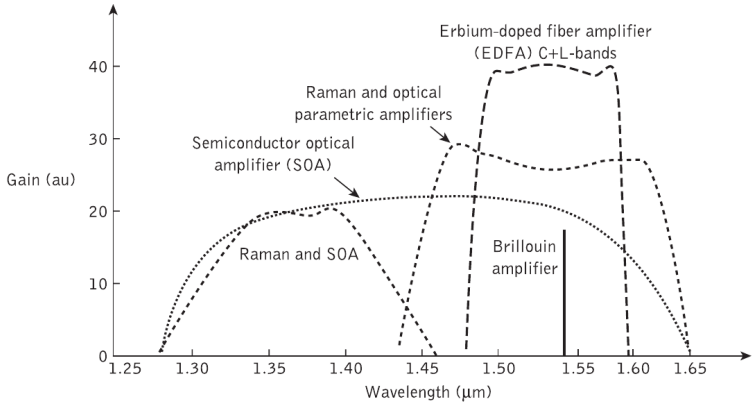

Figure C.1 – Amplifier gain comparison [58].

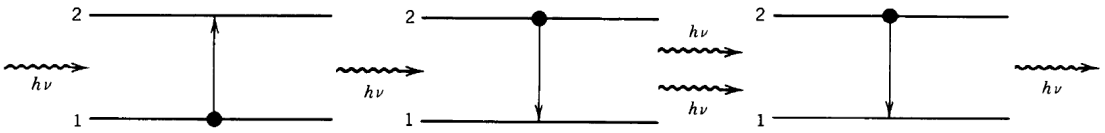

(a) Absorption. (b) Stimulated emission. (c) Spontaneous emission.

Figure C.2 – Interactions between photons and atoms [104].

C.1 Light amplification

Interactions of photons with atoms are the basis of light amplification [104]. In a simple example, an atom with two energy levels, E_1 and E_2 is considered. Assuming photons of frequency $v \approx v_0$ matching the energy level difference $hv_0 = E_2 - E_1$, with h being the Plank constant, three different interactions can be considered:

- Absorption: An atom in the lower level absorbs a photon promoting to the higher level (Fig. C.2a).
- Stimulated emission: An atom in the upper level is stimulated by a photon to emit another photon in the same mode, coherent to the electromagnetic wave (Fig. C.2b). It produces amplification.
- Spontaneous emission: An atom in the upper level, drops spontaneously to the lower level releasing energy in the form of a photon(Fig. C.2c), generating ASE noise.

Of these three interactions, stimulated emission is responsible of the light amplification, exploited by optical amplifiers as EDFAs and SOAs, presented in the next paragraphs.

C.2 EDFAs

Different dopants, as rare earth ions, transition metal ions, semiconductor or metal nanoparticles [293], can be included in glasses in order to become active materials, i.e. laser glass. Rare earth doped glasses, exhibiting long lifetimes at metastable level and high quantum efficiency, have become extensively utilized as fiber amplifiers [294]. Among rare earth dopants, erbium is typically used due to its compatibility with the telecommunication window [295]. Relevant parameters in EDFs are the transition cross sections, plotted in Fig. C.3, representing absorption and emission efficiencies at each wavelength. Several methods can be used in order to measure them [95], [296], [297].

Considering an optical signal with intensity (power per unit area) I_s and wavelength λ_s illuminating an isolated lasing structure (neglecting the effect of the SMF acting as a waveguide) of thickness dz, absorption and emission cross sections at λ_s $\sigma_{12}(\lambda_s)$ and $\sigma_{21}(\lambda_s)$ and atomic

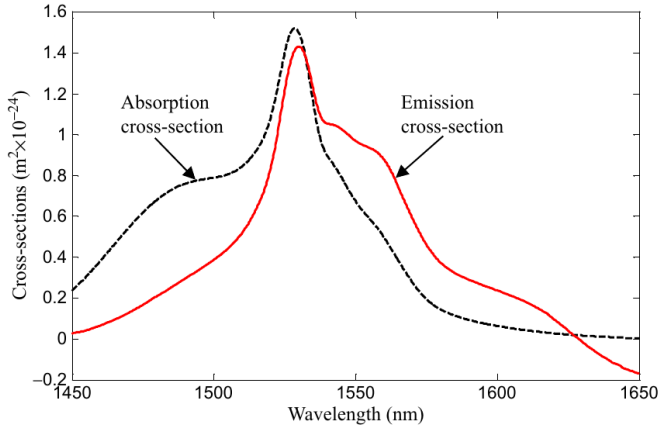

Figure C.3 – Example of absorption and emission cross sections of Lucent HE980 EDF [298].

populations N_1 and N_2, the intensity change dI_s [299] can be written as:

$$dI_s = (\sigma_{21}(\lambda_s) N_2 - \sigma_{12}(\lambda_s) N_1) I_s dz. \tag{C.1}$$

When degeneracy of energy levels are considered, i.e. an energy level can correspond to different quantum states, eq. C.1 turns into [104]:

$$\frac{dI_s}{dz} = \sigma_{12}(\lambda_s) \left(\frac{g_1}{g_2} N_2 - N_1 \right) I_s, \tag{C.2}$$

with g_1 sublevels at the lower level and g_2 sublevels at the higher level. Eq. C.2 is still not precise, as it has assumed identically populated sublevels by using $g_1\sigma_{12} = g_2\sigma_{21}$. In order to improve the accuracy, eq. C.2 is rewritten based on new defined absorption and emission cross system sections ($\sigma_a(\lambda_s)$, $\sigma_e(\lambda_s)$) or cross-section ratio ($\eta(\lambda_s) = \sigma_e(\lambda_s)/\sigma_a(\lambda_s)$) [95]:

$$\frac{dI_s}{dz} = (\sigma_e(\lambda_s) N_2 - \sigma_a(\lambda_s) N_1) I_s = \sigma_a(\lambda_s) \left(\eta(\lambda_s) N_2 - N_1 \right) I_s. \tag{C.3}$$

From eq. C.3, the gain coefficient corresponds to $g = \sigma_a(\lambda_s)(\eta(\lambda_s) N_2 - N_1)$. This result reveals three important aspects about the gain coefficient. First, the gain depends on the wavelength, different EDFA structures possess different emission and absorption cross-sections. This property has a negative effect in WDM systems, with each channel experiencing a different gain. Its mitigation is studied in Chapter 2. Second, gain also exhibits dependence on the relative inversion. When there is no inversion, i.e. all the atoms are in the ground state, the medium absorbs all the wavelengths producing a negative gain coefficient. As the inversion is increased, i.e. there are atoms in excited level, gain coefficient will start also increasing until it will reach a maximum for the complete inversion, i.e. all the atoms in excited level. Third, gain coefficient depends on the longitudinal coordinate z, with the gain changing over the fiber

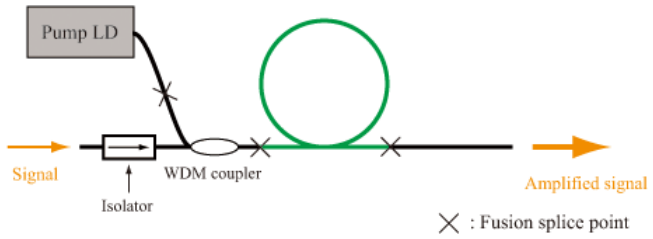

(a) Unidirectional forward pumping.

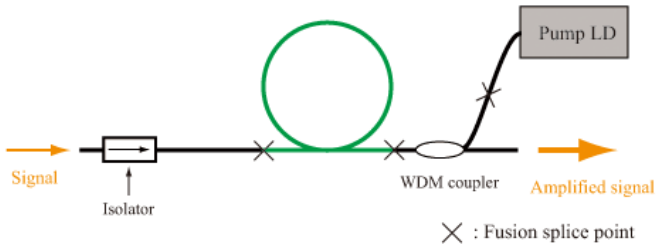

(b) Unidirectional backward pumping.

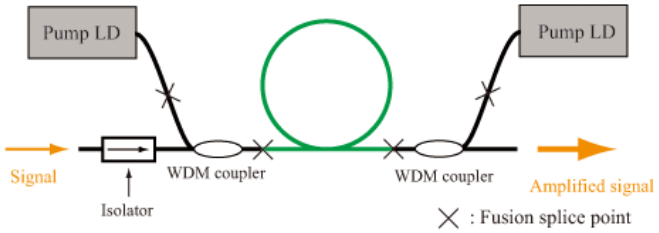

(c) Bidirectional pumping.

Figure C.4 – Different EDFA architectures [300].

length as pump is absorbed by the medium.

C.2.1 Gain characteristics

A complete EDFA module is composed of an EDF, but also of a pump source and various optical components as combiners or isolators to avoid reflections. Different architectures can be conceived, shown in Fig. C.4: unidirectional forward pumping, unidirectional backward pumping and bidirectional pumping.

For any of them, gain is one of the most important characteristics. Directly depending on pump photon absorption, it is limited by the erbium concentration. For a full inverted 3-level laser medium of length L and rare earth concentration ρ, the maximum signal gain is given by [95]:

$$G = \frac{P_s^{out}}{P_s^{in}} = \exp(\rho \sigma_e L). \tag{C.4}$$

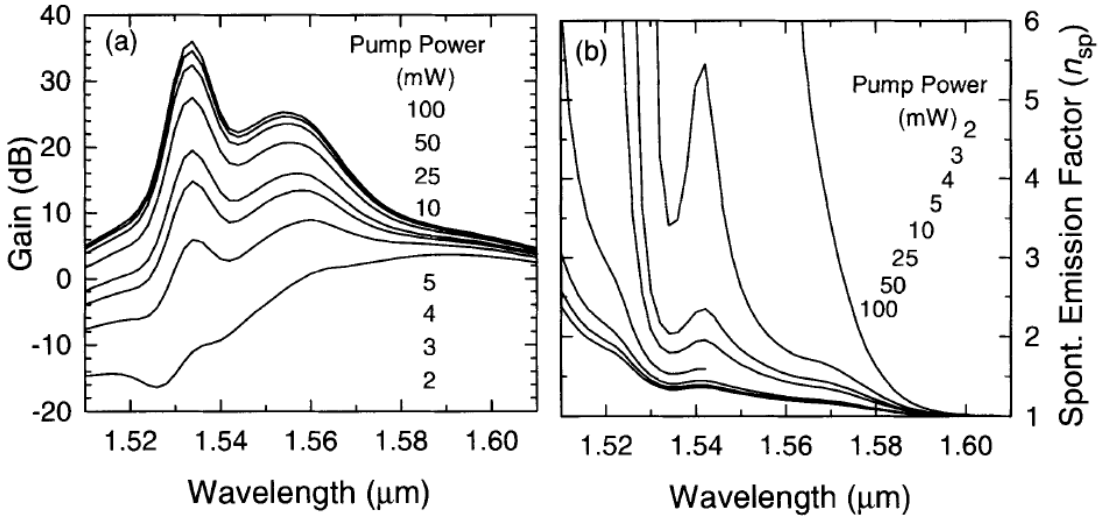

(a) EDFA gain.

(b) EDFA spontaneous emission factor.

Figure C.5 – EDFA gain and spontaneous emission factor for different pump powers [301].

At the same time, gain limits in EDFAs can be found in a straight way by using the energy conservation principle. Defining P_p^{in}, P_s^{in}, P_s^{out} as the input pump power, input signal power and output signal power, and λ_p and λ_s the pump and signal wavelengths, the amplifier's fundamental limits, obtained using eq. C.4 and the energy conservation principle, are expressed as [95]:

$$G \leq \min\left\{\exp(\rho\sigma_e L), 1 + \frac{\lambda_p}{\lambda_s}\frac{P_p^{in}}{P_s^{in}}\right\}, \tag{C.5}$$

$$P_s^{out} \leq \min\left\{P_s^{in}\exp(\rho\sigma_e L), P_s^{in} + \frac{\lambda_p}{\lambda_s}P_p^{in}\right\}. \tag{C.6}$$

Despite these limits, gain varies depending on the injected pump and signal powers. Under varying pump powers, three different regimes are distinguished: underpumped regime, where the signal is absorbed ($G < 1$); incomplete inversion regime, where the gain increases with the pump power; the near complete inversion regime where the gain approaches the maximum. These three regimes are illustrated in Fig. C.5a, where the gain as a function of the wavelength is shown for different pump powers. Differently, two different regimes can be distinguished when signal power variations are considered, called small signal regime and saturation regime, showing a linear behaviour and nonlinear behaviour respectively. The output power at which the gain drops 3 dB is defined as saturation output power P_{sat}^{out}.

C.2.2 Noise characteristics

In order to describe the noise, an m mode amplifier (for SMF, one propagation mode polarization $m = 2$) is considered, with gain $G(z)$. Amplifier noise performance is usually measured in terms of spontaneous emission factor n_{sp}, which for a constant population inversion over the amplifier length, is expressed as [301]:

$$n_{sp} = \frac{\sigma_e N_2}{\sigma_e N_2 - \sigma_a N_1} = 1 + \frac{\sigma_a N_1}{\sigma_e N_2 - \sigma_a N_1}. \tag{C.7}$$

To calculate the NF, SNR variation due to the amplification, it is assumed that: (1) input signal is governed by Poisson statistics (2) shot noise and spontaneous-spontaneous beat noise can be neglected. Thus, NF can be expressed as [95]:

$$NF = \frac{SNR_{in}}{SNR_{out}} = 2n_{sp}\frac{G(z)-1}{G(z)} + \frac{1}{G(z)}, \tag{C.8}$$

where $n_{sp} = P_N/((G-1)h\nu B_0)$ and SNR_{in} and SNR_{out} are SNR at the input and output of the amplifier, respectively. Minimum NF is $2n_{sp}$ (3 dB) obtained for a high gain amplifier. For a linear regime, eq. C.8 can be used. For a saturated regime, no rigorous expression is available. Intuitively, NF will decrease when the amplifier saturates, as the spontaneous emission becomes neglectable. An increasing pump power decreases spontaneous emission factor to a minimum spontaneous emission factor n_{sp}^{min}, as it can be seen in Fig. C.5b.

Noise accumulation in optical links is a critical impairment, limiting the transmission reach (Chapter 3).

C.2.3 Gain dynamics

In EDFAs, typical saturation and recovery times are in the range 100 μs to 1 ms. As a consequence, EDFAs exhibit slow gain dynamics [95]. When operated in the saturation regime, input power changes can lead to gain changes, i.e. gain modulation producing undesired effects as intersymbol interference, patterning and crosstalk. Data modulation is one source of input power fluctuations [103]. Fortunately, high data rates used in optical communications together with the slow gain dynamics in EDFAs make them immune to these issues, contrary to SOAs, as explained in Section C.3.

Modifications in the channel load are another source of input power changes. These modifications can occur as a result of network reconfigurations, e.g. adding or dropping channels at ROADMs or network failures, e.g. a fiber cut. Assume a single stage amplifier working on the saturation region. Before time $t = 0$, the EDFA is operating in a steady state having as input a WDM signal with N channels. At $t = 0$, some number of channels are added (or dropped).

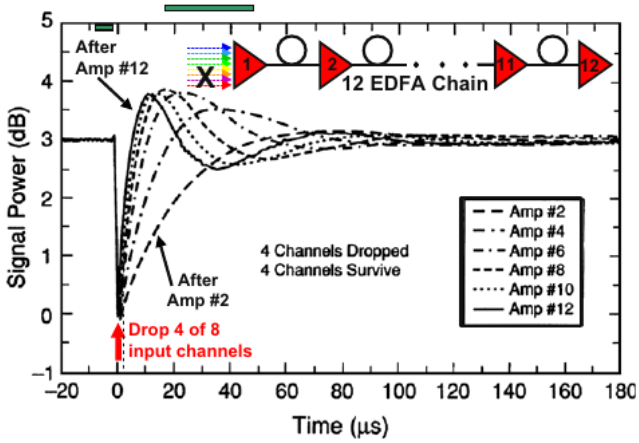

Figure C.6 – Power transients in an EDFA cascade [103].

According to [302], the time evolution of the power at the output of the EDFA, $P^{out}(t)$, follows:

$$P^{out}(t) = P^{out}(\infty)\left(\frac{P^{out}(0)}{P^{out}(\infty)}\right)^{e^{-t/\tau_e}}, \tag{C.9}$$

where $P^{out}(0)$ and $P^{out}(\infty)$ are the output power at the initial state $t = 0$ and the output power at the end of the transient, respectively, which can be calculated analytically or experimentally; τ_e is the effective decay time of the upper level averaged over the fiber length [303] which can be obtained as a fitting parameter, typically in the order of 10-100 μs [304]. This analysis can be applied to different number of channels and even multistage amplifiers. When a cascade of amplifiers is considered, the dynamics of the output power changes are faster, the farther in the cascade of EDFAs the faster are the changes. Fig. C.6 illustrates an example of power transients on the total signal power in an EDFA cascade after dropping 8 of the 12 channels at the input of the first amplifier. Power changes in amplifier 12th are much faster than in the first amplifier.

However, this approximation considers a saturated EDFA operating under a constant pump power. In WDM operation, constant gain is preferred, in order to maintain a constant channel power and not a constant total output power. Gain control is usually implemented by adjusting the pump powers using forward/feedback loops involving electronics, implying a limited response speed. Even using gain control, transients are present, producing a similar response to the one obtained under constant pump [103]. In order to eliminate this optical power surge, which can deteriorate the BER on the surviving channels, some proposed solutions include both feedback and feedforward circuits [98], [99]. In this way, the feedforward reacts on the input power, allowing a fast reaction in the order of 1 μs. After, the feedback circuit, reacting on the output power, allows a fine-adjustment in the order of 1 ms. It is important to distinguish these power transients from the optical power excursions, persistent over the time, which are discussed in Chapter 2 and Chapter 3.

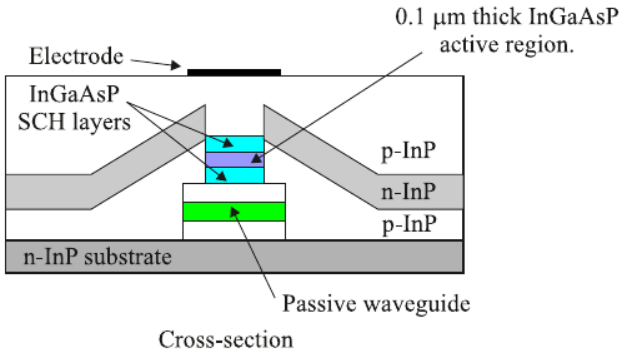

Figure C.7 – SOA structure [308].

C.3 SOAs

In the following, SOAs are briefly presented. In general, SOAs can be classified in two main types: Fabry-Perot SOAs and travelling-waveguide SOAs. Fabry-Perot SOAs present considerable reflections. Allowing the signal to oscillate, passing several times through the amplifier, they are useful for laser structures. On the contrary, reflections at the end facets of travelling-waveguide SOAs can be neglected, restricting the number of passes to one [305].

Light amplification based on stimulated emission is a fundamental working principle in optical amplifiers, also in SOAs. However, whereas EDFAs achieve population inversion by injecting an optical carrier, inversion in SOAs is produced by the injection of electrical current in a p-n junction with an active region in between [306], [307].

C.3.1 Physical characteristics

Typical structure of an SOA includes an active region in between two separate confinement heterostructure (SCH) layers, as seen in Fig. C.7. In this double-heterostructure, an optical waveguide is constructed within the three layers, where the active layer in between has a refractive index greater than the two outer layers [308].

Wavelength operating range can be selected depending on the semiconductor material. Table C.1 [309] shows the bandgap and photon emission wavelength for some semiconductors. For working in the telecommunications band, indium gallium arsenide phosphide (InGaAsP), indium gallium arsenide (InGaAs), and indium phosphide (InP) are commonly used.

Material	Composition	Bandgap (eV)	Wavelength (nm)
Indium phosphide	InP	1.35	920
Gallium arsenide	GaAs	1.42	870
Aluminium gallium arsenide	AlGaAs	1.40-1.55	800-900
Indium gallium arsenide	InGaAs	0.95-1.24	1000-1300
Indium gallium arsenide phosphide	InGaAsP	0.73-1.35	900-1700

Table C.1 – Bandgap of some semiconductor compounds [309].

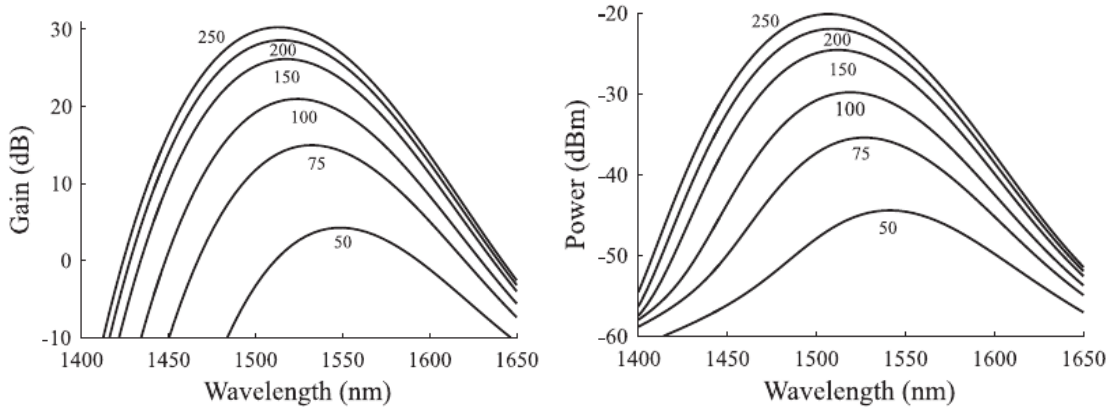

(a) Gain.

(b) ASE spectrum.

Figure C.8 – Typical SOA gain and ASE spectrum for different bias currents [308].

C.3.2 Gain characteristics

As in any optical amplifier, gain and NF (including ASE and coupling losses) are fundamental characteristics. Typical gain and ASE spectrum for different bias currents can be seen in Fig. C.8a and Fig. C.8b, respectively. A brief explanation on SOAs gain is presented in the next paragraphs.

Small signal gain in a Fabry-Perot SOA with input and output facet reflectivities R_1 and R_2 and cavity longitudinal mode spacing $\Delta\nu$ at a frequency ν is given by [310]:

$$G(\nu) = \frac{(1-R_1)(1-R_2)G_s}{(1-\sqrt{R_1R_2}G_s)^2 + 4\sqrt{R_1R_2}G_s \sin^2(\pi(\nu-\nu_0)/\Delta\nu)}, \tag{C.10}$$

with G_s the single pass gain and ν_0 the Fabry–Perot resonant frequency. From eq. C.10, 3 dB bandwidth B can be calculated as [311]:

$$B = \frac{c}{\pi NL} \sin^{-1}\left(\frac{1-\sqrt{R_1R_2}G_s}{2(\sqrt{R_1R_2}G_s)^{\frac{1}{2}}}\right), \tag{C.11}$$

where c is the speed of light, N the material refractive index and L the amplifier length. For travelling-waveguide SOAs, bandwidth is three orders of magnitude larger. The single pass gain can be defined as [58], [305]:

$$G_s = \exp\left(\left(\frac{\Gamma g_0}{1+I/I_s} - \alpha\right)L\right), \tag{C.12}$$

with Γ the optical confinement factor, g_0 unsaturated material gain coefficient, α the absorption coefficient and I_s the saturation intensity.

From eq. C.12, for an increasing signal intensity, single pass gain decreases. The associated phase shift is expressed as [312]:

$$\phi_s = \phi_0 + \frac{g_0 bL}{2}\left(\frac{I}{1+I_s}\right), \tag{C.13}$$

where ϕ_0 is the nominal phase shift and b the linewidth broadening factor. For intensity varying signals, the dependence of gain and phase change with intensity may produce distortion, causing nonlinearities at high powers. Furthermore, when the input power signal is high, the active region becomes depleted. As a consequence, the gain decreases, with the amplifier entering the saturation region.

C.3.3 Noise characteristics

In order to calculate the NF of an SOA with gain G, the SOA output signal is considered to traverse a narrowband filter with bandwidth B_0, before being detected by a photodetector. The input signal is assumed to be noise limited.

For small B_0, signal shot and signal-spontaneous components are dominant, thus, NF can be expressed as [305], [308]:

$$NF = \frac{1}{G} + \frac{2\sigma_{ASE}}{h\nu G}, \tag{C.14}$$

with ν the signal frequency, n_{sp} the spontaneous emission factor and σ_{ASE} the noise power spectral density calculated as $\sigma_{ASE} = n_{sp}h\nu(G-1)$. When gain is much greater than 1, it is possible to estimate NF simply as function of the spontaneous emission factor n_{sp}:

$$NF = 2n_{sp}. \tag{C.15}$$

C.3.4 Gain dynamics

Considering carrier recombination lifetime in SOAs is in the order of hundreds of picoseconds, amplifier gain is able to follow input power signal variations producing distortions, becoming even worst when WDM is considered [305]. Although they can seem inconvenient, nonlinearities as SPM, XPM have been exploited for optical signal processing applications.

D VPI software

VPI, advanced simulation software, allows to analyze the performance of optical communication systems [148]. The objective of this appendix is to provide a brief introduction to this software, as it has been intensively used during this PhD thesis.

Any simulation setup can be developed by using the VPI user interface. After creating a project, the desired optical system can be designed by including built-in or custom modules. A wide library of built-in modules is available, including electrical sources, electrical amplifiers, optical sources, optical modulators, optical filters, optical modulators, fibers, receivers, etc. Once modules are included and connected between them in the schematic, global (affecting the whole project) and local (affecting each module) parameters must be selected in order to model the behaviour of the optical system. Figure D.1 shows an example of schematic developed in VPI, used in Section 2.4 to generate a dataset for power excursion prediction using NNs. The schematic contains an array of transmitters. Then, after multiplexing, the signal traverses 100 km fiber and an amplifier, to finally be acquired by a receiver array. Additionally, the schematic must contain analyzers in order to be able to measure the performance parameters required for each specific application. Built-in modules allow to display spectrum or eye diagrams and to measure EVM or OSNR. Apart from graphical display of these parameters, also file storage is permitted, option useful in this PhD thesis in order to collect the results of multiple simulations. In Fig. D.1, active channels and output powers are stored in files after simulation.

Once the schematic is completed, simulations can be directly run by using the graphical interface. However, as this PhD thesis required to run simulations intensively, we developed a Python script allowing to automatically run any number of simulations. Beyond running the simulations, the Python script permitted to modify parameters (e.g. channel load, active channels, etc.) and to store the results in each simulation.

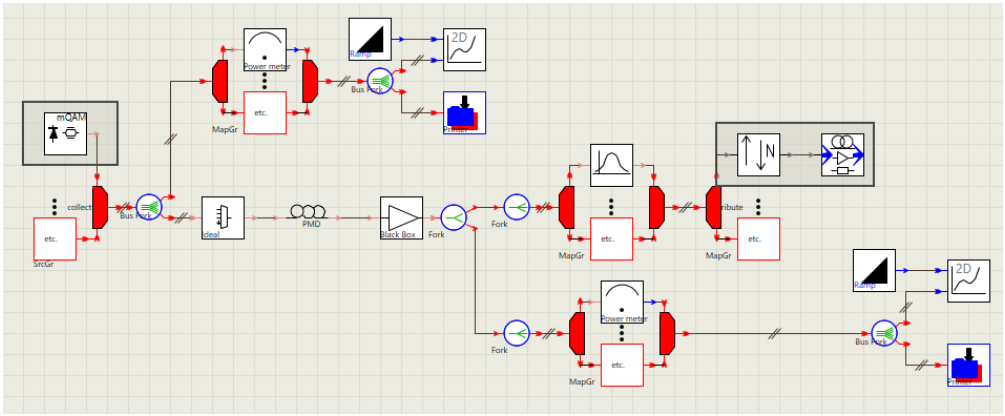

Figure D.1 – VPI schematic.

E Conclusion (Français)

Pour faire face à la montée en débit du trafic, les réseaux optiques doivent gagner en dynamisme et en flexibilité. Dans ces conditions, la gestion des réseaux devient de plus en plus complexe et nécessite de contrôler certains paramètres des dispositifs de la couche physique. L'intégration des techniques d'apprentissage machine dans les contrôleurs SDN, permet d'effectuer ce contrôle tout en respectant des règles d'ingénierie afin que les réseaux restent performants. Afin de réduire leur consommation énergétique, les réseaux optiques évoluent vers des réseaux optiques transparents basés sur la commutation de circuits optiques (OCS : Optical Circuit Switching). Cependant, la commutation de paquets optiques (OPS : Optical Packet Switching) a été étudiée par la communauté scientifique comme une technique de commutation alternative afin d'optimiser l'utilisation des ressources des réseaux. Les deux approches «apprentissage machine appliquée aux réseaux optiques» et «technique OPS» ont fait l'objet des travaux de cette thèse.

Dans la première partie, nous avons étudié différentes approches d'ingénierie de réseaux optiques intelligents en utilisant des techniques d'apprentissage machine. Nous avons focalisé notre étude sur le contrôle des amplificateurs optiques dans les réseaux.

Dans ce contexte, nous avons porté notre attention sur l'atténuation de l'excursion de puissance optique résultant de la dépendance du gain en fonction de la longueur d'onde dans les amplificateurs optiques. Bien que les dispositifs d'amplification commerciaux considèrent des architectures complexes, avec plusieurs étages d'amplification et des filtres d'aplatissement du gain, l'excursion de puissance optique est toujours un problème. En effet, ces dispositifs fonctionnent bien dans des conditions de trafic statique mais l'excursion de puissance optique réapparaît dans des conditions de fonctionnement dynamique lors de l'ajout ou de la suppression de canaux WDM qui modifie le point de fonctionnement des amplificateurs pour lequel le filtre d'aplatissement du gain n'est pas optimisé. L'excursion de puissance est difficile à prévoir, car elle dépend directement des caractéristiques physiques des amplificateurs. Les techniques d'apprentissage machine ont commencé à être appliquées pour lever ce verrou technologique. Dans la thèse, nous avons montré dans un premier temps

qu'il était possible de prédire l'excursion de puissance optique d'un amplificateur optique dopé à l'erbium (amplificateur EDFA) en présence d'un trafic dynamique en utilisant des réseaux de neurones (NNs). Puis, étant donné que la prédiction ne résoud pas le problème de l'excursion de puissance optique, nous avons proposé de pré-compenser la puissance injectée dans le système WDM en utilisant un processus d'apprentissage machine par renforcement (RL : reinforcement learning) et nous avons montré que l'excursion de puissance optique cumulée à la sortie d'une liaison optique, comprenant plusieurs liens optiques pouvait être sensiblement réduite. Le principal avantage de la méthode d'apprentissage par renforcement que nous avons choisie par rapport à d'autres méthodes, réside dans le fait qu'une fois le processus acquis, il est capable de fonctionner de manière autonome en fournissant une réponse rapide. Trois aspects principaux ont été étudiés :

- Comparaison de divers algorithmes : Plusieurs algorithmes RL bien connus (A2C : Advantage Actor Critic, DDPG : Deep Deterministic Policy Gradient, TRPO : Trust Region Policy Optimization et PPO : Proximal Policy Optimization) ont été comparés en termes de performances et de temps d'entrainement requis.
- Complexité de l'environnement : Différents taux de charge en canaux ont été considérées, avec un taux de canaux actifs variable, afin de comparer les performances obtenues.
- Adaptabilité de l'approche dans un contexte réel : Bien que les travaux précédents aient été basés sur des données synthétiques, les modèles d'amplificateur ont utilisé la caractérisation expérimentale d'un véritable amplificateur à double étage, travail effectué en collaboration avec Network Technology Lab (Ecole de Technologie Supérieure, Canada). Une preuve de concept de la technique de précompensation RL (basée sur des données synthétiques) sur un banc d'essai expérimental a été considérée, également en collaboration avec Network Technology Lab, en utilisant l'amplificateur caractérisé expérimentalement.

Les algorithmes DDPG et PPO se sont avérés les plus performants dans notre cas particulier, tous deux étant performants pour les différentes configurations de canaux, réduisant l'excursion de puissance optique moyenne à 0.5 dB. Bien que l'OSNR n'ait pas été mesuré, une amélioration de la QoT a été observée en comparant l'évolution du BER des différents canaux WDM avant et après application de l'apprentissage par renforcement lors de la précompensation. En ce qui concerne la preuve de concept sur un banc d'essai expérimental, des résultats prometteurs ont été trouvés, avec une réduction de l'écart de puissance à la sortie de la liaison.

Dans un deuxième temps, nous nous sommes focalisés sur l'estimation de la qualité de transmission (QoT) dans les réseaux optiques transparents afin de répondre à la problématique d'allocation des chemins et des longueurs d'onde. Les modèles analytiques utilisés pour répondre à cette problématique prennent généralement beaucoup de temps et les techniques

d'apprentissage machine sont intéressantes à considérer pour atteindre les deux objectifs à savoir l'estimation de la qualité de transmission et l'attribution des longueurs d'onde, en utilisant des données issues de la surveillance optique. Dans nos travaux, nous avons procédé à une estimation de la qualité de transmission sur la base de réseaux neuronaux puis nous avons utilisé ces estimations comme environnement de l'algorithme d'apprentissage par renforcement. L'objectif ultime de notre étude a été d'affecter un format de modulation et une longueur d'onde adéquats aux différentes demandes en débit dans les réseaux tout en optimisant la qualité de transmission et en réduisant l'excursion de puissance cumulée dans les amplificateurs optiques. Ce travail a permis de réduire la probabilité de blocage des demandes arrivant dans les nœuds optiques des réseaux, tout en travaillant de manière autonome et en offrant une exécution rapide.

Tout d'abord, un outil d'estimation de la QoT basé sur les NNs incluant l'excursion de puissance optique comme caractéristique d'entrée a été proposé, ce qui a permis d'augmenter la précision des résultats obtenus. Ensuite, les modèles d'estimation de la QoT ont été intégrés comme environnement d'un algorithme d'apprentissage par renforcement afin de pouvoir allouer un format de modulation en tenant compte de la dégradation du signal dans une liaison optique à débit mixte (100G-DP QPSK, 100G-DP-16QAM et 200G-DP-16QAM). Par rapport aux différentes techniques heuristiques, l'approche proposée réduit la probabilité de blocage des demandes arrivant dans les noeuds optiques. L'apprentissage par renforcement réarrange le spectre WDM lors de l'extraction de certains canaux, en proposant de convertir les longueurs d'onde de certains canaux actifs avec celles des canaux extraits ce qui conduit à une défragmentation du spectre. Deux scénarios ont été étudiés :

- Grille fixe : Dans ce scénario, l'algorithme RL décide d'attribuer la plupart des demandes de trafic de 100G et 200G à la DP-QPSK et DP-16-QAM, respectivement, en utilisant les fréquences les plus basses de la bande, en raison des caractéristiques de l'amplificateur.

- Grille flexible : L'algorithme RL attribue à nouveau la plupart du trafic aux créneaux de fréquences inférieures de la bande (en raison des caractéristiques de l'amplificateur). Cependant, il décide d'attribuer les demandes de trafic de 100G et de 200G au DP-16-QAM, qui occupe moins de slots fréquentiels, ce qui permet d'économiser les ressources du spectre.

Dans la deuxième partie, nous avons étudié une nouvelle génération de routeurs optiques pour des réseaux économes en énergie dans le cadre du projet ANR N-GREEN, et nous présentons ici notre contribution de caractérisation expérimentale du commutateur 2×2, composant de base du routeur optique nouvelle génération proposée.

Nous avons considéré la technologie de commutation de paquets colorés. Les travaux présentés ici ont ciblé l'une des deux principales innovations du projet NGREEN : un fond de panier WDM à ultra-haute capacité basé sur la commutation optique. Les composants fondamentaux

de ce fond de panier WDM sont les commutateurs 16 × 16 et 4 × 4, composés de commutateurs plus petits 2 × 2. Dans le cadre de N-GREEN, un commutateur optique 2 × 2 à base d'amplificateurs optiques à semi-conducteur (SOA : semiconductor optical amplifier) a été proposé et fabriqué par le III-V Lab (France). En collaboration avec deux autres partenaires du projet N-GREEN, Nokia Bell Labs (coordinateur du projet) et Télécom Paris, la caractérisation expérimentale d'un commutateur optique à 2 × 2 a été réalisée. Les expériences ont montré que la plage dynamique de la puissance d'entrée du système était élevée et que la capacité à travailler avec des signaux à haut débit était tout à fait envisageable, ouvrant des perspectives d'études d'architectures plus complexes requises pour le fond de panier, comme les commutateurs 16 × 16 et 4 × 4.

De nombreuses perspectives découlent de ce travail de thèse à savoir :

- Pour l'approche de pré-compensation de puissance RL :
  - Application de l'algorithme d'apprentissage par renforcement avec des données expérimentales.
  - Génération d'un nouveau modèle d'environnement à partir d'un grand volume de données expérimentales.
  - Mise en œuvre de modèles d'amplification plus complexes.
  - Lancement de l'optimisation de la puissance pour améliorer la qualité de fonctionnement, par exemple par l'aplatissement de l'OSNR en même temps que la réduction de l'excursion de puissance optique.
- En ce qui concerne la problématique de l'allocation optimisée des longueurs d'onde et des formats de modulation :
  - Examen des fonctions de filtrage des différents routeurs optiques d'insertion/extraction reconfigurables (ROADMs).
  - Scénarios plus complexes, y compris les capacités de routage et/ou les réseaux à grille mixte (combinaison de grilles à nœuds fixes et flexibles).

Bibliography

[1] Cisco, "Cisco annual internet report (2018–2023)", *White paper*, 2018.

[2] Sandvine, "The global internet phenomena report", 2019.

[3] X. Liu, N. Deng, M. Zhou, Y. Wang, M. Tao, L. Zhou, S. Li, H. Zeng, S. Megeed, A. Shen, and F. Effenberger, "Enabling technologies for 5G-oriented optical networks", in *2019 Optical Fiber Communications Conference and Exhibition (OFC)*, 2019, pp. 1–3.

[4] S. Herbst, J.-P. Elbers, C. Fuerst, H. Griesser, H. Wernz, and C. Glingener, "Benefits and challenges in transparent optical networks", in *Optical Transmission Systems and Equipment for WDM Networking III*, International Society for Optics and Photonics, vol. 5596, 2004, pp. 109–118.

[5] D. C. Kilper, G. Atkinson, and S. Korotky, "Optical transparency and network energy efficiency", in *2010 12th International Conference on Transparent Optical Networks*, 2010, pp. 1–1.

[6] I. Kaminow, T. Li, and A. E. Willner, *Optical fiber telecommunications VB: Systems and networks*. Elsevier, 2010.

[7] M. Ilyas and H. T. Mouftah, *The handbook of optical communication networks*. CRC press, 2003.

[8] V. López, L. Velasco, *et al.*, "Elastic optical networks", *Architectures, Technologies, and Control, Switzerland: Springer Int. Publishing*, 2016.

[9] M. Channegowda, R. Nejabati, and D. Simeonidou, "Software-defined optical networks technology and infrastructure: Enabling software-defined optical network operations", *Journal of Optical Communications and Networking*, vol. 5, no. 10, A274–A282, 2013.

[10] M. Freire, S. Mansfeld, D. Amar, F. Gillet, A. Lavignotte, and C. Lepers, "Predicting optical power excursions in erbium doped fiber amplifiers using neural networks", in *2018 Asia Communications and Photonics Conference (ACP)*, 2018, pp. 1–3.

[11] M. Freire, D. Sengupta, A. Lavignotte, C. Tremblay, and C. Lepers, "Dynamic power predistortion implementation with reinforcement learning for excursion-free amplified optical systems", in *24th International Conference on Optical Network Design and Modelling*, Barcelona, Spain, 2020.

[12] D. Amar, P. Samadi, K. Bergman, C. Lepers, M. Lourdiane, C. Ware, and P. Gravey, "Power excursion reduction in flex-grid optical networks with symbol rate adaptation", in *2017 Asia Communications and Photonics Conference (ACP)*, 2017, pp. 1–3.

[13] M. Freire, E. De Carvalho Rodrigues, A. Surampudi, F. Gillet, C. Ware, A. Lavignotte, and C. Lepers, "Experimental characterization of an SOA-based photonic integrated switch", in *2018 Asia Communications and Photonics Conference (ACP)*, 2018, pp. 1–3.

[14] F. Testa and L. Pavesi, *Optical Switching in Next Generation Data Centers*. Springer, 2017.

[15] E. Harstead and R. Sharpe, "Forecasting of access network bandwidth demands for aggregated subscribers using Monte Carlo methods", *IEEE Communications Magazine*, vol. 53, no. 3, pp. 199–207, 2015.

[16] A. Lord, A. Soppera, and A. Jacquet, "The impact of capacity growth in national telecommunications networks", *Philosophical Transactions of the Royal Society A: Mathematical, Physical and Engineering Sciences*, vol. 374, no. 2062, p. 20 140 431, 2016.

[17] A. Willner, *Optical fiber telecommunications*. Academic Press, 2019, vol. 11.

[18] A. Chralyvy, "Plenary paper: The coming capacity crunch", in *2009 35th European Conference on Optical Communication*, 2009, pp. 1–1.

[19] H. Waldman, "The impending optical network capacity crunch", in *2018 SBFoton International Optics and Photonics Conference (SBFoton IOPC)*, 2018, pp. 1–4.

[20] P. J. Winzer, D. T. Neilson, and A. R. Chraplyvy, "Fiber-optic transmission and networking: The previous 20 and the next 20 years (invited)", *Opt. Express*, vol. 26, no. 18, pp. 24 190–24 239, Sep. 2018. DOI: 10.1364/OE.26.024190. [Online]. Available: http://www.opticsexpress.org/abstract.cfm?URI=oe-26-18-24190.

[21] P. J. Winzer, "Spatial multiplexing in fiber optics: The 10x scaling of metro/core capacities", *Bell Labs Technical Journal*, vol. 19, pp. 22–30, 2014.

[22] P. J. Winzer and D. T. Neilson, "From scaling disparities to integrated parallelism: A decathlon for a decade", *Journal of Lightwave Technology*, vol. 35, no. 5, pp. 1099–1115, 2017.

[23] J. Xie, F. R. Yu, T. Huang, R. Xie, J. Liu, C. Wang, and Y. Liu, "A survey of machine learning techniques applied to software defined networking (SDN): Research issues and challenges", *IEEE Communications Surveys Tutorials*, vol. 21, no. 1, pp. 393–430, 2019.

[24] M. J. O'Mahony, D. Simeonidou, D. K. Hunter, and A. Tzanakaki, "The application of optical packet switching in future communication networks", *IEEE Communications Magazine*, vol. 39, no. 3, pp. 128–135, 2001.

[25] J. M. Simmons, *Optical network design and planning*. Springer, 2014.

[26] R. Ramaswami, K. Sivarajan, and G. Sasaki, *Optical networks: A practical perspective*. Morgan Kaufmann, 2009.

[27] I. Kaminow, T. Li, and A. Willner, "Optical fiber telecommunications volume VIB: Systems and networks", *Optics and Photonics. Burlington, MA: Elsevier Science*, 2013.

[28] *Springer Handbook of Optical Networks*, ser. Springer Handbooks. Springer International Publishing, 2020, ISBN: 978-3-030-16249-8. DOI: 10.1007/978-3-030-16250-4. [Online]. Available: http://link.springer.com/10.1007/978-3-030-16250-4.

[29] T. Watanabe, T. Goh, M. Okuno, S. Sohma, T. Shibata, M. Itoh, M. Kobayashi, M. Ishii, A. Sugita, and Y. Hibino, "Silica-based PLC 1/spl times/128 thermo-optic switch", in *Proceedings 27th European Conference on Optical Communication (Cat. No.01TH8551)*, vol. 2, 2001, 134–135 vol.2.

[30] J. Homa and K. Bala, "ROADM architectures and their enabling WSS technology", *IEEE Communications Magazine*, vol. 46, no. 7, pp. 150–154, 2008.

[31] S. Perrin, "Next-generation ROADM architectures and benefits", *Heavy Reading White Paper, Mar*, 2015.

[32] [Online]. Available: https://www.ietf.org/.

[33] L. Berger *et al.*, "Generalized multi-protocol label switching (GMPLS) signaling functional description", RFC 3471, January, Tech. Rep., 2003.

[34] S. Das, G. Parulkar, and N. McKeown, "Why Openflow/SDN can succeed where GMPLS failed", in *2012 38th European Conference and Exhibition on Optical Communications*, 2012, pp. 1–3.

[35] [Online]. Available: http://www.opennetworking.org/.

[36] S. Sezer, S. Scott-Hayward, P. K. Chouhan, B. Fraser, D. Lake, J. Finnegan, N. Viljoen, M. Miller, and N. Rao, "Are we ready for SDN? implementation challenges for software-defined networks", *IEEE Communications Magazine*, vol. 51, no. 7, pp. 36–43, 2013.

[37] Y. Li and D. C. Kilper, "Optical physical layer SDN [invited]", *IEEE/OSA Journal of Optical Communications and Networking*, vol. 10, no. 1, A110–A121, 2018.

[38] [Online]. Available: //openroadm.org/home.html.

[39] N. McKeown, T. Anderson, H. Balakrishnan, G. Parulkar, L. Peterson, J. Rexford, S. Shenker, and J. Turner, "Openflow: Enabling innovation in campus networks", *ACM SIGCOMM Computer Communication Review*, vol. 38, no. 2, pp. 69–74, 2008.

[40] F. Musumeci, C. Rottondi, A. Nag, I. Macaluso, D. Zibar, M. Ruffini, and M. Tornatore, "An overview on application of machine learning techniques in optical networks", *IEEE Communications Surveys Tutorials*, vol. 21, no. 2, pp. 1383–1408, 2019, ISSN: 2373-745X. DOI: 10.1109/COMST.2018.2880039.

[41] I. de Miguel, R. J. Durán, T. Jiménez, N. Fernández, J. C. Aguado, R. M. Lorenzo, A. Caballero, I. T. Monroy, Y. Ye, A. Tymecki, I. Tomkos, M. Angelou, D. Klonidis, A. Francescon, D. Siracusa, and E. Salvadori, "Cognitive dynamic optical networks [invited]", *IEEE/OSA Journal of Optical Communications and Networking*, vol. 5, no. 10, A107–A118, 2013.

[42] T. Jimenez, J. C. Aguado, I. de Miguel, R. J. Duran, M. Angelou, N. Merayo, P. Fernandez, R. M. Lorenzo, I. Tomkos, and E. J. Abril, "A cognitive quality of transmission estimator for core optical networks", *Journal of Lightwave Technology*, vol. 31, no. 6, pp. 942–951, 2013.

[43] C. Rottondi, L. Barletta, A. Giusti, and M. Tornatore, "Machine-learning method for quality of transmission prediction of unestablished lightpaths", *IEEE/OSA Journal of Optical Communications and Networking*, vol. 10, no. 2, A286–A297, 2018. DOI: 10.1364/JOCN.10.00A286.

[44] W. Mo, C. L. Gutterman, Y. Li, S. Zhu, G. Zussman, and D. C. Kilper, "Deep-neural-network-based wavelength selection and switching in ROADM systems", *Journal of optical communications and networking*, vol. 10, no. 10, pp. D1–D11, 2018.

[45] Y. Huang, P. B. Cho, P. Samadi, and K. Bergman, "Power excursion mitigation for flexgrid defragmentation with machine learning", *IEEE/OSA Journal of Optical Communications and Networking*, vol. 10, no. 1, A69–A76, 2018, ISSN: 1943-0639. DOI: 10.1364/JOCN.10.000A69.

[46] R. Boada, R. Borkowski, and I. T. Monroy, "Clustering algorithms for stokes space modulation format recognition", *Optics express*, vol. 23, no. 12, pp. 15 521–15 531, 2015.

[47] S. Zhang, Y. Peng, Q. Sui, J. Li, and Z. Li, "Modulation format identification in heterogeneous fiber-optic networks using artificial neural networks and genetic algorithms", *Photonic Network Communications*, vol. 32, no. 2, pp. 246–252, 2016.

[48] F. N. Khan, K. Zhong, W. H. Al-Arashi, C. Yu, C. Lu, and A. P. T. Lau, "Modulation format identification in coherent receivers using deep machine learning", *IEEE Photonics Technology Letters*, vol. 28, no. 17, pp. 1886–1889, 2016.

[49] X. Lu, M. Zhao, L. Qiao, and N. Chi, "Non-linear compensation of multi-CAP VLC system employing pre-distortion base on clustering of machine learning", in *2018 Optical Fiber Communications Conference and Exposition (OFC)*, 2018, pp. 1–3.

[50] E. Giacoumidis, S. Mhatli, M. F. C. Stephens, A. Tsokanos, J. Wei, M. E. McCarthy, N. J. Doran, and A. D. Ellis, "Reduction of nonlinear intersubcarrier intermixing in coherent optical OFDM by a fast Newton-based support vector machine nonlinear equalizer", *Journal of Lightwave Technology*, vol. 35, no. 12, pp. 2391–2397, 2017.

[51] J. Thrane, J. Wass, M. Piels, J. C. M. Diniz, R. Jones, and D. Zibar, "Machine learning techniques for optical performance monitoring from directly detected PDM-QAM signals", *Journal of Lightwave Technology*, vol. 35, no. 4, pp. 868–875, 2017. DOI: 10.1109/JLT.2016.2590989.

[52] F. Morales, M. Ruiz, L. Gifre, L. M. Contreras, V. Lopez, and L. Velasco, "Virtual network topology adaptability based on data analytics for traffic prediction", *IEEE/OSA Journal of Optical Communications and Networking*, vol. 9, no. 1, A35–A45, 2017.

[53] A. Yu, H. Yang, W. Bai, L. He, H. Xiao, and J. Zhang, "Leveraging deep learning to achieve efficient resource allocation with traffic evaluation in datacenter optical networks", in *2018 Optical Fiber Communications Conference and Exposition (OFC)*, 2018, pp. 1–3.

[54] S. Shahkarami, F. Musumeci, F. Cugini, and M. Tornatore, "Machine-learning-based soft-failure detection and identification in optical networks", in *2018 Optical Fiber Communications Conference and Exposition (OFC)*, 2018, pp. 1–3.

[55] D. Rafique, T. Szyrkowiec, A. Autenrieth, and J. Elbers, "Analytics-driven fault discovery and diagnosis for cognitive root cause analysis", in *2018 Optical Fiber Communications Conference and Exposition (OFC)*, 2018, pp. 1–3.

[56] H. Rastegarfar, M. Glick, N. Viljoen, M. Yang, J. Wissinger, L. Lacomb, and N. Peyghambarian, "TCP flow classification and bandwidth aggregation in optically interconnected data center networks", *IEEE/OSA Journal of Optical Communications and Networking*, vol. 8, no. 10, pp. 777–786, 2016.

[57] T. R. Tronco, M. Garrich, A. C. Cesar, and M. de Lacerda Rocha, "Cognitive algorithm using fuzzy reasoning for software-defined optical network", *Photonic Network Communications*, vol. 32, no. 2, pp. 281–292, 2016.

[58] J. M. Senior and M. Y. Jamro, *Optical fiber communications: Principles and practice*. Pearson Education, 2009.

[59] T. E. Stern, G. Ellinas, and K. Bala, *Multiwavelength optical networks: Architectures, design, and control*. Cambridge University Press, 2009.

[60] S. J. B. Yoo, "Energy efficiency in the future internet: The role of optical packet switching and optical-label switching", *IEEE Journal of Selected Topics in Quantum Electronics*, vol. 17, no. 2, pp. 406–418, 2011.

[61] R. S. Tucker, "Optical packet switching meets mythbusters", in *2011 Optical Fiber Communication Conference and Exposition and the National Fiber Optic Engineers Conference*, 2011, pp. 1–1.

[62] X. Qiu, "[OFC 2013 tutorial OW3G.4] burst-mode receiver technology for short synchronization", in *2013 Optical Fiber Communication Conference and Exposition and the National Fiber Optic Engineers Conference (OFC/NFOEC)*, 2013, pp. 1–28.

[63] A. Pattavina, "Architectures and performance of optical packet switching nodes for IP networks", *Journal of Lightwave Technology*, vol. 23, no. 3, pp. 1023–1032, 2005.

[64] T. S. El-Bawab, *Optical switching*. Springer Science & Business Media, 2008.

[65] H. J. S. Dorren, M. T. Hill, Y. Liu, N. Calabretta, A. Srivatsa, F. M. Huijskens, H. de Waardt, and G. D. Khoe, "Optical packet switching and buffering by using all-optical signal processing methods", *Journal of Lightwave Technology*, vol. 21, no. 1, pp. 2–12, 2003.

[66] Zhangyuan Chen, B. Pesala, and C. Chang-Hasnain, "Experimental demonstration of slow light via four-wave mixing in semiconductor optical amplifiers", in *2006 Optical Fiber Communication Conference and the National Fiber Optic Engineers Conference*, 2006, pp. 2589–2591.

[67] M. G. Herraez, Kwang-Yong Song, and L. Thevenaz, "Broad-bandwidth Brillouin slow light in optical fibers", in *2006 Optical Fiber Communication Conference and the National Fiber Optic Engineers Conference*, 2006, p. 3.

[68] Zhaoming Zhu, A. M. C. Dawes, D. J. Gauthier, Lin Zhang, and A. E. Willner, "12-GHz-bandwidth SBS slow light in optical fibers", in *2006 Optical Fiber Communication Conference and the National Fiber Optic Engineers Conference*, 2006, pp. 1–3.

[69] J. M. H. Elmirghani and H. T. Mouftah, "All-optical wavelength conversion: Technologies and applications in DWDM networks", *IEEE Communications Magazine*, vol. 38, no. 3, pp. 86–92, 2000.

[70] S. J. B. Yoo, "Wavelength conversion technologies for WDM network applications", *Journal of Lightwave Technology*, vol. 14, no. 6, pp. 955–966, 1996.

[71] M. Jinno, "All optical signal regularizing/regeneration using a nonlinear fiber Sagnac interferometer switch with signal-clock walk-off", *Journal of Lightwave Technology*, vol. 12, no. 9, pp. 1648–1659, 1994.

[72] Y. Ueno, S. Nakamura, and K. Tajima, "Penalty-free error-free all-optical data pulse regeneration at 84 Gb/s by using a symmetric-Mach-Zehnder-type semiconductor regenerator", *IEEE Photonics Technology Letters*, vol. 13, no. 5, pp. 469–471, 2001.

[73] T. Otani, T. Miyazaki, and S. Yamamoto, "40-Gb/s optical 3R regenerator using electroabsorption modulators for optical networks", *Journal of Lightwave Technology*, vol. 20, no. 2, pp. 195–200, 2002.

[74] F. Parmigiani, L. Provost, P. Petropoulos, D. J. Richardson, W. Freude, J. Leuthold, A. D. Ellis, and I. Tomkos, "Progress in multichannel all-optical regeneration based on fiber technology", *IEEE Journal of Selected Topics in Quantum Electronics*, vol. 18, no. 2, pp. 689–700, 2012.

[75] C. Ware, W. Samoud, P. Gravey, and M. Lourdiane, "Recent advances in optical and hybrid packet switching", in *2016 18th International Conference on Transparent Optical Networks (ICTON)*, 2016, pp. 1–4.

[76] D. Chiaroni, R. Urata, J. Gripp, J. E. Simsarian, G. Austin, S. Etienne, T. Segawa, Y. Pointurier, C. Simonneau, Y. Suzaki, T. Nakahara, M. Thottan, A. Adamiecki, D. Neilson, J. C. Antona, S. Bigo, R. Takahashi, and V. Radoaca, "Demonstration of the interconnection of two optical packet rings with a hybrid optoelectronic packet router", in *36th European Conference and Exhibition on Optical Communication*, 2010, pp. 1–3.

[77] R. Takahashi, T. Nakahara, Y. Suzaki, T. Segawa, H. Ishikawa, and S. Ibrahim, "Recent progress on the hybrid optoelectronic router", in *2012 International Conference on Photonics in Switching (PS)*, 2012, pp. 1–3.

[78] P. E. T. Platform, "Europe's age of light! How photonics will power growth and innovation", *Multiannual Strategic Roadmap 2021–2027*, 2019.

[79] D. Silver, T. Hubert, J. Schrittwieser, I. Antonoglou, M. Lai, A. Guez, M. Lanctot, L. Sifre, D. Kumaran, T. Graepel, *et al.*, "A general reinforcement learning algorithm that masters Chess, Shogi, and Go through self-play", *Science*, vol. 362, no. 6419, pp. 1140–1144, 2018.

[80] J. Schrittwieser, I. Antonoglou, T. Hubert, K. Simonyan, L. Sifre, S. Schmitt, A. Guez, E. Lockhart, D. Hassabis, T. Graepel, T. Lillicrap, and D. Silver, *Mastering Atari, Go, Chess and Shogi by planning with a learned model*, 2019. arXiv: 1911.08265 [cs.LG].

[81] T. M. Mitchell *et al.*, "Machine learning", *Burr Ridge, IL: McGraw Hill*, vol. 45, no. 37, pp. 870–877, 1997.

[82] I. Goodfellow, Y. Bengio, and A. Courville, *Deep learning*. MIT press, 2016.

[83] R. M. Morais and J. Pedro, "Machine learning models for estimating quality of transmission in DWDM networks", *IEEE/OSA Journal of Optical Communications and Networking*, vol. 10, no. 10, pp. D84–D99, 2018.

[84] [Online]. Available: https://www.7wdata.be/visualization/types-of-machine-learning-algorithms-2/.

[85] C. M. Bishop, *Pattern recognition and machine learning*. springer, 2006.

[86] A. Krizhevsky, I. Sutskever, and G. E. Hinton, "Imagenet classification with deep convolutional neural networks", in *Advances in neural information processing systems*, 2012, pp. 1097–1105.

[87] E. L. Thorndike, *Animal intelligence: Experimental studies*. Transaction Publishers, 1970.

[88] R. S. Sutton, A. G. Barto, *et al.*, *Introduction to reinforcement learning*. MIT press Cambridge, 1998, vol. 135.

[89] M. Lapan, *Deep reinforcement learning hands-on: Apply modern RL methods, with deep Q-networks, value iteration, policy gradients, TRPO, AlphaGo Zero and more*. Packt Publishing Ltd, 2018.

[90] J. Schulman, P. Moritz, S. Levine, M. Jordan, and P. Abbeel, *High-dimensional continuous control using generalized advantage estimation*, 2015. arXiv: 1506.02438 [cs.LG].

[91] V. Mnih, A. P. Badia, M. Mirza, A. Graves, T. P. Lillicrap, T. Harley, D. Silver, and K. Kavukcuoglu, *Asynchronous methods for deep reinforcement learning*, 2016. arXiv: 1602.01783 [cs.LG].

[92] T. P. Lillicrap, J. J. Hunt, A. Pritzel, N. Heess, T. Erez, Y. Tassa, D. Silver, and D. Wierstra, *Continuous control with deep reinforcement learning*, 2015. arXiv: 1509.02971 [cs.LG].

[93] J. Schulman, S. Levine, P. Moritz, M. I. Jordan, and P. Abbeel, *Trust region policy optimization*, 2015. arXiv: 1502.05477 [cs.LG].

[94] J. Schulman, F. Wolski, P. Dhariwal, A. Radford, and O. Klimov, *Proximal policy optimization algorithms*, 2017. arXiv: 1707.06347 [cs.LG].

[95] E. Desurvire and M. Zervas, *Erbium-doped fiber amplifiers: Principles and applications*, 1994.

[96] E. Desurvire, "Analysis of transient gain saturation and recovery in erbium-doped fiber amplifiers", *IEEE Photonics Technology Letters*, vol. 1, no. 8, pp. 196–199, 1989.

[97] Seo Yeon Park, Hyang Kyun Kim, Gap Yeol Lyu, Sun Mo Kang, and Sang-Yung Shin, "Dynamic gain and output power control in a gain-flattened erbium-doped fiber amplifier", *IEEE Photonics Technology Letters*, vol. 10, no. 6, pp. 787–789, 1998.

[98] C. Tian and S. Kinoshita, "Novel solution for transient control of WDM amplifiers using the combination of electrical feedforward and feedback", in *Summaries of Papers Presented at the Lasers and Electro-Optics. CLEO '02. Technical Diges*, vol. 1, 2002, p. 430.

[99] ——, "Analysis and control of transient dynamics of EDFA pumped by 1480- and 980-nm lasers", *Journal of Lightwave Technology*, vol. 21, no. 8, pp. 1728–1734, 2003.

[100] E. Delevaque, T. Georges, J. F. Bayon, M. Monerie, P. Niay, and P. Bernage, "Gain control in erbium-doped fibre amplifiers by lasing at 1480 nm with photoinduced bragg gratings written on fibre ends", *Electronics Letters*, vol. 29, no. 12, pp. 1112–1114, 1993.

[101] M. Zirngibl, "Gain control in erbium-doped fibre amplifiers by an all-optical feedback loop", *Electronics Letters*, vol. 27, no. 7, pp. 560–561, 1991.

[102] Srivastava, J. L. Zyskind, Y. Sun, J. Ellson, G. Newsome, R. W. Tkach, A. R. Chraplyvy, J. W. Sulhoff, T. A. Strasser, C. Wolf, and J. R. Pedrazzani, "Fast-link control protection of surviving channels in multiwavelength optical networks", *IEEE Photonics Technology Letters*, vol. 9, no. 12, pp. 1667–1669, 1997.

[103] J. Zyskind and A. Srivastava, *Optically amplified WDM networks*. Academic press, 2011.

[104] B. E. Saleh and M. C. Teich, *Fundamentals of photonics*. john Wiley & sons, 2019.

[105] S. Bigo, S. Gauchard, A. Bertaina, and J. Hamaide, "Experimental investigation of stimulated Raman scattering limitation on WDM transmission over various types of fiber infrastructures", *IEEE Photonics Technology Letters*, vol. 11, no. 6, pp. 671–673, 1999.

[106] S. Lee, *Dynamical performance of optical amplifiers for long-haul/ultra long-haul transmission systems*.

[107] L. Qiao and P. J. Vella, "ASE analysis and correction for EDFA automatic control", *Journal of Lightwave Technology*, vol. 25, no. 3, pp. 771–778, 2007.

[108] J. Junio, D. C. Kilper, and V. W. S. Chan, "Channel power excursions from single-step channel provisioning", *IEEE/OSA Journal of Optical Communications and Networking*, vol. 4, no. 9, A1–A7, 2012.

[109] V. L. da Silva, Y. Silberberg, J. S. Wang, E. L. Goldstein, and M. J. Andrejco, "Automatic gain flattening in optical fiber amplifiers via clamping of inhomogeneous gain", *IEEE Photonics Technology Letters*, vol. 5, no. 4, pp. 412–414, 1993.

[110] C. R. Giles and D. J. Di Giovanni, "Dynamic gain equalization in two-stage fiber amplifiers", *IEEE Photonics Technology Letters*, vol. 2, no. 12, pp. 866–868, 1990.

[111] R. I. Laming, J. D. Minelly, L. Dong, and M. N. Zervas, "Twincore erbium-doped fibre amplifier with passive spectral gain equalisation", *Electronics Letters*, vol. 29, no. 6, pp. 509–510, 1993.

[112] S. F. Su, R. Olshansky, G. Joyce, D. A. Smith, and J. E. Baran, "Gain equalization multiwavelength lightwave systems using acoustooptic tunable filters", *IEEE Photonics Technology Letters*, vol. 4, no. 3, pp. 269–271, 1992.

[113] K. Inoue, T. Kominato, and H. Toba, "Tunable gain equalization using a Mach-Zehnder optical filter in multistage fiber amplifiers", *IEEE Photonics Technology Letters*, vol. 3, no. 8, pp. 718–720, 1991.

[114] M. Tachibana, R. I. Laming, P. R. Morkel, and D. N. Payne, "Erbium-doped fiber amplifier with flattened gain spectrum", *IEEE Photonics Technology Letters*, vol. 3, no. 2, pp. 118–120, 1991.

[115] M. Wilkinson, A. Bebbington, S. A. Cassidy, and P. McKee, "D-fibre filter for erbium gain spectrum flattening", *Electronics Letters*, vol. 28, no. 2, pp. 131–132, 1992.

[116] R. Kashyap, R. Wyatt, and R. J. Campbell, "Wideband gain flattened erbium fibre amplifier using a photosensitive fibre blazed grating", *Electronics Letters*, vol. 29, no. 2, pp. 154–156, 1993.

[117] H. A. Macleod, *Thin-film optical filters*. CRC press, 2017.

[118] E. Desurvire, D. Bayart, B. Desthieux, S. Bigo, and E.-D. F. Amplifiers, "Device and system developments", *A Wiley-Interscience Publication, New York*, 2002.

[119] C. R. Giles and E. Desurvire, "Modeling erbium-doped fiber amplifiers", *Journal of Lightwave Technology*, vol. 9, no. 2, pp. 271–283, 1991.

[120] A. A. M. Saleh, R. M. Jopson, J. D. Evankow, and J. Aspell, "Modeling of gain in erbium-doped fiber amplifiers", *IEEE Photonics Technology Letters*, vol. 2, no. 10, pp. 714–717, 1990.

[121] I. M. I. Habbab, A. A. M. Saleh, and P. K. Runge, "Erbium-doped fiber amplifiers: Linear approximations", *Journal of Lightwave Technology*, vol. 13, no. 1, pp. 33–36, 1995.

[122] K. Ishii, J. Kurumida, and S. Namiki, "Wavelength assignment dependency of AGC EDFA gain offset under dynamic optical circuit switching", in *Optical Fiber Communication Conference*, Optical Society of America, 2014, W3E–4.

[123] K. Ishii, J. Kurumida, and S. Namiki, "Experimental investigation of gain offset behavior of feedforward-controlled WDM AGC EDFA under various dynamic wavelength allocations", *IEEE Photonics Journal*, vol. 8, no. 1, pp. 1–13, 2016.

[124] D. Baney and J. Stimple, "WDM EDFA gain characterization with a reduced set of saturating channels", *IEEE Photonics technology letters*, vol. 8, no. 12, pp. 1615–1617, 1996.

[125] S. Kulkarni, J. Medberry, and K. L. Lear, "Evaluation of nonuniform WDM source spacing for EDFA gain characterization", *IEEE Photonics Technology Letters*, vol. 14, no. 6, pp. 783–785, 2002.

[126] W. Mo, S. Zhu, Y. Li, and D. C. Kilper, "EDFA wavelength dependent gain spectrum measurement using weak optical probe sampling", *IEEE Photonics Technology Letters*, vol. 30, no. 2, pp. 177–180, 2017.

[127] S. Zhu, C. L. Gutterman, W. Mo, Y. Li, G. Zussman, and D. C. Kilper, "Machine learning based prediction of erbium-doped fiber WDM line amplifier gain spectra", in *2018 European Conference on Optical Communication (ECOC)*, IEEE, 2018, pp. 1–3.

[128] Y. Huang, W. Samoud, C. L. Gutterman, C. Ware, M. Lourdiane, G. Zussman, P. Samadi, and K. Bergman, "A machine learning approach for dynamic optical channel add/drop strategies that minimize EDFA power excursions", in *ECOC 2016; 42nd European Conference on Optical Communication*, VDE, 2016, pp. 1–3.

[129] C. L. Gutterman, W. Mo, S. Zhu, Y. Li, D. C. Kilper, and G. Zussman, "Neural network based wavelength assignment in optical switching", in *Proceedings of the Workshop on Big Data Analytics and Machine Learning for Data Communication Networks*, ACM, 2017, pp. 37–42.

[130] C. J. Bastos-Filho, E. d. A. Barboza, and J. F. Martins-Filho, "Estimating the spectral gain and the noise figure of EDFA using artificial neural networks", in *2017 19th International Conference on Transparent Optical Networks (ICTON)*, IEEE, 2017, pp. 1–4.

[131] S. Zhu, C. Gutterman, A. D. Montiel, J. Yu, M. Ruffini, G. Zussman, and D. Kilper, "Hybrid machine learning EDFA model", in *2020 Optical Fiber Communications Conference and Exhibition (OFC)*, 2020, pp. 1–3.

[132] E. d. A. Barboza, C. J. Bastos-Filho, J. F. Martins-Filho, U. C. de Moura, and J. R. de Oliveira, "Self-adaptive erbium-doped fiber amplifiers using machine learning", in *2013 SBMO/IEEE MTT-S International Microwave & Optoelectronics Conference (IMOC)*, IEEE, 2013, pp. 1–5.

[133] U. Moura, M. Garrich, H. Carvalho, M. Svolenski, A. Andrade, A. C. Cesar, J. Oliveira, and E. Conforti, "Cognitive methodology for optical amplifier gain adjustment in dynamic DWDM networks", *Journal of Lightwave Technology*, vol. 34, no. 8, pp. 1971–1979, 2016.

[134] E. d. A. Barboza, M. J. da Silva, L. D. Coelho, C. J. Bastos-Filho, and J. F. Martins Filho, "Amplifier adaptive control of operating point considering non-linear interference", *IEEE Photonics Technology Letters*, vol. 30, no. 6, pp. 573–576, 2018.

[135] J. Oliveira, A. Caballero, E. Magalhães, U. Moura, R. Borkowski, G. Curiel, A. Hirata, L. Hecker, E. Porto, D. Zibar, J. Maranhão, I. T. Monroy, and J. Oliveira, "Demonstration of EDFA cognitive gain control via GMPLS for mixed modulation formats in heterogeneous optical networks", in *2013 Optical Fiber Communication Conference and Exposition and the National Fiber Optic Engineers Conference (OFC/NFOEC)*, 2013, pp. 1–3. DOI: 10.1364/OFC.2013.OW1H.2.

[136] E. d. A. Barboza, C. J. Bastos-Filho, J. F. Martins Filho, M. J. da Silva, L. D. Coelho, U. C. de Moura, and J. R. de Oliveira, "Local and global approaches for the adaptive control of a cascade of amplifiers", *Photonic Network Communications*, vol. 33, no. 2, pp. 194–207, 2017.

[137] E. d. A. Barboza, M. J. da Silva, L. D. Coelho, J. F. Martins-Filho, C. J. A. Bastos-Filho, U. C. de Moura, and J. R. F. de Oliveira, "Impact of nonlinear effects on the performance of 120 Gb/s 64 QAM optical system using adaptive control of cascade of amplifiers", in *2015 SBMO/IEEE MTT-S International Microwave and Optoelectronics Conference (IMOC)*, 2015, pp. 1–5. DOI: 10.1109/IMOC.2015.7369212.

[138] A. S. Ahsan, C. Browning, M. S. Wang, K. Bergman, D. C. Kilper, and L. P. Barry, "Excursion-free dynamic wavelength switching in amplified optical networks", *Journal of Optical Communications and Networking*, vol. 7, no. 9, pp. 898–905, 2015.

[139] W. Mo, S. Zhu, Y. Li, and D. C. Kilper, "Dual-wavelength source based optical circuit switching and wavelength reconfiguration in multi-hop ROADM systems", *Optics express*, vol. 25, no. 22, pp. 27 736–27 749, 2017.

[140] A. Chraplyvy, J. Nagel, and R. Tkach, "Equalization in amplified WDM lightwave transmission systems", *IEEE Photonics Technology Letters*, vol. 4, no. 8, pp. 920–922, 1992.

[141] M. Menif, L. A. Rusch, and M. Karasek, "Application of preemphasis to achieve flat output OSNR in time-varying channels in cascaded EDFAs without equalization", *Journal of Lightwave Technology*, vol. 19, no. 10, pp. 1440–1452, 2001. DOI: 10.1109/50.956131.

[142] Y. Pan and L. Pavel, "Global convergence of an iterative gradient algorithm for the nash equilibrium in an extended OSNR game", in *IEEE INFOCOM 2007 - 26th IEEE International Conference on Computer Communications*, 2007, pp. 206–212. DOI: 10.1109/INFCOM.2007.32.

[143] L. Pavel, "OSNR optimization in optical networks: Modeling and distributed algorithms via a central cost approach", *IEEE Journal on Selected Areas in Communications*, vol. 24, no. 4, pp. 54–65, 2006.

[144] E. Ciaramella, L. Giorgi, A. D'Errico, F. Cavaliere, G. Gaimari, and G. Prati, "A highly effective technique for setting the power preemphasis in WDM optical systems", *Journal of Lightwave Technology*, vol. 24, no. 1, pp. 342–356, 2006. DOI: 10.1109/JLT.2005.859857.

[145] M. R. Sena, J. R. Mendes, R. C. Almeida, and P. J. F. C. Souza, "An evolutionary method to optimize OSNR margin in elastic optical channels subject to nonlinear physical impairments", in *2018 SBFoton International Optics and Photonics Conference (SBFoton IOPC)*, 2018, pp. 1–5. DOI: 10.1109/SBFoton-IOPC.2018.8610891.

[146] I. Roberts, J. M. Kahn, and D. Boertjes, "Convex channel power optimization in nonlinear WDM systems using gaussian noise model", *Journal of Lightwave Technology*, vol. 34, no. 13, pp. 3212–3222, 2016. DOI: 10.1109/JLT.2016.2569073.

[147] J. Burgmeier, A. Cords, B. Stummer, *et al.*, "A black box model of EDFA's operating in WDM systems", *Journal of lightwave technology*, vol. 16, no. 7, p. 1271, 1998.

[148] VPI Photonics, *VPIphotonics: Simulation software and design services*. [Online]. Available: https://www.vpiphotonics.com/index.php.

[149] ITU Recommendation, "G. 694.1 spectral grids for WDM applications: DWDM frequency grid", *International Telecommunications Union, Tech. Rep*, 2012.

[150] M. Abadi, P. Barham, J. Chen, Z. Chen, A. Davis, J. Dean, M. Devin, S. Ghemawat, G. Irving, M. Isard, *et al.*, "Tensorflow: A system for large-scale machine learning", in *12th {USENIX} Symposium on Operating Systems Design and Implementation ({OSDI} 16)*, 2016, pp. 265–283.

[151] D. P. Kingma and J. Ba, *Adam: A method for stochastic optimization*, 2014. arXiv: 1412.6980 [cs.LG].

[152] L. Matignon, G. J. Laurent, and N. Le Fort-Piat, "Reward function and initial values: Better choices for accelerated goal-directed reinforcement learning", in *International Conference on Artificial Neural Networks*, Springer, 2006, pp. 840–849.

[153] A. Hill, A. Raffin, M. Ernestus, A. Gleave, A. Kanervisto, R. Traore, P. Dhariwal, C. Hesse, O. Klimov, A. Nichol, M. Plappert, A. Radford, J. Schulman, S. Sidor, and Y. Wu, *Stable baselines*, https://github.com/hill-a/stable-baselines, 2018.

[154] P. Dhariwal, C. Hesse, O. Klimov, A. Nichol, M. Plappert, A. Radford, J. Schulman, S. Sidor, Y. Wu, and P. Zhokhov, *OpenAI Baselines*, https://github.com/openai/baselines, 2017.

[155] G. Bosco, V. Curri, A. Carena, P. Poggiolini, and F. Forghieri, "On the performance of Nyquist-WDM terabit superchannels based on PM-BPSK, PM-QPSK, PM-8QAM or PM-16QAM subcarriers", *Journal of Lightwave Technology*, vol. 29, no. 1, pp. 53–61, 2011.

[156] H. Venghaus and N. Grote, *Fibre optic communication: Key devices*. Springer, 2017, vol. 161.

[157] K. Christodoulopoulos, K. Manousakis, and E. Varvarigos, "Offline routing and wavelength assignment in transparent WDM networks", *IEEE/ACM Transactions on Networking*, vol. 18, no. 5, pp. 1557–1570, 2010.

[158] H. Zang, J. P. Jue, B. Mukherjee, *et al.*, "A review of routing and wavelength assignment approaches for wavelength-routed optical WDM networks", *Optical networks magazine*, vol. 1, no. 1, pp. 47–60, 2000.

[159] B. Jaumard, C. Meyer, and B. Thiongane, "ILP formulations for the routing and wavelength assignment problem: symmetric systems", in *Handbook of Optimization in Telecommunications*, M. G. C. Resende and P. M. Pardalos, Eds. Boston, MA: Springer US, 2006, pp. 637–677, ISBN: 978-0-387-30165-5. DOI: 10.1007/978-0-387-30165-5_23. [Online]. Available: https://doi.org/10.1007/978-0-387-30165-5_23.

[160] B. Jaumard, C. Meyer, and B. Thiongane, "Comparison of ILP formulations for the RWA problem", *Optical Switching and Networking*, vol. 4, no. 3-4, pp. 157–172, 2007.

[161] D. Banerjee and B. Mukherjee, "A practical approach for routing and wavelength assignment in large wavelength-routed optical networks", *IEEE Journal on Selected Areas in Communications*, vol. 14, no. 5, pp. 903–908, 1996.

[162] I. Chlamtac, A. Ganz, and G. Karmi, "Lightpath communications: An approach to high bandwidth optical WAN's", *IEEE Transactions on Communications*, vol. 40, no. 7, pp. 1171–1182, 1992.

[163] M. S. Kumar and P. S. Kumar, "Static lightpath establishment in WDM networks—New ILP formulations and heuristic algorithms", *Computer Communications*, vol. 25, no. 1, pp. 109–114, 2002.

[164] S. Baroni, P. Bayvel, and R. J. Gibbens, "On the number of wavelengths in arbitrarily-connected wavelength-routed optical networks", in *Optical Networks and Their Applications*, Optical Society of America, 1998, MN2.

[165] B. Chen, G. N. Rouskas, and R. Dutta, "On hierarchical traffic grooming in WDM networks", *IEEE/ACM Transactions on Networking*, vol. 16, no. 5, pp. 1226–1238, 2008.

[166] H. Siregar, H. Takagi, and Y. Zhang, "Efficient routing and wavelength assignment in wavelength-routed optical networks", in *Proc. 7th Asia-Pacific Network Oper. and Mgmt Symposium*, 2003, pp. 116–127.

[167] S. Subramaniam and R. A. Barry, "Wavelength assignment in fixed routing WDM networks", in *Proceedings of ICC'97 - International Conference on Communications*, vol. 1, 1997, 406–410 vol.1.

[168] Xijun Zhang and Chunming Qiao, "Wavelength assignment for dynamic traffic in multi-fiber WDM networks", in *Proceedings 7th International Conference on Computer Communications and Networks (Cat. No.98EX226)*, 1998, pp. 479–485.

[169] A. Birman and A. Kershenbaum, "Routing and wavelength assignment methods in single-hop all-optical networks with blocking", in *Proceedings of INFOCOM'95*, vol. 2, 1995, 431–438 vol.2.

[170] S. Pachnicke, T. Paschenda, and P. M. Krummrich, "Physical impairment based regenerator placement and routing in translucent optical networks", in *OFC/NFOEC 2008 - 2008 Conference on Optical Fiber Communication/National Fiber Optic Engineers Conference*, 2008, pp. 1–3.

[171] B. Ramamurthy, D. Datta, H. Feng, J. P. Heritage, and B. Mukherjee, "Impact of transmission impairments on the teletraffic performance of wavelength-routed optical networks", *Journal of Lightwave Technology*, vol. 17, no. 10, pp. 1713–1723, 1999.

[172] H. A. Pereira, D. A. R. Chaves, C. J. A. Bastos-Filho, and J. F. Martins-Filho, "Impact of physical layer impairments in all-optical networks", in *2007 SBMO/IEEE MTT-S International Microwave and Optoelectronics Conference*, 2007, pp. 536–541.

[173] Yurong Huang, J. P. Heritage, and B. Mukherjee, "Connection provisioning with transmission impairment consideration in optical WDM networks with high-speed channels", *Journal of Lightwave Technology*, vol. 23, no. 3, pp. 982–993, 2005.

[174] R. Cardillo, V. Curri, and M. Mellia, "Considering transmission impairments in configuring wavelength routed optical networks", in *2006 Optical Fiber Communication Conference and the National Fiber Optic Engineers Conference*, 2006, p. 3.

[175] S. Zsigmond, G. Németh, and T. Cinkler, "Mutual impact of physical impairments and grooming in multilayer networks", in *International IFIP Conference on Optical Network Design and Modeling*, Springer, 2007, pp. 38–47.

[176] Jun He, M. Brandt-Pearce, Y. Pointurier, C. L. Brown, and S. Subramaniam, "Adaptive wavelength assignment using wavelength spectrum separation for distributed optical networks", in *2007 IEEE International Conference on Communications*, 2007, pp. 2406–2411.

[177] J. He, M. Brandt-Pearce, and S. Subramaniam, "QoS-aware wavelength assignment with BER and latency guarantees for crosstalk limited networks", in *2007 IEEE International Conference on Communications*, 2007, pp. 2336–2341.

[178] J. He, M. Brandt-Pearce, Y. Pointurier, and S. Subramaniam, "QoT-aware routing in impairment-constrained optical networks", in *IEEE GLOBECOM 2007 - IEEE Global Telecommunications Conference*, 2007, pp. 2269–2274.

[179] A. Marsden, A. Maruta, and K. Kitayama, "Routing and wavelength assignment encompassing FWM in WDM lightpath networks", in *2008 International Conference on Optical Network Design and Modeling*, 2008, pp. 1–6.

[180] G. S. Pavani, L. G. Zuliani, H. Waldman, and M. Magalhaes, "Distributed approaches for impairment-aware routing and wavelength assignment algorithms in GMPLS networks", *Computer Networks*, vol. 52, no. 10, pp. 1905–1915, 2008.

[181] G. Markidis, S. Sygletos, A. Tzanakaki, and I. Tomkos, "Impairment-constraint-based routing in ultralong-haul optical networks with 2R regeneration", *IEEE Photonics Technology Letters*, vol. 19, no. 6, pp. 420–422, 2007.

[182] E. Marin, S. Sanchez, X. Masip, J. Sole, G. Maier, W. Erangoli, S. Santoni, and M. Quagliotti, "Applying prediction concepts to routing on semi-transparent optical transport networks", in *2007 9th International Conference on Transparent Optical Networks*, vol. 3, 2007, pp. 32–36.

[183] S. Pachnicke, T. Paschenda, and P. Krummrich, "Assessment of a constraint-based routing algorithm for translucent 10 Gbits/s DWDM networks considering fiber nonlinearities", *Journal of Optical Networking*, vol. 7, no. 4, pp. 365–377, 2008.

[184] P. Kulkarni, A. Tzanakaki, C. M. Machuka, and I. Tomkos, "Benefits of Q-factor based routing in WDM metro networks", in *2005 31st European Conference on Optical Communication, ECOC 2005*, vol. 4, 2005, 981–982 vol.4.

[185] T. Deng and S. Subramaniam, "Adaptive QoS routing in dynamic wavelength-routed optical networks", in *2nd International Conference on Broadband Networks, 2005.*, 2005, 184–193 Vol. 1.

[186] Xi Yang, Lu Shen, and B. Ramamurthy, "Survivable lightpath provisioning in WDM mesh networks under shared path protection and signal quality constraints", *Journal of Lightwave Technology*, vol. 23, no. 4, pp. 1556–1567, 2005.

[187] J. F. Martins-Filho, C. J. A. Bastos-Filho, E. A. J. Arantes, S. C. Oliveira, L. D. Coelho, J. P. G. de Oliveira, R. G. Dante, E. Fontana, and F. D. Nunes, "Novel routing algorithm for transparent optical networks based on noise figure and amplifier saturation", in *Proceedings of the 2003 SBMO/IEEE MTT-S International Microwave and Optoelectronics Conference - IMOC 2003. (Cat. No.03TH8678)*, vol. 2, 2003, 919–923 vol.2.

[188] A. Coiro, M. Listanti, and A. Valenti, "Dynamic power-aware routing and wavelength assignment for green WDM optical networks", in *2011 IEEE international conference on communications (ICC)*, IEEE, 2011, pp. 1–6.

[189] A. Morea, N. Brogard, F. Leplingard, J.-C. Antona, T. Zami, B. Lavigne, and D. Bayart, "QoT function and A* routing: An optimized combination for connection search in translucent networks", *Journal of Optical Networking*, vol. 7, no. 1, pp. 42–61, 2008.

[190] Y. Zhai, Y. Pointurier, S. Subramaniam, and M. Brandt-Pearce, "QoS-aware RWA algorithms for path-protected DWDM networks", in *OFC/NFOEC 2007 - 2007 Conference on Optical Fiber Communication and the National Fiber Optic Engineers Conference*, 2007, pp. 1–3.

[191] E. M. G. de Queiroz and A. C. César, "A heuristic approach for border node selection and traffic routing in multi-domain optical networks", *Optical Switching and Networking*, vol. 15, pp. 87–96, 2015.

[192] M. A. C. Lima, A. C. Cesar, and A. F. R. Araujo, "Optical network optimization with transmission impairments based on genetic algorithm", in *Proceedings of the 2003 SBMO/IEEE MTT-S International Microwave and Optoelectronics Conference - IMOC 2003. (Cat. No.03TH8678)*, vol. 1, 2003, 361–365 vol.1.

[193] I. Tomkos, D. Vogiatzis, C. Mas, I. Zacharopoulos, A. Tzanakaki, and E. Varvarigos, "Performance engineering of metropolitan area optical networks through impairment constraint routing", *IEEE Communications Magazine*, vol. 42, no. 8, S40–S47, 2004.

[194] N. Sengezer and E. Karasan, "Static lightpath establishment in multilayer traffic engineering under physical layer impairments", *IEEE/OSA Journal of Optical Communications and Networking*, vol. 2, no. 9, pp. 662–677, 2010.

[195] P. Pavon-Marino, S. Azodolmolky, R. Aparicio-Pardo, B. Garcia-Manrubia, Y. Pointurier, M. Angelou, J. Sole-Pareta, J. Garcia-Haro, and I. Tomkos, "Offline impairment aware RWA algorithms for cross-layer planning of optical networks", *Journal of Lightwave Technology*, vol. 27, no. 12, pp. 1763–1775, 2009.

[196] W. Zhang, J. Tang, K. Nygard, and C. Wang, "REPARE: Regenerator placement and routing establishment in translucent networks", in *GLOBECOM 2009 - 2009 IEEE Global Telecommunications Conference*, 2009, pp. 1–7.

[197] Sang-Wan Kim, Seung-Woo Seo, and Seong Cheol Kim, "Regenerator placement algorithms for connection establishment in all-optical networks", in *Globecom '00 - IEEE. Global Telecommunications Conference. Conference Record (Cat. No.00CH37137)*, vol. 2, 2000, 1205–1209 vol.2.

[198] H. Zang, R. Huang, and J. Pan, "Methodologies on designing a hybrid shared-mesh-protected WDM network with sparse wavelength conversion and regeneration", in *Optical Networking II*, International Society for Optics and Photonics, vol. 4910, 2002, pp. 188–196.

[199] A. Szodenyi, S. Zsigmond, B. Megyer, and T. Cinkler, "Design of traffic grooming optical virtual private networks obeying physical limitations", in *Second IFIP International Conference on Wireless and Optical Communications Networks, 2005. WOCN 2005.*, 2005, pp. 221–225.

[200] N. Sengezer and E. Karasan, "Multi-layer virtual topology design in optical networks under physical layer impairments and multi-hour traffic demand", *IEEE/OSA Journal of Optical Communications and Networking*, vol. 4, no. 2, pp. 78–91, 2012.

[201] J. Shao, X. Liang, and S. Kumar, "Comparison of split-step Fourier schemes for simulating fiber optic communication systems", *IEEE Photonics Journal*, vol. 6, no. 4, pp. 1–15, 2014.

[202] K. V. Peddanarappagari and M. Brandt-Pearce, "Volterra series transfer function of single-mode fibers", *Journal of Lightwave Technology*, vol. 15, no. 12, pp. 2232–2241, 1997.

[203] A. Splett, C. Kurtzke, and K. Petermann, "Ultimate transmission capacity of amplified optical fiber communication systems taking into account fiber nonlinearities", 1993.

[204] P. Poggiolini, "The GN model of non-linear propagation in uncompensated coherent optical systems", *Journal of Lightwave Technology*, vol. 30, no. 24, pp. 3857–3879, 2012.

[205] G. Bosco, A. Carena, V. Curri, P. Poggiolini, and F. Forghieri, "Performance limits of Nyquist-WDM and CO-OFDM in high-speed PM-QPSK systems", *IEEE Photonics Technology Letters*, vol. 22, no. 15, pp. 1129–1131, 2010.

[206] P. Poggiolini, G. Bosco, A. Carena, V. Curri, Y. Jiang, and F. Forghieri, "The GN-model of fiber non-linear propagation and its applications", *Journal of Lightwave Technology*, vol. 32, no. 4, pp. 694–721, 2014.

[207] P. Poggiolini, G. Bosco, A. Carena, R. Cigliutti, V. Curri, F. Forghieri, R. Pastorelli, and S. Piciaccia, "The LOGON strategy for low-complexity control plane implementation in new-generation flexible networks", in *2013 Optical Fiber Communication Conference and Exposition and the National Fiber Optic Engineers Conference (OFC/NFOEC)*, 2013, pp. 1–3.

[208] S. Azodolmolky, J. Perelló, M. Angelou, F. Agraz, L. Velasco, S. Spadaro, Y. Pointurier, A. Francescon, C. V. Saradhi, P. Kokkinos, E. Varvarigos, S. A. Zahr, M. Gagnaire, M. Gunkel, D. Klonidis, and I. Tomkos, "Experimental demonstration of an impairment aware network planning and operation tool for transparent/translucent optical networks", *Journal of Lightwave Technology*, vol. 29, no. 4, pp. 439–448, 2011.

[209] Y. Qin, K. C. S. Cheng, J. Triay, E. Escalona, G. S. Zervas, G. Zarris, N. Amaya-Gonzalez, C. Cervelló-Pastor, R. Nejabati, and D. Simeonidou, "Demonstration of C/S based hardware accelerated QoT estimation tool in dynamic impairment-aware optical network", in *36th European Conference and Exhibition on Optical Communication*, 2010, pp. 1–3.

[210] Y. Pointurier, "Design of low-margin optical networks", in *2016 Optical Fiber Communications Conference and Exhibition (OFC)*, 2016, pp. 1–3.

[211] A. Morea, T. Zami, and F. Leplingard, "Introduction of confidence levels for transparent network planning", in *2009 35th European Conference on Optical Communication*, 2009, pp. 1–2.

[212] F. Leplingard, A. Morea, T. Zami, and N. Brogard, "Interest of an adaptive margin for the Quality of Transmission estimation for lightpath establishment", in *2009 Conference on Optical Fiber Communication - incudes post deadline papers*, 2009, pp. 1–3.

[213] S. Azodolmolky, Y. Pointurier, M. Angelou, D. Careglio, J. Solé-Pareta, and I. Tomkos, "A novel impairment aware RWA algorithm with consideration of QoT estimation inaccuracy", *IEEE/OSA Journal of Optical Communications and Networking*, vol. 3, no. 4, pp. 290–299, 2011.

[214] S. Oda, M. Miyabe, S. Yoshida, T. Katagiri, Y. Aoki, T. Hoshida, J. C. Rasmussen, M. Birk, and K. Tse, "A learning living network with open ROADMs", *Journal of Lightwave Technology*, vol. 35, no. 8, pp. 1350–1356, 2017.

[215] E. Seve, J. Pesic, C. Delezoide, and Y. Pointurier, "Learning process for reducing uncertainties on network parameters and design margins", in *2017 Optical Fiber Communications Conference and Exhibition (OFC)*, 2017, pp. 1–3.

[216] A. Mahajan, R. Martínez, and R. Muñoz, "Machine learning assisted EDFA gain ripple modelling for accurate QoT estimation", 2019.

[217] M. Bouda, S. Oda, O. Vasilieva, M. Miyabe, S. Yoshida, T. Katagiri, Y. Aoki, T. Hoshida, and T. Ikeuchi, "Accurate prediction of quality of transmission with dynamically configurable optical impairment model", in *2017 Optical Fiber Communications Conference and Exhibition (OFC)*, 2017, pp. 1–3.

[218] N. Sambo, Y. Pointurier, F. Cugini, L. Valcarenghi, P. Castoldi, and I. Tomkos, "Lightpath establishment assisted by offline QoT estimation in transparent optical networks", *IEEE/OSA Journal of Optical Communications and Networking*, vol. 2, no. 11, pp. 928–937, 2010.

[219] D. B. Chua, E. D. Kolaczyk, and M. Crovella, "Network kriging", *IEEE Journal on Selected Areas in Communications*, vol. 24, no. 12, pp. 2263–2272, 2006.

[220] H. H. Song, L. Qiu, and Y. Zhang, "NetQuest: A flexible framework for large-scale network measurement", *IEEE/ACM Transactions on Networking*, vol. 17, no. 1, pp. 106–119, 2009.

[221] A. Coates, A. O. Hero III, R. Nowak, and Bin Yu, "Internet tomography", *IEEE Signal Processing Magazine*, vol. 19, no. 3, pp. 47–65, 2002.

[222] M. Angelou, Y. Pointurier, D. Careglio, S. Spadaro, and I. Tomkos, "Optimized monitor placement for accurate QoT assessment in core optical networks", *IEEE/OSA Journal of Optical Communications and Networking*, vol. 4, no. 1, pp. 15–24, 2012.

[223] I. Sartzetakis, K. Christodoulopoulos, C. P. Tsekrekos, D. Syvridis, and E. Varvarigos, "Estimating QoT of unestablished lightpaths", in *2016 Optical Fiber Communications Conference and Exhibition (OFC)*, 2016, pp. 1–3.

[224] ——, "Quality of transmission estimation in WDM and elastic optical networks accounting for space–spectrum dependencies", *IEEE/OSA Journal of Optical Communications and Networking*, vol. 8, no. 9, pp. 676–688, 2016.

[225] Y. Pointurier, M. Coates, and M. Rabbat, "Cross-layer monitoring in transparent optical networks", *IEEE/OSA Journal of Optical Communications and Networking*, vol. 3, no. 3, pp. 189–198, 2011.

[226] A. Caballero, J. C. Aguado, R. Borkowski, S. Saldaña, T. Jiménez, I. de Miguel, V. Arlunno, R. J. Durán, D. Zibar, J. B. Jensen, R. M. Lorenzo, E. J. Abril, and I. T. Monroy, "Experimental demonstration of a cognitive quality of transmission estimator for optical communication systems", in *2012 38th European Conference and Exhibition on Optical Communications*, 2012, pp. 1–3.

[227] L. Barletta, A. Giusti, C. Rottondi, and M. Tornatore, "QoT estimation for unestablished lighpaths using machine learning", in *2017 Optical Fiber Communications Conference and Exhibition (OFC)*, 2017, pp. 1–3.

[228] J. Mata, I. de Miguel, R. J. Durán, J. C. Aguado, N. Merayo, L. Ruiz, P. Fernández, R. M. Lorenzo, and E. J. Abril, "A SVM approach for lightpath QoT estimation in optical transport networks", in *2017 IEEE International Conference on Big Data (Big Data)*, 2017, pp. 4795–4797.

[229] S. Aladin and C. Tremblay, "Cognitive tool for estimating the QoT of new lightpaths", in *2018 Optical Fiber Communications Conference and Exposition (OFC)*, 2018, pp. 1–3.

[230] C. Tremblay and S. Aladin, "Machine learning techniques for estimating the quality of transmission of lightpaths", in *2018 IEEE Photonics Society Summer Topical Meeting Series (SUM)*, 2018, pp. 237–238.

[231] A. A. Díaz-Montiel, J. Yu, W. Mo, Y. Li, D. C. Kilper, and M. Ruffini, "Performance analysis of QoT estimator in SDN-controlled ROADM networks", in *2018 International Conference on Optical Network Design and Modeling (ONDM)*, 2018, pp. 142–147.

[232] A. A. Dıaz-Montiel, S. Aladin, C. Tremblay, and M. Ruffini, "Active wavelength load as a feature for QoT estimation based on support vector machine", p. 6,

[233] T. Panayiotou, G. Ellinas, and S. P. Chatzis, "A data-driven QoT decision approach for multicast connections in metro optical networks", in *2016 International Conference on Optical Network Design and Modeling (ONDM)*, 2016, pp. 1–6.

[234] T. Panayiotou, S. P. Chatzis, and G. Ellinas, "Performance analysis of a data-driven quality-of-transmission decision approach on a dynamic multicast- capable metro optical network", *IEEE/OSA Journal of Optical Communications and Networking*, vol. 9, no. 1, pp. 98–108, 2017.

[235] S. Yan, F. N. Khan, A. Mavromatis, D. Gkounis, Q. Fan, F. Ntavou, K. Nikolovgenis, F. Meng, E. H. Salas, C. Guo, C. Lu, A. P. T. Lau, R. Nejabati, and D. Simeonidou, "Field trial of machine-learning-assisted and SDN-based optical network planning with network-scale monitoring database", in *2017 European Conference on Optical Communication (ECOC)*, 2017, pp. 1–3. DOI: 10.1109/ECOC.2017.8346091.

[236] D. Wang, M. Zhang, Z. Li, J. Li, M. Fu, Y. Cui, and X. Chen, "Modulation format recognition and OSNR estimation using CNN-based deep learning", *IEEE Photonics Technology Letters*, vol. 29, no. 19, pp. 1667–1670, 2017.

[237] T. Tanimura, T. Hoshida, J. C. Rasmussen, M. Suzuki, and H. Morikawa, "OSNR monitoring by deep neural networks trained with asynchronously sampled data", in *2016 21st OptoElectronics and Communications Conference (OECC) held jointly with 2016 International Conference on Photonics in Switching (PS)*, 2016, pp. 1–3.

[238] T. Tanimura, T. Hoshida, T. Kato, S. Watanabe, and H. Morikawa, "Data-analytics-based optical performance monitoring technique for optical transport networks", in *2018 Optical Fiber Communications Conference and Exposition (OFC)*, 2018, pp. 1–3.

[239] R. Proietti, X. Chen, A. Castro, G. Liu, H. Lu, K. Zhang, J. Guo, Z. Zhu, L. Velasco, and S. J. B. Yoo, "Experimental demonstration of cognitive provisioning and alien wavelength monitoring in multi-domain EON", in *2018 Optical Fiber Communications Conference and Exposition (OFC)*, 2018, pp. 1–3.

[240] W. Mo, Y. Huang, S. Zhang, E. Ip, D. C. Kilper, Y. Aono, and T. Tajima, "ANN-based transfer learning for QoT prediction in real-time mixed line-rate systems", in *2018 Optical Fiber Communications Conference and Exposition (OFC)*, 2018, pp. 1–3.

[241] R. Shankar, M. Florjańczyk, T. J. Hall, A. Vukovic, and H. Hua, "Multi-degree ROADM based on wavelength selective switches: Architectures and scalability", *Optics Communications*, vol. 279, no. 1, pp. 94–100, 2007.

[242] F. Heismann, "System requirements for WSS filter shape in cascaded ROADM networks", in *2010 Conference on Optical Fiber Communication (OFC/NFOEC), collocated National Fiber Optic Engineers Conference*, 2010, pp. 1–3.

[243] C. Pulikkaseril, L. A. Stewart, M. A. Roelens, G. W. Baxter, S. Poole, and S. Frisken, "Spectral modeling of channel band shapes in wavelength selective switches", *Optics express*, vol. 19, no. 9, pp. 8458–8470, 2011.

[244] R. Kudo, T. Kobayashi, K. Ishihara, Y. Takatori, A. Sano, and Y. Miyamoto, "Coherent optical single carrier transmission using overlap frequency domain equalization for long-haul optical systems", *Journal of Lightwave Technology*, vol. 27, no. 16, pp. 3721–3728, 2009, ISSN: 0733-8724. DOI: 10.1109/JLT.2009.2024091.

[245] S. J. Savory, "Digital filters for coherent optical receivers", *Opt. Express*, vol. 16, no. 2, pp. 804–817, 2008. DOI: 10.1364/OE.16.000804. [Online]. Available: http://www.opticsexpress.org/abstract.cfm?URI=oe-16-2-804.

[246] H. Louchet, K. Kuzmin, and A. Richter, "Improved DSP algorithms for coherent 16-QAM transmission", in *2008 34th European Conference on Optical Communication*, 2008, pp. 1–2. DOI: 10.1109/ECOC.2008.4729195.

[247] M. Selmi, Y. Jaouen, and P. Ciblat, "Accurate digital frequency offset estimator for coherent polmux QAM transmission systems", in *2009 35th European Conference on Optical Communication*, 2009, pp. 1–2.

[248] G. Bosco, A. Carena, V. Curri, P. Poggiolini, E. Torrengo, and F. Forghieri, "Investigation on the robustness of a Nyquist-WDM terabit superchannel to transmitter and receiver non-idealities", in *36th European Conference and Exhibition on Optical Communication*, 2010, pp. 1–3. DOI: 10.1109/ECOC.2010.5621166.

[249] A. Mitra, A. Lord, S. Kar, and P. Wright, "Effect of link margins and frequency granularity on the performance and modulation format sweet spot of multiple flexgrid optical networks", in *OFC 2014*, 2014, pp. 1–3. DOI: 10.1364/OFC.2014.Th4E.3.

[250] A. Carena, V. Curri, G. Bosco, P. Poggiolini, and F. Forghieri, "Modeling of the impact of nonlinear propagation effects in uncompensated optical coherent transmission links", *Journal of Lightwave Technology*, vol. 30, no. 10, pp. 1524–1539, 2012, ISSN: 0733-8724. DOI: 10.1109/JLT.2012.2189198.

[251] J. P. Gordon and L. F. Mollenauer, "Effects of fiber nonlinearities and amplifier spacing on ultra-long distance transmission", *Journal of Lightwave Technology*, vol. 9, no. 2, pp. 170–173, 1991, ISSN: 0733-8724. DOI: 10.1109/50.65874.

[252] T. Ahmed, S. Rahman, M. Tornatore, X. Yu, K. Kim, and B. Mukherjee, "Dynamic routing and spectrum assignment in co-existing fixed/flex-grid optical networks", in *2018 IEEE International Conference on Advanced Networks and Telecommunications Systems (ANTS)*, IEEE, 2018, pp. 1–3.

[253] M. Zhang, C. You, and Z. Zhu, "On the parallelization of spectrum defragmentation reconfigurations in elastic optical networks", *IEEE/ACM Transactions on Networking*, vol. 24, no. 5, pp. 2819–2833, 2016. DOI: 10.1109/TNET.2015.2487366.

[254] E. J. Dávalos, M. F. Romero, S. M. Galeano, D. A. Báez, A. Leiva, and B. Baran, "Spectrum defragmentation in elastic optical networks: Two approaches with metaheuristics", *IEEE Access*, vol. 7, pp. 119 835–119 843, 2019. DOI: 10.1109/ACCESS.2019.2937032.

[255] S. P. Singh and D. P. Bertsekas, "Reinforcement learning for dynamic channel allocation in cellular telephone systems", in *Advances in neural information processing systems*, 1997, pp. 974–980.

[256] C. Ware and D. Chiaroni, "Towards WDM slot switching for aggregation access and metropolitan applications: The ANR N-GREEN project", in *2017 19th International Conference on Transparent Optical Networks (ICTON)*, 2017, pp. 1–4.

[257] K. Padmanabhan and A. Netravali, "Dilated networks for photonic switching", *IEEE Transactions on Communications*, vol. 35, no. 12, pp. 1357–1365, 1987.

[258] C. Clos, "A study of non-blocking switching networks", *The Bell System Technical Journal*, vol. 32, no. 2, pp. 406–424, 1953.

[259] S.-J. Chua and B. Li, *Optical Switches: Materials and Design*. Elsevier, 2010.

[260] D. E. Sene, J. W. Grantham, V. M. Bright, and J. H. Comtois, "Development and characterization of micro-mechanical gratings for optical modulation", in *Proceedings of Ninth International Workshop on Micro Electromechanical Systems*, 1996, pp. 222–227.

[261] Sangyoon Han, Tae Joon Seok, N. Quack, B. Yoo, and M. C. Wu, "Monolithic 50×50 MEMS silicon photonic switches with microsecond response time", in *OFC 2014*, 2014, pp. 1–3.

[262] [Online]. Available: https://agiltron.com/product/mems-32x32-fiber-optical-switch/.

[263] C. Technologies, *Product user guide – "S320 photonic switch getting started guide"*.

[264] [Online]. Available: https://www.eospace.com/high-speed-switch-matrices.

[265] [Online]. Available: https://www.eospace.com/high-speed-switch.

[266] EpiPhotonics, *Nano-second speed 1xN optical switches*. [Online]. Available: http://epiphotonics.com/1xN_Optical_Switches.html.

[267] ——, *Nano-second speed NxN optical switches*. [Online]. Available: http://epiphotonics.com/NxN_Optical_Switches.html.

[268] Finisar, *Single wavelength selective switch (WSS)*, 2018.

[269] *I-QS041-5C10V5-x5-ST3 Q-switch*. [Online]. Available: https://gandh.com/product/i-qs041-5c10v5-x5-st3-q-switch/.

[270] [Online]. Available: https://www.ntt-electronics.com/en/products/photonics/nxn_n_o_m_s.html.

[271] [Online]. Available: https://agiltron.com/category/fiber-optic-switches/high-reliability-optical-switches-crystalatch/.

[272] Thorlabs, *High-speed optical shutter/switch*. [Online]. Available: https://www.thorlabs.com/newgrouppage9.cfm?objectgroup_id=4336&pn=SOA1013SXS.

[273] M. C. Wu, O. Solgaard, and J. E. Ford, "Optical MEMS for lightwave communication", *Journal of Lightwave Technology*, vol. 24, no. 12, pp. 4433–4454, 2006.

[274] D. Miller and H. Ozaktas, "Limit to the bit-rate capacity of electrical interconnects from the aspect ratio of the system architecture", *Journal of Parallel and Distributed Computing*, vol. 41, no. 1, pp. 42–52, 1997, ISSN: 07437315. DOI: 10.1006/jpdc.1996.1285.

[275] M. Stucchi, S. Cosemans, J. Van Campenhout, Z. Tőkei, and G. Beyer, "On-chip optical interconnects versus electrical interconnects for high-performance applications", *Microelectronic Engineering*, vol. 112, pp. 84–91, 2013, ISSN: 01679317. DOI: 10.1016/j.mee.2013.03.080.

[276] Hoyeol Cho, P. Kapur, and K. C. Saraswat, "Power comparison between high-speed electrical and optical interconnects for interchip communication", *Journal of Lightwave Technology*, vol. 22, no. 9, pp. 2021–2033, 2004.

[277] Guoqing Chen, Hui Chen, M. Haurylau, N. Nelson, D. Albonesi, P. M. Fauchet, and E. G. Friedman, "Electrical and optical on-chip interconnects in scaled microprocessors", in *2005 IEEE International Symposium on Circuits and Systems*, 2005, 2514–2517 Vol. 3.

[278] N. Farrington, G. Porter, S. Radhakrishnan, H. H. Bazzaz, V. Subramanya, Y. Fainman, G. Papen, and A. Vahdat, "Helios: A hybrid electrical/optical switch architecture for modular data centers", in *Proceedings of the ACM SIGCOMM 2010 conference*, 2010, pp. 339–350.

[279] G. Wang, D. G. Andersen, M. Kaminsky, K. Papagiannaki, T. E. Ng, M. Kozuch, and M. Ryan, "C-Through: Part-time optics in data centers", *SIGCOMM Comput. Commun. Rev.*, vol. 40, no. 4, pp. 327–338, 2010, ISSN: 0146-4833. DOI: 10.1145/1851275.1851222. [Online]. Available: https://doi.org/10.1145/1851275.1851222.

[280] A. Michaels and E. Yablonovitch, "Reinventing circuit boards with high density optical interconnects", in *2016 IEEE Photonics Society Summer Topical Meeting Series (SUM)*, 2016, pp. 68–69.

[281] K. Chen, A. Singla, A. Singh, K. Ramachandran, L. Xu, Y. Zhang, X. Wen, and Y. Chen, "OSA: An optical switching architecture for data center networks with unprecedented flexibility", *IEEE/ACM Transactions on Networking*, vol. 22, no. 2, pp. 498–511, 2014.

[282] L. Dittmann, C. Develder, D. Chiaroni, F. Neri, F. Callegati, W. Koerber, A. Stavdas, M. Renaud, A. Rafel, J. Sole-Pareta, W. Cerroni, N. Leligou, L. Dembeck, B. Mortensen, M. Pickavet, N. Le Sauze, M. Mahony, B. Berde, and G. Eilenberger, "The european IST project DAVID: A viable approach toward optical packet switching", *IEEE Journal on Selected Areas in Communications*, vol. 21, no. 7, pp. 1026–1040, 2003.

[283] D. Chiaroni, "Optical packet add/drop multiplexers for packet ring networks", in *2008 34th European Conference on Optical Communication*, 2008, pp. 1–4.

[284] D. Chiaroni, G. Buforn, C. Simonneau, J. Antona, A. Gravey, B. Uscumlic, P. Gravey, D. Barth, and C. Cadere, "Cost and performance issues of a packet-optical add/drop multiplexer technology", in *2009 International Conference on Photonics in Switching*, 2009, pp. 1–2.

[285] D. Chiaroni, G. B. Santamaria, C. Simonneau, S. Etienne, J. Antona, S. Bigo, and J. Simsarian, "Packet OADMS for the next generation of ring networks", *Bell Labs Technical Journal*, vol. 14, no. 4, pp. 265–283, 2010.

[286] N. Wada, "New generation of optical packet switching network based on multi-colored packets", in *2009 11th International Conference on Transparent Optical Networks*, 2009, pp. 1–4.

[287] D. Chiaroni and B. Uscumlic, "Potential of WDM packets", in *2017 International Conference on Optical Network Design and Modeling (ONDM)*, 2017, pp. 1–6.

[288] D. Derickson, C. Hentschel, and J. Vobis, *Fiber optic test and measurement*. Prentice Hall PTR New Jersey, 1998, vol. 8.

[289] R. A. Shafik, M. S. Rahman, and A. R. Islam, "On the extended relationships among EVM, BER and SNR as performance metrics", in *2006 International Conference on Electrical and Computer Engineering*, 2006, pp. 408–411.

[290] R. Bonk, G. Huber, T. Vallaitis, S. Koenig, R. Schmogrow, D. Hillerkuss, R. Brenot, F. Lelarge, G.-H. Duan, S. Sygletos, C. Koos, W. Freude, and J. Leuthold, "Linear semiconductor optical amplifiers for amplification of advanced modulation formats", *Opt. Express*, vol. 20, no. 9, pp. 9657–9672, 2012. DOI: 10.1364/OE.20.009657. [Online]. Available: http://www.opticsexpress.org/abstract.cfm?URI=oe-20-9-9657.

[291] L. Ebringer and S. C. Petler, *Burst mode receiver*, US Patent 6,094,464, 2000.

[292] N. Calabretta, W. Miao, K. Mekonnen, and K. Prifti, "SOA based photonic integrated WDM cross-connects for optical metro-access networks", *Applied Sciences*, vol. 7, no. 9, p. 865, 2017.

[293] S. Kasap and P. Capper, *Springer handbook of electronic and photonic materials*. Springer, 2017.

[294] M. J. Digonnet, *Rare-earth-doped fiber lasers and amplifiers, revised and expanded*. CRC press, 2001.

[295] M. Yamane and Y. Asahara, *Glasses for photonics*. Cambridge University Press, 2000.

[296] C. R. Giles and D. Di Gioanni, "Spectral dependence of gain and noise in erbium-doped fiber amplifiers", *IEEE Photonics Technology Letters*, vol. 2, no. 11, pp. 797–800, 1990.

[297] W. L. Barnes, R. I. Laming, E. J. Tarbox, and P. R. Morkel, "Absorption and emission cross section of Er/sup 3+/ doped silica fibers", *IEEE Journal of Quantum Electronics*, vol. 27, no. 4, pp. 1004–1010, 1991.

[298] R. Hui, "Chapter 5 - Optical amplifiers", in *Introduction to Fiber-Optic Communications*, R. Hui, Ed., Academic Press, 2020, pp. 155–207, ISBN: 978-0-12-805345-4. DOI: https://doi.org/10.1016/B978-0-12-805345-4.00005-6. [Online]. Available: http://www.sciencedirect.com/science/article/pii/B9780128053454000056.

[299] A. E. Siegman, "Lasers university science books", *Mill Valley, CA*, vol. 37, no. 208, p. 169, 1986.

[300] [Online]. Available: http://en.optipedia.info/lsource-index/fiberlaser-index/fiberamp/rdfiber-amp/.

[301] N. Grote and H. Venghaus, *Fibre optic communication devices*. Springer Science & Business Media, 2012, vol. 4.

[302] Y. Sun, J. L. Zyskind, A. K. Srivastava, and L. Zhang, "Analytical formula for the transient response of erbium-doped fiber amplifiers", *Applied optics*, vol. 38, no. 9, pp. 1682–1685, 1999.

[303] A. K. Srivastava, Y. Sun, J. L. Zyskind, and J. W. Sulhoff, "EDFA transient response to channel loss in WDM transmission system", *IEEE Photonics Technology Letters*, vol. 9, no. 3, pp. 386–388, 1997.

[304] Y. Sun, J. L. Zyskind, and A. K. Srivastava, "Average inversion level, modeling, and physics of erbium-doped fiber amplifiers", *IEEE Journal of Selected Topics in Quantum Electronics*, vol. 3, no. 4, pp. 991–1007, 1997.

[305] M. J. Connelly, *Semiconductor optical amplifiers*. Springer Science & Business Media, 2007.

[306] W. Qiang *et al.*, *Semiconductor optical amplifiers*. World scientific, 2013.

[307] T. P. Pearsall, *Photonics essentials*. Society of Photo Optical, 2006.

[308] B. D. Guenther and D. Steel, *Encyclopedia of modern optics*. Academic Press, 2018.

[309] A. Stavdas, *Core and metro networks*. John Wiley & Sons, 2010.

[310] T. Saitoh and T. Mukai, "Recent progress in semiconductor laser amplifiers", *Journal of Lightwave Technology*, vol. 6, no. 11, pp. 1656–1664, 1988.

[311] M. J. O'Mahony, "Semiconductor laser optical amplifiers for use in future fiber systems", *Journal of Lightwave Technology*, vol. 6, no. 4, pp. 531–544, 1988.

[312] M. Adams, H. Westlake, M. O'Mahony, and I. Henning, "A comparison of active and passive optical bistability in semiconductors", *IEEE Journal of Quantum Electronics*, vol. 21, no. 9, pp. 1498–1504, 1985.